



UCL

On the Synthesis and Chemical Vapour Deposition of Group 13 Precursors Towards Metal Oxide Thin Films

This thesis is submitted in partial fulfilment of the requirements
for the Degree of Doctor of Philosophy (Chemistry)

Leanne Grace Bloor

Supervised by Professor C. J. Carmalt and Professor I. P. Parkin

University College London
Christopher Ingold Laboratories,
20 Gordon Street,
WC1H 0AJ

2012

I, Leanne G. Bloor, confirm that the work presented in this thesis is my own. Where information has been derived from other sources, I confirm that this has been indicated in the thesis.

Abstract

This work is concerned with the synthesis and characterisation of precursors to group 13 metal oxide thin films, their subsequent deposition *via* aerosol assisted chemical vapour deposition (AACVD), and functional testing for the applications of these resultant thin films.

The synthesis and characterisation of novel gallium bis(alkoxides) of the type $[\text{GaCl}(\text{OR})_2]$ ($\text{R} = \text{CH}_2\text{CH}_2\text{NMe}_2$ (**2**); $\text{CH}_2\text{CH}_2\text{NEt}_2$ (**3**); $\text{CH}_2\text{CH}_2\text{CH}_2\text{NMe}_2$ (**5**)) is described. The two-step reaction of gallium trichloride and two equivalents of lithium dimethylamide, followed by amide/alcohol exchange was utilised for the formations of **2**, **3** and **5**. Compounds **2**, **3**, and **5** were found to be diastereotopic and ^1H NMR investigation was conducted. $[\text{GaCl}_2(\text{OCH}_2\text{CH}_2\text{NEt}_2)]_2$ (**4**) was also formed as a by-product during the synthesis of **3**. The two-step amido/alkoxide exchange route was also used to synthesise heteroleptic gallium alkoxides of the formula $[\text{Ga}(\text{OR})_2(\text{OR}')]_n$ ($\text{R} = \text{CH}_2\text{CH}_2\text{NMe}_2$ and $\text{R}' = \text{Me}$, $n = 2$ (**8**), Et , $n = 1$ (**9**), ^iPr , $n = 1$ (**10**); $\text{R} = \text{CH}_2\text{CH}_2\text{NEt}_2$ and $\text{R}' = ^i\text{Pr}$, $n = 1$ (**12**)) from starting materials **2** and **3**. Additionally compounds of the type $[\text{Ga}(\text{OR})\text{Cl}(\text{O}^t\text{Bu})]$ ($\text{R} = \text{CH}_2\text{CH}_2\text{NMe}_2$ (**11a**); $\text{CH}_2\text{CH}_2\text{NEt}_2$ (**13a**)) were formed on the addition of *tert*-butanol to compounds **2** and **3**.

The thermal decomposition and successful AACVD of compounds **2**, **3**, **5**, **8** and **11a** were investigated and the subsequent Ga_2O_3 thin films were characterised. Precursors were dissolved in toluene and deposited onto glass and quartz at temperatures of 450-550 °C *via* AACVD. The as-deposited gallium oxide films were transparent, amorphous thin films. Subsequent annealing at 1000 °C in air crystallised the films which were monoclinic $\beta\text{-Ga}_2\text{O}_3$. EDXA confirmed the Ga_2O_3 film composition and SEM showed very smooth morphology before annealing and a crystallite size increase after annealing. Optical measurements of **2**, **3** and **5** show films have similar transparency to glass and the band gap was calculated to be 3.8-3.7 eV, suggesting some additional doping had occurred.

In situ single-source precursors were also used to deposit In_2O_3 thin films. The indium amido/alcohol exchange reaction was employed as the precursor to these films using stoichiometric quantities of each to allow small incorporation of nitrogen into the

indium oxide lattice. $[\text{In}\{\text{N}^t\text{Bu}(\text{SiMe}_3)\}_3]$ was used with $\text{HOCH}_2\text{CH}_2\text{NMe}_2$ and thin, transparent and adherent films were deposited. These films obtained were crystalline cubic In_2O_3 at all temperatures. XPS analysis showed films had a metal to oxygen ratio of 1:1.5 confirming the formation of In_2O_3 . XPS also showed films had 1.5-5.5 atomic% interstitial nitrogen incorporation suggesting nitrogen-doped $\text{In}_2\text{O}_3:\text{N}$ films. SEM analysis showed temperature, solvent used and substrate have an effect on morphology.

Optical measurements reveal that the hexane deposited samples transmitted 64-79% of visible light, whereas toluene deposited samples transmitted only 33-36% of visible light. The band gaps of the $\text{In}_2\text{O}_3:\text{N}$ films were calculated to be between 2.9-3.1 eV, which is a reduction compared to the literature values for undoped In_2O_3 of 3.5 eV. Films deposited using hexane were shown to have contact angles to water droplets of 75-110° whereas films deposited using toluene had contact angles of 40-100°. After irradiation, In_2O_3 on titanium deposited using hexane became the only notable hydrophilic sample with a contact angle to a water droplet of 12°. Films deposited on stainless steel or titanium substrates exposed to solar radiation evolved H_2 at rates of 2-11 $\mu\text{mol hr}^{-1}\text{m}^{-2}$ and were unchanged after testing.

The gas sensing response of indium oxide sensors to a number of reducing and oxidising gases was studied. In_2O_3 nanopowders and $\text{In}_2\text{O}_3:\text{Ta}$ thin films show selectivity towards the reducing gas ethanol over other gases. In_2O_3 nanopowders produced from continuous hydrothermal flow synthesis (CHFS) had the greatest response at 14.7 to 20 ppm of ethanol compared to the $\text{In}_2\text{O}_3:\text{Ta}$ sensors prepared by AACVD with a response of 7.9 also to 20 ppm ethanol. This is due to the larger surface area of the nanopowders providing more surface sites for gases to adsorb, compared to the thin films. However both sensors show a greater response to ethanol than other previously reported nanomaterial indium oxide sensors.

Acknowledgements

I would firstly like to thank my very patient and understanding supervisors Claire and Ivan for all their input, leadership and support during my PhD and of course for appointing me as the PhD student for this project at UCL. I'd also like to thank the EPSRC for the studentship.

I thank past and current members of UCL especially Dr. Caroline Knapp for her support on both an academic and personal level, and never allowing a dull day to pass. Dr. David Pugh for his endless guidance and that encyclopaedia brain of his and solving the crystal structures in this work, Dr. Geoff Hyett for his help with materials characterisation and chats about food and theatre. Dr. Chris Blackman for his help with materials chemistry and Dr. Russell Binions for the collaborative work in gas sensing, wonderful academic support and speed of returning a paper/chapter back for corrections.

I would also like to thank the people who helped me with the many technical issues I have had: Lisa Harris for providing an immediate mass spectrometry service – you are a star! Jill Maxwell for elemental analysis, Martin Vickers for his help with X-ray diffraction and the general improvements with the whole service. Steve Firth for his help with TGA, Ayo for her remarkable electronics skills during gas sensing and Kevin Reeves for his help with SEM analysis, good supply of music and dry sense of humour. Special thanks to Dr. Abil Aliev for his help with NMR and DFT calculations.

I would also like to thank the 'behind the scenes' staff, without whom my PhD day to day life wouldn't be as pleasant. Dave Knapp and Joe Nolan for their constant help over the three years. Mike Williams for his brilliant glass blowing skills, Phil Hayes and Dr. Ian Watts for their help in teaching labs. All the lads in the workshop for the rig equipment and Charles Willoughby and Dave Ladd for their IT help.

I'd like to especially thank Prof. Andrea Sella, Dr. Dewi Lewis and Dr. Wendy Brown for their support and advice in running the outreach activities at UCL as well as external events that have been very enjoyable to be a part of.

Thank you to Sofia Elouali for her preparation of the indium nanopowder gas sensors and help with water-splitting measurements. Also to Joe Manzi, the best project student a PhD student could ever hope for, for providing indium oxide gas sensors and brightening up each day. Thank you to past and present members of UCL, with special thanks to (in chronological order) Dr. Kris Page, Dr. Charlie Dunnill, Dr. Tegan Thomas, Dr. Luanne Alice, Sanjay Sathasivam, Savio Moniz, Charlie Hunston, Danvinder Bachu, Dr. Rachael Hazael, Ralph Leech, Dr. Nathan Hollingsworth, Pete Marchand and Penny Carmichael. Special thanks to Anna Roffey and Allie Cross for being there when times were at their worst.

Finally I'd like to thank my family and friends. Lin and Glyn Bloor, my Mum and Dad for their endless patience and emotional (and financial) support. My brother Simon Bloor, Great Uncle John and Great Aunt Betty for being important influences in my life. Maren Burrowes for her amazing understanding, support and advice, and to Stephen Bailey, whose inspiration has become an invaluable gift in my life.

Contents

ABSTRACT	III
ACKNOWLEDGEMENTS.....	V
CONTENTS	VI
LIST OF FIGURES	X
LIST OF SCHEMES	XIV
LIST OF TABLES.....	XVI
ABBREVIATIONS.....	XVII
1. INTRODUCTION.....	2
1.1. Band theory.....	2
1.1.1. Semiconductors.....	5
1.1.2. Effect of dopants	6
1.1.3. Direct and indirect band gap semiconductors.....	7
1.2. Film deposition.....	8
1.2.1. Chemical vapour deposition.....	9
1.3. Applications.....	18
1.3.1. Metal oxide semiconductor gas sensing.....	19
1.3.2. Transparent conducting oxides.....	19
1.3.3. Photovoltaics and water splitting.....	20
1.4. Summary	20
2. SYNTHESIS.....	23
2.1. Introduction	23
2.1.1. Gallium mono(alkoxides)	24
2.1.2. Indium mono(alkoxides).....	29

2.1.3.	Gallium bis(alkoxides).....	32
2.1.4.	Indium bis(alkoxides).....	35
2.1.5.	Gallium tris(alkoxides).....	35
2.1.6.	Indium tris(alkoxides).....	38
2.1.7.	Summary.....	39
2.2.	Results and Discussion	40
2.2.1.	Reaction of trimethyl gallium and two equivalents of alcohol	41
2.2.2.	Attempted synthesis of $[\text{Ga}(\text{iPr})(\text{OR})_2]$ via the alkoxide/alcohol exchange route	41
2.2.3.	Attempted synthesis of $[\text{GaCl}(\text{OR})_2]$ using a lithiated alkoxide	42
2.2.4.	Synthesis of chloro gallium alkoxides via chloro gallium amide intermediates	43
2.2.5.	Gallium bis(alkoxides).....	44
2.2.6.	Nuclear magnetic resonance studies of chloro gallium bis(alkoxide) complexes	51
2.2.7.	Heteroleptic gallium alkoxides.....	57
2.2.8.	Summary of reactions	64
2.2.9.	Attempted Synthesis of Gallium bis(β -diketonate) Complexes.....	65
2.3.	Conclusion	68
2.4.	Experimental.....	70
2.4.1.	General Procedures.....	70
2.4.2.	Physical Measurements.....	70
3.	CVD OF GALLIUM OXIDE THIN FILMS.....	79
3.1.	Precursors to gallium oxide.....	79
3.1.1.	Monodentate alkoxides	79
3.1.2.	Donor-functionalised alkoxides.....	84
3.2.	Results and Discussion	91
3.3.	Gallium oxide thin films from gallium bis(alkoxides)	92
3.3.1.	Thermal decomposition analysis	92
3.3.2.	Decomposition pathway.....	96
3.3.3.	CVD of Chloro Gallium Bis(alkoxide) Precursors	97
3.3.4.	Summary.....	100
3.4.	Gallium oxide thin films from heteroleptic gallium alkoxides	101
3.4.1.	TGA of heteroleptic gallium alkoxides.....	101
3.4.2.	Ga_2O_3 thin films from heteroleptic gallium alkoxides	102
3.4.3.	Summary.....	105

3.5.	Conclusion	105
3.6.	Experimental	107
3.6.1.	General Procedures – AACVD	107
3.6.2.	Analysis Techniques.....	108
4.	CVD OF INDIUM OXIDE THIN FILMS	110
4.1.	Precursors to indium oxide	110
4.1.1.	Monodentate alkoxides	110
4.1.2.	Donor-functionalised alkoxides.....	113
4.2.	Results and Discussion	117
4.2.1.	CVD of indium oxide thin films.....	117
4.2.2.	X-ray powder diffraction studies.....	120
4.2.3.	Film Composition.....	121
4.2.4.	Film morphology.....	125
4.2.5.	Optical measurements.....	127
4.2.6.	Electrical properties.....	128
4.2.7.	Water contact angle measurements.....	128
4.2.8.	Hydrogen evolution	130
4.3.	Conclusion	132
4.4.	Experimental	134
4.4.1.	General Procedures – AACVD	134
4.4.2.	Analysis Techniques.....	135
5.	GAS SENSING	138
5.1.	Metal Oxide Semiconductor Gas Sensors	138
5.1.1.	Indium Oxide Gas Sensors.....	140
5.2.	Gas sensing of nano-indium oxides prepared <i>via</i> continuous hydrothermal flow synthesis	141
5.2.1.	Background.....	141
5.2.2.	Sensor characterisation	142
5.2.3.	Summary.....	150
5.3.	Gas sensing of tantalum- and titanium- doped indium oxide thin films <i>via</i> AACVD	151
5.3.1.	Background.....	151
5.3.2.	Sensor characterisation	152

5.3.3. Summary.....	159
5.4. Conclusions	159
5.5. Experimental.....	160
5.5.1. Preparation of nano-indium oxides <i>via</i> continuous hydrothermal flow synthesis.....	162
5.5.2. Gas sensing of tantalum and titanium-doped indium oxide thin films <i>via</i> AACVD.....	163
6. CONCLUSIONS AND FUTURE WORK.....	166
6.1. Conclusions	166
6.2. Future work	170
7. REFERENCES.....	172
8. PUBLICATIONS	185
9. APPENDIX - CRYSTALLOGRAPHIC DATA.....	186

List of Figures

Figure 1.1. The derivation of band theory <i>via</i> cumulative addition of atomic/molecular orbitals.....	3
Figure 1.2. Density of states representation of a half filled band.....	4
Figure 1.3. Density of states diagrams illustrating the differences between a semimetal, semiconductor and insulator.....	5
Figure 1.4. Intrinsic <i>p</i> -type and <i>n</i> -type extrinsic semiconductors.	7
Figure 1.5. The difference between direct (left) and indirect (right) transitions in semiconductor materials.....	8
Figure 1.6. The thin film deposition process in CVD.....	10
Figure 1.7. The three main types of film growth.....	14
Figure 1.8. Schematic of an AACVD rig.....	18
Figure 2.1. A series of known gallium mono(alkoxides) incorporating donor-functionalised ligands. ^{11, 20, 57, 69-71}	26
Figure 2.2. Crystal structure of $[\text{GaCl}_2(\text{OC}(\text{CH}_3)_2\text{CH}_2\text{OMe})_2]$. ⁷²	27
Figure 2.3. A series of gallium monoalkoxide complexes synthesised by Willner <i>et al.</i> Compounds a-f are monomers whereas compounds g and h are dimers.....	27
Figure 2.4. View along the <i>z</i> -axis of $[\text{GaMe}_2(\text{O}(\text{CH}_2)_3\text{NHMe})]$ (c) showing a chain formation by N-H \cdots O hydrogen bonds. ⁷³	28
Figure 2.5. A series of indium monoalkoxide complexes synthesised by Basharat <i>et al.</i>	31
Figure 2.6. Crystal structure of $[\text{InCl}_2(\text{OC}(\text{CH}_3)_2\text{CH}_2\text{OMe})_2]$. ¹⁹	32
Figure 2.7. Crystal structure of $[\text{GaCl}(\text{OCH}_2\text{CH}_2\text{NMe}_2)_2]$. ⁷²	34
Figure 2.8. Structure of $[\text{GaCl}(\text{NMe}_2)_2]_2$ (1) showing terminal and bridging -NMe ₂ groups.....	44
Figure 2.9. ORTEP diagram of $[\text{GaCl}(\text{OCH}_2\text{CH}_2\text{NEt}_2)_2]$ (3) with thermal ellipsoids drawn at 50 % probability. H atoms are omitted for clarity.....	46
Figure 2.10. ORTEP diagram of $[\text{GaCl}_2(\text{OCH}_2\text{CH}_2\text{NEt}_2)_2]$ (4) with thermal ellipsoids drawn at 50 % probability. H atoms are omitted for clarity. Symmetry code: (i) 2-x, -y, 1-z.	49
Figure 2.11. ORTEP diagram of $[\text{GaCl}(\text{OCH}_2\text{CH}_2\text{CH}_2\text{NMe}_2)_2]$ (5) with thermal ellipsoids drawn at 50 % probability. H atoms are omitted for clarity.	51

Figure 2.12. ^1H NMR spectra of $[\text{GaCl}(\text{OR}_2)_2]$ in CD_2Cl_2 where $\text{R} = \text{CH}_2\text{CH}_2\text{NMe}_2$ (2) bottom; $\text{CH}_2\text{CH}_2\text{NEt}_2$ (3) middle; $\text{CH}_2\text{CH}_2\text{CH}_2\text{NMe}_2$ (5) top; collected at 293, 233 and 213 K respectively. Note: for 5 , hydrogen signal H_{2b} is hidden underneath signal H_{4a} .	52
Figure 2.13. Variable temperature ^1H NMR spectra of 5 in toluene- d_8 over temperatures between 213 and 373 K. The spectrum at 213 K shows the correct chemical shift and the subsequent spectra have been staggered for clarity.	54
Figure 2.14. Variable temperature ^1H NMR of 5 in toluene- d_8 over temperatures between 253 and 261 K to determine the coalescence temperature	55
Figure 2.15. Dynamic exchange expected for 5 based on DFT calculations. Colour key: gallium - pink, chlorine - green, oxygen - red, carbon - black, and nitrogen - blue.	56
Figure 2.16. Possible mechanism for the dynamic exchange expected for 5	57
Figure 2.17. Proposed structure of $[\text{Ga}(\text{OCH}_2\text{CH}_2\text{NMe}_2)_2(\text{NR}_2)]$; $\text{R} = \text{Me}$, 6 ; SiMe_3 , 7 .	59
Figure 2.18. Proposed structure of a) $[\text{Ga}(\text{OCH}_2\text{CH}_2\text{NR}_2)_2(\text{OR}')]$. ($\text{R} = \text{Me}$, $\text{R}' = \text{Me}$, 8 ; Et , 9 , $i\text{Pr}$, 10 ; $\text{R} = \text{Et}$, $\text{R}' = i\text{Pr}$, 12 and b) $[\text{GaCl}(\text{OCH}_2\text{CH}_2\text{NR}_2)(\text{O}^t\text{Bu})]$ ($\text{R} = \text{Me}$, 11a ; Et , 13a)	60
Figure 3.1. Structure of $[\text{Ga}(\text{OR})_3]_n$ as a dimer for large R groups ($n = 2$, $\text{R} = ^t\text{Bu}$) and a tetramer for small R groups ($n = 4$, $\text{R} = \text{Et}$)	80
Figure 3.2. Diagram showing the gas-phase structure of compound 24 as determined by GED	87
Figure 3.3. SEM image of Ga_2O_3 grown by AACVD of $[\text{Ga}(\text{OCH}_2\text{CH}_2\text{OMe})_3]_2$. ¹⁰	90
Figure 3.4. TGA and DSC of $[\text{GaCl}(\text{OCH}_2\text{CH}_2\text{NMe}_2)_2]$ (2)	94
Figure 3.5. TGA and DSC of $[\text{GaCl}(\text{OCH}_2\text{CH}_2\text{NEt}_2)_2]$ (3)	95
Figure 3.6. TGA and DSC of $[\text{GaCl}(\text{OCH}_2\text{CH}_2\text{CH}_2\text{NMe}_2)_2]$ (5)	96
Figure 3.7. X-ray powder diffraction pattern of monoclinic $\beta\text{-Ga}_2\text{O}_3$ as obtained from depositing $[\text{GaCl}(\text{OCH}_2\text{CH}_2\text{NMe}_2)_2]$ (2) into quartz substrates and annealing for 12 hours at 1000 °C.	99
Figure 3.8. SEM images of gallium oxide thin films a) $[\text{GaCl}(\text{OCH}_2\text{CH}_2\text{NMe}_2)_2]$ (2), b) $[\text{GaCl}(\text{OCH}_2\text{CH}_2\text{NEt}_2)_2]$ (3) and c) $[\text{GaCl}(\text{OCH}_2\text{CH}_2\text{CH}_2\text{NMe}_2)_2]$ (5) deposited by AACVD in toluene at 450 °C. Images <i>x</i> i show the as-deposited amorphous films on SiCO coated float glass. Images <i>x</i> ii show the annealed films on quartz.	100
Figure 3.9. Typical TGA of heteroleptic gallium alkoxide. The TGA of $[\text{Ga}(\text{OCH}_2\text{CH}_2\text{NMe}_2)_2(\text{OMe})]$ (8) is shown here.	102

Figure 3.10. SEM images of Ga ₂ O ₃ thin films deposited from a) [Ga(OCH ₂ CH ₂ NMe ₂) ₂ (OMe)] (8) from DCM, b) [GaCl(OCH ₂ CH ₂ NMe ₂)(O ^{<i>t</i>} Bu)] (11a) from DCM and c) [GaCl(OCH ₂ CH ₂ NMe ₂)(O ^{<i>t</i>} Bu)] (11a) from toluene. Images x) i show as-deposited films on SiCO coated float glass, images x) ii show films after annealing at 1000 °C on quartz.	104
Figure 4.1. ORTEP diagram of the indium cluster [In ₅ (μ ₅ -O)(μ ₃ -O ^{<i>i</i>} Pr) ₄ (μ ₂ -O ^{<i>i</i>} Pr) ₄ (O ^{<i>i</i>} Pr) ₅]. Hydrogen and carbon atoms omitted for clarity; the oxo anion (O1) is at the centre of the cluster. ¹⁴⁷	111
Figure 4.2. An ORTEP diagram of the indium alkoxide [InMe ₂ (OCH(CH ₂ CH ₂ NMe ₂)CH ₂ NMe ₂)] ₂ showing an unusual coordination mode whereby both “arms” bind to different metal centres. H atoms omitted for clarity. ¹⁹ ..	115
Figure 4.3. XRD pattern of In ₂ O ₃ :N thin film deposited by hexane at 450 °C on SiCO coated float glass. A typical X-ray powder diffraction spectrum obtained for In ₂ O ₃ thin films.	121
Figure 4.4. Indium XPS 3d peaks from a sample of nitrogen-doped indium oxide formed from the reaction of [In{N ^{<i>t</i>} Bu(SiMe ₃) ₃ }] ₃ and 3 HOCH ₂ CH ₂ NMe ₂ with hexane, at 450 °C on SiCO float glass.....	122
Figure 4.5. Oxygen 1s XPS peaks from a sample of nitrogen-doped indium oxide formed from the reaction of [In{N ^{<i>t</i>} Bu(SiMe ₃) ₃ }] ₃ and 3 HOCH ₂ CH ₂ NMe ₂ with hexane, at 450 °C on SiCO float glass.....	123
Figure 4.6. Nitrogen 1s XPS peaks from a sample of nitrogen-doped indium oxide formed from the reaction of [In{N ^{<i>t</i>} Bu(SiMe ₃) ₃ }] ₃ and 3 HOCH ₂ CH ₂ NMe ₂ with hexane, at 450 °C on SiCO float glass.....	124
Figure 4.7. In ₂ O ₃ thin film deposited from [In{NPh(SiMe ₃) ₃ }] ₃ and 3 HOME using toluene at 450 °C, deposited on SiCO coated float glass. A typical SEM of amorphous In ₂ O ₃ deposited using [In{N(SiMe ₃) ₂ }] ₃ or [In{NPh(SiMe ₃) ₃ }] ₃ <i>via</i> conditions outlined in Table 4.1.....	125
Figure 4.8. SEM images of In ₂ O ₃ :N deposited on glass at different temperatures using hexane or toluene.....	126
Figure 4.9. SEM images of In ₂ O ₃ :N deposited on steel and titanium coupons at 450 °C using hexane or toluene.....	127
Figure 4.10. Water contact angle measurements before and after irradiation at 254 nm for 15hrs. Top images show typical before and after measurements, bottom images show In ₂ O ₃ :N grown on a titanium coupon at 450 °C with hexane.	130

Figure 5.1. Gas response (R/R_0) of In_2O_3 sensors, prepared by CHFS, upon exposure to differing concentrations of ethanol in flowing air over time at an operating temperature of 300 °C. Arrows indicate when gas flow of ethanol was turned on and off.	143
Figure 5.2. Gas response (R/R_0) of In_2O_3 sensors, prepared by CHFS, upon exposures to differing concentrations of ammonia in flowing air over time at an operating temperature of 400 °C. Arrows indicate when gas flow of ammonia was turned on and off.....	145
Figure 5.3. Gas response (R/R_0) of In_2O_3 sensors, prepared by CHFS, upon exposures to differing concentrations of a) butane and b) carbon monoxide in flowing air over time at an operating temperature of 450 °C. Arrows indicate when gas flow of ammonia was turned on and off.....	146
Figure 5.4. Gas response (R_0/R) of In_2O_3 sensors, prepared by CHFS, upon exposures to differing concentrations of NO_2 in flowing air over time at an operating temperature of 450 °C. Arrows indicate when gas flow of NO_2 was turned on and off.....	148
Figure 5.5. Maximum gas response of three-coat In_2O_3 sensors, prepared by CHFS, to different gases in flowing air at their optimum operating temperatures.....	149
Figure 5.6. Gas response (R/R_0) of In_2O_3 sensors, prepared by AACVD, upon exposures to differing concentrations of ethanol in flowing air over time at an operating temperature of 500 °C. Arrows indicate when gas flow of ethanol was turned on and off.	152
Figure 5.7. Gas response (R/R_0) of In_2O_3 sensors, prepared by AACVD, as a function of temperature. Sensors are exposed to 100 ppm of ethanol in dry air.....	154
Figure 5.8. Gas response (R/R_0) of In_2O_3 sensors, prepared by AACVD, upon exposures to differing concentrations of a) ammonia and b) carbon monoxide in flowing air over time at an operating temperature of 450 °C. Arrows indicate when gas flow was turned on and off.	155
Figure 5.9. Gas response (R_0/R) of In_2O_3 sensors, prepared by AACVD, upon exposures to differing concentrations of NO_2 in flowing air over time at an operating temperature of 400 °C. Arrows indicate when gas flow of NO_2 was turned on and off.....	157
Figure 5.10. Maximum gas response of In_2O_3 and $\text{In}_2\text{O}_3:\text{Ta}$ sensors, prepared by AACVD, to different gases in flowing air at optimum operating temperatures. $\text{In}_2\text{O}_3:\text{Ti}$ results are omitted as their performance was very similar to that of In_2O_3	157
Figure 5.11. Schematic of a gas sensor chip. The chip consists of an alumina tile with interdigitized gold electrodes on the surface.....	161

Figure 5.12. Schematic of gas sensing test rig used to investigate the response of both indium oxide nanopowder and CVD films. Sensors are loaded into the cell. MFC – Mass Flow Controller, DMM – Digital MultiMeter, MUX – Multiplexing, CPU – Computer Processing Unit.	162
---	-----

List of Schemes

Scheme 2.1. Salt metathesis and phosphide/alcohol exchange synthetic routes to indium mono(alkoxides).	29
Scheme 2.2. Synthetic route towards indium mono- and bis(alkoxides).	30
Scheme 2.3. Routes employed for the formation of homoleptic gallium tris(alkoxides)	36
Scheme 2.4. Synthetic procedures used to synthesis a series of metal tris(alkoxide) cluster compounds synthesised by Daniele <i>et al.</i> ¹⁰⁰	37
Scheme 2.5. Routes explored to synthesise homoleptic indium tris(alkoxides)	38
Scheme 2.6. Attempted route towards the synthesis of [GaCl(OR) ₂] by lithiating the donor-functionalised alcohol followed by salt metathesis.	42
Scheme 2.7. Two step route towards chloro gallium alkoxide compounds <i>via</i> a chloro gallium amide intermediate	43
Scheme 2.8. Synthetic routes to amido gallium bis(alkoxides) and heteroleptic gallium alkoxides.....	58
Scheme 2.9. Summary of all reactions carried out during this work to synthesise heteroleptic gallium alkoxides <i>via</i> the four step process and other related complexes. .	64
Scheme 2.10. Formation of [Ga(bdk) ₃] (bdk = β -diketonate, acac or thd) <i>via</i> the attempted synthetic routes towards gallium bis(β -diketonates)	66
Scheme 2.11. Formation of [In(bdk) ₃] (bdk = β -diketonate, acac or thd) <i>via</i> the attempted synthetic routes towards indium bis(β -diketonates)	67
Scheme 3.1. Plausible decomposition of “[Ga(O ⁱ Pr) ₃]” under CVD conditions.....	81
Scheme 3.2. Formation of dimeric and tetrameric gallium alkoxides	82
Scheme 3.3. Synthesis of fluorinated gallium alkoxides stabilised by Lewis bases	83
Scheme 3.4. First synthesis of gallium alkoxides using donor-functionalised alkoxides	85

Scheme 3.5. Synthesis of non-fluorinated gallium alkoxides from trialkylgallium reagents	86
Scheme 3.6. Synthesis of homoleptic gallium alkoxides with donor-functionalised alkoxides	88
Scheme 3.7. Likely mechanism for the decomposition of a typical group 13 alkoxide.	97
Scheme 5.1. A formal model for sensor response at reactions sites, sensitive to the partial pressure of carbon monoxide. k – rate constant of surface reaction.	139
Scheme 5.2. AACVD reaction of InMe_3 and $\text{HOCH}_2\text{CH}_2\text{NMe}_2$ with $\text{M}(\text{NMe}_2)_x$ and $\text{HOCH}_2\text{CH}_2\text{NMe}_2$ to deposit In_2O_3 and $\text{In}_2\text{O}_3:\text{M}$ onto gas sensing substrates.....	164

List of Tables

Table 2.1. Selected bond lengths (Å) and angles (°) for [GaCl(OCH ₂ CH ₂ NEt ₂) ₂] (3)...	45
Table 2.2. Selected bond lengths (Å) and angles (°) for [Cl ₂ Ga(OCH ₂ CH ₂ NEt ₂) ₂] (4) [Symmetry code: (i) 2-x, -y, 1-z].....	48
Table 2.3. Selected bond lengths (Å) and angles (°) for [GaCl(OCH ₂ CH ₂ CH ₂ NMe ₂) ₂] (5).....	50
Table 3.1 Deposition conditions and Ga ₂ O ₃ thin film properties.....	98
Table 3.2. Precursor conditions from heteroleptic gallium alkoxides and resulting thin film properties.....	103
Table 4.1. Conditions used for CVD of indium oxide thin films.....	119
Table 4.2. Thin film compositions, optical properties and electronic properties of In ₂ O ₃ thin films formed from the reaction of [In{N ⁱ Bu(SiMe ₃) ₃ }] ₃ and 3 HOCH ₂ CH ₂ NMe ₂ and deposited on SiCO coated float glass.....	122
Table 4.3. Water contact angles of In ₂ O ₃ samples before and after irradiation 254 nm for 15 hours.....	129
Table 4.4. Hydrogen evolution for In ₂ O ₃ :N deposited on metal coupon substrates under solar simulated conditions.....	131
Table 5.1. Sign of resistance change (increase) to change in gas atmosphere. ¹⁸⁰	140
Table 5.2. Maximum gas response (R/R_0) of two- and three-coat In ₂ O ₃ gas sensors at optimum operating temperatures on exposure to different concentrations of reducing gases ethanol, ammonia, butane and carbon monoxide.....	144
Table 5.3. Maximum response R/R_0 of the sensors to increasing concentrations of ethanol at an operating temperature of 500 °C; ammonia at 450 °C; carbon monoxide at 450 °C and of R_0/R to increasing concentrations of NO ₂ at an operating temperature of 400 °C.	153
Table 8.1. Crystal data and structure refinement for [GaCl(OCH ₂ CH ₂ NEt ₂) ₂] (3)....	186
Table 8.2. Crystal data and structure refinement for [GaCl ₂ (OCH ₂ CH ₂ NEt ₂) ₂] (4)....	187
Table 8.3. Crystal data and structure refinement for [GaCl(OCH ₂ CH ₂ CH ₂ NMe ₂) ₂] (5).	188

Abbreviations

Å	Angstrom
AACVD	Aerosol assisted chemical vapour deposition
acac	acetylacetonate
Anal.	Analytical
APCVD	Atmospheric pressure chemical vapour deposition
Ar	Aryl
bdk	Betadiketonate
Calc.	Calculated
CI	Chemical Ionisation
cm	Centimetre
CVD	Chemical vapour deposition
Cy	Cyclohexyl
d	Doublet
δ	Chemical shift / ppm
DSC	Differential scanning calorimetry
Et	Ethyl
EDXA	Energy dispersive X-ray analysis
eV	electron volts
g	Gram
GED	Gas Phase Electron Diffraction
h	Hour
J	Coupling constant
ⁱ Bu	iso-butyl
ⁱ Pr	iso-propyl
ⁿ Bu	Normal-butyl
^t Bu	Tertiary-butyl
IR	Infra-red
LPCVD	Low pressure chemical vapour deposition
m	Multiplet (NMR spectra)
Me	Methyl
mmol	Millimole
MOCVD	Metal-Organic Chemical Vapour Deposition
MS	Mass spectrometry
Py	Pyrdine
ⁱ Pr	Iso-propyl
ⁿ Pr	Normal-propyl

NMR	Nuclear Magnetic Resonance
PECVD	Plasma enhanced chemical vapour deposition
Ph	Phenyl
ppm	Parts per million
PVD	Physical vapour deposition
Q	Quartet (in NMR spectra)
quin	Quintet (in NMR spectra)
R	Organic substituent
SEM	Scanning electron microscopy
S	Singlet (in NMR spectra)
Sept	Septet (NMR)
SiMe ₃	Trimethyl silyl
T	Triplet
thd	2,2,6,6-tetramethylheptane-3,5-dionate
THF	Tetrahydrofuran
TGA	Thermal gravimetric analysis
tmp	Tetramethylpyridine
UV	Ultraviolet
vis	Visible
WDX	Wavelength dispersive X-ray analysis
XRD	X-ray diffraction
XPS	X-ray photoelectron spectroscopy

Chapter 1

Introduction

1. Introduction

Gallium and indium alkoxides have had increasing interest for use as precursors to group 13 oxide thin films in recent years. These materials find applications as gas sensors, amorphous oxide semiconductors within thin film transistor (TFT) technology, as photoelectric coatings and as transparent conducting coatings. Gallium and indium alkoxides have been shown to act as excellent precursors to their oxides *via* decomposition processes, at relatively low temperature, where chemical vapour deposition (CVD) has been utilised to form metal oxide thin films.

The focus of this work has been to synthesise novel group 13 precursors, deposit metal oxide thin films and test their applications. Synthesis of the precursors has been tailored towards use in aerosol-assisted (AA)CVD incorporating donor-functionalised alkoxide ligands and focusing on the formation of monomeric complexes. Precursor properties were adapted in order to optimise process parameters, such as deposition temperature, layer purity, uniformity and evaporation temperature. These designer precursors were used to deposit thin films of group 13 metal oxides on a variety of substrates and subsequently the resultant thin films were tested for their properties in applications. These have included gas sensing properties to different reducing and oxidising gases, as well as their activity in visible light photocatalysis.

This chapter gives a background introduction to the work reported in this thesis. Included are an overview of semiconductors, thin film deposition by CVD, precursors and design, and group 13 metal oxide thin film applications

1.1. Band theory

As a consequence of quantum theory and the combination of atomic orbitals, molecules have discrete quantised energy levels called molecular orbitals. These molecular orbitals may be bonding, non-bonding or anti-bonding; they may or may not be occupied with electrons. In a solid many similar molecules are brought and packed

together (Figure 1.1). As a result, the molecular orbitals combine and rather than producing an extensive degenerate energy level they form a "band".

This non-degeneracy is a consequence of the Pauli Exclusion Principle, which states that no two electrons may have the same set of quantum numbers associated with them.¹ Hence these molecular orbitals in a solid must all be slightly perturbed in order for the molecules to pack in a solid. Therefore, a band is a collection of similar energy molecular orbitals, and the band structure of a material corresponds (broadly) to the molecular orbital energy levels of the constituent molecules. This can lead to filled or unfilled bands. The bands in some cases may overlap or be partially filled. The Pauli Exclusion Principle also governs the filling of bands, as each energy level can only contain two electrons and these must have opposing spin quantum numbers. Hence a band may contain $2N$ electrons where N is the number of energy levels in a band.

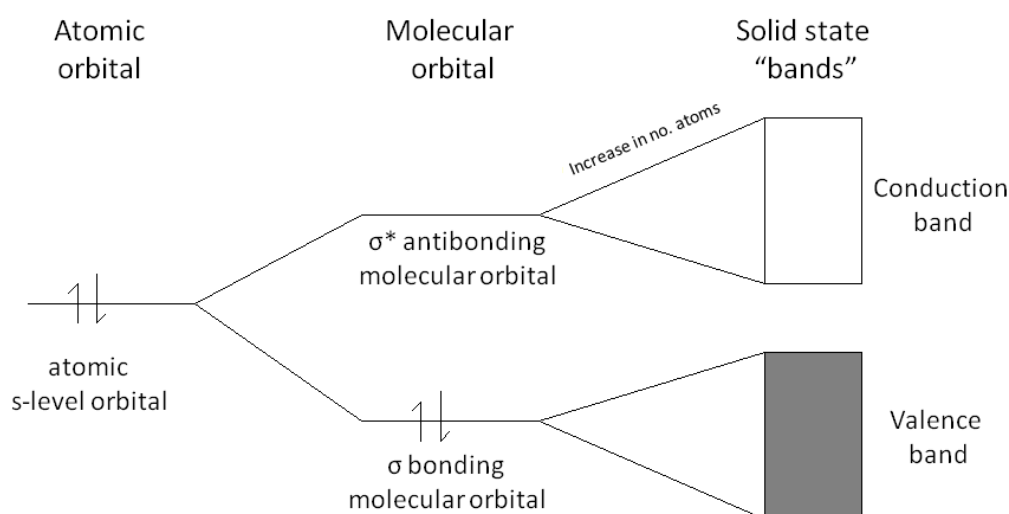


Figure 1.1. The derivation of band theory *via* cumulative addition of atomic/molecular orbitals.

For example, a metal such as lithium, contains only one $2s$ electron and so the $2s$ band in lithium metal will contain only N electrons (one for every $2s$ level). Figure 1.2 shows the band illustration for a metal where one energy level contains N electrons and is therefore half full. Other metals such as magnesium or calcium have filled s levels so could be expected to be insulators as their electrons are immobile. However, the next energy level up, the p level, overlaps with the s level giving the effect of a partially

filled band. The highest filled energy level at absolute zero is known as the Fermi level where the energy of this level is the Fermi energy, denoted E_f .

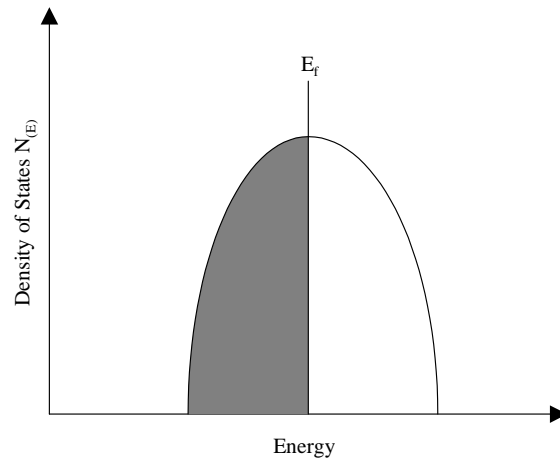


Figure 1.2. Density of states representation of a half filled band.

A metallic conductor is defined when E_f falls where $N(E)$ (the density of states) is greater than zero. Superconductors are identical to metallic conductors with the exception that the resistance of a superconducting material is zero below a critical temperature (T_c). Hence, superconductivity is only observed at low temperatures ($\sim 10 - 80$ K), and at temperatures above the critical temperature this effect no longer occurs and the material behaves like a metallic conductor. This phenomenon comes about due to lattice vibrations caused by elevated temperature which hinders the motion of electrons. This effect is observed in all superconductors and increase of resistivity with temperature is seen in all metallic conductors.

The same effect is not observed in semimetals, semiconductors or insulators (Figure 1.3) because E_f lies where $N(E)$ is equal to zero. The effect of heating these systems reduces resistivity.

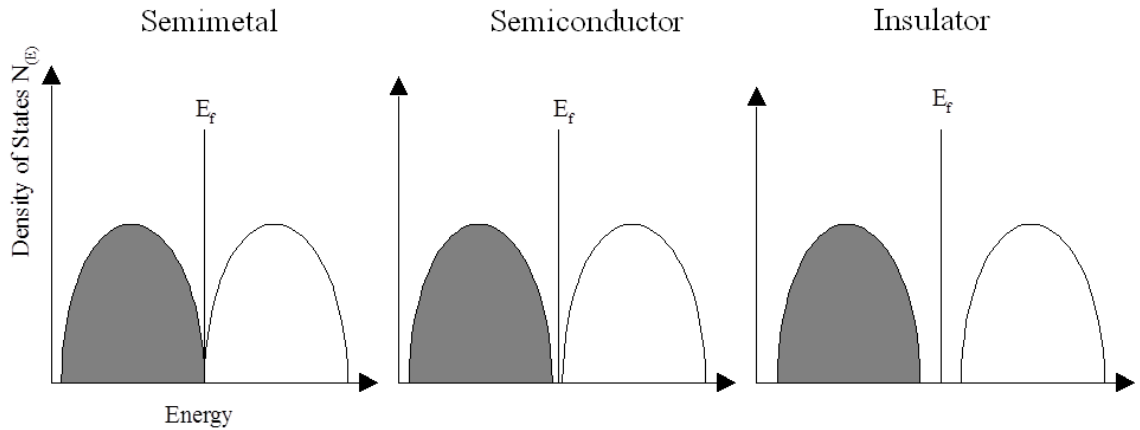


Figure 1.3. Density of states diagrams illustrating the differences between a semimetal, semiconductor and insulator.

This reduction in resistance occurs because thermal energy allows the redistribution of electrons about the bands according to the Boltzmann distribution law (Equation 1.1). This, the highest filled energy bands may be higher than E_f and some electronic conductivity will be allowed.

$$N_j = N e^{-\beta \epsilon_i} / \sum e^{-\beta \epsilon_j} \quad 1.1$$

N = number of states, $\beta = 1/kT$ (k = Boltzmann constant, T = thermodynamic temperature) and ϵ_i = the energy of state i .

1.1.1. Semiconductors

In insulators and semiconductors at absolute zero the valence band is completely filled and the conduction band is vacant. Neither full nor empty bands are able to carry any current and so a semiconductor is insulating at absolute zero. For electron conduction to be possible, electrons must be excited into the conduction band. This can be achieved by thermal excitation or doping the semiconductor material. Doping can be achieved by replacing one of the atoms of the semiconductor material with a different atom, which has one or more electrons than the constituent atoms. This leads either to

an excess of electrons or an absence of electrons in the valence band. An absence of an electron in the valence band is called a “hole”. A hole is the equal opposite of an electron, with positive charge, effective mass and mobile velocity. At absolute zero no hole states are observed since the valence band is fully occupied.

If an electron is promoted from the valence band to the conduction band by light, thermal energy or similar, then it leaves a vacancy or hole behind. Interesting properties can result from this, for example the hole may recombine with an electron re-entering the valence band, leading to an emission of electromagnetic radiation or a phonon. The energy of this emission corresponds to the energy gap between the valence and conduction band. A phonon is a mechanical vibration of energy $h\nu$, and relates to sound waves in the same way that photons relate to electromagnetic radiation. The hole may also migrate through the semiconductor material. Electrons in the valence band will want to move towards this positive charge. As an electron does so, it creates a hole in its original location whilst filling the previous hole. In this way holes are able to migrate.

Intrinsic conduction is when the number of holes is equal to the number of promoted electrons. In this case the Fermi level lies in the middle of the band gap. Pure silicon and germanium are such semiconductor materials.

1.1.2. Effect of dopants

Extra atoms such as impurities or atoms deliberately doped into the material can lead to an excess of electrons or holes. Semiconductors of this type are called extrinsic semiconductors. Indium oxide is often doped with tin to improve conductivity of the thin films.² Tin contains four valence electrons compared to that of indium’s three. This spare electron has to go into the conduction band. The majority charge carrier in the Sn doped In_2O_3 semiconducting material is negatively charged and is denoted n -type. The opposite is true if silicon is doped with an element such as gallium, which has only three valence shell electrons. In this instance the material will be electron deficient and so there will be additional holes in the valence band. Holes are considered to be positive charge carriers hence this type of semiconductor is denoted p -type.

Dopant atoms can be incorporated into a host material by replacement of the atoms in the original material (substitutional doping) or cause defects in the original crystal lattice (interstitial doping). The addition of dopants also leads to donor or acceptor levels being introduced into the band illustration of the material depicted in Figure 1.4. This occurs because dopants have different molecular orbitals to that of the host material. It is possible for a semiconductor to contain both p -type and n -type dopants. These materials are known as compensated semiconductors.

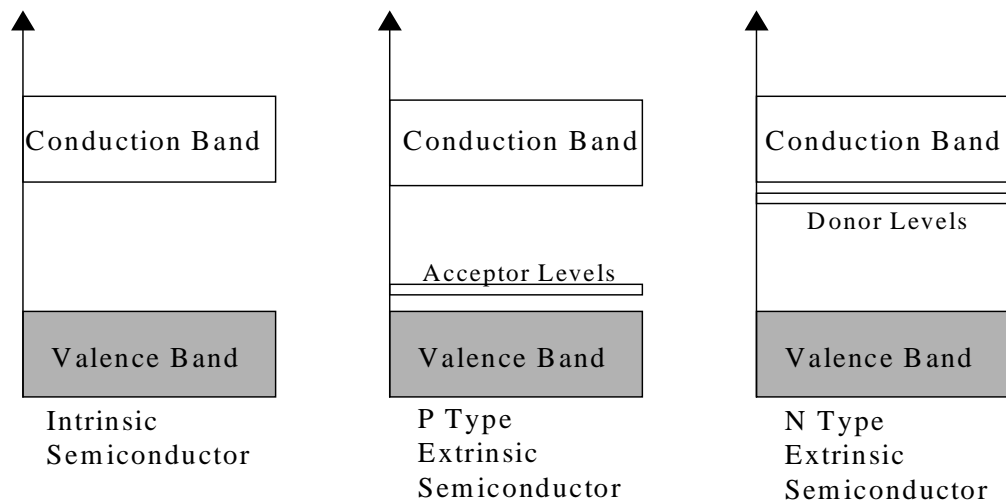


Figure 1.4. Intrinsic p -type and n -type extrinsic semiconductors.

1.1.3. Direct and indirect band gap semiconductors

Intrinsic and extrinsic descriptions of semiconductors only describe allowed and disallowed states. They do not describe the associated transitions. In a crystalline material, the condition for carrier excitation by electromagnetic radiation to occur is that the wave vector must be conserved.

$$k_e + k_{\text{photon}} = k'_e \quad 1.2$$

Where k_e and k'_e are the electron wave vectors before and after excitation respectively.

Direct transitions occur when no perturbation of the wave vector of the system is necessary. The wave vector of the system is a measure of the momentum of the system. These transitions typically occur when the band gap is small where the lowest energy point of the conduction band is directly above the highest energy point of the valence band on a wave vector versus energy plot (Figure 1.5) and so Equation 1.2 reduces to $k_e = k'_e$.

Indirect transitions occur when perturbation of the wave vector is necessary because the momentum of an electron being promoted is altered. Indirect processes necessitates a photon interaction in order that the wave vector is conserved. Gallium oxide is an example of an indirect semiconductor,³ however there is much debate as to whether indium oxide is a direct or indirect semiconductor.⁴

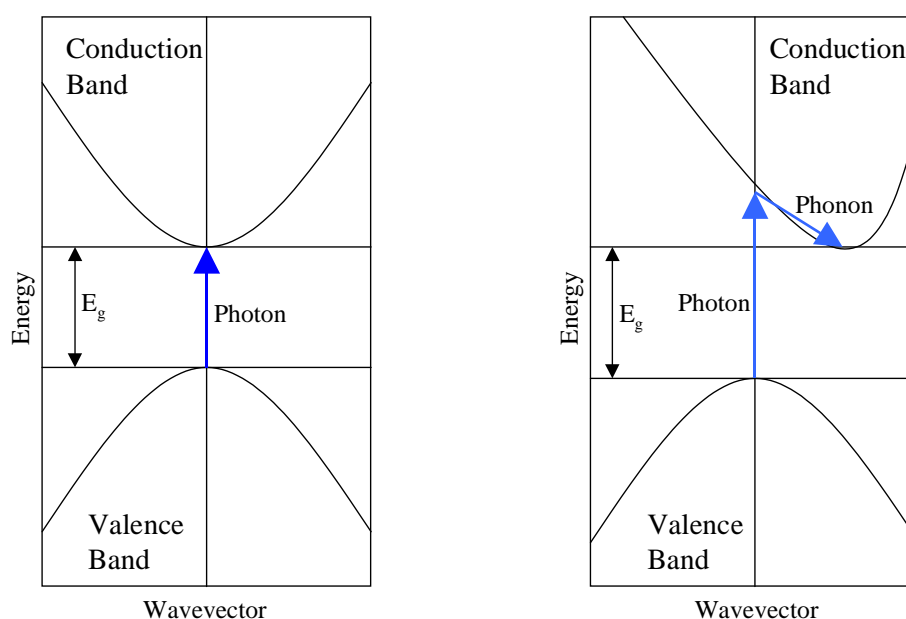


Figure 1.5. The difference between direct (left) and indirect (right) transitions in semiconductor materials.

1.2. Film deposition

Group 13 metal oxide semiconductors have been deposited by a variety of techniques. These include molecular beam epitaxy,⁵ sputtering methods,^{6,7} the sol-gel method⁸ and metal organic chemical vapour deposition (MOCVD) techniques.⁹⁻¹³ MOCVD is the

most promising of these techniques as it is a practical method for preparing thin films of large scale applications as well as being inexpensive, reproducible and affording adhesive films with low impurity levels. In this work, CVD has been the key technique employed to deposit thin films of group 13 metal oxide thin films.

There are many different methods to deposit films and there are a variety of ways in which the deposited film may interact with the target substrate. Films may be epitaxial, polycrystalline or amorphous. The type of film obtained depends on the conditions used for the production and the nature of the substrate. Film deposition often requires additional energy, for example from a heated substrate or by activation of the precursor species.

1.2.1. Chemical vapour deposition

Chemical vapour deposition (CVD) is an important technique and is used for the mass production of thin films in the semiconductor industry.¹⁴ It is one of the most widely used applications for the production of thin films and is able to utilize a wide range of materials as well as offering benefits of being low cost, fast and suitable for large scale production. Thin films produced from CVD are of high purity and are high performance solid materials.

The process of CVD involves the decomposition or chemical reaction of gaseous phase particles onto an activated substrate. Heterogeneous and/or homogeneous reactions occur resulting in the deposition of a solid stable thin film. A number of forms of CVD are in wide use and are frequently referenced in the literature.¹⁴⁻¹⁸ These CVD techniques differ in the means by which chemical reactions are initiated (e.g. activation process) and process conditions.

1.2.1.1. The CVD process

The processes involved during CVD are complex and have many variables. This section aims to give an overview of some of these variables, however in reality, the CVD

system is very complex. Certain features are always present in a CVD system, including a source of gases or vapours, a reaction chamber and an exit for the exhaust gases. However, some CVD systems require additional items such as a vacuum pump for low-pressure systems, piezoelectric devices, lasers or plasma generators. Finally there must be a place for a target substrate for deposition to occur upon. There are a wide variety of processes which may take place in a CVD system. These are common to all CVD systems and are illustrated in Figure 1.6.

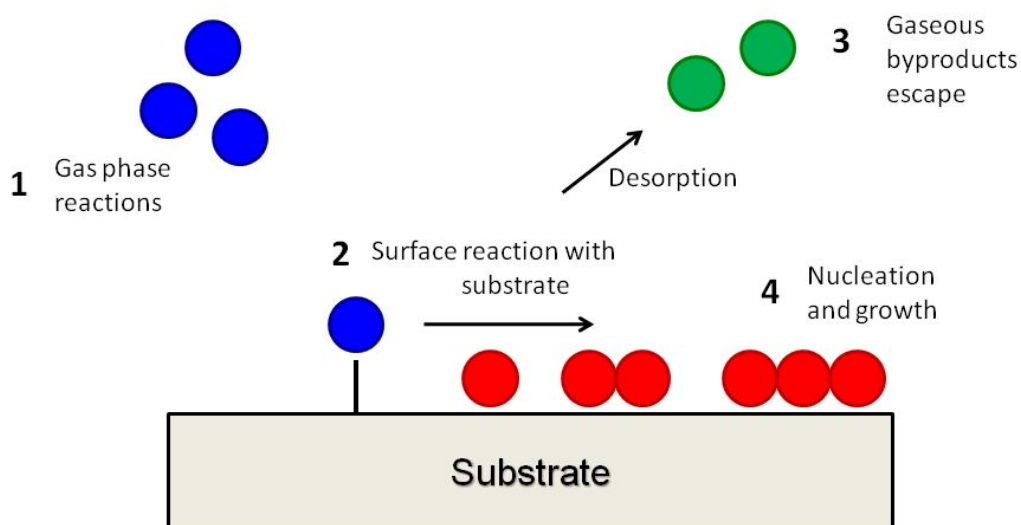


Figure 1.6. The thin film deposition process in CVD.

Figure 1.6 depicts the CVD process. The gas phase reactants (1) must decompose on the substrate (or in the gas phase) to form small molecules that will eventually be part of the growing film. The molecules at this stage are physisorbed onto the surface (2) and are able to move around. Precursor molecules then react with the substrate and by-products and excess precursor escape as gaseous exhaust (3).

The molecule may also desorb or move to a low energy site and may bond to the surface or a cluster of other molecules. Successful film production occurs when films nucleate and grow to cover a substrate (4).

1.2.1.2. Kinetics – mass transport

The transport of gaseous precursors can be affected by convection and diffusion. The motion of these materials is measured most simply by the flux (Equation 1.3) of the precursor, defined simply as the motion of a volume (V) across an area (A) in a time (t). This can be simplified further to:

$$\text{Flux} = \text{Density} \times \text{Velocity} \quad 1.3$$

The velocity is commonly the overall velocity of a moving gas flow. Convection is when flux is due to the overall motion of fluid. Diffusion is a more subtle mechanism but is just as important as convection. Diffusion results from the thermal motion of molecules. The flux due to diffusion is proportional to the gradient in concentration. When molecules are evenly distributed diffusion tends to have no importance. However, where there is a concentration gradient the diffusive motion of molecules produces a net flux that reduces the gradient in concentration. Diffusion can also result from gradients in temperature (thermodiffusion) but this is usually unimportant in CVD except where there is a large difference in the molecular masses of precursors; e.g. tungsten deposition from tungsten hexafluoride and hydrogen. It is important to note that from Fick's Law, diffusion is always the dominant transport mechanism near the substrate surface because it is not possible for a convective flux to be set up through a solid object.

Mass transport can occur due to the motion of a fluid or gas regardless of the existence of a concentration gradient. Working out flow type can be difficult, but may be characterised with various measurements such as the Reynolds number (Equation 1.4).

$$\text{Re} = UL/\nu \quad 1.4$$

Re = Reynolds number, U = overall velocity of the flow through the reactor, L = characteristic length of the reaction chamber, ν = kinematic viscosity defined as the viscosity of the system divided by the mass density of the system.

When Re is large ($Re > 2400$), momentum of the fluid or gas diffuses ineffectively and velocities vary greatly in the system. This is described as turbulent flow. When Re is small ($Re < 2400$), then momentum diffuses rapidly across the chamber and velocity varies in a simple manner and is described as laminar or creeping flow conditions. Most CVD reactors operate in the laminar flow region because turbulent flow conditions are not conducive to reproducibility.

The Reynolds number is unaffected by changes in pressure where there is constant molar flow. This is in essence, because the viscosity is independent of pressure and is determined by the product of the density and the mean free path; one being proportional to the pressure and the other inversely proportional. However, at low pressure where the mean free length is similar to the reactor dimensions, molecules are just as likely to hit the walls of the reactor as they are each other. At this point the description of fluid flow becomes invalid. The validity of the fluid flow description may be calculated from the Knudsen number (Kn). This is the ratio of the molecular mean free path length to a representative physical length scale. If $Kn \gg 1$ then the description of flow conditions is still valid. If $Kn \ll 1$ then computational methods must be employed to glean an insight to what is happening inside the reactor.

1.2.1.3. Thermodynamics – heat transport

Most CVD processes operate at temperatures above room temperature. Heat transfer has three main facets: conduction, convection and radiation. Conduction is the motion of heat through a stationary solid, liquid or gas. Conduction in a gas takes place by the same mechanisms as with mass transport. The main difference is that heat fluxes do not necessarily reduce to zero at a surface. Convection is the physical transfer of gases or liquids containing energy. Radiative heat transfer dominates in a vacuum through the transfer of photons. The thermal conductivity varies a great deal between different materials, much more so than diffusion constants for common gases. As such large temperature gradients may be set up near the substrate surface (and in hot walled reactors the walls), which will aid thermodiffusion.

When temperature is raised, a gas it expands and there is a change in density. This change in density creates a change in the body forces, which can lead to flow without any external force being applied. This natural convection is highly undesirable in CVD systems as it represents an uncontrolled gas flow. In most CVD systems it is insignificant as the applied flow velocity (forced convection) is usually much larger.

1.2.1.4. Film growth

The growth of a thin film in CVD is achieved by exposing a suitably prepared substrate to the precursors in the reaction chamber. Substrates often include materials such as glass,¹⁹ quartz,²⁰ silica,²¹ and metals such as steel and titanium.²² Substrate choice depends on the desired properties of the final thin film. The resulting growth and microstructure of the film is determined by the surface diffusion and nucleation that take place at the growth interface. These are influenced by substrate temperature, reactor pressure, and gas phase composition.

Amorphous films tend to be created at lower temperatures and high growth rates where the surface diffusion is slow relative to the arrival rate of film precursors. At high temperatures and low growth rates where surface diffusion is fast relative to the incoming flux the adsorbed species are able to diffuse to step growth sites and produce a film replicating the substrate surface; this is known as an epitaxial layer. The intermediate case sees nucleation at many points on the surface and also surface diffusion to form “islands” of growth (Figure 1.7).

Growth rates depend on a number of factors such as substrate temperatures, reactor pressure and gas-phase composition. There are three main regimes to consider. At low temperatures, the growth rate is limited by chemical kinetics and increases exponentially with temperature according to the Arrhenius expression shown in Equation 1.5.

$$\text{Rate} = A \exp (E_a / RT) \quad 1.5$$

E_a = apparent activation energy, R = gas constant, T = temperature.

The rate is limited by chemical kinetics and uniform film thickness can be achieved by minimising temperature variations. In the intermediate temperature regime, growth rate is almost independent of temperature as mass transport to the surface controls the rate. This temperature independence is quite desirable in cold walled systems where it is difficult to obtain completely uniform substrate heating. At high temperatures growth rates may decrease due to an increase in the rate of reactant desorption. Alternative reaction pathways may also become available. Gas phase reactions become increasingly important with increasing temperature and partial pressure of reactants. High reactant concentrations may lead to gas phase nucleation which can lead to a decline in film quality and yield.

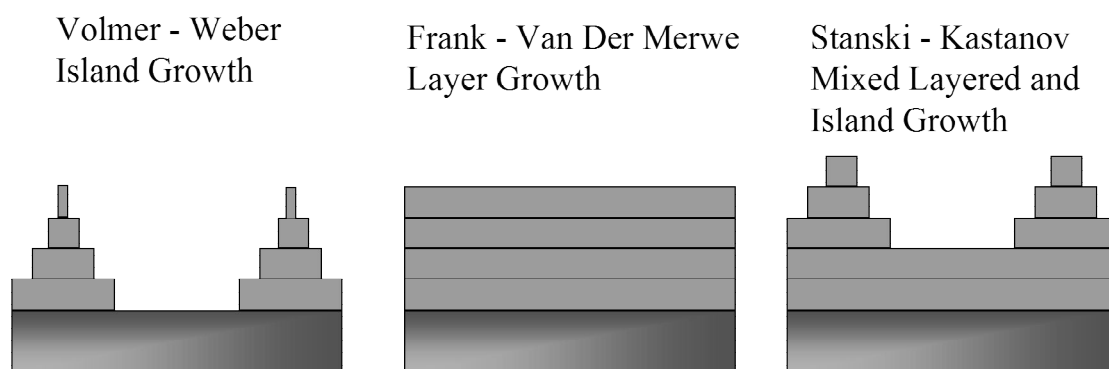


Figure 1.7. The three main types of film growth.

For a film to grow successfully the rate of nucleation must be greater than the rate of desorption. There are several ways in which films can grow and these are depicted in Figure 1.7. In Volmer–Weber (island) growth, adatom-adatom interactions are stronger than those of the adatom with the surface, leading to the formation of three-dimensional adatom clusters or islands.²³ Growth of these clusters, along with coarsening, will cause rough multi-layer films to grow on the substrate surface. Conversely, during Frank–van der Merwe (layer) growth, adatoms attach preferentially to surface sites resulting in atomically smooth, fully formed layers. This layer-by-layer growth is two dimensional, indicating that complete films form prior to growth of subsequent layers.²³ Stranski–Krastanov growth is an intermediary process characterised by both 2D layer and 3D island growth. Transition from the layer-by-layer to island-based growth occurs at a critical layer thickness which is highly dependent on the chemical and physical

properties, such as surface energies and lattice parameters, of the substrate and film. Gallium and indium oxide CVD films often form *via* the island growth mechanism.^{9,24}

1.2.1.5. Precursor design

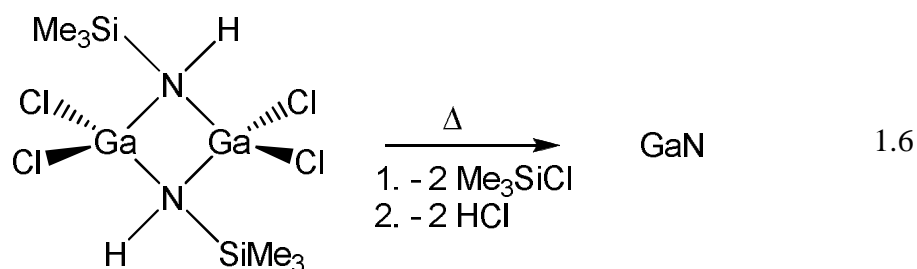
A wide variety of precursors may be used in CVD. Precursors can be tailored to fulfil optimum properties to make them suitable for formation of the desired final film. Common requirements for designer precursors towards ideal thin film deposition can include:

- Sufficient volatility (for LP/APCVD) or solubility (for AACVD) to generate gaseous reactant species for achieving suitable growth rates within reasonable temperatures.
- Adequate stability at room temperature and during the vapour phase.
- Have considerable temperature difference between stable gas phase and decomposition for film growth.
- Have a suitable deposition rate. As previously mentioned, a low deposition rate is preferred for thin film growth
- Decomposition should occur below the temperature that the substrate would melt or undergo phase transformation.
- Be free from contaminants. For example carbon and halide incorporation can act as electrical poisons.
- Precursors should decompose cleanly with all by-products being removed *via* the exhaust.
- Low toxicity and low risk for safe handling. Important in industrial applications.
- Readily produced in high yield and at low cost.

When synthesising precursors for CVD it is important to tailor the design of the precursor towards the above optimum requirements.

Precursor delivery occurs either from a single-source or multiple sources. Single-source precursors are compounds where bonds between the elements of the target material are already present within the precursor. For example, for the formation of a gallium nitride

(GaN) thin film, the single-source precursor must contain Ga-N bonds, as illustrated in Equation 1.6.¹



Single-source precursors are useful in that their decomposition and reaction properties can be tuned by changing the ligands. These precursors may suffer from contamination as they have bonds to species that are undesirable in the resultant film, for example carbon. They may also be used in lower temperature depositions. Often the limiting step in such cases is the temperature at which the compound decomposes. Single-source precursors tend to be less toxic, but are generally not commercially available.

Multi-source precursors are when two or more different compounds are reacted together in the reaction chamber. This can often involve an additional oxygen source in the case of metal oxides including H_2O , H_2O_2 , O_2 and O_3 .²⁵⁻²⁷ The advantages of this methodology are that these compounds tend to be cheap, thermally stable in transport and volatile. Disadvantages can include that film contamination can often occur, higher substrate temperatures are often required and many of the compounds used are either toxic or have toxic by-products and may be pyrophoric.¹

1.2.1.6. CVD Variations

A variety of CVD techniques exist for depositing metal oxide thin films. These include low pressure (LP), atmospheric pressure (AP), photo-assisted (PA), plasma-enhanced (PE) and aerosol-assisted (AA) CVD. For LPCVD a vacuum is required to transport precursors into the gas phase and into the reaction area. With APCVD a carrier gas is bubbled through the precursor and relies on the evaporation of the precursor into the gas phase. Consequently only precursors with adequate volatility can be used with LPCVD and APCVD.

PACVD may help grow a film in two ways. Firstly in a photolytic manner, when a laser beam is shone across or just above the surface, the laser light excites the gaseous precursor species meaning less heating of the substrate is needed to initiate reaction. The second way lasers can be used is in a pyrolytic sense. A laser is focused on one spot on the surface of a substrate and this point heats up and a film can be selectively deposited. By using optical technology intricate and precise patterns on the substrate can be produced. By varying the power of the laser the surface may also be selectively etched. This technology has applications in the microelectronics industry.

Plasma-enhanced CVD (PECVD) works in a similar way to photolytic PACVD in that precursor species are activated before they reach the surface of the substrate. Species are activated by travelling through a plasma, created using a radio frequency electric field. This field interacts with gaseous electrons and accelerates them; this causes the electrons to collide with precursor species and potentially ionise them. The field also interacts with ions but because of the larger mass of these has negligible effect.

This work has utilised AACVD and this technique is discussed in the following section.

1.2.1.7. Aerosol-Assisted CVD

The principal difference between AACVD and other CVD techniques is the use of a liquid aerosol to transport the precursor to the substrate. In AACVD, the precursor can either be dissolved in a solvent, from which an aerosol is formed, or the precursor can be a liquid. This eliminates the requirement for volatility, opening up a large range of precursors for use in CVD that would otherwise be unsuitable.

Figure 1.8 shows the schematic of a typical AACVD rig. Once in solution, an aerosol mist of the precursor solution is generated by a piezoelectric device, which is then transported through to the reaction chamber using a suitable carrier gas. Upon entering the heated reactor, *via* a brass baffle for uniform control of the mist, the solvent evaporates in the high temperatures and the precursor is left in the gas phase to react,

adsorb, nucleate and grow into the desired thin film on the substrate. By-products are allowed to escape as exhaust out of the chamber.

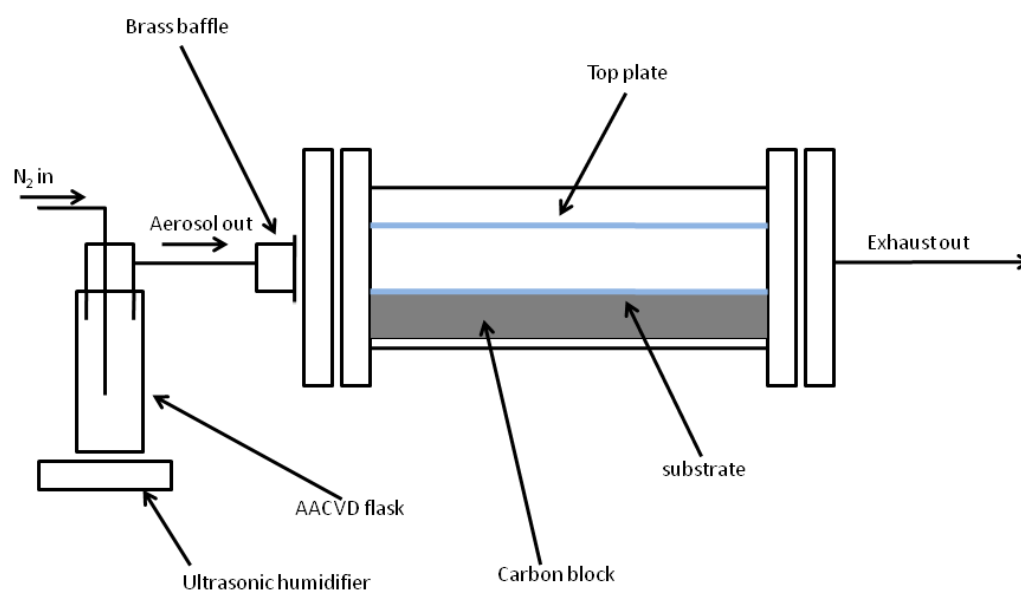


Figure 1.8. Schematic of an AACVD rig.

AACVD is a cost-effective process, the humidifier removes the need for high vacuum or temperature which are used in conventional bubbler or vaporisation methods. Additionally, because the system is solution based, it follows that *in situ* reactions are possible, so that reactants can be mixed together before they enter the reactor without decomposition occurring. This eliminates the need for several starting ‘pots’ containing many volatile precursors and is often known as the ‘one pot’ approach.

1.3. Applications

Group 13 metal oxides play important roles in a variety of applications. Gallium oxide (Ga₂O₃) has applications for gas sensing as well as catalysts,²⁸ phosphor host material for emissive display applications²⁹ and blue light emitting nanowires.^{30, 31} Doped and undoped indium oxide (In₂O₃) thin films are attractive materials for use as transparent conducting oxides (TCOs), in applications such as optoelectronic devices, flat panel displays and solar cell windows,^{32, 33} as well as gas sensing materials.³⁴ Herein, the focus applications of this work are described in more detail.

1.3.1. Metal oxide semiconductor gas sensing

Gas sensors have practical use in monitoring and controlling systems of combustion engines, waste gases and chemical processes, with present research focusing on novel materials for fast, stable, sensitive and selective gas sensing.³⁵

Polycrystalline gallium oxide thin films have emerged as *viable* gas sensing materials at high temperatures.³⁶ Gallium oxide is an electrical insulator at room temperature and semiconductor above 500 °C; it is chemically and thermally stable. At temperatures above 900 °C the electrical conductivity changes depend on the concentration of oxygen. This property means that Ga₂O₃ can be used as a gas sensor for detecting oxygen concentration. Below 900 °C, gallium oxide thin films can be used as sensors that are responsive to reducing gases on the basis of surface effects, e.g. H₂, CO and EtOH.⁶ The function of gallium oxide thin films may be able to switch with temperature.

Indium oxide is used in industrial and technological applications such as toxic/dangerous gas detection. The material has particular sensitivity to reducing gases ethanol³⁴ and ammonia³⁷ and oxidising gases such as O₃.³⁸

Despite the wide interest in group 13 metal oxide thin films as gas sensors there have been few reports using MOCVD to deposit Ga₂O₃ or In₂O₃ thin films. Of these, further problems have been encountered. Carbon and fluorine contamination from precursors is common^{12, 39, 40} as well as oxygen deficiency when using LPCVD.^{11, 12} AACVD provides a method for the formation of stoichiometric metal oxide thin films.

1.3.2. Transparent conducting oxides

Transparent conducting oxides (TCOs) are materials of much interest due to their high transparency in the visible region and high conductivity properties.⁴¹ Indium oxide is a very important TCO material as it is physically stable and chemically inert and has a wide band gap of about 3.7 eV. Undoped indium oxide can be used as gas sensors.⁴² Indium oxide can be doped with other metals to enhance its electronic properties; Sn-

doped indium oxide (ITO) can be prepared and its band-gap and resistivity vary with its level of doping.⁴³

1.3.3. Photovoltaics and water splitting

Solar-driven water splitting (converting water to hydrogen and oxygen) is an ideal clean and renewable energy source. However the discovery of new and more efficient photocatalysts for water splitting is very challenging. TiO₂ has been demonstrated to split water to produce H₂ and O₂ after UV photoexcitation and is the most widely studied material in the field of solar hydrogen conversion.⁴⁴ Different transition metals have been studied along with various dopants in attempt to reduce the band-gap and allow the materials to absorb visible light. Nitrogen doping has attracted much attention for the development of visible-light photocatalysts. The most widely investigated N-doped materials are those of N-doped TiO₂ where the optical absorption becomes red shifted into the visible range ($\lambda > 380$ nm),⁴⁵ However good activity under solar conditions for water spitting has not yet been demonstrated successfully.

Indium oxide (In₂O₃) has been described as a photocatalyst for water splitting however the activity is low under visible-light irradiation.^{44, 46} Nitrogen doping has been positive in reducing the band gap of metal oxides and is utilized by Reyes-Gil *et al.* with indium oxide.⁴⁵ By nitrogen doping indium oxide, they have reduced the band gap from 3.4 eV to 2.0 eV thus being a suitable energy for visible light water splitting. The photocurrent densities of N-doped In₂O₃ electrodes were at least double of undoped In₂O₃ and approximately 50 times better than N-doped TiO₂ electrodes in the visible region. However optimisation is still required to deliver high photocurrents.

1.4. Summary

Chemical vapour deposition has been developed into a highly advanced and efficient thin film growth technology in recent decades. CVD proves to be an efficient way of depositing high quality thin films of metal oxides. Group 13 metal oxide thin films of gallium and indium are semiconductors above 450 °C and at room temperature respectively. Their transparent and conducting properties make them suitable for

applications such as gas sensors, transparent conducting oxides used in optoelectronic devices, photovoltaics and flat panel screens. Additionally doping of indium oxide has found to be a visible light photocatalyst for water splitting.

Tailoring of precursors to metal oxide thin films *via* CVD is important for obtaining films with specific properties. Chapter 2 explores a range of single-source precursors to group 13 metal oxide thin films and reports the synthesis and characterisation of customized gallium alkoxide precursors for their deposition to gallium oxide thin films.

Chapter 2

Synthesis

2. Synthesis

In this chapter the synthesis and characterisation of a range of gallium(III) alkoxide compounds are described. The compounds were prepared with a view to their use as single-source precursors for the chemical vapour deposition (CVD) of group 13 metal oxide thin films, as discussed in Chapter 3. Also included are details on the attempted synthesis of gallium bis(β -diketonate) compounds. Section 2.1 gives an overview of routes to known gallium(III) and indium(III) alkoxide complexes in the literature. The synthesis and characterisation of the gallium compounds prepared for this study are discussed in Section 2.2, with conclusions in Section 2.3 and experimental details given in Section 2.4.

2.1. Introduction

The development of molecular precursors for metal oxides has been the subject of much study.^{47, 48} Extensive work goes towards the tailoring or designing of these compounds so that the final thin film is obtained in high quality.^{49, 50} An outline of the requirements of an ideal precursor was described in Section 1.2.1.5.

For gallium and indium oxide thin film precursors, a number of types of compound can be used, namely metal alkylamides, metal alkyls, metal β -diketonates and metal alkoxides. The focus of this research is metal alkoxide compounds, but it will also cover an overview of work conducted within the group on metal bis(β -diketonates).

Although gallium oxide has been extensively studied as a gas sensor, these films are commonly produced using the sol-gel method and there are few reports using CVD. Those reported have included the use of gallium tris(β -diketonates) in the presence of oxygen *via* LPCVD.^{12, 13, 51} The gas sensing properties of these films have also not been investigated. Using β -diketonates as ligands can be advantageous as the physical and chemical properties can be fine-tuned by altering the structure of the ligand.⁵² By increasing the steric bulk of the alkyl group, or substituting with fluorinated groups, the

precursor becomes more volatile. However the resultant metal oxide films can often be left with contaminants of carbon or fluorine.⁵³

Group 13 alkoxides are currently being investigated as precursors to the corresponding metal oxide films.^{10, 54} Metal alkoxides can be used for the deposition of metal oxide thin films including their growth at relatively low temperatures and formation of high purity films containing little or no carbon contamination can be obtained in the absence of added oxygen.⁴⁷

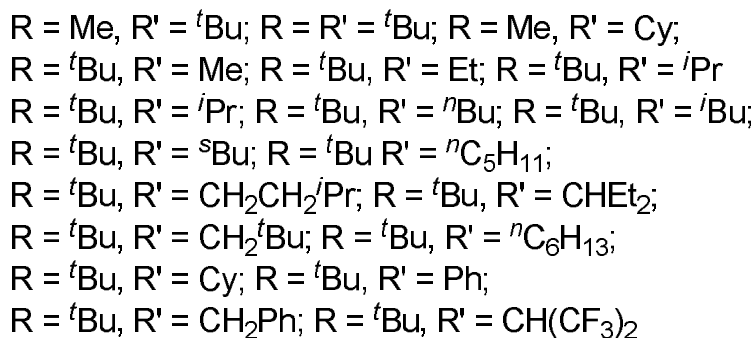
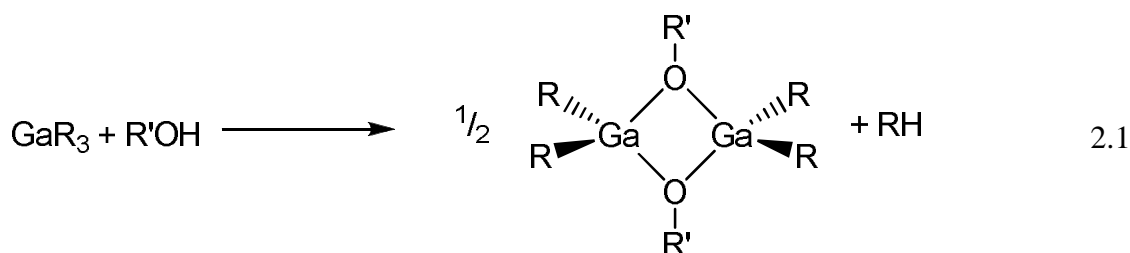
Many gallium and indium alkoxide compounds have been synthesised and reviewed.⁵⁵⁻⁵⁷ The following section gives an overview of the relevant metal mono-, bis- and tris(alkoxides) and also reports more recently published compounds.

2.1.1. Gallium mono(alkoxides)

Gallium mono(alkoxides) have been known for almost 60 years when $[\text{GaMe}_2(\text{OMe})]_3$ was reported and synthesised by the addition of one equivalent of methanol to trimethyl gallium.⁵⁸ Since then a range of gallium mono(alkoxides) have been reported. These include a variety of substituents (Equation 2.1), which have been synthesised in a number of ways. The alkyl/alcohol exchange route has also been used to synthesise compounds of the general formula $[\text{GaMe}_2(\text{OR})]_n$ ($\text{R} = \text{}^t\text{Bu}, \text{}^n\text{Bu}, \text{Me}, \text{PhCH}_2$), as well as $[\text{GaEt}_2(\text{OEt})]_n$ from the reaction of GaEt_3 with EtOH .⁵⁹⁻⁶¹ The compounds $[\text{GaMe}(\text{Cl})(\text{OMe})]_n$, $[\text{GaCl}_2(\text{OMe})]_n$ and $[\text{GaEt}_2(\text{OMe})]_n$ have also been reported.⁶² The reaction of GaMe_3 with cyclohexanol was shown to yield the dimeric complex $[\text{GaMe}_2(\text{OCy})]_2$, *via* evolution of methane.⁶³ Similarly, the reaction of GaR_3 with one equivalent of $\text{}^t\text{BuOH}$ afforded the complexes $[\text{GaR}_2(\text{O}^t\text{Bu})]_2$ ($\text{R} = \text{Me}, \text{}^t\text{Bu}$).^{64, 65}

Reaction of $[\text{Ga}^t\text{Bu}_2(\mu\text{-OO}^t\text{Bu})]_2$ with two equivalents of PR_3 or AsPh_3 , under anaerobic conditions, leads to the isolation of Lewis acid-base complexes $[\text{Ga}^t\text{Bu}_2(\text{O}^t\text{Bu})(\text{O}=\text{PR}_3)]$ ($\text{R} = \text{Et}, \text{}^i\text{Pr}, \text{}^n\text{Bu}, \text{Ph}; \text{R}_3 = \text{Ph}_2\text{Me}$) and $[\text{Ga}^t\text{Bu}_2(\text{O}^t\text{Bu})(\text{O}=\text{AsPh}_3)]$.⁶⁵ Compounds of the type $[\text{Ga}^t\text{Bu}_2(\text{OR}')_2]$ ($\text{R}' = \text{Me}, \text{Et}, \text{}^n\text{Pr}, \text{}^i\text{Pr}, \text{}^n\text{Bu}, \text{}^i\text{Bu}, \text{}^s\text{Bu}, \text{}^n\text{C}_5\text{H}_{11}, \text{CH}_2\text{CH}_2\text{}^i\text{Pr}, \text{CH}_2\text{Et}, \text{CH}_2\text{}^t\text{Bu}, \text{}^n\text{C}_6\text{H}_{13}, \text{Cy}, \text{Ph}, \text{CH}_2\text{Ph}, \text{CH}(\text{CF}_3)_2$), have been synthesised *via* the reaction of Ga^tBu_3 with $\text{R}'\text{OH}$, according to Equation 2.1.^{66, 67} A number of structures have been

determined by single crystal X-ray diffraction, which showed that the complexes are dimeric.



Most gallium mono(alkoxides) reported in the literature are dimeric in the solid-state, however *via* the reaction of [GaMe₂Cl] and one equivalent of ⁿBuOH or ^tBuOH, trimeric structures, of the type [GaMe(Cl)(OR)]₃ (R = ⁿBu or ^tBu) were isolated.⁶⁸

A range of donor-functionalised gallium mono(alkoxides), of the type [GaR₂(OR')]₂, have been synthesised and are shown in Figure 2.1. This range of compounds includes dialkyl gallium monoalkoxides synthesised from the reaction of trialkyl gallium and donor-functionalised alcohol, where R = Me, H; R' = CH₂CH₂NMe₂,⁵⁷ R = Et; R' = CH₂CH₂NMe₂, CH(CH₂NMe₂)₂, CH₂CH₂OMe, CH(CH₃)CH₂NMe₂, C(CH₃)₂CH₂OMe,¹¹ R = Me, Et; R' = CH₂CH₂(2-C₃H₄N),⁶⁹ R = Me; R' = CH(CH₃)CH₂NMe₂,²⁰ R = Me; R = C(CH₃)₂CH₂OMe,⁷⁰ and R = Me; R' = CH₂CHR''NMe₂; R'' = Me, Et, ⁱPr, ^tBu, Bz.⁷¹ Dichloro gallium mono(alkoxides) [GaCl₂(OR)]₂ were also reported from the reaction of [GaCl₂(NMe₂)₂] and 2 ROH, where R = CH₂CH₂NMe₂.²⁰

The synthesis of a range of alkyl/chloro-gallium alkoxide and amido/alkoxide compounds was achieved *via* a series of protonolysis and alcoholysis steps. From this process a number of gallium mono(alkoxides) were also synthesised, of the type [GaRR'(OR'')]₂, as shown in Figure 2.1, where R = Me; R' = Cl; R'' = ^tBu, CH₂CH₂OMe, CH(CH₃)CH₂NMe₂, CH₂CH₂NMe₂, R = Me, R' = N(SiMe₃)₂, R'' =

$\text{CH}_2\text{CH}_2\text{OMe}$, $\text{R} = \text{Cl}$, $\text{R}' = \text{N}(\text{SiMe}_3)_2$, $\text{R}'' = \text{CH}_2\text{CH}_2\text{NMe}_2$.²⁰ The mixed dimer $[\text{GaMe}(\text{Cl})\{\text{N}(\text{SiMe}_3)_2\}(\mu_2\text{-OR})\text{Ga}(\text{Cl})\text{Me}]$ was also formed which represents an intermediate in the formation of dimeric complexes, of the type $[\text{Me}(\text{Cl})\text{Ga}(\text{OR})]_2$, when formed from compound $[\text{Me}(\text{Cl})\text{Ga}\{\text{N}(\text{SiMe}_3)_2\}]_2$.²⁰

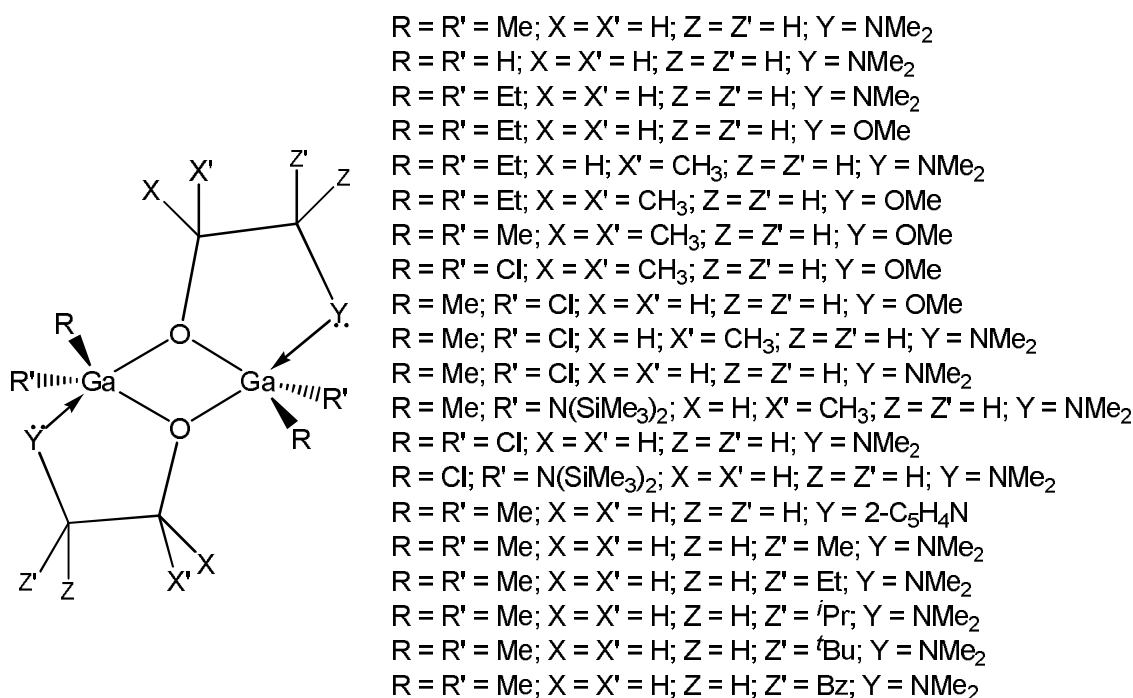


Figure 2.1. A series of known gallium mono(alkoxides) incorporating donor-functionalised ligands.^{11, 20, 57, 69-71}

More recently, the compound $[\text{GaCl}_2(\text{OC}(\text{CH}_3)_2\text{CH}_2\text{OMe})]_2$ (Figure 2.2) was reported by Basharat *et al.*⁷² Initially the gallium mono(alkoxide) was a by-product from the reaction of $[\text{Ga}(\text{NMe}_2)_3]_2$ with an excess of alcohol. The gallium mono(alkoxide) was then synthesised *via* the reaction of $[\text{GaCl}_2(\text{NMe}_2)]_2$ with equimolar amounts of the donor-functionalised alcohol $\text{HOC}(\text{CH}_3)_2\text{CH}_2\text{OMe}$.

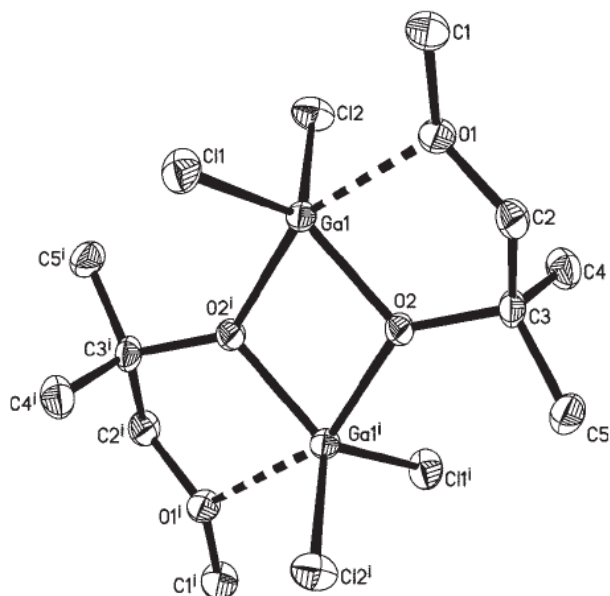


Figure 2.2. Crystal structure of $[\text{GaCl}_2(\text{OC}(\text{CH}_3)_2\text{CH}_2\text{OMe})]_2$.⁷²

Analytical and spectroscopic data for the compound were consistent with the formulation $[\text{GaCl}_2(\text{OC}(\text{CH}_3)_2\text{CH}_2\text{OMe})]_2$ and the dimeric nature was confirmed by mass spectrometry. The resonance of protons positioned α to the donor heteroatom showed a downfield shift in the ^1H NMR spectrum of $[\text{GaCl}_2(\text{OC}(\text{CH}_3)_2\text{CH}_2\text{OMe})]_2$ compared to the free ligand, indicating a dative ligand-metal interaction.

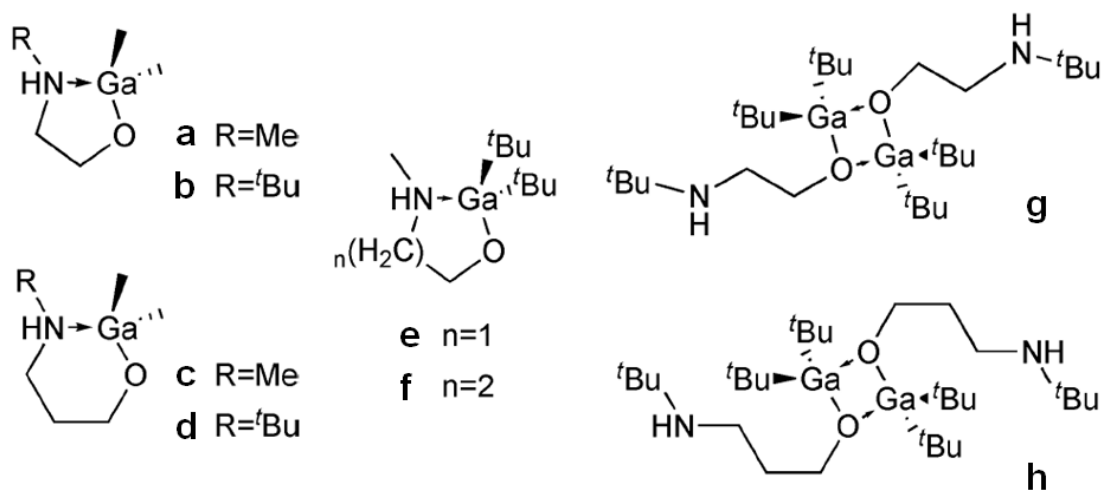


Figure 2.3. A series of gallium monoalkoxide complexes synthesised by Willner *et al.* Compounds **a-f** are monomers whereas compounds **g** and **h** are dimers.

A range of gallium mono(alkoxide) complexes were reported by Willner *et al.*⁷³ (Figure 2.3) where a series of compounds were synthesized with the general formula $[\text{GaR}_2(\text{OR}'')]_x$ ($\text{R} = \text{Me}, \text{}^t\text{Bu}$; $\text{R}'' = (\text{CH}_2)_2\text{NHR}'''$, $(\text{CH}_2)_3\text{NHR}'''$; $\text{R}''' = \text{Me}, \text{}^t\text{Bu}$). The compounds shown in Figure 2.3 were synthesized by the reaction of GaMe_3 with equimolar quantities of the relevant donor-functionalised alcohol.

The ^1H NMR spectra of the compounds reported by Willner *et al.* confirm the structures of the compounds shown in Figure 2.3. The N-H peak was broad or undetectable and together with the substantially broadened N-H bands in the IR spectra this was indicative of hydrogen bridging. The absence of coordination dimers for compounds **a-f** was proven by single crystal X-ray diffraction. Thus in these six compounds, intramolecular ring closure (as shown in the schematic in Figure 2.3) plus hydrogen bridging (Figure 2.4) was favoured over dimerisation. Analytical data of compounds **g** and **h** were consistent with dimer formation.

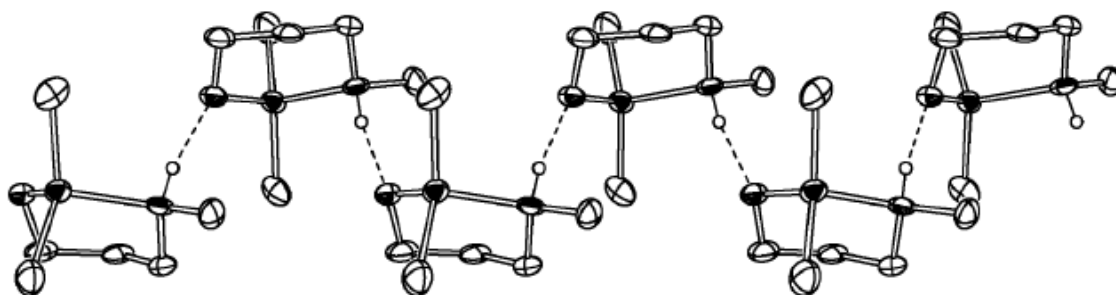


Figure 2.4. View along the z -axis of $[\text{GaMe}_2(\text{O}(\text{CH}_2)_3\text{NHMe})]$ (**c**) showing a chain formation by N-H \cdots O hydrogen bonds.⁷³

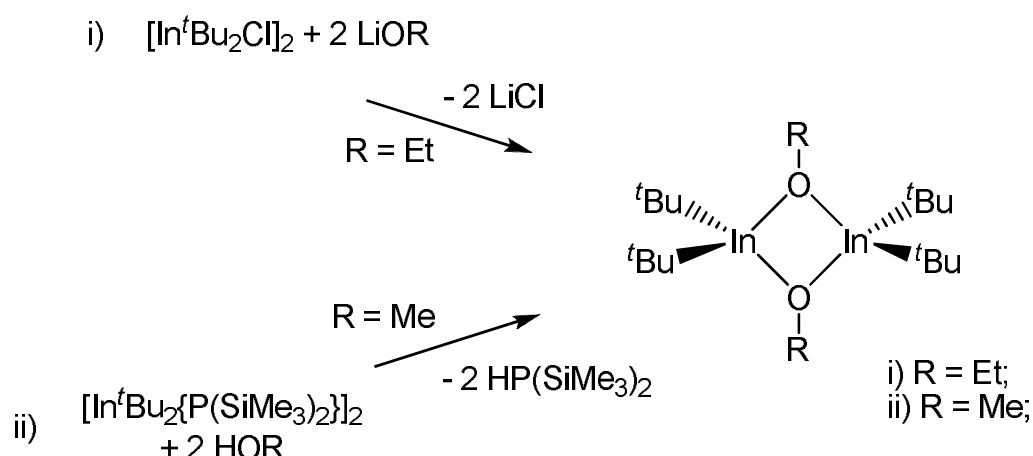
In this series of gallium mono(alkoxide) complexes steric bulk plays an important role in the outcome of the arrangement of the complexes. When too many *tert*-butyl groups are present at the metal or nitrogen atoms, the resulting weaker dative bonds led to the presence of more than one aggregated form. With the gallium alkyl complexes, coordination numbers of four were observed, either *via* cyclisation (low steric bulk, Ga-N bonds) or dimerisation (high steric bulk, Ga-O bonds, but no Ga-N dative bonds).

The gallium mono(alkoxides) reported Willner *et al.* have not been used to deposit gallium oxide thin films, either by CVD or other techniques. The majority of gallium

mono(alkoxides) reported are dimeric and are thought to be less volatile for CVD purposes. The monomeric compounds reported by Willner *et al.* are likely to be more volatile, however hydrogen bonding between each monomeric unit may decrease volatility compared to other monomeric structures which are discussed in Section 2.1.3. Additionally, compounds $[\text{GaMe}_2\text{OR}]_2$ ($\text{R} = \text{CH}_2\text{CH}_2\text{NMe}_2, \text{CH}_2\text{CH}_2\text{OMe}$), deposited by LPCVD was found to be monomeric in the gas phase *via* gas phase electron diffraction (GED). This study suggests that dimeric metal mono(alkoxides) incorporating donor-functionalised ligands could be volatile enough for use as precursors to thin films in comparison to the GED study of $[\text{GaMe}_2(\text{O}^t\text{Bu})]_2$ which revealed a dimeric structure in the gas phase.^{74,75}

2.1.2. Indium mono(alkoxides)

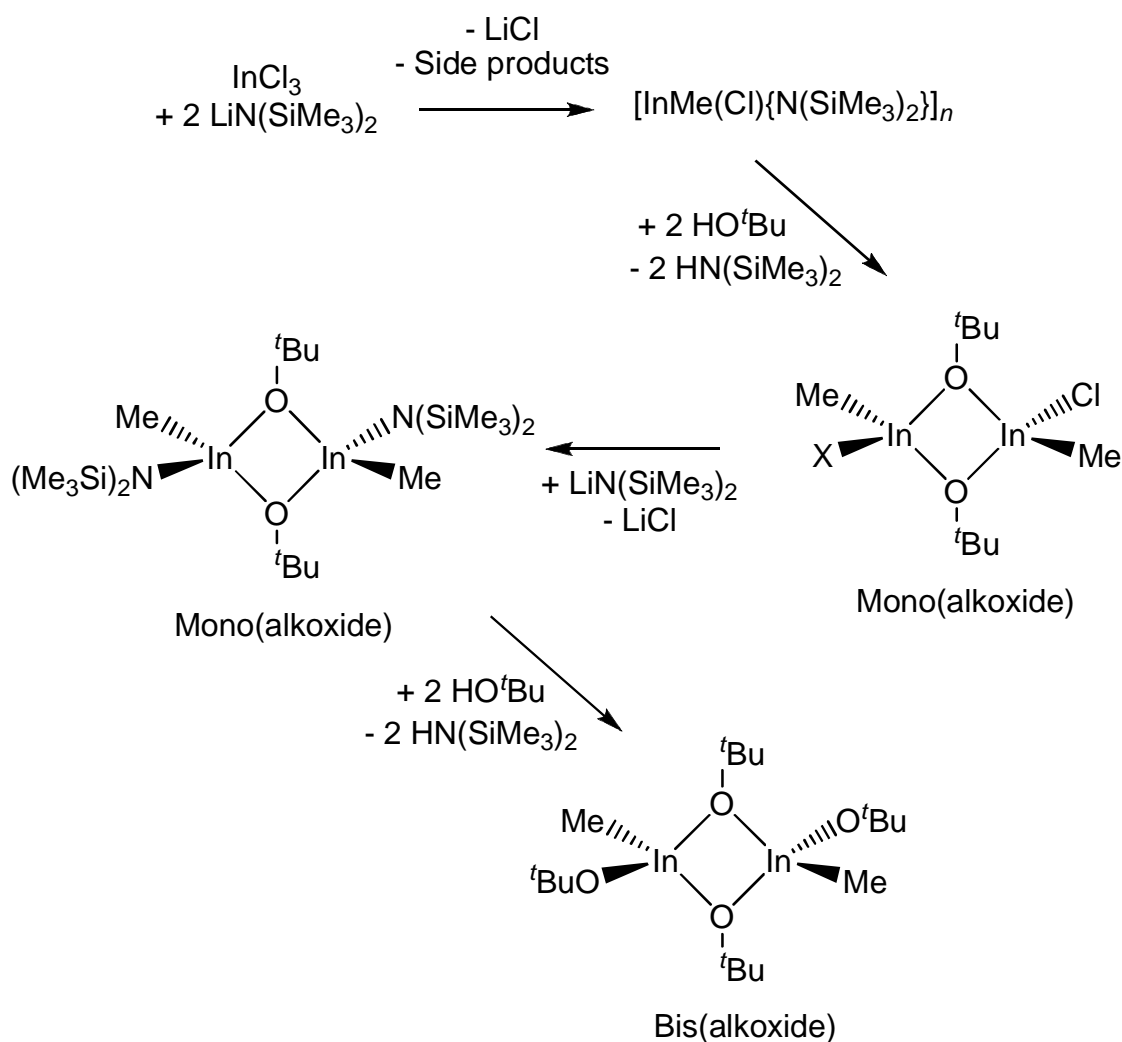
Indium mono(alkoxide) compounds have been formed from a variety of routes. These include salt metathesis and amide/alcohol exchange (Scheme 2.1). Early preparative routes to dialkylindium monoalkoxides involved the reaction of InMe_3 with ROH. The compounds $[\text{InR}_2(\text{OR}')]_n$ ($\text{R} = \text{Me}, \text{R}' = \text{Me}, \text{CD}_3, ^t\text{Bu}, \text{SiMe}_3$; $\text{R} = \text{Et}, \text{R}' = \text{Me}, \text{Et}$) were isolated and characterised.⁷⁶⁻⁸²



Scheme 2.1. Salt metathesis and phosphide/alcohol exchange synthetic routes to indium mono(alkoxides).

Salt elimination was used for the preparation of $[\text{Et}_2\text{In}(\text{OEt})]_2$ *via* the reaction of $[\text{In}^t\text{Bu}_2\text{Cl}]_2$ with two equivalents of LiOEt in diethyl ether, as shown in Scheme 2.1.⁸³ In

contrast, $[\text{In}^t\text{Bu}_2(\text{OMe})]_2$ was isolated from the reaction of $[\text{In}^t\text{Bu}_2\{\text{P}(\text{SiMe}_3)_2\}]_2$ with methanol, with concomitant formation of $\text{HP}(\text{SiMe}_3)_2$, as depicted in Scheme 2.1.⁸⁴ Interestingly, subsequent reaction with $\text{HP}(\text{SiMe}_3)_2$ yielded $[\text{In}^t\text{Bu}_2\{\text{PH}(\text{SiMe}_3)\}]_2$. The reaction of $[\text{In}^t\text{Bu}_2\{\text{PH}(\text{SiMe}_3)\}]_2$ with two equivalents of methanol also afforded $[\text{In}^t\text{Bu}_2(\text{OMe})]_2$ or the trimer $[\text{In}^t\text{Bu}_2(\text{PH}_2)]_3$ after longer reaction times. The compounds $[\text{InMe}(\text{Cl})(\text{O}^t\text{Bu})]_2$ and $[\text{InMe}(\text{Br})(\text{O}^t\text{Bu})]_2$ were synthesised *via* alcoholysis of the indium amide $[\text{InMe}(\text{X})\{\text{N}(\text{SiMe}_3)_2\}]_n$ ($\text{X} = \text{Cl}, \text{Br}$), as shown in Scheme 2.2. $[\text{InMe}(\text{Cl})(\text{O}^t\text{Bu})]_2$ was then reacted with $\text{LiN}(\text{SiMe}_3)_2$ to afford $[\text{InMe}(\text{O}^t\text{Bu})\{\text{N}(\text{SiMe}_3)_2\}]_2$ with concomitant formation of LiCl . $[\text{InMe}(\text{O}^t\text{Bu})\{\text{N}(\text{SiMe}_3)_2\}]_2$ was used as a precursor to the formation of an indium bis(alkoxide) (Section 2.1.4).



Scheme 2.2. Synthetic route towards indium mono- and bis(alkoxides).

Fewer reports of donor-functionalised indium mono(alkoxides) have been described than for the gallium equivalents. Recently a series of indium mono(alkoxide) precursors (Figure 2.5) have been reported by Basharat *et al.*¹⁹ and used for the AACVD of In_2O_3 . Thin films were deposited by reacting InMe_3 with ROH ($\text{R} = \text{CH}_2\text{CH}_2\text{NMe}_2$, $\text{CH}(\text{CH}_3)\text{CH}_2\text{NMe}_2$, $\text{C}(\text{CH}_3)_2\text{CH}_2\text{OMe}$, $\text{CH}_2\text{CH}_2\text{OMe}$) in toluene, *in situ* under AACVD conditions. Solution-based reactions were then investigated to gain an insight into the compounds present in the aerosol mist. Compounds of the formula $[\text{InMe}_2(\text{OR})]_2$ ($\text{R} = \text{CH}_2\text{CH}_2\text{NMe}_2$, $\text{CH}(\text{CH}_3)\text{CH}_2\text{NMe}_2$, $\text{C}(\text{CH}_3)_2\text{CH}_2\text{OMe}$, $\text{CH}_2\text{CH}_2\text{OMe}$) were isolated and characterised (Figure 2.5).

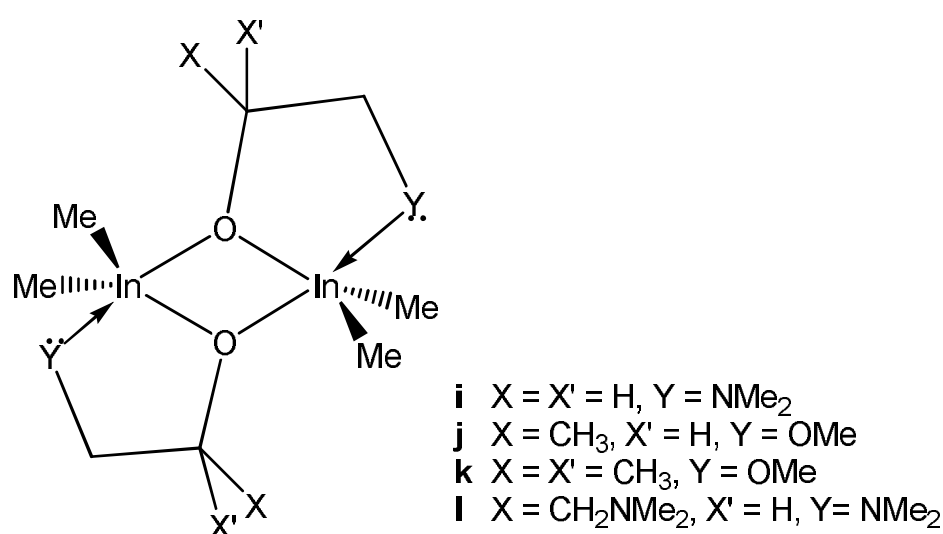


Figure 2.5. A series of indium monoalkoxide complexes synthesised by Basharat *et al.*

White solids (**i** and **k**) or colourless oils (**j** and **l**) were isolated, from which X-ray quality colourless crystals of compounds **i-l** were afforded in 41-68% yields. Analytical and spectroscopic data for **i-l** indicated that the complexes were dimeric and this was confirmed by single crystal X-ray diffraction. The centrosymmetric, four-membered In_2O_2 ring that is common to this type of complex was observed for each of compounds **i-l**.⁸⁵

Each indium atom in compounds **i-k** adopts a distorted trigonal bipyramidal geometry with two methyl groups in equatorial positions (shown in Figure 2.6 with compound **k** as an example). The bridging alkoxide groups are located in both axial and equatorial positions, while the donor atom (Y) of the alkoxide ligand (N for **i** and **j**; O for **k**) is in the axial position. The equatorial In-O bond lengths in **i-k** are significantly shorter than

the axial In-O bond distances. The In-Y distances in **i-k** range from 2.5161(16) to 2.5810(13) Å and can be attributed to $Y \rightarrow \text{In}$ dative bonding. Compound **i** and related compounds, such as $[\text{InMe}_2(\text{OC}(\text{CF}_3)_2\text{CH}_2\text{NHR})]_2$ ($\text{R} = \text{CH}_2\text{CH}_2\text{OMe}$), have been previously reported with comparable bond lengths and angles.^{57, 86, 87} Compound **I** also exhibits a dimeric molecular arrangement similar to **i-k**, and the centrosymmetric, four-membered In_2O_2 ring is planar. However, each indium atom in **I** can be considered to be six-coordinate due to the presence of two donor (NMe_2) groups in the alkoxide ligand.

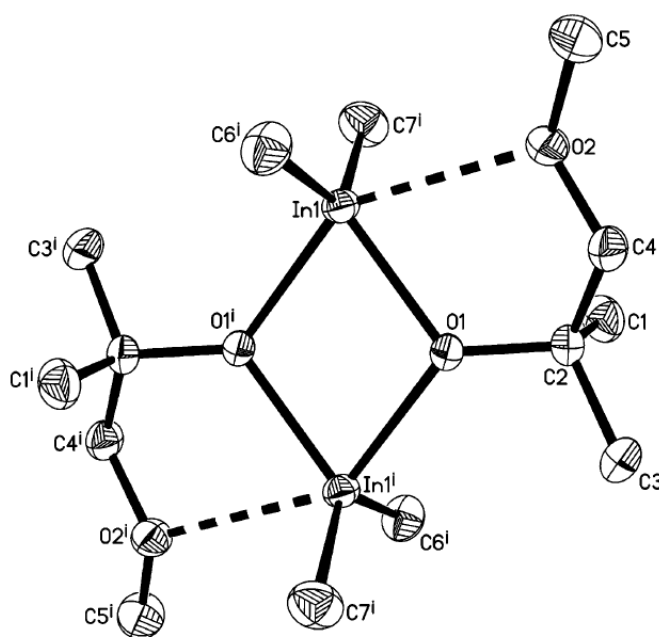


Figure 2.6. Crystal structure of $[\text{InCl}_2(\text{OC}(\text{CH}_3)_2\text{CH}_2\text{OMe})]_2$.¹⁹

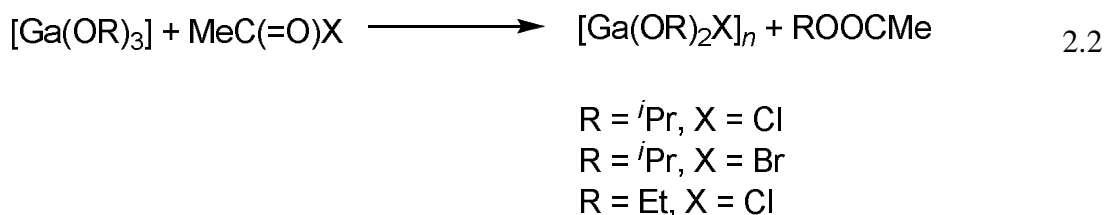
The In_2O_3 thin films obtained from precursors **i-l** were crystalline cubic phase films and no evidence of carbon or nitrogen contamination was found. This was the first report of indium oxide thin films grown by AACVD. Another example of dialkyl indium mono(alkoxides) was reported by Shen *et al.* of the type $[\text{InR}_2(\text{CH}_2\text{CH}_2(2\text{-C}_5\text{H}_4\text{N}))]_2$ ($\text{R} = \text{Me}$ or Et) and incorporates the use of a pyridyl donor ligand.⁸⁸

2.1.3. Gallium bis(alkoxides)

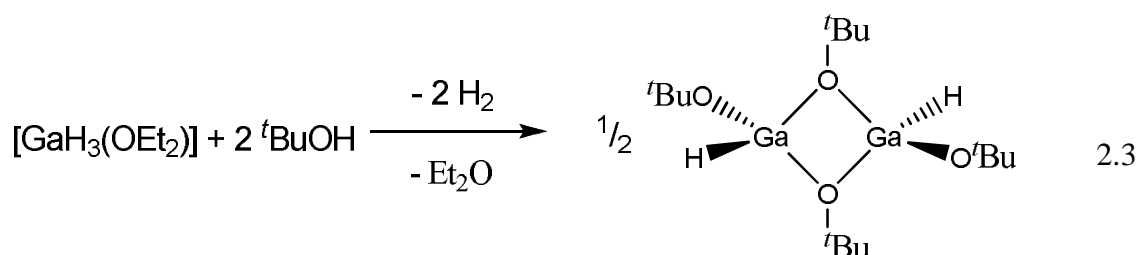
Gallium and indium bis(alkoxide) compounds are uncommon in comparison to the well-known diorganoalkoxometallane analogues. As described in Sections 2.1.1 and 2.1.2, the reaction of an alkyl gallane or indane with an equimolar amount of alcohol affords

the diorganoalkoxometallane complex $[\text{MR}_2(\text{OR}')_n]$ in high yield. However, reaction of a gallane or indane with two equivalents or an excess of alcohol does not typically yield the expected gallium and indium bis(alkoxide) compounds $[\text{MR}(\text{OR}')_2]_n$. Instead reaction of MMe_3 with an excess of alcohol often results in the formation of sesquialkoxides.⁸⁹ The synthesis and characterisation of the few examples of gallium and indium bis(alkoxide) complexes reported in the literature are described in the following sections.

In 1968, Mehrotra and co-workers reported the preparation of gallium bis(alkoxides) *via* the reaction of gallium alkoxides, $[\text{Ga}(\text{OR})_3]$ (Section 2.1.5) with acyl halides.⁹⁰ The reaction of $[\text{Ga}(\text{OR})_3]$ with CH_3COX yielded $[\text{GaX}(\text{OR})_2]$ ($\text{R} = {}^i\text{Pr}$, $\text{X} = \text{Cl}$, Br ; $\text{R} = \text{Et}$, $\text{X} = \text{Cl}$), as shown in Equation 2.2. Compounds $[\text{GaCl}(\text{O}^i\text{Pr})_2]$ and $[\text{GaBr}(\text{O}^i\text{Pr})_2]$ were shown to be trimeric by molecular weight ebullioscopic measurements. In contrast, the compound $[\text{GaCl}(\text{OEt})_2]$ showed dimeric behaviour in a benzene solution.



Gallium bis(alkoxide) incorporating a simple monodentate alkoxide group have been synthesised, of the type $[\text{GaR}(\text{OR}')_2]_2$ ($\text{R} = \text{H}$, $\text{R}' = {}^t\text{Bu}$;⁹¹ $\text{R} = \text{Me}$, $\text{R}' = \text{Et}$, ${}^n\text{Bu}$;⁹² $\text{R} = \text{Et}$, $\text{R}' = \text{CH}_2\text{CH}_2\text{NMe}_2$, $\text{CH}(\text{CH}_3)\text{CH}_2\text{OMe}$ ¹¹). $[\text{GaH}(\text{O}^t\text{Bu})_2]_2$ was synthesised by the 1:2 reaction of $[\text{GaH}_3(\text{OEt}_2)]$ and ${}^t\text{BuOH}$ in diethyl ether at 0 °C, the compound was then isolated by fractional sublimation or distillation under vacuum, as shown in Equation 2.3. The structure of $[\text{GaH}(\text{O}^t\text{Bu})_2]_2$ was determined by single crystal X-ray diffraction, which showed that the complex was dimeric with each gallium centre four-coordinate and approximately tetrahedral (terminal Ga-O 1.783(4) Å; *av.* bridging Ga-O 1.906(4) Å). The bridging oxygen atoms were in a trigonal planar environment. $[\text{GaEt}(\text{OR})_2]$ ($\text{R} = \text{CH}_2\text{CH}_2\text{NMe}_2$, $\text{CH}(\text{CH}_3)\text{CH}_2\text{OMe}$) were isolated as a 1:1 mixture with the gallium mono(alkoxide) $[\text{GaEt}_2(\text{OR})]_2$ *via* the reaction of GaEt_3 with ROH at elevated temperatures.



There are very few reports of gallium and indium bis(alkoxides) incorporating donor-functionalised ligands. In the report by Basharat *et al.*⁷² the gallium bis(alkoxides) $[\text{GaCl}(\text{OCH}_2\text{CH}_2\text{NMe}_2)_2]$ and $[\text{GaCl}(\text{OCH}(\text{CH}_3)\text{CH}_2\text{NMe}_2)_2]$ (Figure 2.7) were isolated as by-products from the reaction of $[\text{Ga}(\text{NMe}_2)_3]_2$ and excess donor functional alcohol, ROH (R = $\text{CH}_2\text{CH}_2\text{NMe}_2$, $\text{CH}(\text{CH}_3)\text{CH}_2\text{NMe}_2$). The gallium bis(alkoxides) were then systematically synthesised directly from $[\text{GaCl}(\text{NMe}_2)_2]_2$ and four molar equivalents of alcohol.

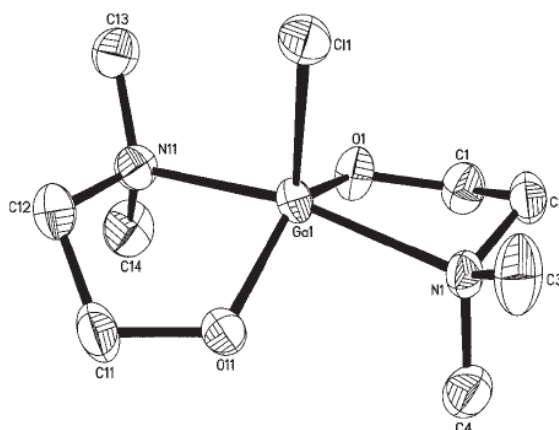


Figure 2.7. Crystal structure of $[\text{GaCl}(\text{OCH}_2\text{CH}_2\text{NMe}_2)_2]$.⁷²

A pale yellow crystalline solid was isolated for both complexes. Spectroscopic and analytical data indicated that the chlorodialkoxogallanes $[\text{GaCl}(\text{OCH}_2\text{CH}_2\text{NMe}_2)_2]$ and $[\text{GaCl}(\text{OCH}(\text{CH}_3)\text{CH}_2\text{NMe}_2)_2]$ had been formed (54-60% yield). A dative ligand-metal interaction in both complexes was confirmed by a comparison of proton resonances of the alkoxide ligand in the product compared to the free ligand. Thus, in the ^1H NMR spectrum of both complexes, a downfield shift in the resonance of protons positioned α to the donor heteroatom was observed. The crystal structures of each complex revealed that the complexes were monomeric.

2.1.4. Indium bis(alkoxides)

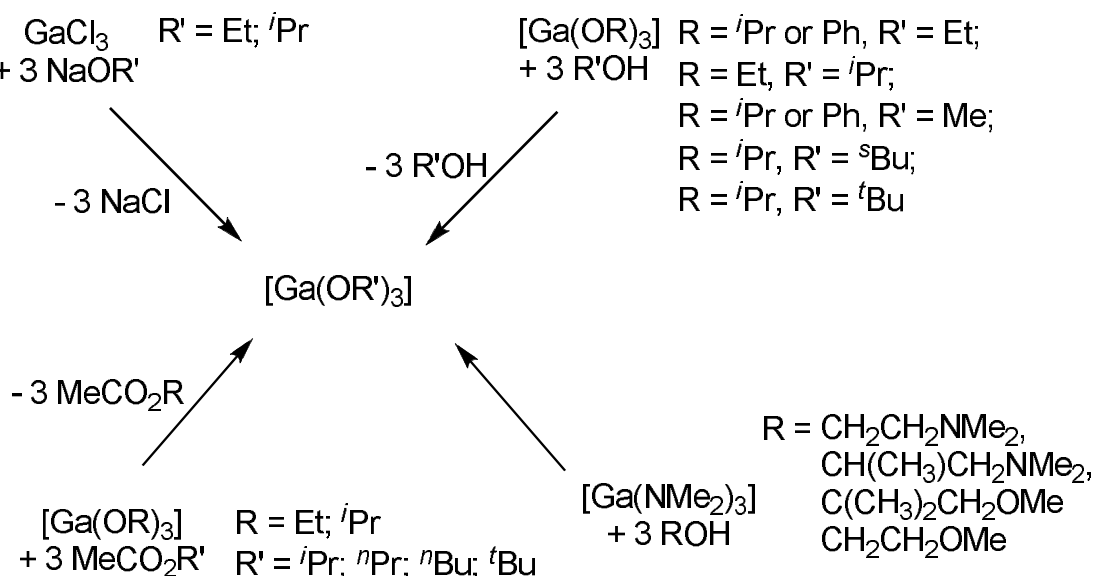
The only well-characterised example of an indium bis(alkoxide) incorporating a monodentate alkoxide is $[\text{InMe}(\text{O}^t\text{Bu})_2]_2$.⁹³ The synthetic procedure was outlined in Scheme 2.2. Initially, the amido complex $[\text{InMe}(\text{Cl})\{\text{N}(\text{SiMe}_3)_2\}]_2$ was reacted with two equivalents of $^t\text{BuOH}$ to afford the alkyl indium mono(alkoxide) $[\text{InMe}(\text{Cl})(\text{O}^t\text{Bu})]$ (previously discussed in Section 2.1.2). Subsequent reaction with $\text{LiN}(\text{SiMe}_3)_2$, followed by ligand exchange with $^t\text{BuOH}$ resulted in the formation of $[\text{InMe}(\text{O}^t\text{Bu})_2]_2$. The solid-state structure comprised of a dimeric molecule with bridging alkoxide groups ($\text{In-O-In } 103.6(2)^\circ$, $\text{O-In-O } 76.4(2)^\circ$). The indium centre adopts a distorted tetrahedral coordination geometry with the In-O bond lengths to the terminal oxygen atoms being 0.12 \AA shorter than the bond lengths in the In_2O_2 ring (bridging In-O $2.128(8) \text{ \AA}$; terminal In-O $2.006(4) \text{ \AA}$).

An indium bis(alkoxide) incorporating a donor-functionalised ligand has also been reported.⁹⁴ Reaction of InCl_3 with two equivalents of $\text{LiOCH}_2\text{CH}_2\text{NMe}_2$ afforded the chloro indium bis(alkoxide) $[\text{InCl}(\text{OCH}_2\text{CH}_2\text{NMe}_2)_2]$. No structural information was reported, however, the indium compounds was shown to react with $[\text{SnMe}_2(\text{CH}_2\text{Li})_2]$ to produce the heterometallic alkoxide $[\text{SnMe}_2(\text{CH}_2\text{In}(\text{OCH}_2\text{CH}_2\text{NMe}_2)_2)_2]$.

2.1.5. Gallium tris(alkoxides)

The first synthesis of homoleptic gallium alkoxide compounds, of the type $[\text{Ga}(\text{OR})_3]_n$ ($\text{R} = \text{alkyl}$), were reported in 1964 in separate papers by Mehrotra and Mehrotra,⁹⁵ and Funk and Paul.⁹⁶ A number of routes have been explored towards the formation of these compounds which are displayed in Scheme 2.3. The reaction of GaCl_3 with three equivalents of NaOR ($\text{R} = \text{Et}$, ^iPr) resulted in the formation of gallium tris(ethoxide) and gallium tris(isopropoxide). A range of homoleptic gallium alkoxides were subsequently prepared and published *via* an alkoxide/alcohol exchange reaction. Gallium tris(isopropoxide) was isolated from the reaction of $[\text{Ga}(\text{OEt})_3]$ and three equivalents of $^i\text{PrOH}$.⁹⁷ In the same year, Funk and co-workers described the synthesis of $[\text{Ga}(\text{OMe})_3]$ and $[\text{Ga}(\text{OEt})_3]$ *via* exchange of the appropriate alcohol with $[\text{Ga}(\text{OPh})_3]$.⁹⁸ An extensive series of normal and branched gallium alkoxides were reported by Mehrotra

and co-workers from the alcohol exchange reactions of $[\text{Ga}(\text{O}^i\text{Pr})_3]$ with ROH ($\text{R} = \text{Me}$, Et, ^nPr , ^nBu , ^sBu and ^tBu) and transesterification reactions.⁹⁹

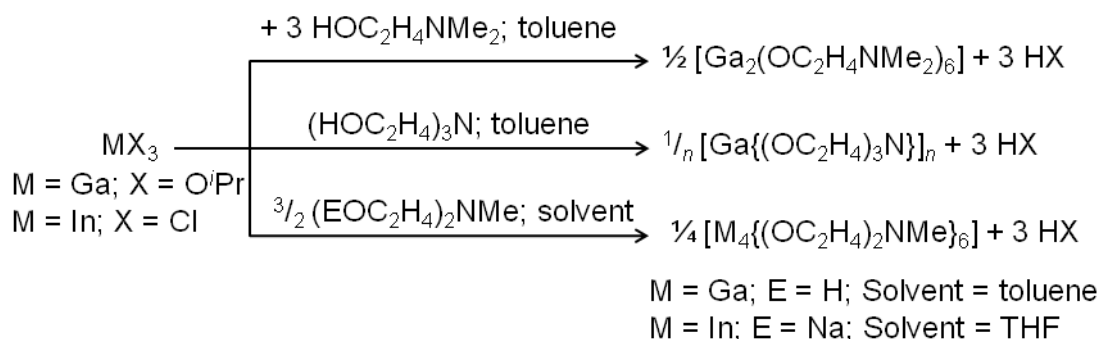


Scheme 2.3. Routes employed for the formation of homoleptic gallium tris(alkoxides)

In the report by Basharat *et al.*⁷² a series of gallium tris(alkoxides) were described consisting of the formula $[\text{Ga}(\text{OR})_3]$ ($\text{R} = \text{CH}_2\text{CH}_2\text{NMe}_2$, $\text{CH}(\text{CH}_3)\text{CH}_2\text{NMe}_2$, $\text{C}(\text{CH}_3)_2\text{CH}_2\text{OMe}$, $\text{CH}_2\text{CH}_2\text{OMe}$), as shown in Scheme 2.3. These gallium tris(alkoxides) were isolated as colourless oils from the reaction of $[\text{Ga}(\text{NMe}_2)_3]_2$ with an excess of ROH. Although crystallographic data were not obtained for these compounds, mass spectrometric data suggested that the compounds were dimeric, as well as infra red spectroscopy showing stretches at 557 and 538 cm^{-1} which are characteristic of Ga_2O_2 ring modes. The oils contained the by-products $[\text{GaCl}_2(\text{OC}(\text{CH}_3)_2\text{CH}_2\text{OMe})_2]$ and $[\text{GaCl}(\text{OCH}_2\text{CH}_2\text{NMe}_2)_2]$, shown in Figure 2.2 and Figure 2.7, which have not been used to produce gallium oxide thin films *via* AACVD.

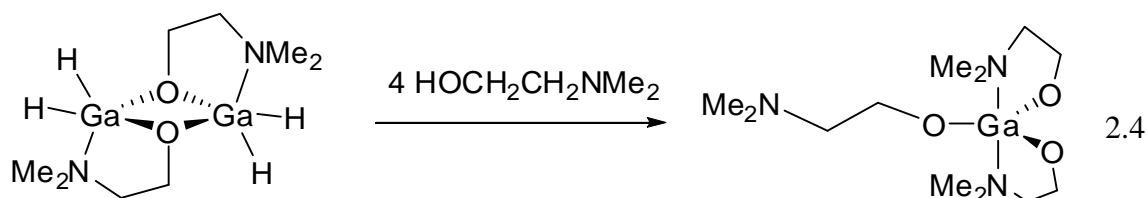
A series of homoleptic gallium and indium alkoxides, of the type $[\text{Ga}_2(\text{OCH}_2\text{CH}_2\text{NMe}_2)_6]$, $[\text{M}_4\{\text{NMe}(\text{OC}_2\text{H}_4)_2\}_6]$ ($\text{M} = \text{Ga}, \text{In}$) and $[\text{Ga}\{\text{N}(\text{OC}_2\text{H}_4)_3\}]_n$ have been prepared by isopropoxo(chloro)-alkoxo exchange reactions (Scheme 2.4).^{30, 100} These metal tris(alkoxide) compounds result in cluster complexes which have been characterised by elemental analysis, FT-IR and ^1H NMR spectroscopy, as well as single crystal X-ray diffraction for $[\text{M}_4\{\text{NMe}(\text{OC}_2\text{H}_4)_2\}_6]$. The use of the ligand $-\text{N}(\text{C}_2\text{H}_4\text{OH})_3$

is different to those previously described, having four donor groups within the ligand, and thus only one ligand is required per metal to obtain the metal tris(alkoxide).



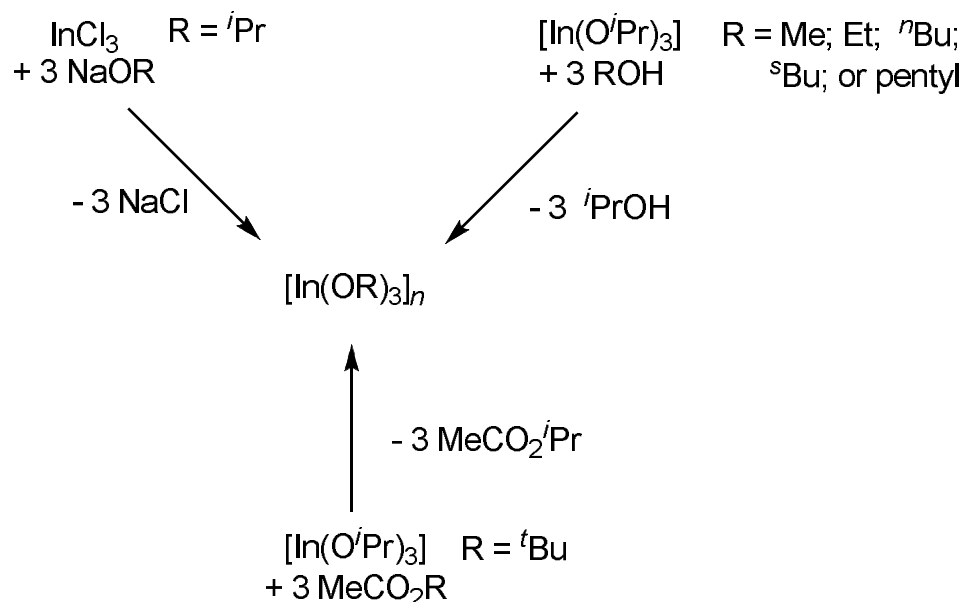
Scheme 2.4. Synthetic procedures used to synthesis a series of metal tris(alkoxide) cluster compounds synthesised by Daniele *et al.*¹⁰⁰

The monomeric gallium tris(alkoxide), $[\text{Ga}(\text{OCH}_2\text{CH}_2\text{NMe}_2)_3]$, was also synthesised within the Carmalt group, starting from $[\text{GaH}_2(\text{OCH}_2\text{CH}_2\text{NMe}_2)]_2$ and reacting with two equivalents of alcohol (Equation 2.4).¹⁰¹ Whilst the single crystal X-ray diffraction dataset was merely sufficient to show the atom connectivity, it confirmed the monomeric nature of the complex as a 5-coordinate species with one ‘dangling’ Lewis base. This is in contrast to the oil of $[\text{Ga}(\text{OCH}_2\text{CH}_2\text{NMe}_2)_3]_2$ previously isolated *via* the reaction of $[\text{Ga}(\text{NMe}_2)_3]_2$ and $\text{HOCH}_2\text{CH}_2\text{NMe}_2$ which were characterized as dimeric based on spectroscopic data.⁷² The ^1H NMR spectrum of $[\text{Ga}(\text{OCH}_2\text{CH}_2\text{NMe}_2)_3]$ showed broad peaks, indicating probable fluxionality on the NMR timescale, with the ‘dangling’ amine exchanging with other donor-functionalised ligands attached to the gallium centre. This is the only known monomeric gallium tris(alkoxide) however it is not easily reproduced in high yield.



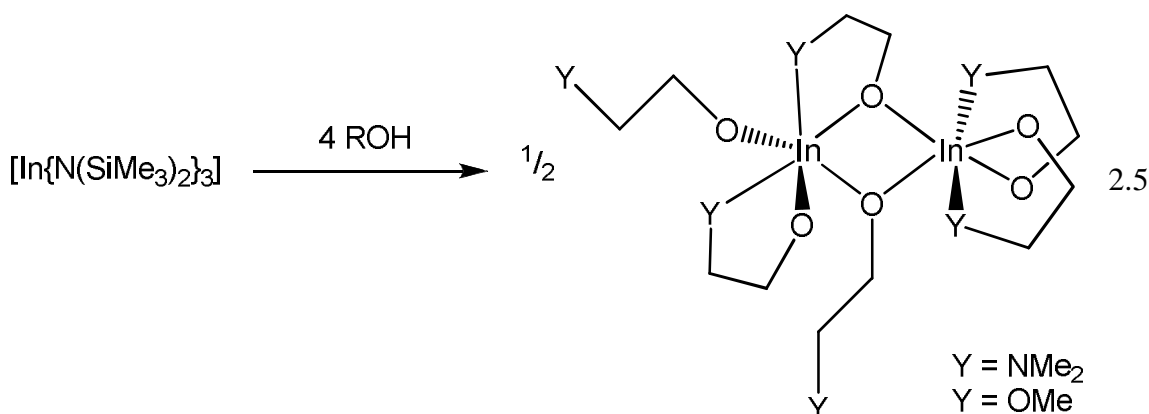
2.1.6. Indium tris(alkoxides)

Recently the synthesis of homoleptic indium alkoxides has been explored due to their suitability as precursors to indium oxide. A series of routes have been used for the formation of indium tris(alkoxides), as outlined in Scheme 2.5. The synthesis of $[\text{In}(\text{O}^i\text{Pr}_3)]_n$ was first reported over 30 years ago by Mehrotra and co-workers.¹⁰² Synthesised from the reaction of InCl_3 and three equivalents of NaO^iPr in refluxing 2-propanol, the compound was determined to have a molecular complexity of four in boiling 2-propanol. An extensive series of other indium tris(alkoxide) compounds $[\text{In}(\text{OR})_3]_n$ were subsequently prepared from $[\text{In}(\text{O}^i\text{Pr}_3)]_n$ by alcohol/alkoxide exchange ($\text{R} = \text{Me}, \text{Et}, {}^n\text{Bu}, {}^s\text{Bu}, \text{pentyl}$) or transesterification ($\text{R} = {}^t\text{Bu}$), also outlined in Scheme 2.5.



Scheme 2.5. Routes explored to synthesise homoleptic indium tris(alkoxides)

There is a report of homoleptic donor-functionalised indium alkoxides $[\text{In}(\text{OR})_3]_2$ ($\text{R} = \text{CH}_2\text{CH}_2\text{OMe}, \text{CH}_2\text{CH}_2\text{NMe}_2$) which were prepared by the amide/alcohol exchange alcoholysis of $[\text{In}\{\text{N}(\text{SiMe}_3)_2\}_3]$,¹⁰³ as shown in Equation 2.5. An X-ray crystallographic study of $[\text{In}(\text{OCH}_2\text{CH}_2\text{NMe}_2)_3]_2$ showed that in the solid-state the unsymmetrical dimeric structure was adopted with two $[\text{InO}_6]$ octahedra sharing a common edge. The In-O bond distances (2.056(4)-2.189(4) Å) were longer than for alkoxides attached to four coordinate indium centres. The In-N bond distances (2.324(6)-2.477(5) Å) were in the range observed for In-N coordination bonds.¹⁰⁴



2.1.7. Summary

Many group 13 alkoxide compounds have been reported and reviewed. These include mono-, bis- and tris(alkoxide) complexes of both gallium and indium. Of these, gallium mono(alkoxides) are most common and generally dimeric in nature.

Metal alkoxides are reported as being good precursors to metal oxides *via* CVD however there has not been much investigation of gallium and indium alkoxides, particularly bis(alkoxides), as precursors for CVD. Therefore there is a real requirement for new highly volatile precursors to deposit Ga₂O₃ and In₂O₃ films that are free from contamination (such as carbon or halides) and to investigate the gas sensing and TCO properties of the resulting films.

The volatility of metal alkoxides is heavily influenced by their tendency to form oligomeric $[\text{M}(\text{OR})_x]_n$ clusters. Oligomerisation is likely to occur around an incomplete coordination sphere. This can be prevented by introducing bulky alkoxide ligands which sterically shield metal centres from metal-oxygen intermolecular interactions. Another approach to inhibit oligomerisation that has been widely studied is to use donor-functionalised alcohols as opposed to monodentate alkoxides.¹⁰⁵ This approach is often used for metal alkoxide precursor synthesis and has been used to deposit metal oxide thin films *via* CVD techniques.¹⁰⁶ These alcohols can chelate *via* an extra donor group, leading to a fully saturated metal centre. This makes the precursor more volatile as oligomerisation is inhibited or reduced and can also lead to improved solubility for

solution based routes. The donor ligand is seen to stabilise the metal centre in the gas phase.

From previously reported structures, metal complexes of monomeric donor-functionalised alkoxides are expected to be better CVD precursors as they are likely to be liquids or low melting solids, hence will be more volatile. Donor-functionalised bis(alkoxide) metal complexes were found to be consistently monomeric in nature and therefore more likely to be volatile as opposed to the mono- and tris(alkoxides) which tend to be dimers or clusters. Therefore, gallium bis(alkoxides) have been the focus of this work with specific attention on the preparation of monomeric heteroleptic gallium alkoxides to improve the Ga:O ratio and reduce the chance of halide contamination during use in CVD reactions.

2.2. Results and Discussion

As discussed in Section 2.1.4, a number of synthetic routes have been investigated for the formation of homoleptic gallium alkoxides $[\text{Ga}(\text{OR})_3]_x$.⁵⁷ The general procedures include the salt metathesis of gallium trihalide, alkoxide/alcohol exchange and transesterification reactions. These routes have been successful for the production of homoleptic gallium alkoxides, however when producing heteroleptic gallium alkoxides the synthesis became more complicated due to a tendency to form a mixture of alkoxide complexes.⁷²

Some of the routes reported have been utilised towards the synthesis of monomeric heteroleptic gallium alkoxides. Herein, the routes tried as part of this work towards target compounds are described. The first stage for synthesising heteroleptic gallium alkoxides was the addition of two alkoxide groups to alkyl gallanes, generating gallium bis(alkoxide) type complexes.

2.2.1. Reaction of trimethyl gallium and two equivalents of alcohol

The addition of trimethyl¹⁰⁷ or triethyl¹⁰ gallium and two equivalents or an excess of alcohol, as described in Section 2.1.3 and outlined in Equation 2.6, has been previously explored in an effort to synthesise $[\text{GaR}'(\text{OR})_2]$ ($\text{R}' = \text{Me}$ or Et , $\text{R} =$ donor-functionalised ligands), however a mixture of products results.



Attempts were made to repeat this route to form $[\text{GaR}'(\text{OR})_2]$, however a mixture of gallium mono- and bis(alkoxides) were formed after the addition of alcohol to either trimethyl or triethyl gallium. Even after the addition of excess alcohol the third alkyl group was not removed. Due to the uncertainty of the final product and the difficulty in removing the final alkyl group, another approach was taken using the alkoxide/alcohol exchange route as discussed in Section 2.2.2.

2.2.2. Attempted synthesis of $[\text{Ga}(\text{O}^i\text{Pr})(\text{OR})_2]$ via the alkoxide/alcohol exchange route

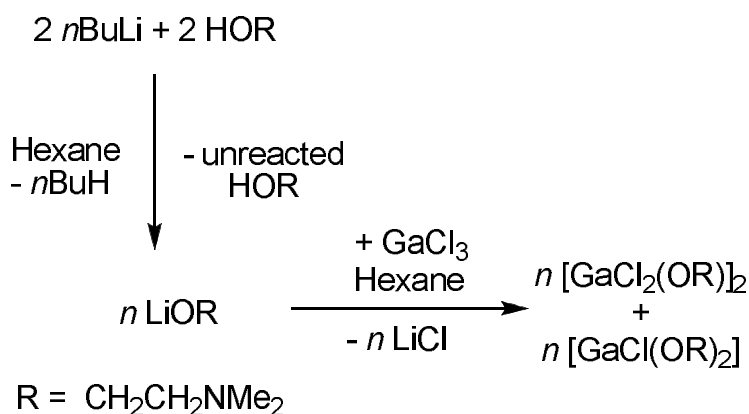
Alkoxide/alcohol exchange reactions have been used to synthesise homoleptic gallium alkoxides.⁹⁹ By adding two equivalents of alcohol to gallium tri(*iso*-propoxide) the formation of $[\text{Ga}(\text{O}^i\text{Pr})(\text{OR})_2]$ was expected (Equation). Two equivalents of the donor-functionalised alcohol, $\text{HOCH}_2\text{CH}_2\text{NMe}_2$, were added to a stirred solution of gallium tris(*iso*-propoxide) in toluene. However, addition of the alcohol did not displace the *iso*-propoxide groups even after lengthy stirring. Subsequently, reflux conditions were exploited which resulted in the decomposition of the compound to a brown oily product. The identity of this oil was difficult to determine from spectroscopic data due to a large mixture of products, none of which corresponded to the target compound.



As the reaction outlined in Equation 2.7 was unsuccessful as a direct route towards heteroleptic gallium alkoxides, a two step reaction was employed based on salt elimination routes, as described in Section 2.2.3.

2.2.3. Attempted synthesis of $[\text{GaCl}(\text{OR})_2]$ using a lithiated alkoxide

The direct lithiation of donor-functionalised alcohols was undertaken in order to use the resulting lithium alkoxide for salt elimination reactions with gallium trichloride (Scheme 2.6). The lithiated alkoxide was prepared according to a modified literature preparation by Chi *et al.*¹⁰⁸ A 1:1 ratio of *n*-butyl lithium and donor-functionalised alcohol were added together in hexane at room temperature. The product consisted of a mixture of compounds including unreacted starting material and the desired lithium alkoxides. This meant it was difficult to calculate a yield and thus determine the correct molar ratio for use in the subsequent stage of the reaction. On addition to gallium trichloride, a mixture of the gallium mono- and bis(alkoxide) products were formed.

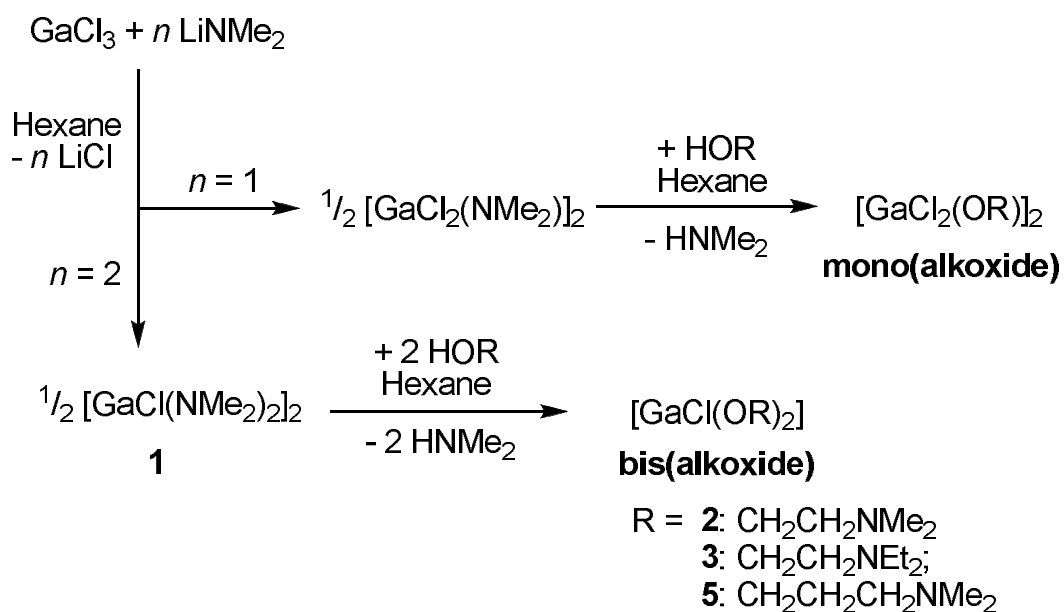


Scheme 2.6. Attempted route towards the synthesis of $[\text{GaCl}(\text{OR})_2]$ by lithiating the donor-functionalised alcohol followed by salt metathesis.

For a more accurate synthetic method where solely the gallium bis(alkoxide) derivative was isolated, the chloro gallium bis(amide) was first synthesised followed by amide/alcohol exchange. This preparation is outlined in Section 2.2.4.

2.2.4. Synthesis of chloro gallium alkoxides *via* chloro gallium amide intermediates

A two step route was employed to synthesise chloro gallium alkoxides (Scheme 2.7) as previously described by Basharat *et al.*⁷² The first step involved the addition of stoichiometric quantities of lithium dimethylamide to a solution of GaCl₃ in hexane. Lithium dimethylamide was used as the amide of choice for this reaction because past examples of using LiN(SiMe₃)₂ with MCl₃ (M = Ga, In) and LiN(SiMe₂Ph)₂ with GaCl₃ have resulted in methyl and phenyl migration to produce [MMe{N(SiMe₂)₂}(μ-Cl)]₂^{20, 107} and [GaPh{N(SiMe₂Ph)₂}(μ-Cl)]₂.¹¹ The second step involved the addition of stoichiometric amounts of a donor-functionalised alcohol to the product, also in hexane. After work-up, the resulting crystalline gallium mono- or bis(alkoxides) were obtained in high yield, as described in detail in Section 2.2.5.



Scheme 2.7. Two step route towards chloro gallium alkoxide compounds *via* a chloro gallium amide intermediate

2.2.4.1. Reaction of GaCl₃ with two equivalents of LiNMe₂

The reaction of GaCl₃ with two equivalents of LiNMe₂ in hexane, initially at -78 °C, followed by stirring for 24 hours at room temperature, afforded the dichloro gallium amide [GaCl(NMe₂)₂]₂ (**1**) as a free flowing white powder in high yield. This method was carried out based on that previously reported by Atwood *et al.*¹⁰⁹ The ¹H NMR spectrum of **1** shows two broad peaks at 2.35 and 2.78 ppm in a 1:1 ratio, corresponding to the terminal and bridging amide methyl environments (-N(CH₃)₂), shown in Figure 2.8, which is in agreement with values previously reported by Atwood *et al.*

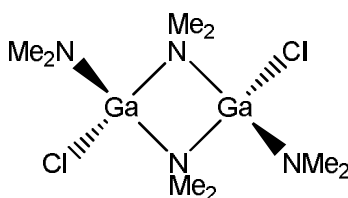


Figure 2.8. Structure of [GaCl(NMe₂)₂]₂ (**1**) showing terminal and bridging -NMe₂ groups.

2.2.5. Gallium bis(alkoxides)

2.2.5.1. Reaction of [GaCl(NMe₂)₂]₂ (**1**) and four equivalents of HOCH₂CH₂NMe₂

The reaction of **1** with four equivalents of the donor-functionalised alcohol HOCH₂CH₂NMe₂ in hexane, followed by stirring for 24 hours at room temperature, afforded the white crystalline product [GaCl(OCH₂CH₂NMe₂)₂]₂ (**2**). Single crystals of **2** were isolated after the solvent was reduced to approximately 5 cm³ and the solution left to cool to -18 °C. This preparation was identical to that previously reported by Carmalt *et al.* where the crystal structure of **2** was also described.⁷² Spectroscopic and analytical techniques confirmed the formation of compound **2**. ¹H NMR and ¹³C{¹H} NMR spectra supported the formation of **2** and are discussed separately in Section 2.5. In the mass spectrum of **2** taken in toluene, a peak was observed for the molecular ion at *m/z* = 281.

2.2.5.2. Reaction of $[\text{GaCl}(\text{NMe}_2)_2]_2$ (**1**) and four equivalents of $\text{HOCH}_2\text{CH}_2\text{NEt}_2$

The synthetic route employed in the production of **2** (Section 2.2.5.1) was also used to produce $[\text{GaCl}(\text{OCH}_2\text{CH}_2\text{NEt}_2)_2]$ (**3**) using four equivalents of the donor-functionalised alcohol $\text{HOCH}_2\text{CH}_2\text{NEt}_2$. Single crystals of **3** were isolated after the solvent was reduced to approximately 5 cm^3 and the solution left to cool at $-18 \text{ }^\circ\text{C}$. Spectroscopic and analytical techniques confirmed the formation of compound **3**. ^1H NMR and $^{13}\text{C}\{^1\text{H}\}$ NMR spectra supported the formation of **3** and are also discussed separately in Section 2.2.6. In the mass spectrum of **3** taken in toluene, a peak was observed for the molecular ion at $m/z = 337$.

2.2.5.3. X-ray crystallographic studies of $[\text{GaCl}(\text{OCH}_2\text{CH}_2\text{NEt}_2)_2]$ (**3**)

The crystal structure of compound **3**, shown in Figure 2.9, was determined by single crystal X-ray diffraction and selected bond lengths and angles are given in Table 2.1. Compound **3** crystallised into the monoclinic $P2_1/c$ space group and is monomeric in the solid-state with the gallium atom adopting a distorted trigonal bipyramidal geometry. The oxygen atoms of each alkoxide ligand and the chlorine atom occupy the equatorial positions whilst the nitrogen atoms of the donor-functionalised group reside in the axial positions (Figure 2.9).

Table 2.1. Selected bond lengths (\AA) and angles ($^\circ$) for $[\text{GaCl}(\text{OCH}_2\text{CH}_2\text{NEt}_2)_2]$ (**3**)

N(1)-Ga(1)	2.1797(14)	O(2)-Ga(1)	1.8407(12)
N(2)-Ga(1)	2.2080(15)	Cl(1)-Ga(1)	2.2323(5)
O(1)-Ga(1)	1.8341(13)		
O(1)-Ga(1)-O(2)	127.60(6)	N(1)-Ga(1)-N(2)	170.33(5)
O(1)-Ga(1)-N(1)	85.10(6)	O(1)-Ga(1)-Cl(1)	115.13(5)
O(2)-Ga(1)-N(1)	92.34(5)	O(2)-Ga(1)-Cl(1)	117.23(5)
O(1)-Ga(1)-N(2)	90.63(6)	N(1)-Ga(1)-Cl(1)	95.18(4)
O(2)-Ga(1)-N(2)	83.38(6)	N(2)-Ga(1)-Cl(1)	94.49(4)

The N1-Ga-N2 bond angle is $170.33(5)^\circ$, which deviates from the ideal 180° , although it is not as pronounced as with the dimeric alkoxogallanes such as $[\text{GaCl}_2(\text{OCH}_2\text{CH}_2\text{NEt})_2]$ (**4**) (see Section 2.2.5.5), due to the lack of constraint in the monomer versus the dimer. The sum of the bond angles in the equatorial plane of **3** is 360.00° , which is a measure of the planarity of the equatorial groups. The two equatorial Ga-O bond lengths are very similar ($1.8341(13)$ and $1.8407(12)$ Å) which is indicative of the same Ga-O bond type. The Ga-N distances are $2.1797(14)$ and $2.2080(15)$ Å and significantly shorter than the sum of the van der Waals radii and so indicative of a strong dative bonding interaction. The difference between the two Ga-N bond lengths could be a result of crystal packing effects which is also observed with other gallium mono- and bis(alkoxide) compounds.⁷²

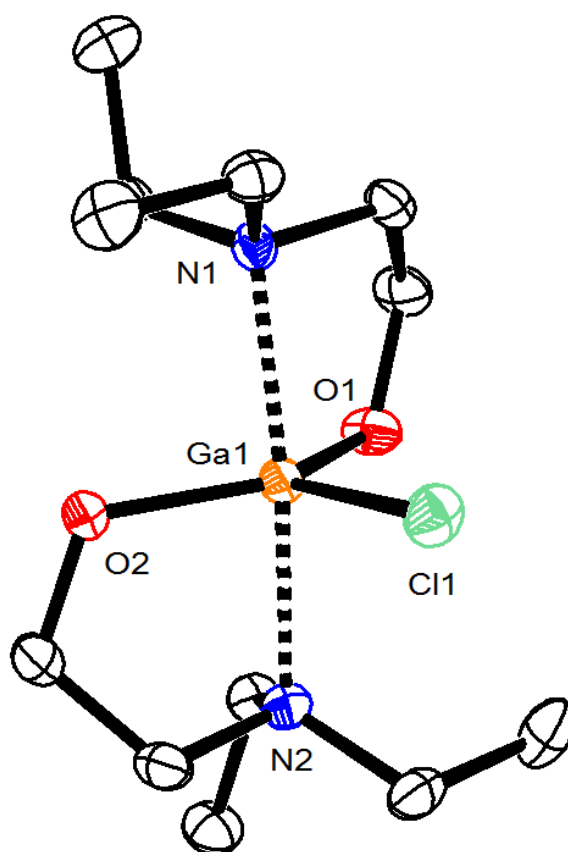


Figure 2.9. ORTEP diagram of $[\text{GaCl}(\text{OCH}_2\text{CH}_2\text{NEt}_2)_2]$ (**3**) with thermal ellipsoids drawn at 50 % probability. H atoms are omitted for clarity.

Similar trigonal bipyramidal geometry at the gallium centre has been observed previously in the related intramolecularly stabilised alkoxogallanes

[GaEt(OCH₂CH₂NMe₂)₂] and [GaCl(OR)₂] (R = C(CF₃)₂CH₂C(CH₃)NMe; C(CF₃)₂CH₂NMe₂; OCH₂CH₂NMe₂ and OCH(CH₃)CH₂NMe₂).^{11, 72, 108} The Ga-O and Ga-N bond distances in these compounds are similar to those observed in **3**.

2.2.5.4. Formation of [GaCl₂(OCH₂CH₂NEt₂)₂] (**4**)

During one reaction to synthesise compound **3**, colourless crystals in a different morphology to the desired product were obtained. These were identified as the compound [GaCl₂(OCH₂CH₂NEt)₂] (**4**) and were isolated in low yield. The production of **4** during the reaction of **3** was observed during only one batch reaction and is likely to have occurred due to inadvertent use of the incorrect stoichiometry of reagents. Single crystal X-ray diffraction and ¹H NMR spectroscopy confirmed the formation of compound **4**. The ¹H NMR spectrum of **4** showed a triplet at 0.99 ppm corresponding to -NCH₂CH₃, a multiplet at 2.65 corresponding to overlapping signals of -NCH₂CH₃ and -OCH₂CH₂, and a triplet at 3.45 corresponding to -OCH₂ in a 3:3:1 ratio. Further evidence for compound **4** was not obtained owing to the low yield collected, however X-ray diffraction confirmed the dimeric nature of **4**.

2.2.5.5. X-Ray crystallographic studies of [GaCl₂(OCH₂CH₂NEt₂)₂] (**4**)

The crystal structure of compound **4** was determined by X-ray crystallography, the results of which are shown in Figure 2.10; selected bond lengths and angles are given in Table 2.2. Compound **4** crystallised into the monoclinic, *P*2₁/*c* space group. As shown in Figure 2.10, the compound adopts a dimeric molecular arrangement. The centrosymmetric, four-membered Ga₂O₂ ring that is common to this type of complex is planar,¹¹ and the bidentate ligand forms a five-membered ring.

Table 2.2. Selected bond lengths (Å) and angles (°) for [Cl₂Ga(OCH₂CH₂NEt₂)₂] (4)
[Symmetry code: (i) 2-x, -y, 1-z].

N(1)-Ga(1)	2.1406(18)	Ga(1)-O(1) ⁱ	1.9989(15)
O(1)-Ga(1)	1.8995(15)	Cl(1)-Ga(1)	2.2020(6)
O(1)-Ga(1) ⁱ	1.9989(15)	Cl(2)-Ga(1)	2.1859(6)
Ga(1)-O(1)-Ga(1) ⁱ	106.58(7)	N(1)-Ga(1)-Cl(2)	99.34(5)
O(1)-Ga(1)-O(1) ⁱ	73.42(7)	O(1)-Ga(1)-Cl(1)	117.31(6)
O(1)-Ga(1)-N(1)	81.22(6)	O(1) ⁱ -Ga(1)-Cl(1)	96.54(5)
O(1)-Ga(1)-Cl(2)	128.59(6)	N(1)-Ga(1)-Cl(1)	97.78(5)
O(1) ⁱ -Ga(1)-Cl(2)	94.15(5)	Cl(2)-Ga(1)-Cl(1)	113.54(2)
O(1) ⁱ 1-Ga(1)-N(1)	154.45(6)		

Each gallium atom in **4** adopts a distorted trigonal bipyramidal geometry with a chlorine atom in two of the equatorial positions. The bridging alkoxide groups are located in both axial and equatorial positions, while the nitrogen atom (N1) of the alkoxide group is in the axial position with the O1ⁱ-Ga-N1 bond angle to the opposite, axial alkoxide group being 154.45(6)°. This deviation from 180° is due to the constraints of the internal O1ⁱ-Ga-O1 angle (73.42(7)°) in the Ga₂O₂ ring and the geometry of the ligand. The sum of the bond angles in the equatorial plane of **4** is 359.77°, which is a measure of the planarity of the equatorial groups. The equatorial Ga-O bond length (1.8995(15) Å) is slightly shorter than the axial Ga-Oⁱ bond distance (1.9989(15) Å) which is indicative of two active bonding Ga-O bond types. The longer Ga-N1 distance (2.1406(18) Å) in **4**, can be attributed to N1→Ga dative bonding. Similar distorted trigonal bipyramidal geometry at the metal centre has been noted in the closely related intramolecularly stabilised diorganoalkoxometallanes, of the type [MMe₂(OR)]₂ (M = Ga, R = OCH₂CH₂NMe₂, OCH₂CH₂OMe, OCH(CH₃)CH₂NMe₂ and OCH(CH₃)CH₂OMe).^{19, 54, 110-112} These structures are also dimeric in the solid-state and consist of planar, or nearly planar, M₂O₂ rings. The metal centres are also coordinated in a distorted trigonal bipyramidal geometry with comparable bond lengths and angles.

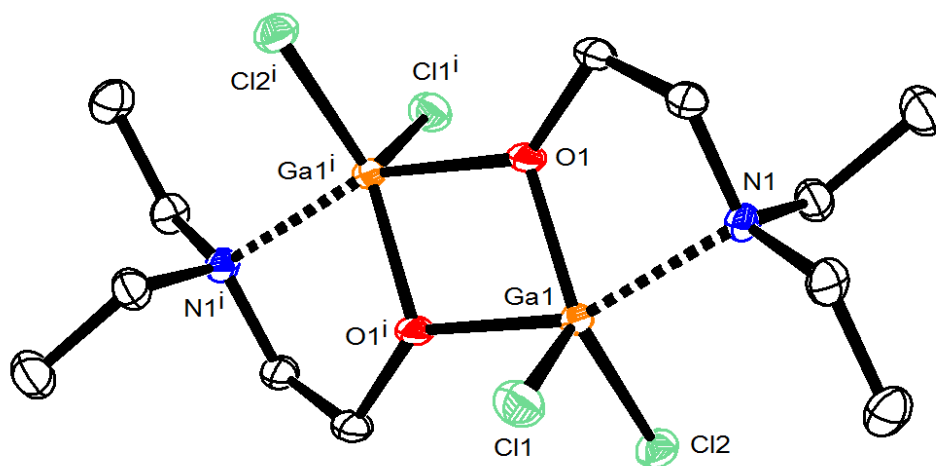


Figure 2.10. ORTEP diagram of $[\text{GaCl}_2(\text{OCH}_2\text{CH}_2\text{NEt}_2)_2]$ (**4**) with thermal ellipsoids drawn at 50 % probability. H atoms are omitted for clarity. Symmetry code: (i) $2-x, -y, 1-z$.

2.2.5.6. Reaction of $[\text{GaCl}(\text{NMe}_2)_2]_2$ (**1**) and four equivalents of $\text{HOCH}_2\text{CH}_2\text{CH}_2\text{NMe}_2$

The synthetic route employed in the production of **2** (Section 2.2.5.1) was also used to produce $[\text{GaCl}(\text{OCH}_2\text{CH}_2\text{CH}_2\text{NMe}_2)_2]$ (**5**) using four equivalents of the donor-functionalised alcohol $\text{HOCH}_2\text{CH}_2\text{CH}_2\text{NMe}_2$. Single crystals of **5** were isolated after the solvent was reduced approximately 5 cm^3 and the solution cooled to $-18 \text{ }^\circ\text{C}$. Spectroscopic and analytical techniques confirmed the formation of compound **5**. ^1H NMR and $^{13}\text{C}\{^1\text{H}\}$ NMR spectra which support the formation of **5**, are discussed separately in Section 2.2.6. In the mass spectrum of **5** taken in toluene, a peak was observed for the molecular ion at $m/z = 309$.

2.2.5.7. X-ray crystallographic studies of $[\text{GaCl}(\text{OCH}_2\text{CH}_2\text{CH}_2\text{NMe}_2)_2]$ (**5**)

The crystal structure of compound **5**, shown in Figure 2.11, was determined by single crystal X-ray diffraction and selected bond lengths and angles are given in Table 2.3.

Table 2.3. Selected bond lengths (Å) and angles (°) for [GaCl(OCH₂CH₂CH₂NMe₂)₂]

(5)

Ga(1)-O(1)	1.8235(13)	Ga(1)-N(2)	2.1725(16)
Ga(1)-O(2)	1.8302(14)	Ga(1)-N(1)	2.2109(17)
Ga(1)-Cl(1)	2.2296(6)		
O(1)-Ga(1)-O(2)	129.35(6)	N(2)-Ga(1)-N(1)	171.32(6)
O(1)-Ga(1)-N(2)	88.16(6)	O(1)-Ga(1)-Cl(1)	114.89(5)
O(2)-Ga(1)-N(2)	89.10(6)	O(2)-Ga(1)-Cl(1)	115.74(5)
O(1)-Ga(1)-N(1)	88.50(6)	N(2)-Ga(1)-Cl(1)	94.92(5)
O(2)-Ga(1)-N(1)	86.83(6)	N(1)-Ga(1)-Cl(1)	93.76(5)

Compound **5** crystallised into the monoclinic $P2_1/c$ space group and was monomeric in the solid-state with the gallium atom adopting a distorted trigonal bipyramidal geometry. The oxygen atoms of each alkoxide ligand and the chloride group occupy the equatorial positions whilst the nitrogen atoms of the donor-functionalised group reside in the axial positions (Figure 2.11). The N1-Ga-N2 bond angle is 171.32(6)°, which deviates from 180°, although it is not as pronounced as with the dimeric alkoxogallanes such as **4** due to the lack of constraint in the monomer versus similar dimeric derivatives. The sum of the bond angles in the equatorial plane of **5** is 360.00°, which is a measure of the planarity of the equatorial groups. The two equatorial Ga-O bond lengths are very similar (1.8235(13) and 1.8302(14) Å) which is indicative of the same Ga-O bond type. The Ga-N distances are 2.1725(16) and 2.2109(17) Å and are significantly shorter than the sum of the van der Waals radii, hence they are indicative of a strong dative bonding interaction. These bond angles and lengths are comparable to those found in **5** and the other related alkoxogallanes as described in Section 2.2.5.3. The difference between the two Ga-N bond lengths could be a result of crystal packing effects as previously described for **3**.

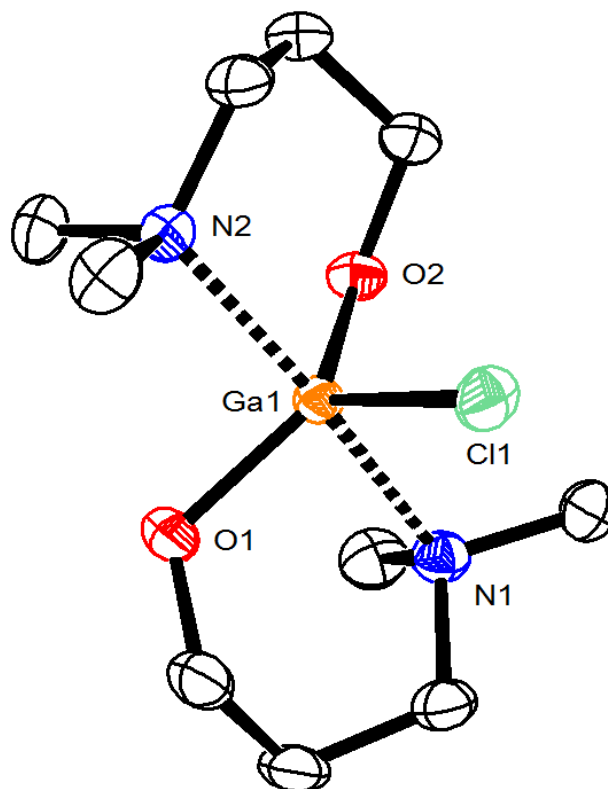


Figure 2.11. ORTEP diagram of $[\text{GaCl}(\text{OCH}_2\text{CH}_2\text{CH}_2\text{NMe}_2)_2]$ (**5**) with thermal ellipsoids drawn at 50 % probability. H atoms are omitted for clarity.

2.2.6. Nuclear magnetic resonance studies of chloro gallium bis(alkoxide) complexes

The ^1H NMR spectra of the chloro gallium bis(alkoxides) (compounds **2**, **3** and **5**) varied with the nature of the ligand. In the case of compound **2**, the room temperature, 293 K, spectrum shows a pair of peaks arising from each of the methyl and methylene groupings in the molecule. This observation is entirely consistent with the crystal structure reported previously by Basharat et al,⁷² indicating a C_2 symmetric molecule with equivalent alkoxide ligands each bearing pairs of diastereotopic hydrogens. Crucially this assignment implies a rigid coordination sphere for compounds **2**. By contrast for compounds **3** and **5**, the room temperature spectrum was broad and featureless, apart from a singlet assigned to the methyl protons, implying a fluxional coordination sphere. On cooling the **3** and **5** to low temperature, 233 and 213 K respectively, the spectra sharpened to give spectra broadly analogous to those of **2** with pairs of mutually coupled diastereotopic hydrogens as shown in Figure 2.12.

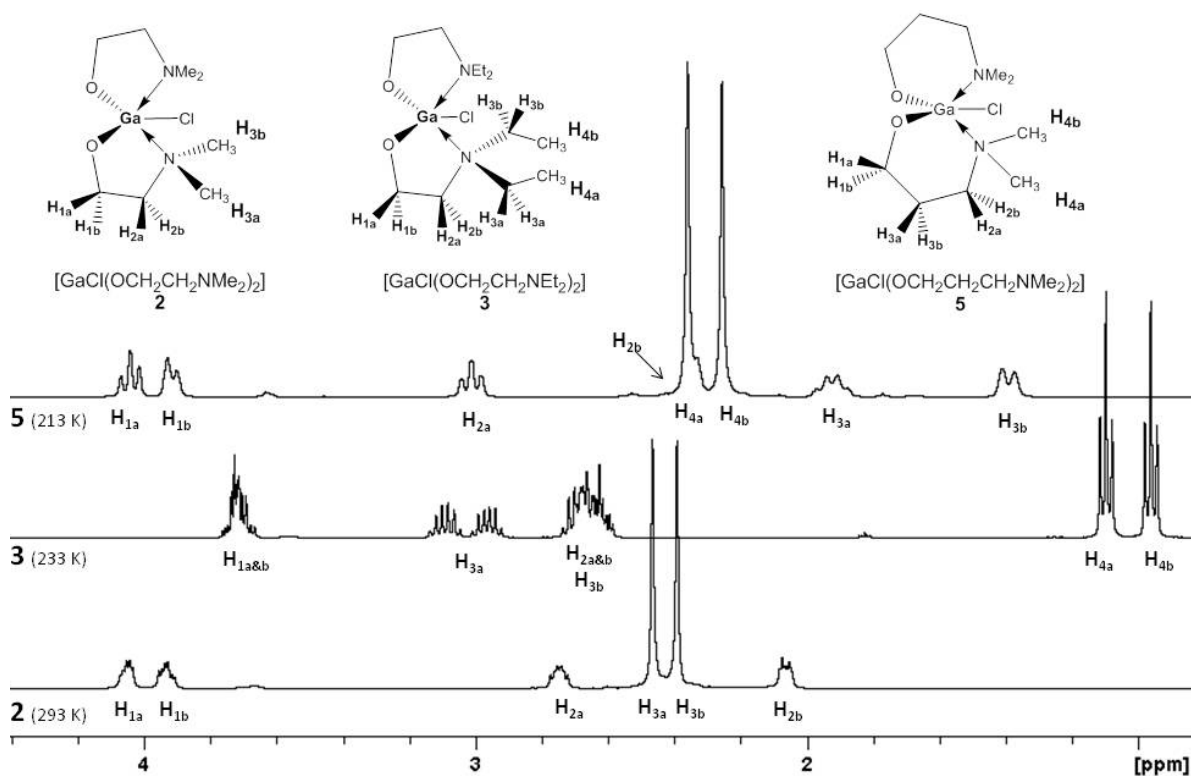


Figure 2.12. ^1H NMR spectra of $[\text{GaCl}(\text{OR})_2]$ in CD_2Cl_2 where $\text{R} = \text{CH}_2\text{CH}_2\text{NMe}_2$ (**2**) bottom; $\text{CH}_2\text{CH}_2\text{NEt}_2$ (**3**) middle; $\text{CH}_2\text{CH}_2\text{CH}_2\text{NMe}_2$ (**5**) top; collected at 293, 233 and 213 K respectively. Note: for **5**, hydrogen signal H_{2b} is hidden underneath signal H_{4a} .

The ^1H NMR of compound **2** in CD_2Cl_2 at room temperature (Figure 2.12) shows two multiplets at 2.00 and 2.80 ppm corresponding to each $-\text{OCH}_2\text{CH}_2$; two singlets at 2.38 and 2.42 ppm, corresponding to each $-\text{N}(\text{CH}_3)_2$ group and two multiplets at 3.93 and 4.05 ppm corresponding to each $-\text{OCH}_2$. The two $-\text{OCH}_2\text{CH}_2$ proton environments come either side of the two methyl peaks. The higher shift of the $-\text{N}(\text{CH}_3)_2$ can be attributed to the close proximity to the $-\text{OCH}_2\text{CH}_2$ protons causing deshielding and a large separation of the two $-\text{OCH}_2\text{CH}_2$ environments. The low shift of the $-\text{OCH}_2$ protons can be attributed to deshielding by the oxygen atom and is expected in compounds of this type. ^1H NMR spectra of **3** and **5**, show similar behaviour to that of **2** with additional peaks for the additional atoms within the molecules.

The presence of an ethyl group in **3**, in place of the methyl group in **2**, allows for increased fluctuation and movement around the nitrogen atom which requires the sample to be cooled to 233 K before the spectrum is resolved. Compound **5** has an

additional -CH₂ group giving it a three carbon backbone compared to the two carbon backbone analogue **2**. This additional -CH₂ group gives **5** extra flexibility within the backbone and allows the donor-functionalised ligand to move more readily around the gallium centre compared to that of **2**, hence the need to cool the sample to 213 K before a resolved spectrum is observed.

Figure 2.13 shows a stack plot of variable temperature experiments carried out in toluene-d⁸ with **5** between 213 and 373 K, in which the diastereotopic pairs of protons can be seen to coalesce as the temperature was raised. Coalescence is defined as the temperature at which a single peak with a flat top is observed (Figure 2.14).¹¹³ The rate constant at the coalescence temperature was determined using the standard expression for an equally populated two-site exchange:

$$k_{coal} = \frac{\pi \Delta\nu}{\sqrt{2}} \quad 2.8$$

k_{coal} = free energy of activation, $\Delta\nu$ = chemical shift difference of the peak.

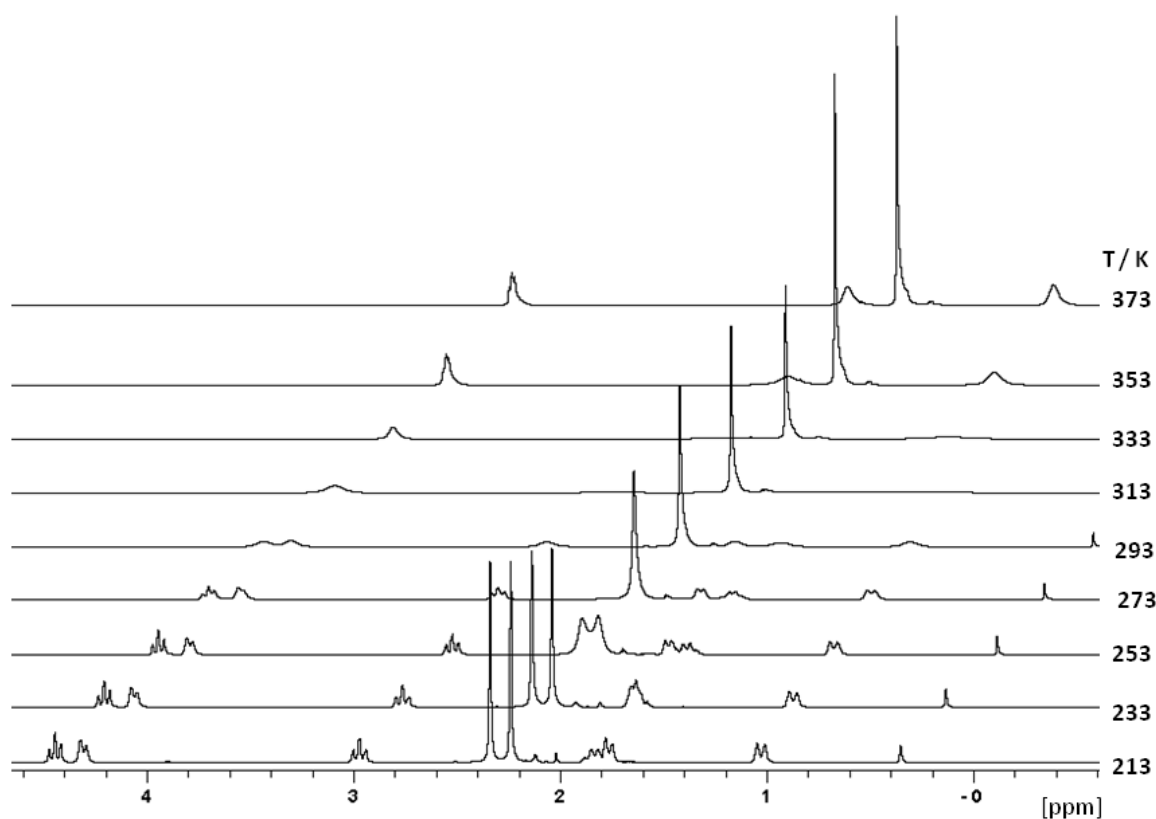


Figure 2.13. Variable temperature ^1H NMR spectra of **5** in toluene- d_8 over temperatures between 213 and 373 K. The spectrum at 213 K shows the correct chemical shift and the subsequent spectra have been staggered for clarity.

In the case of the methyl singlets the frequency separation under conditions of slow exchange was measured to be 39.7 Hz at 259 K implying a rate constant $k_{\text{exch}} = 88$ Hz. Using the Eyring equation (2.9) the free energy of activation was determined to be $527.1 \text{ kJ mol}^{-1}$.

$$k = \frac{k_B T}{h} e^{-\frac{\Delta G^\ddagger}{RT}} \quad 2.9$$

Where k is the free energy of activation, k_B is the Boltzmann's constant, T is the temperature during coalescence, h is Planck's constant and ΔG^\ddagger the Gibbs energy of free activation.

As the temperature increases past the coalescence temperature, the two singlets of $-N(CH_3)_2$, at 2.24 and 2.37 ppm begin to broaden at -253 K, converging to one singlet at 2.28 ppm at 273 K. The signals corresponding to the carbon backbone begin to broaden at 20 °C so that at room temperature, the 1H NMR spectrum of **5** appears broad. The fluxional nature of the donor-functionalised alkoxide ligands can cause the donor amide group to dissociate from the gallium centre, resulting in the broad spectrum.

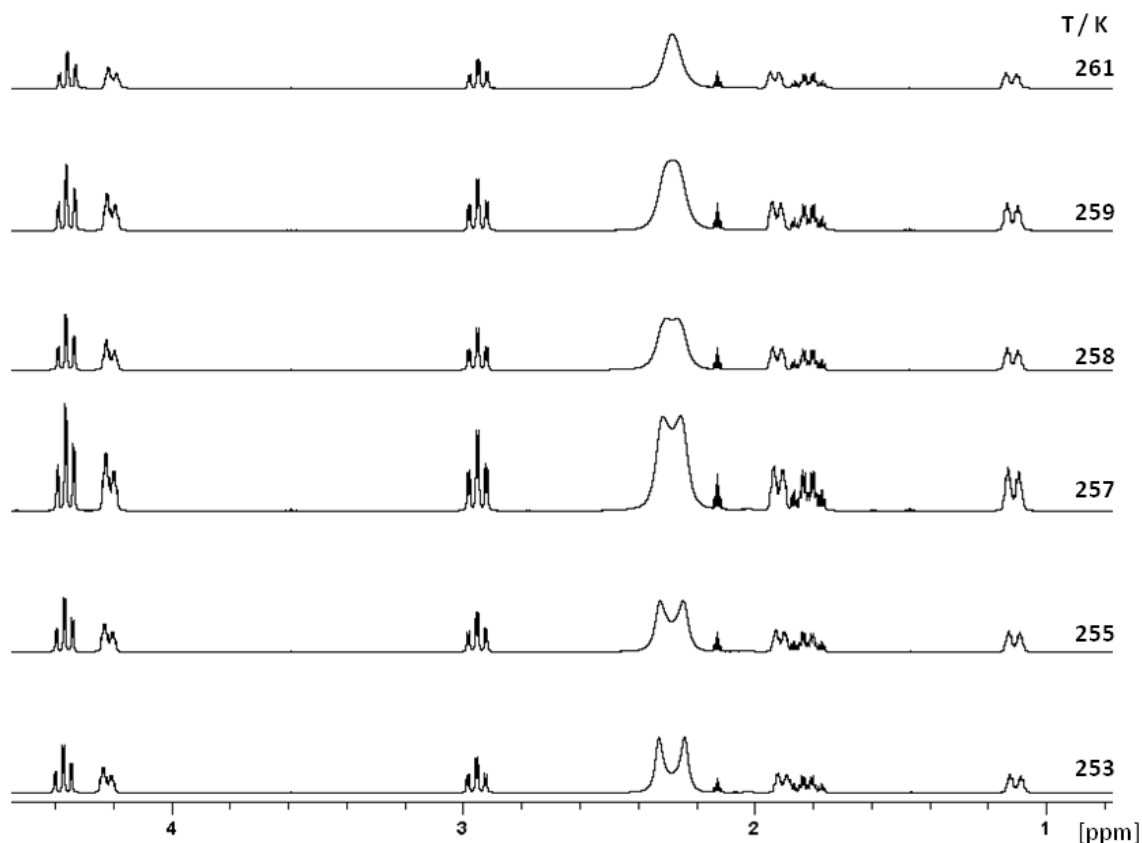


Figure 2.14. Variable temperature 1H NMR of **5** in toluene- d_8 over temperatures between 253 and 261 K to determine the coalescence temperature

The fluxionality observed for compounds **3** and **5** is not surprising; five-coordinate trigonal bipyramidal systems are notoriously susceptible to rearrangement of the coordination sphere. Classic examples include PF_5 and $Fe(CO)_5$ which are textbook examples of the Berry pseudo-rotation mechanism in which a D_{3h} (trigonal pyramidal) molecule exchanges axial and equatorial environments via a C_{4v} (square based pyramidal) intermediate.¹¹⁴ However, with a labile metal centre such as Ga(III) with weakly bound donor groups in axial positions it is also possible to envisage a

dissociative mechanism in which detachment of one or both of the arms of the alkoxide ligands permits inversion of configuration at the metal centre, followed by re-coordination of the two amines.

Based on the X-ray structure of **5** and the observed 1:1 ratio of the two exchanging species in low-temperature NMR spectra in toluene- d^8 (Figure 2.12), Figure 2.15 shows the likely type of dynamic exchange in **5**, in the solution state, based on DFT calculations carried out by Dr. Abil Aliev, UCL. The view in Figure 2.15 is along the Ga-Cl bond.

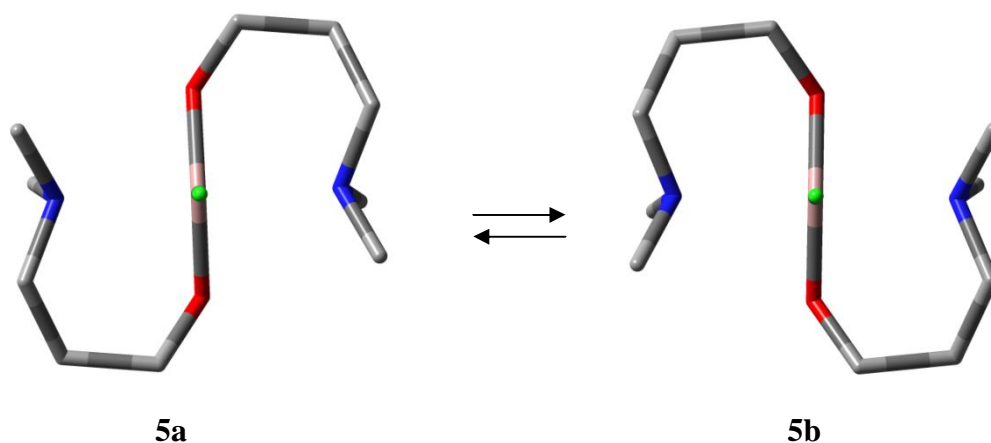


Figure 2.15. Dynamic exchange expected for **5** based on DFT calculations. Colour key: gallium - pink, chlorine - green, oxygen - red, carbon - black, and nitrogen - blue.

The symmetry of **5b** corresponds to that found in the solid-state as determined by single crystal X-ray diffraction. One possible mechanism by which the rearrangement in Figure 2.15 can take place involves concerted interconversions of the pseudo-six-membered rings (assuming formation of N-Ga dative bonds), followed by concerted rotations about the O-Ga bonds shown in Figure 2.16.

Figure 2.16 shows structures of **5a**, **5b** and **5c** which were optimised using DFT M06/def2-TZVP calculations (Gaussian 09). From these calculations, the relative free energy of **5c** relative to **5a** (or **5b**) is 13.4 kJ mol^{-1} . Other mechanisms, including direct interconversion of the pseudo-six-membered rings, are unlikely as they would be energetically unfavourable due to steric repulsions. Additionally, the ^1H NMR spectrum of this mechanism would be observed with different integrals and peaks.

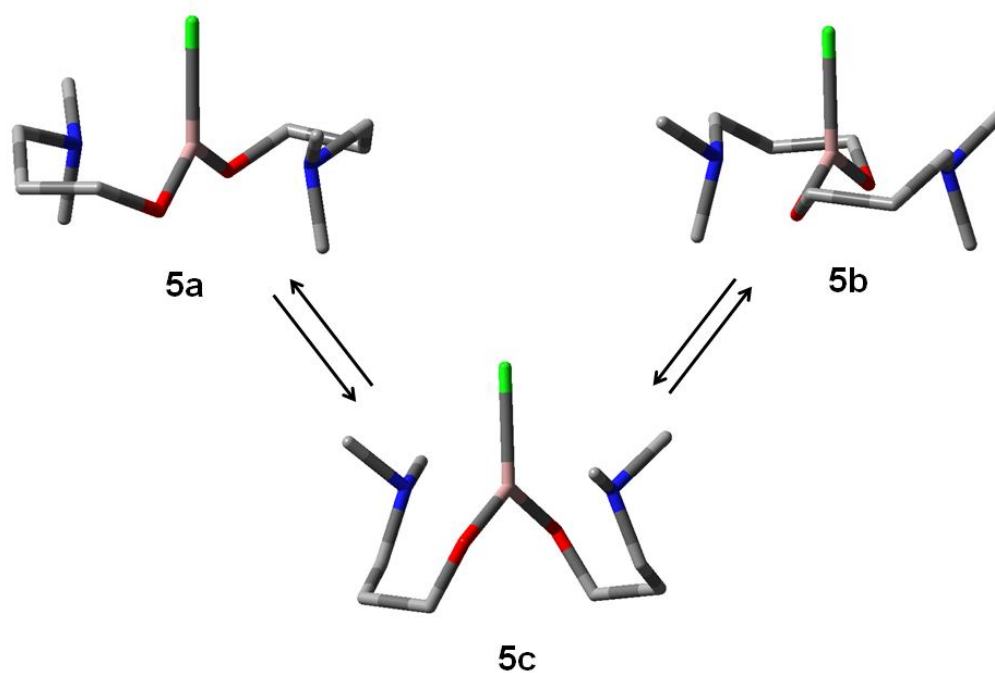


Figure 2.16. Possible mechanism for the dynamic exchange expected for **5**.

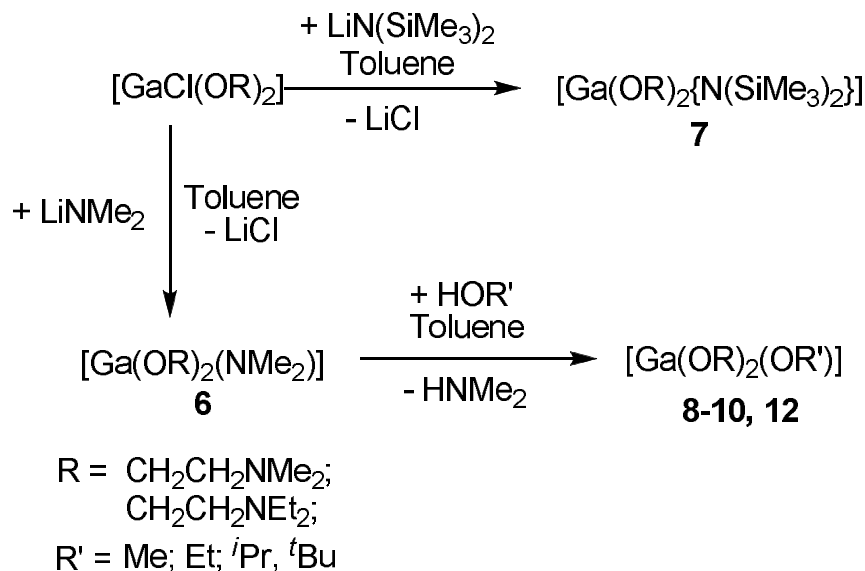
Chloro gallium bis(alkoxides) have interesting NMR properties due to their diastereotopic nature. These properties have not been previously reported in detail and have only been observed in metal mono(alkoxides) $[\text{MMe}_2(\text{OCH}_2\text{CHRNMMe}_2)]_2$ using chiral donor-functionalised alcohols ($\text{M} = \text{Ga}, \text{In}$; $\text{R} = \text{Me} (S), ^i\text{Pr} (S), ^i\text{Bu} (S), \text{Bz} (S), \text{Et} (R:S > 90:10)$).^{71, 115}

By varying the alkyl groups attached to the amine functional group or altering the number of carbon atoms found in the backbone of the ligand, the ^1H NMR spectra can significantly change with the protons found on certain functional groups having different chemical shifts to similar complexes. Additional carbon atoms within the backbone can increase fluxionality and flexibility in the complexes and require reduced temperature experiments to obtain resolvable spectra.

2.2.7. Heteroleptic gallium alkoxides

Following the successful synthesis of chloro gallium bis(alkoxides), shown in Scheme 2.8, the same procedure was adopted in order to cleanly replace the remaining chloride with a different alkoxide group. Scheme 2.8 outlines the two step route used to

synthesise heteroleptic gallium alkoxides. The chloride group was first replaced by an amido group and following work-up, the amido group was subsequently replaced by an alternative alkoxide.



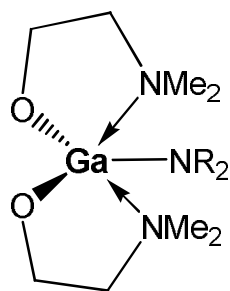
Scheme 2.8. Synthetic routes to amido gallium bis(alkoxides) and heteroleptic gallium alkoxides.

2.2.7.1. Reaction of $[\text{GaCl}(\text{OCH}_2\text{CH}_2\text{NMe}_2)_2]$ (**2**) and one equivalent of a lithiated amide (LiNMe_2 or $\text{LiN}(\text{SiMe}_3)_2$)

The first step towards heteroleptic gallium alkoxide compounds following the route outlined in Scheme 2.8 was salt metathesis. Lithium dimethylamide and lithium hexamethyldisilazide were used to substitute the chloride, in compounds of the type $[\text{GaCl}(\text{OR})_2]$, for the corresponding amide. The reaction of **2** with one equivalent of LiNMe_2 or $\text{LiN}(\text{SiMe}_3)_2$ in toluene, heated to 90 °C for 24 hours, afforded the crude white powder of $[\text{Ga}(\text{OCH}_2\text{CH}_2\text{NMe}_2)_2(\text{NMe}_2)]$ (**6**) and an off-white sticky solid of $[\text{Ga}(\text{OCH}_2\text{CH}_2\text{NMe}_2)_2\{\text{N}(\text{SiMe}_3)_2\}]$ (**7**), after work-up in a 13% and 95% yield, respectively (Figure 2.17).

^1H NMR spectroscopic data indicated that the amidodialkoxogallanes, $[\text{Ga}(\text{OCH}_2\text{CH}_2\text{NMe}_2)_2(\text{NMe}_2)]$ (**6**) and $[\text{Ga}(\text{OCH}_2\text{CH}_2\text{NMe}_2)_2\{\text{N}(\text{SiMe}_3)_2\}]$ (**7**) were

formed showing peaks for the amido groups at 1.96 ppm for $-NMe_2$ (**6**) and at 0.28 ppm for $-N(SiMe_3)_2$ (**7**). The ratios of the peaks observed were also in agreement with the formulation of **6** and **7**. A $^{13}C\{^1H\}$ NMR spectrum was obtained for **7** and was consistent with the formation of $[Ga(OCH_2CH_2NMe_2)_2\{N(SiMe_3)_2\}]$ (**7**), containing peaks at 2.9 ppm corresponding to $-Si(CH_3)_3$; 43.9 ppm corresponding to $-OCH_2CH_2$; 58.7 ppm corresponding to $-N(CH_3)_3$; 60.5 ppm corresponding to $-OCH_2$.



R = Me, **6**; SiMe₃, **7**

Figure 2.17. Proposed structure of $[Ga(OCH_2CH_2NMe_2)_2(NR_2)]$; R = Me, **6**; SiMe₃, **7**.

However, the product was difficult to purify and separate from the starting material, hence accurate elemental analysis and mass spectrometry could not be obtained. LiNMe₂ was replaced with LiN(SiMe₃)₂ in an attempt to crystallise the amidoalkoxogallane, but this was unsuccessful. Solvent-based purification methods were employed to produce crystalline material of **6** and **7**, however these attempts were also unsuccessful due to compounds **2**, **6** and **7** being soluble in the same solvents. Due to the difficulty in purifying compounds **6** and **7**, the subsequent amide/alkoxide exchange reaction was performed *in situ* using **6** as an intermediate to eliminate any chance of methyl migration from the $-N(SiMe_3)_2$ group to the gallium metal centre as previously observed.¹⁰⁷

2.2.7.2. Reaction of $[Ga(OCH_2CH_2NR_2)_2(NMe_2)]$ (**6**) and one equivalent of HOR'

The final stage of the synthesis was the amide/alkoxide exchange to form heteroleptic gallium alkoxides as outlined in Scheme 2.8. Due to the difficulty in isolating pure amidoalkoxogallane compounds, the two stage reaction was performed *in situ*. Firstly

spectrum of compound **9**. There were no peaks observed for free ethanol. The spectrum of compound **10** has additional peaks at 1.16 and 3.95 ppm corresponding to $-\text{OCH}(\text{CH}_3)_2$ and $-\text{OCH}(\text{CH}_3)_2$ and there is no evidence for free *iso*-propanol. $^{13}\text{C}\{^1\text{H}\}$ NMR spectroscopy also supports the formation of **9** and **10**, showing no peaks for the free alcohols. The $^{13}\text{C}\{^1\text{H}\}$ spectrum for compound **9** shows peaks at 43.6 and 45.5 ppm corresponding to the two $-\text{N}(\text{CH}_3)_2$ groups, 45.8 and 58.5 ppm for $-\text{OCH}_2\text{CH}_3$ and $-\text{OCH}_2\text{CH}_3$ respectively (free alcohol 18.7 and 57.6 ppm), 60.2 and 62.1 ppm corresponding to the backbone carbons $-\text{OCH}_2\text{CH}_2$ and $-\text{OCH}_2$ respectively. The spectrum for compound **10** shows peaks at 43.8 and 45.5 ppm corresponding to the two $-\text{N}(\text{CH}_3)_2$ groups, 25.5 and 46.0 ppm for $-\text{OCH}(\text{CH}_3)_2$ and $-\text{OCH}(\text{CH}_3)_2$ respectively (free alcohol 25.2 and 64.2 ppm), 60.4 and 62.2 ppm corresponding to the backbone carbons, $-\text{OCH}_2\text{CH}_2$ and $-\text{OCH}_2$, respectively were obtained.

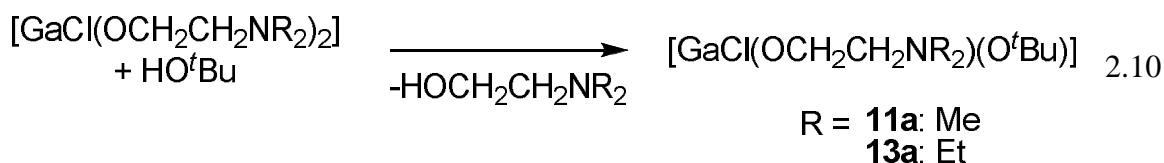
Mass spectrometry of **8** shows a mass ion at $m/z = 582$ which corresponds to two units of $[\text{Ga}(\text{OCH}_2\text{CH}_2\text{NMe}_2)_2(\text{OMe})]$. This is probably due to temperature and pressure (caused by the methane carrier gas) effects within the mass spectrometer and was not further investigated. For compounds **9** and **10** a mass ion peaks at $m/z = 292$ and 305 was observed corresponding to one unit of compound unlike that seen with **8**. A peak was also seen at $m/z = 281$ in both spectra for the mass ion peak of the starting material $[\text{GaCl}(\text{OCH}_2\text{CH}_2\text{NMe}_2)_2]$ and another at $m/z = 245$ corresponding to $[\text{Ga}(\text{OCH}_2\text{CH}_2\text{NMe}_2)_2]^+$ having lost either the alkoxy ligand or the chloride of the starting material.

Interestingly, when the analogous chloro gallium alkoxide, $[\text{GaCl}(\text{OCH}_2\text{CH}_2\text{NEt}_2)_2]$, was reacted with methanol and ethanol, the desired products were not obtained. Spectroscopic and analytical data for both reactions showed only starting material. However, when reacted with *iso*-propanol, the monomeric alkoxygallane $[\text{Ga}(\text{OCH}_2\text{CH}_2\text{NEt}_2)_2(\text{O}^i\text{Pr})]$ (**12**) was obtained. The ^1H NMR spectrum of **12** in CD_2Cl_2 at -40°C was broad and difficult to integrate due to a mixture of product and starting material, however peaks corresponding to the formation of **12** were observed. Peaks for the donor-functionalised ligands were observed at 0.93 and 1.14 ppm for each $-\text{N}(\text{CH}_2\text{CH}_3)_2$, the multiplet corresponding to $-\text{OCH}_2\text{CH}_2$ and one of the diastereotopic protons from the $-\text{N}(\text{CH}_2\text{CH}_3)_2$ groups at 2.66 ppm with the other proton observed at 3.00 ppm for $-\text{N}(\text{CH}_2\text{CH}_3)_2$. Additional peaks were found at 1.17 and 3.76 ppm for

-OCH(CH₃)₂ and -OCH(CH₃)₂ respectively for the *iso*-propoxy ligand with an absence of peaks corresponding to the free alcohol. ¹³C{¹H} NMR spectroscopy at -40 °C is also consistent with the structure of **12**, with peaks seen at 6.0 and 9.5 ppm for each -N(CH₂CH₃)₂, 40.1 and 44.9 ppm for each -N(CH₂CH₃)₂, and 53.2 and 57.8 ppm for the backbone carbon atoms -OCH₂CH₂ and -OCH₂, respectively. Peaks were also observed at 9.2 and 57.6 ppm for the *iso*-propoxy ligand -OCH(CH₃)₂ and -OCH(CH₃)₂ respectively, with an absence of peaks corresponding to the free alcohol.

Mass spectrometry shows a mass ion peak at *m/z* = 361 confirming the formation of [Ga(OCH₂CH₂NEt₂)₂(O^{*i*}Pr)] (**12**). A peak is also seen at *m/z* = 337 for the mass ion peak of the starting material [GaCl(OCH₂CH₂NEt₂)₂] giving further evidence that a mixture of products were obtained.

When R = Me or Et and R' = ^{*t*}Bu, the expected compounds, [Ga(OCH₂CH₂NR₂)₂(O^{*t*}Bu)], do not form. Instead, compounds of the formula [GaCl(OCH₂CH₂NR₂)(O^{*t*}Bu)] (R = Me, **11a**; Et, **13a**) were observed (Figure 2.18). This is likely to have occurred after *tert*-butanol was added during the second stage of the reaction (Scheme 2.8) where a donor functionalized alkoxide ligand originating from unreacted starting material, was replaced by the *tert*-butoxide ligand. The large steric bulk of the *tert*-butoxide group is the probable cause of the alkoxide/alcohol exchange (Equation 2.10), whereas when R' = Me, Et, or ^{*i*}Pr, this exchange was not observed.



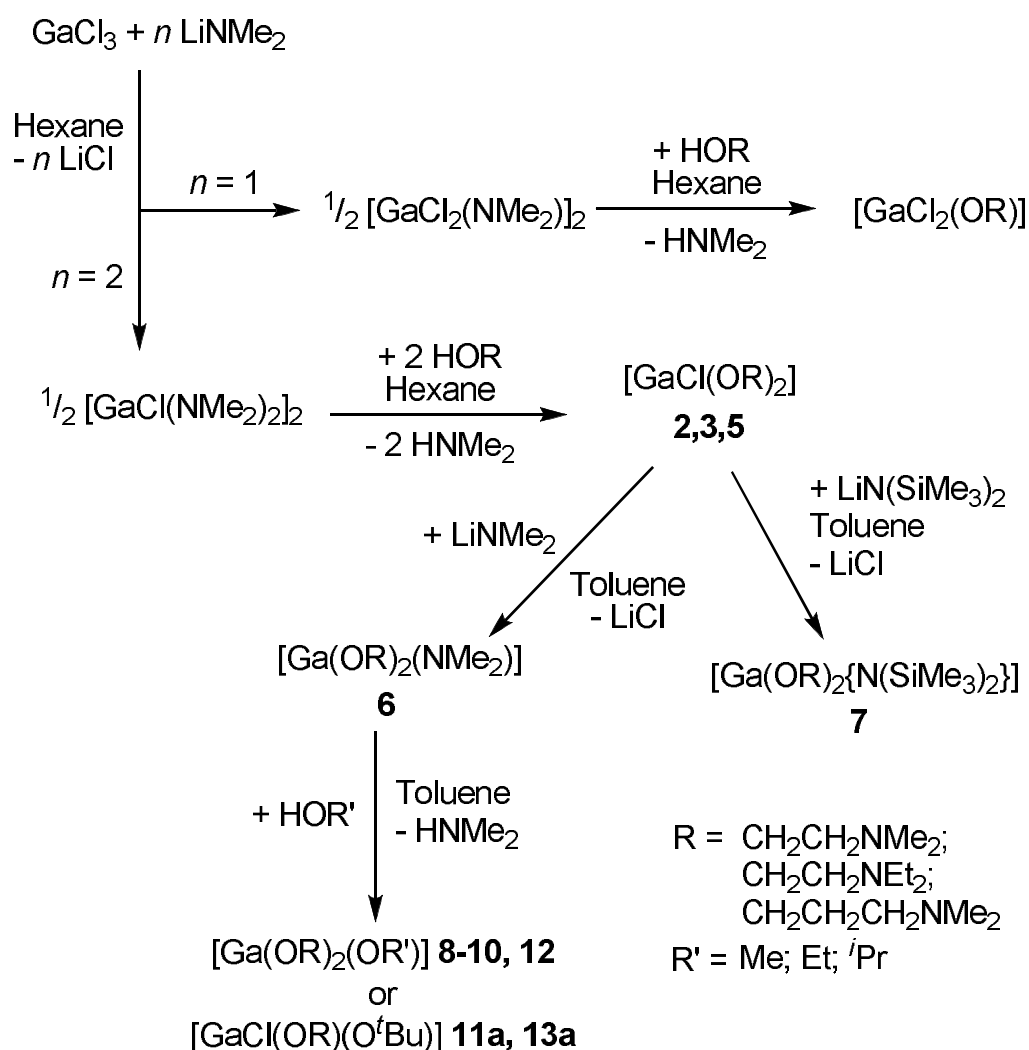
As with all the heteroleptic gallium alkoxides formed during this work, spectroscopic and analytical data also showed contamination with starting material [GaCl(OCH₂CH₂NR₂)₂], however evidence for the formation of **11a** and **13a** was obtained. ¹H NMR spectra in C₆D₆ for **11a** and CD₂Cl₂ at -40 °C for **13a** showed peaks for the relevant donor-functionalised alkoxide ligands as described for compounds **8** and **12** respectively. An additional broad singlet was observed at 2.31 and 2.65 ppm for **11a** and **13a** respectively corresponding to -OC(CH₃)₃. A ¹³C{¹H} NMR spectrum of **11a** was unobtainable due to lack of material, but the ¹³C{¹H} NMR spectrum of **13a**

showed ligand peaks as described for compound **12**. Peaks for the *tert*-butoxy ligands were seen at 33.2 and 59.2 ppm corresponding to $-\text{OC}(\text{CH}_3)_3$ and $-\text{OC}(\text{CH}_3)_3$ respectively. No peaks were observed for the free ligand in both ^1H and $^{13}\text{C}\{^1\text{H}\}$ NMR spectra.

Mass spectrometry confirmed the formation of **11a** and **13a** with mass ion peaks of $m/z = 279$ (**11a**) and 293 (**13a**). As previously observed, mass ion peaks for the corresponding starting materials are also seen at $m/z = 281$ for **11a** and 337 for **13a**.

2.2.8. Summary of reactions

After exploring a number of routes towards gallium bis(alkoxides), outlined in Section 2.2.1, the amide/alkoxide exchange route was utilised *via* a two step reaction starting with gallium trichloride and followed by the use of a chloro gallium diamide intermediate. This two stage process was successful in producing both gallium mono- and bis(alkoxides). Subsequently, an analogous two-step procedure was utilised to synthesise heteroleptic gallium alkoxides from chloro gallium bis(alkoxides). The remaining chloride was exchanged with an amide group which was then replaced by an alternative alkoxide group. This overall four-step reaction is described in Scheme 2.9, giving an overview of the synthetic routes employed in this work.



Scheme 2.9. Summary of all reactions carried out during this work to synthesise heteroleptic gallium alkoxides *via* the four step process and other related complexes.

The amido intermediates were not isolated cleanly, nor in high yield, and so the subsequent heteroleptic gallium alkoxides were synthesised *in situ*. For this range of complexes, it was difficult to isolate the final product and a mixture of product and starting material was observed. Single crystals were not obtained however spectroscopic methods provided evidence for the formation of $[\text{Ga}(\text{OCH}_2\text{CH}_2\text{NR}_2)_2(\text{OR}')_n]$ ($\text{R} = \text{Me}$, $\text{R}' = \text{Me}$, **8**; Et , **9**; $i\text{Pr}$, **10**; $\text{R} = \text{Et}$, $\text{R}' = i\text{Pr}$, **12**). When $\text{R}' = t\text{Bu}$, the products $[\text{GaCl}(\text{OCH}_2\text{CH}_2\text{NR}_2)(\text{O}^t\text{Bu})]$ ($\text{R} = \text{Me}$, **11a** and Et , **13a**) form instead of the expected heteroleptic gallium alkoxide. This could be a result of incomplete reaction with LiNMe_2 followed by alkoxide/alcohol exchange. The total of four steps to synthesise the final heteroleptic gallium alkoxides provides a suitable route towards these novel group 13 compounds however further work is needed to isolate pure samples.

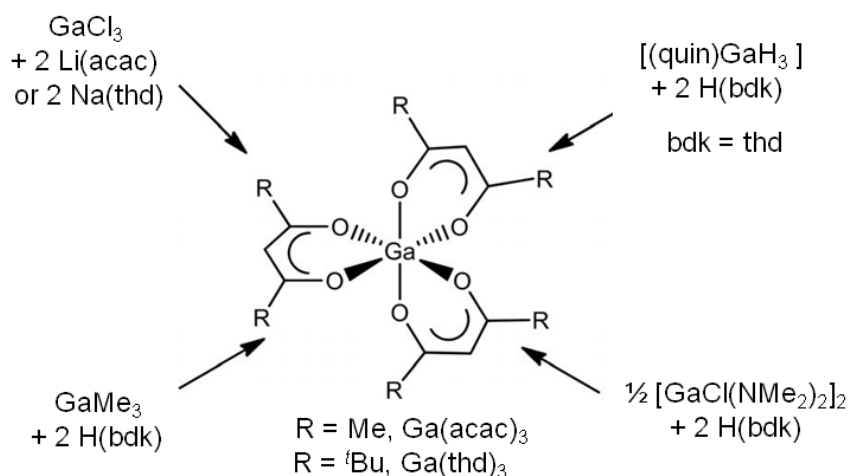
2.2.9. Attempted Synthesis of Gallium bis(β -diketonate) Complexes

Homoleptic gallium β -diketonates are a class of compound which have previously been used as precursors for the CVD of gallium oxide. The complexes $[\text{Ga}(\text{acac})_3]$,¹¹⁶ $[\text{Ga}(\text{dbm})_3]$,¹¹⁷ $[\text{Ga}(\text{thd})_3]$ ¹³ and $[\text{Ga}(\text{hfac})_3]$ ¹² ($\text{acac} = \text{acetylacetonate}$, $\text{dbm} = \text{dibenzoylmethanoate}$, $\text{thd} = 2,2,6,6\text{-tetramethylheptane-3,5-dionate}$, $\text{hfac} = 1,1,1,5,5,5\text{-hexafluoroacetylacetonate}$) are all six-coordinate, octahedral species which contain a Ga:O coordination ratio of 1:6 thus providing a rich metal:oxygen ratio. $[\text{Ga}(\text{acac})_3]$, which is commercially available, is not an ideal precursor owing to its high melting point and low volatility.^{116, 118-120} Fluorine substitution on the diketonate has been shown to significantly increase the volatility of the precursor, but the decomposition pathway of $[\text{Ga}(\text{hfac})_3]$ contains GaF_3 as one possible product, something which could contaminate the resulting gallium oxide film, adversely affecting its gas sensing properties.¹²

Homoleptic indium β -diketonates, such as $[\text{In}(\text{acac})_3]$ and $[\text{In}(\text{thd})_3]$, are potential molecular precursors for In_2O_3 thin films. However, they are high-melting solids (melting point of $[\text{In}(\text{acac})_3]$ -190 °C) hence they are far from ideal for conventional CVD experiments. However, $[\text{In}(\text{thd})_3]$ is sufficiently soluble that it can be employed in solution-based CVD experiments, albeit at very low concentrations of *ca.* 0.05 molL^{-1} in

a non-polar solvent (hexane).^{121, 122} $[\text{In}(\text{thd})_3]$ has also been used in plasma-enhanced chemical vapour deposition (PECVD)¹²³ and it has recently been reported its use in AACVD¹²⁴ as a precursor to thin films of In_2O_3 .

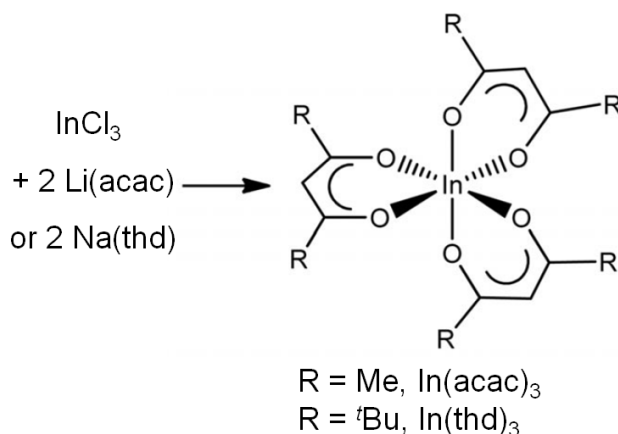
As with heteroleptic gallium alkoxide complexes, the use of heteroleptic gallium and indium β -diketonates as CVD precursors should improve upon the poor volatility of non-fluorinated homoleptic tris(β -diketonates). Gallium mono(β -diketonate) complexes have been known since 1953 when the synthesis of $[\text{Me}_2\text{Ga}(\text{acac})]$ was reported.⁵⁸ Only one example of a gallium bis(β -diketonate) exists in the literature.¹²⁵ It was isolated from a ligand redistribution reaction of $[\text{Cl}_2\text{Ga}(\text{acac})]$ in THF, which crystallised as the involatile ion pair $[\text{Ga}(\text{acac})_2(\text{THF})_2]^+[\text{GaCl}_4]^-$ and therefore is unsuitable for conventional CVD purposes. Similarly, an indium mono(β -diketonate) has previously been reported and used as a precursor for the CVD of Cu-In thin films,¹²⁶ but no indium bis(β -diketonates) have been reported.



Scheme 2.10. Formation of $[\text{Ga}(\text{bdk})_3]$ (bdk = β -diketonate, acac or thd) via the attempted synthetic routes towards gallium bis(β -diketonates)

The synthesis of gallium and indium bis(β -diketonates) is desirable primarily for their potential as highly volatile and soluble precursors for CVD. As previously stated, $[\text{In}(\text{thd})_3]$ has been used as a molecular precursor to thin films of indium oxide using AACVD, affording transparent, crystalline films.¹²⁴ However for $[\text{Ga}(\text{bdk})_3]$ and $[\text{In}(\text{bdk})_3]$, both have poor solubility and high thermal stability led to the attempted synthesis of bis(β -diketonate) complexes of gallium and indium, as shown in Scheme

2.10 and Scheme 2.11. A variety of routes were explored for gallium (Scheme 2.10) including salt metathesis, hydride elimination, methane elimination and amine elimination. Each one of these routes led to the formation of gallium tris(β -diketonate) and not the proposed bis(β -diketonate), confirmed by standard spectroscopic methods and single crystal X-ray analysis. The salt metathesis approach was also utilised in the attempt to synthesise indium bis(β -diketonates), as shown in Scheme 2.11. This also resulted in the isolation of indium tris(β -diketonate).



Scheme 2.11. Formation of $[\text{In}(\text{bdk})_3]$ ($\text{bdk} = \beta$ -diketonate, acac or thd) via the attempted synthetic routes towards indium bis(β -diketonates)

These synthetic routes have failed for two reasons: (i) the high kinetic and thermodynamic stability of $[\text{M}(\text{bdk})_3]$ ($\text{M} = \text{Ga}, \text{In}$) and (ii) a facile rearrangement of the intermediate $[\text{GaCl}(\text{bdk})_2]$ to the stable homoleptic gallium β -diketonates. The synthesis of gallium bis[benzoyl(thiobenzoyl)methanoate] chloride has been previously reported, although it was thought that steric crowding at the gallium centre due to the size of the sulfur atoms was the reason for the stability of the five-coordinate product.¹²⁷ However, it was not possible to isolate $[\text{GaX}(\text{bdk})_2]$ complexes even when increasing the size of the diketonate ligand.

A number of routes have been approached in the attempt to synthesise gallium and indium bis(β -diketonates) with the intention of developing more soluble and volatile precursors to metal oxide thin films. These have been unsuccessful and the metal tris(β -diketonate) analogues have formed instead. These are not suitable for use as precursors to metal oxide thin films due to their high melting points, low volatility and low solubility.

2.3. Conclusion

In Chapter 2, gallium and indium alkoxide compounds were reviewed with specific attention to donor-functionalised metal oxides due to their ability to form coordinatively saturated coordination spheres around the metal centre.

Gallium bis(alkoxides) were the focus of the donor-functionalised gallium alkoxides as they were expected to be monomeric in the solid-state, potentially leading to more soluble and volatile precursors, which are required for use with aerosol-assisted CVD. Several routes towards chloro gallium bis(alkoxides) were explored. The two step reaction of gallium trichloride and two equivalents of lithium dimethylamide, followed by amide/alcohol exchange resulted in the cleanest and highest yielding route to the target materials. Compounds of the type $[\text{GaCl}(\text{OR})_2]$ ($\text{R} = \text{CH}_2\text{CH}_2\text{NMe}_2$ (**2**); $\text{CH}_2\text{CH}_2\text{NEt}_2$ (**3**); $\text{CH}_2\text{CH}_2\text{CH}_2\text{NMe}_2$ (**5**)) were synthesised and characterised using elemental analysis, mass spectrometry, ^1H and $^{13}\text{C}\{^1\text{H}\}$ NMR and single crystal X-ray diffraction analysis. $[\text{GaCl}_2(\text{OCH}_2\text{CH}_2\text{NEt}_2)_2]$ (**4**) was also formed as a by-product during the synthesis of compound **3**.

Chloro gallium bis(alkoxides) **2**, **3**, and **5** were found to be diastereotopic and their ^1H NMR spectra were compared. Compound **5** was investigated by variable temperature ^1H NMR and the free energy of activation at the coalescence temperature of 259 K was estimated to be $12.6 \text{ kcal mol}^{-1}$. The interconversion of compound **5** was also explored using DFT calculations. Inversion of the six membered ($\text{Ga-OCH}_2\text{CH}_2\text{CH}_2\text{NMe}_2$) ring followed by rotation about the Ga-O bond was thought to be the mechanism by which the interconversion occurs, which was made possible due to the dative $\text{N} \rightarrow \text{Ga}$ bond. Other possible mechanisms would be energetically unfavourable and would result in more complex spectra.

An analogous two-step route to compounds **2**, **3** and **5** was employed to replace the remaining chloride with an alkoxide ligand, forming heteroleptic gallium alkoxides. Attempts to isolate the intermediate amido gallium bis(alkoxides) were unsuccessful as the products were difficult to separate from the starting material making the yield indeterminable. Subsequently the two-step synthetic procedure was carried out *in situ*

and compounds of the formula $[\text{Ga}(\text{OR})_2(\text{OR}')_n]$ ($\text{R} = \text{CH}_2\text{CH}_2\text{NMe}_2$ and $\text{R}' = \text{Me}$, $n = 2$ (**8**), Et , $n = 1$ (**9**), ${}^i\text{Pr}$, $n = 1$ (**10**); $\text{R} = \text{CH}_2\text{CH}_2\text{NEt}_2$ and $\text{R}' = {}^i\text{Pr}$, $n = 1$ (**12**) were observed. Additionally compounds of the type $[\text{Ga}(\text{OR})\text{Cl}(\text{O}^t\text{Bu})]$ ($\text{R} = \text{CH}_2\text{CH}_2\text{NMe}_2$ (**11a**); $\text{CH}_2\text{CH}_2\text{NEt}_2$ (**13a**) were formed on the addition of *tert*-butanol. These compounds were also difficult to isolate in high purity however spectroscopic data suggested the formation of the named products.

The synthesis of group 13 bis(β -diketonate) complexes was also attempted. A variety of routes were explored including salt metathesis, hydride elimination, methane elimination and amine elimination. These procedures all resulted in the formation of gallium tris(β -diketonate). The salt metathesis approach was also utilised in the attempt to synthesise indium bis(β -diketonates). This also resulted in the indium tris(β -diketonate). These synthetic routes have failed due to the high kinetic and thermodynamic stability of $[\text{M}(\text{bdk})_3]$ ($\text{M} = \text{Ga}, \text{In}$) and also a facile rearrangement of the intermediate $[\text{GaCl}(\text{bdk})_2]$ to the extremely stable homoleptic gallium β -diketonates.

Novel chloro gallium bis(alkoxides) and heteroleptic gallium alkoxides have been synthesised during this work. Due to their monomeric nature and good metal to oxygen ratio they possess suitable qualities for single-source precursors to Ga_2O_3 thin films using CVD. Since chloro gallium bis(alkoxides) contain a direct Ga-Cl bond which could potentially lead to film contamination of the final metal oxide films, the CVD of these compounds has not so far been explored. In Chapter 3, the thermal decomposition and AACVD of these compounds are investigated and the subsequent Ga_2O_3 thin films are characterised.

2.4. Experimental

2.4.1. General Procedures

All manipulations were performed under a dry, oxygen-free dinitrogen atmosphere using standard Schlenk techniques or in an Mbraun Unilab glovebox. All solvents used dried over activated alumina by the Grubbs method.¹²⁸ All other reagents were procured commercially from Aldrich and used without further purification. Microanalytical data were obtained at University College London.

2.4.2. Physical Measurements

All ^1H and $^{13}\text{C}\{^1\text{H}\}$ NMR spectra were obtained on a Bruker AMX400 spectrometer. All spectra were recorded using C_6D_6 , CD_2Cl_2 or toluene- d_8 which were dried and degassed over molecular sieves prior to use; ^1H and $^{13}\text{C}\{^1\text{H}\}$ chemical shifts are reported relative to SiMe_4 (δ 0.00). All IR spectra were recorded using a Shimadzu FTIR-8200 spectrometer, operating in the region of $4000\text{--}400\text{ cm}^{-1}$. The mass spectra were obtained using a Micromass 70-SE spectrometer using Chemical Ionisation (CI) with methane reagent gas. Elemental analysis was carried out using an Elemental Analyser (CE-440) (Exeter Analytical Inc).

2.4.2.1. Attempted synthesis of $[\text{Ga}(\text{O}^i\text{Pr})(\text{OCH}_2\text{CH}_2\text{NMe}_2)_2]$

Two equivalents of the donor-functionalised alcohol $\text{HOCH}_2\text{CH}_2\text{NMe}_2$ (1.00 cm^3 , 8.85 mmol) were added to a stirring solution of gallium tris(*iso*-propoxide) (1.00 g, 4.05 mmol) in toluene. Addition of the alcohol did not displace the *iso*-propoxide groups after stirring for 16 hours. Subsequently, reflux conditions were exploited which resulted in the decomposition of the compound to a brown oily product.

2.4.2.2. Synthesis of $[\text{GaCl}(\text{NMe}_2)_2]_2$ (1)

A cooled solution of LiNMe_2 (2.90 g, 56.8 mmol) in hexane (200 cm^3) was added to a stirred solution of GaCl_3 (5.00 g, 28.4 mmol) in hexane (100 cm^3) at $-78\text{ }^\circ\text{C}$. The reaction mixture was allowed to warm to room temperature and stirred for 24 h

resulting in a white slurry. The solution was filtered from the resulting white solid and the solvent removed *in vacuo*. A white powder was isolated yielding $[\text{GaCl}(\text{NMe}_2)_2]_2$ (4.53 g, 82%).

Anal. Calc. for $\text{C}_8\text{H}_{24}\text{N}_4\text{Cl}_2\text{Ga}_2$: C, 24.85; H, 6.26; N, 14.49. Found: C, 24.16; H, 6.06; N, 14.97%. ^1H NMR δ/ppm (C_6D_6): 2.35 (s, 12H ($\text{N}(\text{CH}_3)_2$ terminal)), 2.78 (s, 12H ($\text{N}(\text{CH}_3)_2$ bridging)). LRMS (Cl^+ , CH_4): $m/z = 387$ ($[\text{M}]^+$), 308 ($[\text{M}^+]-\text{Cl}$, $-\text{NMe}_2$).

2.4.2.3. Synthesis of $[\text{GaCl}(\text{OCH}_2\text{CH}_2\text{NMe}_2)]_2$ (2)

$\text{HOCH}_2\text{CH}_2\text{NMe}_2$ (3.40 cm^3 , 38.9 mmol) was added to a stirred solution of $[\text{GaCl}(\text{NMe}_2)_2]_2$ (3.76 g, 9.70 mmol) in diethyl ether (40 cm^3). The reaction mixture was left to stir for 24 h. The solvent was then removed *in vacuo* to a minimum (*ca.* 10 cm^3) and cooled to -18 °C. A white powder of $[\text{GaCl}(\text{OCH}_2\text{CH}_2\text{NMe}_2)]_2$ (2) was obtained (4.70 g, 86%).

Anal. Calc. for $\text{C}_8\text{H}_{20}\text{ClN}_2\text{O}_2\text{Ga}$: C, 34.14; H, 7.16; N, 9.95. Found: C, 34.89; H, 7.53; N, 9.40%. M.p: 121 °C. ^1H NMR δ/ppm (C_6D_6): 1.86 (m, 2H ($-\text{OCH}_2\text{CH}_2$)), 2.20 (s, 6H ($-\text{N}(\text{CH}_3)_2$ of alkoxide)), 2.28 (s, 6H ($-\text{N}(\text{CH}_3)_2$ of alkoxide)), 2.57 (m, 2H ($-\text{OCH}_2\text{CH}_2$)), 3.76 (m, 2H ($-\text{OCH}_2$)), 3.89 (m, 2H ($-\text{OCH}_2$)). LRMS (Cl^+ , CH_4): $m/z = 281$ ($[\text{M}]^+$), 245 ($[\text{M}]^+-\text{Cl}$).

2.4.2.4. Synthesis of $[\text{GaCl}(\text{OCH}_2\text{CH}_2\text{NEt}_2)]_2$ (3)

The same procedure was used to synthesise $[\text{GaCl}(\text{OCH}_2\text{CH}_2\text{NEt}_2)]_2$ as for compound 2 but using $\text{HOCH}_2\text{CH}_2\text{NEt}_2$ (5.30 cm^3 , 40.2 mmol) and $[\text{GaCl}(\text{NMe}_2)_2]_2$ (3.79 g, 9.80 mmol). Colourless crystals of $[\text{GaCl}(\text{OCH}_2\text{CH}_2\text{NEt}_2)]_2$ (3) were obtained (5.95 g, 90%).

Anal. Calc. for $\text{C}_{12}\text{H}_{28}\text{ClN}_2\text{O}_2\text{Ga}$: C, 42.7; H, 8.36; N, 8.30. Found: C, 40.42; H, 8.05; N, 7.21%. M.p: 81 °C. ^1H NMR δ/ppm (CD_2Cl_2) -20 °C: 0.96 (t, 6H $J = 7.2$ Hz, ($-\text{N}(\text{CH}_2\text{CH}_3)_2$)), 1.10 (t, 6H $J = 7.2$ Hz, ($-\text{N}(\text{CH}_2\text{CH}_3)_2$)), 2.65 (m, 8H ($-\text{N}(\text{CH}_2\text{CH}_3)_2$ and $-\text{OCH}_2\text{CH}_2$)), 2.96 (m, 2H ($-\text{N}(\text{CH}_2\text{CH}_3)_2$)), 3.08 (m 2H ($-\text{N}(\text{CH}_2\text{CH}_3)_2$)), 3.72 (m, 4H ($-\text{OCH}_2$)). $^{13}\text{C}\{^1\text{H}\}$ NMR δ/ppm (CD_2Cl_2) -20 °C: 6.1 ($-\text{N}(\text{CH}_2\text{CH}_3)_2$), 9.3 ($-\text{N}(\text{CH}_2\text{CH}_3)_2$), 40.4 ($-\text{N}(\text{CH}_2\text{CH}_3)_2$), 44.7 ($-\text{N}(\text{CH}_2\text{CH}_3)_2$), 53.3 ($-\text{OCH}_2\text{CH}_2$), 57.9 ($-\text{OCH}_2$). LRMS (Cl^+ , CH_4): $m/z = 337$ ($[\text{M}]^+$), 301 ($[\text{M}]^+-\text{Cl}$).

2.4.2.5. Synthesis of $[\text{GaCl}_2(\text{OCH}_2\text{CH}_2\text{NEt}_2)]_2$ (4)

$[\text{GaCl}_2(\text{OCH}_2\text{CH}_2\text{NEt}_2)]_2$ (4) was isolated as a minor by-product from one batch of 3. The same procedure was followed for 3, however when the solution was cooled to -18 °C, colourless crystals of 4 were obtained along with 3 as a minor product.

Anal. Calc. for $C_{12}H_{28}Cl_4N_2O_2Ga_2$: C, 28.06; H, 5.49; N, 5.45. Found: C, 27.26; H, 5.87; N, 5.45%. 1H NMR δ /ppm (CD_2Cl_2) -20 °C: 0.99 (t, 12H, $J = 7.1$ Hz, (-N(CH₂CH₃)₂)), 2.65 (m, 12H (-N(CH₂CH₃)₂), (-OCH₂CH₂)), 3.46 (t, 4H, $J = 5.3$ Hz, (-OCH₂)),

2.4.2.6. Synthesis of [GaCl(OCH₂CH₂CH₂NMe₂)₂] (5)

The same procedure was used to synthesise [GaCl(OCH₂CH₂CH₂NMe₂)₂] as for compound 2. HOCH₂CH₂CH₂NMe₂ (2.50 cm³, 21.2 mmol) was added to a stirring solution of [GaCl(NMe₂)₂]₂ (2.00 g, 5.17 mmol) in diethyl ether (40 cm³). The reaction mixture was left to stir for 24 h. The solvent was then removed *in vacuo* yielding a white powder of [GaCl(OCH₂CH₂CH₂NMe₂)₂] (5) (1.31 g, 82%).

Anal. Calc. for $C_{10}H_{24}ClN_2O_2Ga$: C, 38.81; H, 7.82; N, 9.05. Found: C, 38.19; H, 7.90; N, 8.54%. M.p: 48°C. 1H NMR δ /ppm (CD_2Cl_2) -60 °C: 1.39 (m, 2H (-OCH₂CH₂CH₂)), 1.92 (m, 2H (-OCH₂CH₂CH₂)), 2.30 (s, 6H (-N(CH₃)₂)), 2.41 (m, 8H (-N(CH₃)₂) & (-OCH₂CH₂CH₂)), 3.01 (m, 2H (-OCH₂CH₂CH₂)), 3.96 (m, 2H (-OCH₂)), 4.09 (m, 2H (-OCH₂)). $^{13}C\{^1H\}$ NMR δ /ppm (CD_2Cl_2) -20 °C: 28.5 (-OCH₂CH₂), 44.2 (-N(CH₃)₂), 47.2 (-N(CH₃)₂), 60.3 (-OCH₂CH₂CH₂), 66.3 (-OCH₂). LRMS (Cl^+ , CH₄): $m/z = 309$ ([M]⁺).

2.4.2.7. Synthesis of [Ga(OCH₂CH₂NMe₂)₂(NMe₂)] (6)

A suspension of LiNMe₂ (0.18 g, 3.56 mmol) in toluene (20 cm³) was added to a stirred solution of [GaCl(OCH₂CH₂NMe₂)₂] (2) (1.00 g, 3.56 mmol) in toluene (40 cm³), which was then left to stir for 24 h. The reaction mixture was filtered to remove a fine white powder (LiCl) and the solvent was then removed *in vacuo* to yield a colourless oil. Cooling of the solution to -20 °C for one month resulted in a colourless microcrystalline material. The crystalline material was dried under vacuum yielding [Ga(OCH₂CH₂NMe₂)₂(NMe₂)] as a white powder (0.12 g, 13%).

1H NMR δ /ppm (C_6D_6): 1.86 (dt, 2H $^1J = 11.2$, $^2J = 4.1$ Hz (-OCH₂CH₂)), 1.96 (s, 6H (-N(CH₃)₂)), 2.20 (s, 6H (-N(CH₃)₂ of alkoxide)), 2.28 (s, 6H (-N(CH₃)₂ of alkoxide)), 2.57 (dt, 2H $^1J = 14.5$, $^2J = 5.8$ Hz (-OCH₂CH₂)), 3.76 (dt, 2H $^1J = 14.7$, $^2J = 4.7$ Hz (-OCH₂)), 3.89 (dt, 2H $^1J = 10.8$, $^2J = 3.5$ Hz (-OCH₂)). LRMS (Cl^+ , CH₄): $m/z = 281$ (starting material [GaCl(OCH₂CH₂NMe₂)₂]), 245 ([M]-NMe₂).

2.4.2.8. Synthesis of [Ga(OCH₂CH₂NMe₂)₂{N(SiMe₃)₂}] (7)

Compound **7** was prepared using the same method as **6** using LiN(SiMe₃)₂·OEt₂ (0.47 g, 1.96 mmol) in toluene (10 cm³) and [GaCl(OCH₂CH₂NMe₂)₂] (0.50 mg, 1.78 mmol) in toluene (20 cm³). Removal of the solvent yielded a colourless oil and after cooling for 48 h a colourless microcrystalline material was obtained. The crystalline material was dried under vacuum yielding a white powder of [Ga(OCH₂CH₂NMe₂)₂{N(SiMe₃)₂}] (0.36 g, 50%).

¹H NMR δ/ppm (C₆D₆): 0.28 (s, 18H (SiMe₃)), 1.87 (m, 2H (-OCH₂CH₂)), 2.19 (s, 6H (-N(CH₃)₂)), 2.27 (s, 6H (-N(CH₃)₂)), 2.52 (m, 2H (-OCH₂CH₂)), 3.73 (m, 2H (-OCH₂)), 3.87 (m, 2H (-OCH₂)). ¹³C{¹H} NMR δ/ppm (C₆D₆): 2.5 (SiMe₃), 43.8 (-N(CH₃)₂), 46.0 (-N(CH₃)₂), 58.7 (-OCH₂CH₂), 60.4 (-OCH₂). LRMS (CI⁺, CH₄): *m/z* = 245 ([M]-N(SiMe₃)₂).

2.4.2.9. Synthesis of [Ga(OCH₂CH₂NMe₂)₂(OMe)] (8)

A suspension of LiNMe₂ (0.46 g, 8.99 mmol) in toluene (60 cm³) was added to a stirred solution of [GaCl(OCH₂CH₂NMe₂)₂] (2.30 g, 8.17 mmol) in toluene (120 cm³), which was then left to stir for 24 h. The reaction mixture was filtered and dry methanol (0.36 cm³, 8.99 mmol) was added *in situ* to the stirred solution of [Ga(OCH₂CH₂NMe₂)₂(NMe₂)] and allowed to stir for a further 24 h. Removal of the solvent *in vacuo* yielded a colourless oil and after cooling for 48 h a colourless microcrystalline material was obtained. The crystalline material was dried under vacuum yielding a white powder of [Ga(OCH₂CH₂NMe₂)₂(OMe)] (1.22 g, 66%).

M.p: 91°C. ¹H NMR δ/ppm (C₆D₆): 1.86 (m, 2H (-OCH₂CH₂)), 2.10 (s, 3H (-OCH₃)), 2.20 (s, 6H (-N(CH₃)₂)), 2.27 (s, 6H (-N(CH₃)₂)), 2.59 (m, 2H (-OCH₂CH₂)), 3.54 (m, 2H (-OCH₂)), 3.74 (m, 2H (-OCH₂)). LRMS (CI⁺, CH₄): *m/z* = 582 (2[M]⁺), 520 ([M]⁺-2 OMe), 245 ([M]⁺-2 OMe, -Ga(OCH₂CH₂NMe₂)₂). HRMS (EI): C₁₇H₄₃N₄O₄Ga₂ 2(M⁺) requires: 521.1745; found 521.1751; error: 1.00 ppm.

2.4.2.10. Synthesis of [Ga(OCH₂CH₂NMe₂)₂(OEt)] (9)

Compound **9** was prepared using the same method as **8** but using LiNMe₂ (0.46 g, 8.99 mmol), [GaCl(OCH₂CH₂NMe₂)₂] (2.30 g, 8.17 mmol), ethanol (0.55 cm³, 8.99 mmol). The solvent was removed *in vacuo* to reduce the volume of solvent and after cooling for 48 h a white solid was obtained. The solid was dried under vacuum yielding a white powder of [Ga(OCH₂CH₂NMe₂)₂(OEt)] (1.87 g, 79%).

^1H NMR δ /ppm (C_6D_6): 1.46 (br 3H (-OCH₂CH₃)), 1.86 (br, 2H (-OCH₂CH₂)), 2.20 (s, 6H (-N(CH₃)₂)), 2.26 (s, 6H (-N(CH₃)₂)), 2.54 (br, 2H (-OCH₂CH₂)), 3.54 (br, (-OCH₂CH₃)), 3.60 (br, 2H (-OCH₂)), 3.73 (br, 2H (-OCH₂)). $^{13}\text{C}\{^1\text{H}\}$ NMR δ /ppm (C_6D_6): 43.6 (-N(CH₃)₂), 45.5 (-N(CH₃)₂), 45.8 (-OCH₂CH₃), 58.5 (-OCH₂CH₃), 60.2 (-OCH₂CH₂), 62.1 (-OCH₂). LRMS (Cl^+ , CH_4): m/z = 292 ($[\text{M}]^+$), 281 ($[\text{M}]^+$ starting material $[\text{GaCl}(\text{OCH}_2\text{CH}_2\text{NMe}_2)_2]$), 245 ($[\text{M}]^+ - \text{OEt}$). HRMS (EI): $\text{C}_{10}\text{H}_{24}\text{O}_3\text{N}_2\text{Ga}$ (M^+) requires: 289.1043; found 289.1031; error: 3.98 ppm.

2.4.2.11. Synthesis of $[\text{Ga}(\text{OCH}_2\text{CH}_2\text{NMe}_2)_2(\text{O}^i\text{Pr})]$ (**10**)

Compound **10** was prepared using the same method as **8** but using LiNMe_2 (0.46 g, 8.99 mmol), $[\text{GaCl}(\text{OCH}_2\text{CH}_2\text{NMe}_2)_2]$ (2.30 g, 8.17 mmol), propan-2-ol (0.69 cm³, 8.99 mmol). The solvent was removed *in vacuo* to reduce the volume of solvent and after cooling for 48 h a white solid was obtained. The solid was dried under vacuum yielding a white powder of $[\text{Ga}(\text{OCH}_2\text{CH}_2\text{NMe}_2)_2(\text{O}^i\text{Pr})]$ (1.95 g, 78%).

^1H NMR δ /ppm (C_6D_6): 1.16 (d, 6H J = 6.12 Hz, (-OCH(CH₃)₂)), 1.85 (m, 2H (-OCH₂CH₂)), 2.20 (s, 6H (-N(CH₃)₂)), 2.27 (s, 6H (-N(CH₃)₂)), 2.53 (br, 2H (-OCH₂CH₂)), 3.72 (br, 2H (-OCH₂)), 3.95 (m, 3H (-OCH₂) and -OCH(CH₃)₂). $^{13}\text{C}\{^1\text{H}\}$ NMR δ /ppm (C_6D_6): 25.5 (-OCH(CH₃)₂), 43.8 (-N(CH₃)₂), 45.5 (-N(CH₃)₂), 46.0 (-OCH(CH₃)₂), 60.4 (-OCH₂CH₂), 62.2 (-OCH₂). LRMS (Cl^+ , CH_4): m/z = 305 ($[\text{M}]^+$), 281 (starting material $[\text{GaCl}(\text{OCH}_2\text{CH}_2\text{NMe}_2)_2]$), 245 ($[\text{M}]^+ - \text{O}^i\text{Pr}$). HRMS (EI): $\text{C}_{11}\text{H}_{26}\text{O}_3\text{N}_2\text{Ga}$ (M^+) requires: 303.1199; found 303.1204; error: 1.55 ppm.

2.4.2.12. Synthesis of $[\text{GaCl}(\text{OCH}_2\text{CH}_2\text{NMe}_2)(\text{O}^t\text{Bu})]$ (**11a**)

Compound **11a** was prepared using the same method as **8** in attempt to synthesise $[\text{Ga}(\text{OCH}_2\text{CH}_2\text{NMe}_2)_2(\text{O}^t\text{Bu})]$ **11** using LiNMe_2 (0.46 g, 8.99 mmol), $[\text{GaCl}(\text{OCH}_2\text{CH}_2\text{NMe}_2)_2]$ (2.30 g, 8.17 mmol) and *tert*-butanol (0.86 cm³, 8.99 mmol). The solvent was removed *in vacuo* to reduce the volume of solvent and after cooling for 48 h a white solid was obtained. The solid was dried under vacuum yielding a white powder of $[\text{GaCl}(\text{OCH}_2\text{CH}_2\text{NMe}_2)(\text{O}^t\text{Bu})]$ (2.55 g, 97%).

^1H NMR δ /ppm (C_6D_6): 1.86 (m, 1H (-OCH₂CH₂)), 2.20 (s, 3H (-N(CH₃)₂)), 2.31 (s, 3H (-N(CH₃)₂)), 2.31 (br, 9H (-OC(CH₃)₃)), 2.54 (1H (-OCH₂CH₂)), 3.75 (br, 1H (-OCH₂)), 3.89 (m, 1H (-OCH₂)). LRMS (Cl^+ , CH_4): m/z = 281 (starting material $[\text{GaCl}(\text{OCH}_2\text{CH}_2\text{NMe}_2)_2]$), 279 ($[\text{M}]^+$), 245 (starting material-Cl). HRMS (EI): $\text{C}_8\text{H}_{19}\text{O}_2\text{NClGa}$ ($\text{M} - \text{O}^t\text{Bu}$) requires: 191.9707; found 197.9715; error: 4.06 ppm.

2.4.2.13. Attempted Synthesis of [Ga(OCH₂CH₂NEt₂)₂(OR')] R' = Me or Et

The attempted synthesis of [Ga(OCH₂CH₂NEt₂)₂(OR')] (R' = Me, Et) was investigated using the same method as **8** with LiNMe₂ (0.50 g, 9.78 mmol), [GaCl(OCH₂CH₂NEt₂)₂] (3.00 g, 8.89 mmol) and methanol (0.40 cm³, 9.78 mmol) or ethanol (0.58 cm³, 9.78 mmol). The solvent was removed *in vacuo* to reduce the volume of solvent and after cooling for 48 h a white solid was obtained. The product was dried under vacuum yielding a sticky cream solid of [GaCl(OCH₂CH₂NEt₂)] (**3**). Spectroscopic and analytical data were in agreement with that stated in Section 2.4.2.4.

2.4.2.14. Synthesis of [Ga(OCH₂CH₂NEt₂)₂(OⁱPr)] (**12**)

Compound **12** was prepared using the same method as **8** but using LiNMe₂ (0.50 g, 9.78 mmol), [GaCl(OCH₂CH₂NMe₂)₂] (3.00 g, 8.89 mmol) and propan-2-ol (0.75 cm³, 9.78 mmol). The solvent was removed *in vacuo* to reduce the volume of solvent and after cooling for 48 h a white solid was obtained. The solid was dried under vacuum yielding a white powder of [Ga(OCH₂CH₂NEt₂)₂(OⁱPr)] (1.01 g, 31%).

¹H NMR δ/ppm (CD₂Cl₂) -40 °C: 0.93 (m, 6H (-N(CH₂CH₃)₂)), 1.14 (m, 6H (-N(CH₂CH₃)₂)), 1.17 (d, 6H *J* = 6.00 Hz, (-OCH(CH₃)₂)), 2.66 (m 6H (-OCH₂CH₂) & (-N(CH₂CH₃)₂)), 3.00 (m 2H (-N(CH₂CH₃)₂)), 3.76 (m 5H (-OCH₂) & (-OCH(CH₃)₂)). ¹³C{¹H} NMR δ/ppm (CD₂Cl₂) -40 °C: 6.0 (-N(CH₂CH₃)₂), 9.2 (-OCH(CH₃)₂), 9.5 (-N(CH₂CH₃)₂), 40.1 (-N(CH₂CH₃)₂), 44.9 (-N(CH₂CH₃)₂), 53.2 (-OCH₂CH₂), 57.6 (-OCH(CH₃)₂), 57.8 (-OCH₂). LRMS (CI⁺, CH₄): *m/z* = 361 ([M]⁺), 337 (starting material [GaCl(OCH₂CH₂NEt₂)₂]), 302 ([M]⁺-OⁱPr or -Cl). HRMS (EI): C₁₅H₃₄O₃N₂Ga (M⁺) requires: 359.1825; found 359.1831; error: 1.50 ppm.

2.4.2.15. Synthesis of [GaCl(OCH₂CH₂NEt₂)(O^tBu)] (**13a**)

Compound **13a** was prepared using the same method as **8** in attempt to synthesise [Ga(OCH₂CH₂NEt₂)₂(O^tBu)] **13a** from LiNMe₂ (0.50 g, 9.78 mmol), [GaCl(OCH₂CH₂NMe₂)₂] (3.00 g, 8.89 mmol) and *tert*-butanol (0.94 cm³, 9.78 mmol). The solvent was removed *in vacuo* to reduce the volume of solvent and after cooling for 48 h a white solid was obtained. The solid was dried under vacuum yielding a white powder of [GaCl(OCH₂CH₂NEt₂)(O^tBu)] (2.21 g, 84%).

¹H NMR δ/ppm (CD₂Cl₂) -40 °C: 0.93 (m, 3H (-N(CH₂CH₃)₂)), 1.09 (m, 3H (-N(CH₂CH₃)₂)), 1.29 (s, 9H (-OC(CH₃)₃)), 2.66 (m, 3H (-OCH₂CH₂) & (-N(CH₂CH₃)₂)), 3.03 (m, 1H (-N(CH₂CH₃)₂)), 3.76 (m, 2H (-OCH₂)). ¹³C{¹H} NMR δ/ppm (CD₂Cl₂) -

40 °C: 6.0 (-N(CH₂CH₃)₂), 9.5 (-N(CH₂CH₃)₂), 33.2 (-OC(CH₃)₃), 40.1 (-N(CH₂CH₃)₂), 44.9 (-N(CH₂CH₃)₂), 53.2 (-OCH₂CH₂), 57.8 (-OCH₂), 59.2 (-OC(CH₃)₃). LRMS (Cl⁺, CH₄): m/z = 337 (starting material [GaCl(OCH₂CH₂NEt₂)₂]), 293 [M]⁺. HRMS (EI): C₁₀H₂₂O₂NClGa (M⁺) requires: 292.0595; found 292.0588; error: 2.40 ppm.

2.4.2.16. Attempted Synthesis of [MCl(bdk)₂]: Salt Metathesis

A suspension of the alkali metal diketonate (Li(acac) or Na(thd)) (2.0 mmol) in toluene (10 cm³) at -78 °C was added slowly to the metal chloride, MCl₃ (M = Ga, In) (1.0 mmol) dissolved in toluene (10 cm³) at -78 °C and stirred for 15 min, before warming to room temp, and stirring for 5 h. After this time the reaction was filtered, concentrated to ca. 5 cm³ in vacuo and cooled to -18° for one week where colourless crystals of [M(bdk)₃] were deposited.

2.4.2.17. Attempted Synthesis of [GaH(bdk)₂]: Hydride Elimination

[Ga(Quin)H₃]¹²⁹ (184 mg, 1.0 mmol) was dissolved in Et₂O (20 cm³) and cooled to -78 °C. The diketone (2.0 mmol) was added via syringe, resulting in vigorous evolution of H₂. The reaction was stirred for 15 min, then warmed to room temp, and stirred for 16 h. After this time, the solution was filtered and concentrated, then cooled to -18 °C where colourless crystals of [Ga(bdk)₃] were deposited.

2.4.2.18. Attempted Synthesis of [GaMe(bdk)₂]: Methane Elimination

GaMe₃ (0.50 g, 4.40 mmol) was cooled to -78 °C and dissolved in toluene (20 cm³). The diketone (17.4 mmol) was added via syringe, the solution was stirred at -78 °C for 15 min, warmed to room temp, then refluxed for 16 h. After cooling and removal of solvents, the residue was dissolved in Et₂O and cooled to -18 °C where a white crystalline solid of [Ga(bdk)₃] precipitated.

2.4.2.19. Attempted Synthesis of [GaCl(bdk)₂]: Amine Elimination

[GaCl(NMe₂)₂]₂ (0.19 g, 0.50 mmol) was dissolved in Et₂O (20 cm³) and cooled to -78 °C. The diketone (2.00 mmol) was added via syringe; the reaction was stirred for 15 min then warmed to room temp, and stirred for 5 h. After this time, removal of volatiles in vacuo afforded a white solid of [Ga(bdk)₃].

2.4.2.20. Synthesis of [Ga(acac)₃] (14)

The salt metathesis route with 0.18 g of GaCl₃ and 0.24 mg of Na(acac) resulted in the formation of [Ga(acac)₃] (**14**) in 37% yield. The hydride elimination route with 0.20 cm³ of Hacac afforded **14** in 41% yield. The methane elimination route with 1.79 cm³ of Hacac led to the isolation of **14** in 77% yield. Finally, the amine metathesis route with 0.20 cm³ of Hacac afforded **14** in 36% yield. All products gave spectroscopic data consistent with known literature values.¹³⁰

Anal. Calc. for C₁₅H₂₁GaO₆: C, 49.08, H, 5.77; found: C 49.10, H, 5.65 {calcd. for [Ga(acac)₂Me]: C, 46.69, H, 6.06}. ¹H NMR δ/ppm (CDCl₃): 1.99 (s, 18H, CH), 5.40 (s, 3H, CH₃) ppm. LRMS (CI⁺, CH₄): *m/z* = 183/185 [Ga-(acac)(CH₄)]⁺ (100 %), 267/269 [Ga(acac)₂]⁺, 283/285 [Ga(acac)₂-(CH₄)]⁺, 366/368 [Ga(acac)₃]⁺.

2.4.2.21. Synthesis of [Ga(thd)₃] (15)

Using the hydride elimination route with 0.42 cm³ of Hthd, [Ga(thd)₃] (**15**) was formed in 59% yield. The methane elimination route with 3.63 cm³ of Hthd resulted in the formation of **15** in 82% yield. The amine metathesis route with 0.42 cm³ of Hthd afforded **15** in 43% yield. All products gave spectroscopic data consistent with known literature values.¹³

Anal. Calc. for C₃₃H₅₇GaO₆: C, 63.98, H, 9.27; found C, 64.10, H, 9.35 {calcd. for [Ga(thd)₂Me]: C, 61.21, H, 9.16}. ¹H NMR δ/ppm (CDCl₃): 1.19 (s, 54H, CH₃) ppm, 5.82 (s, 3H, CH). LRMS (CI⁺, CH₄): *m/z* = 435/437 [Ga(thd)₂]⁺, 451/453 [Ga(thd)₂(CH₄)]⁺ (100 %), 618/620 [Ga-(thd)₃]⁺.

2.4.2.22. Synthesis of [In(acac)₃] (16)

Using the salt metathesis route with 0.22 g of InCl₃ and 0.24 g of Na(acac), [In(acac)₃] (**16**) was formed in 44% yield. Spectroscopic data were consistent with known literature values.¹³¹ ¹H NMR δ/ppm (CD₂Cl₂): 2.02 (s, 18 H, CH₃) ppm, 5.42 (s, 3 H, CH).

2.4.2.23. Synthesis of [In(thd)₃] (17)

Using the salt metathesis route with 0.22 g of InCl₃ and 0.38 g of Li(thd), [In(thd)₃] (**17**) was formed in 56% yield. Spectroscopic data were consistent with known literature values.¹³² ¹H NMR δ/ppm (CD₂Cl₂): 1.17 (s, 54 H, CH₃) ppm, 5.85 (s, 3 H, CH).

Chapter 3

Chemical Vapour Deposition of Gallium Oxide Thin Films

3. CVD of Gallium Oxide Thin Films

Chapter 2 described the synthesis of gallium bis(alkoxides) and heteroleptic gallium alkoxides. These compounds were synthesised as they were expected to be monomeric in nature and likely to be volatile and suitable as potential precursors for gallium oxide thin films using the CVD technique. This chapter describes synthesis and characterisation of single-source gallium alkoxide precursors to gallium oxide, as well as the reactor conditions used to deposit thin films of gallium oxide in Section 3.1. Followed by the review, in Section 3.2, are the results and discussion of a selection of the precursors synthesised in Chapter 2 and their use as single-source precursors to gallium oxide thin films using AACVD.

3.1. Precursors to gallium oxide

Thin films of gallium oxide, Ga_2O_3 , are commonly found in the monoclinic β form which has good chemical and thermal stability, as well as possessing interesting electrical properties. Although at room temperature it is an electrical insulator, it becomes semiconducting above 500 °C whilst exhibiting a response to reducing gases (e.g. CO, EtOH) and above 900 °C its electrical resistivity is sensitive to the presence of oxygen.¹³³

3.1.1. Monodentate alkoxides

The structure of simple homoleptic gallium tris(alkoxides) of the type $[\text{Ga}(\text{OR})_3]$ is dependent on the nature of R. For bulky R groups (e.g. R = ^tBu), a dimeric structure with two bridging alkoxide groups and four terminal alkoxide groups arranged around two tetrahedral gallium centres is adopted. For slightly less bulky R groups (e.g. R = ⁱPr, ^tBu) an analogous dimeric structure is in equilibrium with a tetrameric $[\text{Ga}\{\text{Ga}(\text{OR})_4\}_3]$ structure (Figure 3.1). These tetramers contain a central 6-coordinate octahedral gallium centre bound to three tetrahedral $\text{Ga}(\text{OR})_4$ moieties through two bridging alkoxide groups per tetrahedral gallium centre. Two terminal alkoxide groups per tetrahedral

gallium centre complete the coordination sphere. Gallium alkoxides with small R groups (e.g. R = Et) exclusively adopt the tetrameric structure.

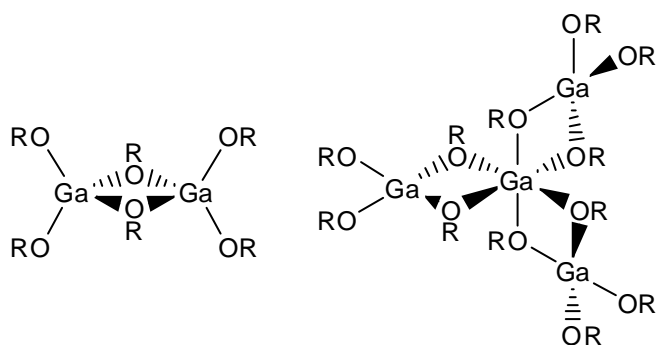
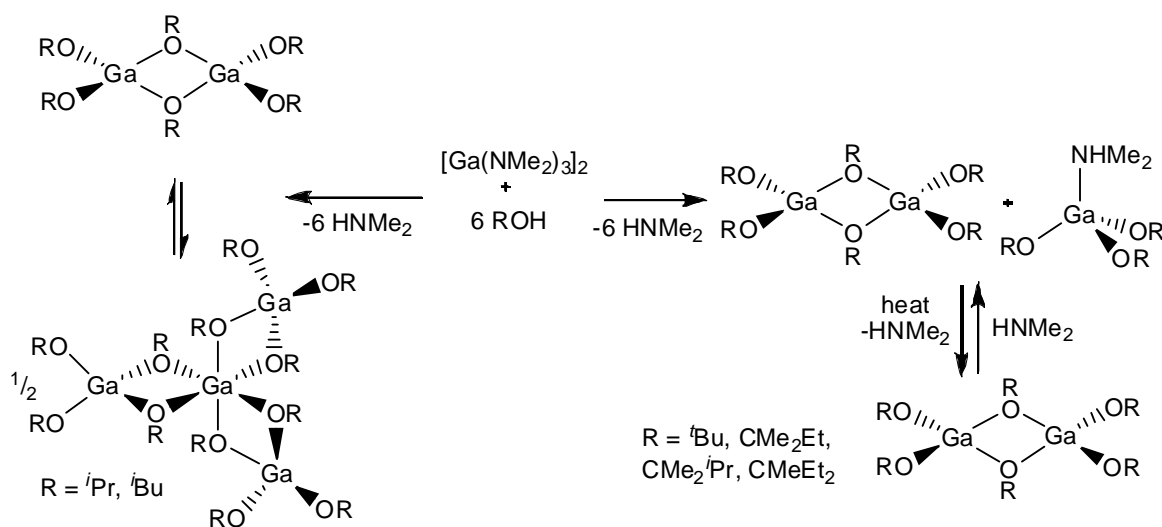


Figure 3.1. Structure of $[\text{Ga}(\text{OR})_3]_n$ as a dimer for large R groups ($n = 2$, R = $t\text{Bu}$) and a tetramer for small R groups ($n = 4$, R = Et)

The first synthesis of gallium alkoxides utilised the salt metathesis method, starting with GaCl_3 and three equivalents of NaOEt or NaO^iPr , forming $[\text{Ga}(\text{OEt})_3]$ and $[\text{Ga}(\text{O}^i\text{Pr})_3]$ respectively as discussed in Section 2.1.5. $[\text{Ga}(\text{O}^i\text{Pr})_3]_n$ is commercially available, making it a particularly attractive precursor. Kim *et al.* were the first group to take advantage of this, using it in a low pressure LPCVD chamber to deposit thin films of Ga_2O_3 .¹³⁴ The films were grown on a Si substrate heated to 400-800 °C at 1×10^{-7} Torr whilst $[\text{Ga}(\text{O}^i\text{Pr})_3]$ was heated to 90-110 °C. The type and quality of film deposited was heavily dependent on the substrate temperature: below 500 °C the films were oxygen-deficient with a Ga:O ratio of 1:1. Above 700 °C the Ga:O ratio was much improved (1:1.6) but there was a significant amount of carbon contamination, mostly on the surface of the film. Between 500-600 °C, the films contained the correct Ga:O ratio and there was no trace of carbon contamination. All films grown were amorphous.

The organic byproducts from the CVD reaction were analysed by GCMS, revealing that propylene, 2-propanol and acetone were the major byproducts. One proposed mechanism of decomposition involved β -hydrogen elimination of acetone followed by reductive elimination of 2-propanol, resulting in “ $\text{Ga}(\text{O}^i\text{Pr})$ ”. This would then undergo γ -hydrogen elimination, forming propylene and “ HGaO ” which would further decompose, with loss of hydrogen, to Ga_2O_3 (Scheme 3.1)

Conversely, the amine-stabilised monomer could be exclusively formed by adding a large excess of dimethylamine to the dimeric alkoxide at room temperature.

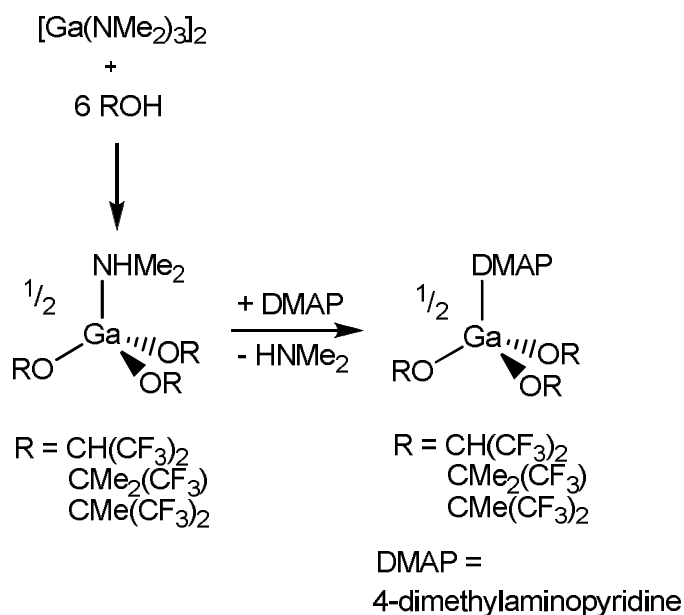


Scheme 3.2. Formation of dimeric and tetrameric gallium alkoxides

The precursor chosen for LPCVD studies was compound $[\text{Ga}(\text{O}^t\text{Bu})_3]_2$, mainly due to its low vapour pressure which was noted when sublimation of $[\text{Ga}(\text{O}^t\text{Bu})_3]_2$ was attempted. Films were grown on silicon, quartz and glass substrates at a range of temperatures (300-700 °C). Although these films were grown with O_2 as a co-precursor, a film was grown at 400 °C without O_2 and proved to be of similar quality to the films grown with O_2 . All films had the correct Ga:O ratio as judged from Rutherford backscattering spectra (RBS), although XPS data indicated that the films were slightly oxygen deficient (Ga:O ratio 1:1.1). All films grown proved to be amorphous and subsequent annealing at 700 °C and 1000 °C for four hours was carried out. Annealing at the lower temperature did not furnish crystalline material, but after heating the films to 1000 °C, crystalline Ga_2O_3 was obtained: XRD data indicated that the monoclinic β form had been obtained.

Similar work had been published two years earlier, again by Hoffman *et al.*, this time utilising fluorinated alkoxides.³⁹ Again using $[\text{Ga}(\text{NMe}_2)_3]_2$ as a starting material, reaction with six equivalents of fluorinated alcohol (both secondary and tertiary) led exclusively to the formation of the amine-stabilised monomer (Scheme 3.3). In this case, heating the amine-stabilised monomer under vacuum did not lead to dissociation of the

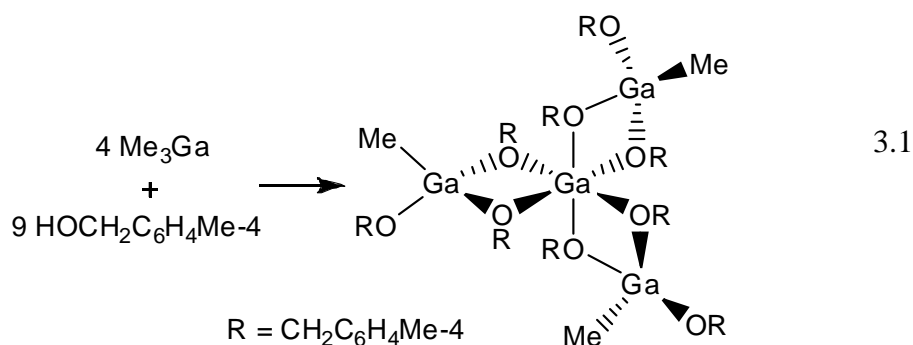
amine and formation of a dimer, indicating that the amine ligands are much more strongly bound to the fluorinated alkoxides.



Scheme 3.3. Synthesis of fluorinated gallium alkoxides stabilised by Lewis bases

The crude dimethylamine gallium alkoxides were all liquids which proved difficult to purify. Replacement of the dimethylamine ligand with 4-dimethylaminopyridine (DMAP) led to the formation of solid compounds, which were easily crystallised. Nonetheless, for LPCVD, liquids are generally favoured over solids due to their increased volatility and $[\text{Ga}\{\text{OCH}(\text{CF}_3)_2\}_3(\text{NHMe}_2)]$ was used to deposit thin films of Ga_2O_3 on glass. Amorphous films were obtained for substrate temperatures between 250 and 450 °C with thicker films being obtained at higher temperatures. As measured by RBS, the films contained negligible levels of contaminants (C, N, F) but the Ga:O ratio indicated the films were slightly gallium deficient.

A tetrameric gallium alkoxide was synthesised by Carmalt *et al.* from GaMe_3 and 4-methylbenzyl alcohol in a 4:9 ratio.¹³⁸ However, in this case a homoleptic gallium alkoxide was not isolated, retention of one of the methyl groups was observed on each of the tetrahedral gallium centres forming the product $[\{\text{Ga}(\text{OR})_6\}\{\text{GaMe}(\text{OR})\}]$ $\text{R} = \text{CH}_2\text{C}_6\text{H}_4\text{Me}$ -4 (Equation 3.1). Perhaps the biggest drawback to this methodology was the retention of a Ga–C bond in the precursor, which could possibly lead to increased levels of carbon contamination in the resulting films.



This tetrameric heteroleptic gallium alkoxide was used to deposit Ga₂O₃ thin films *via* LPCVD on glass at a substrate temperature of 600 °C. The Ga:O ratio could not be accurately determined by WDX owing to the thinness of the films; X-rays penetrated the films and breakthrough to the underlying glass substrate was observed. However, WDX did reveal the amount of carbon contamination was 1-2%. Interestingly, crystalline Ga₂O₃ was grown without the need for annealing: XRD of the films revealed the usual monoclinic β phase of Ga₂O₃ had been formed. Although this result is consistent with data reported by Kobukon *et al.*, it is nevertheless unusual for crystalline films of Ga₂O₃ to be formed at temperatures as low as 600 °C.¹³⁵ The formation of crystalline films at such low temperatures may be the result of the ‘core’ of the precursor (i.e. not the ‘terminal’ substituents) containing the correct Ga:O ratio of 4:6.

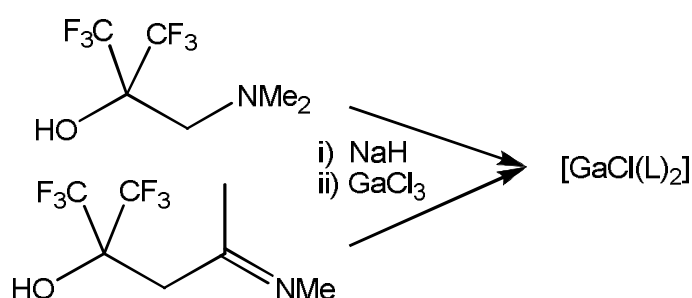
3.1.2. Donor-functionalised alkoxides

Monomeric compounds are desirable as precursors for CVD, as outlined in Section 1.2.1.5, owing to their higher volatility when compared to dimeric or tetrameric equivalents. Due to the electron-deficient nature of gallium, all the alkoxides described in Section 3.1.1 were dimeric/tetrameric, with the exception when an additional Lewis base was used. Increasing the steric bulk at the gallium centre by use of bulky alkoxides (e.g. OPh₃) does result in the formation of a monomeric compound, but this comes at a cost of vastly increasing the molecular weight of the precursor, hence reducing the volatility.

Another method of overcoming the oligomer problem is to use donor-functionalised alkoxides. These are alkoxides with one or more “arms”, on the end of which is a Lewis

base. These “arms” coordinate to the gallium centre, reducing the propensity to form dimers and tetramers. The most popular donor-functionalised alkoxides are based on an alkyl backbone (C2 or C3) with simple Lewis bases (NMe₂, OMe), although more esoteric examples do exist in the literature.

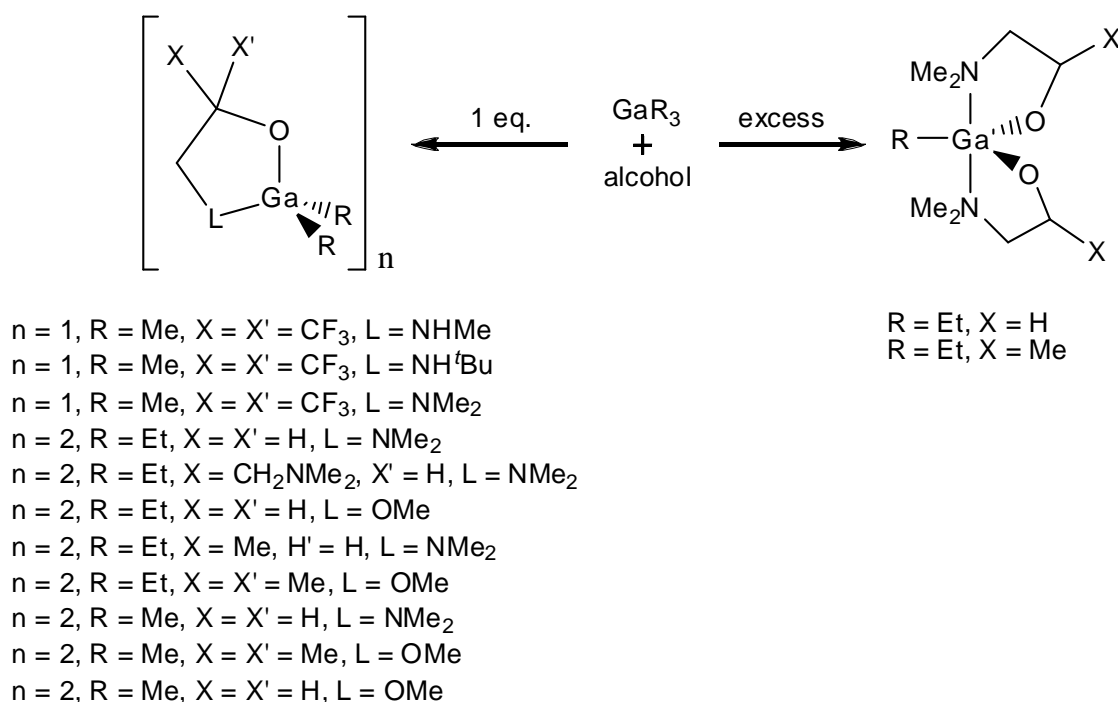
Gallium compounds containing donor-functionalised alkoxides were first used as precursors to thin films of Ga₂O₃ in 2004. Chi *et al.* used the salt metathesis method, reacting GaCl₃ with the sodium salts of fluorinated alkoxides to isolate bis(alkoxide) compounds of gallium (Scheme 3.4).¹⁰⁸



Scheme 3.4. First synthesis of gallium alkoxides using donor-functionalised alkoxides

Compounds [GaCl(L)₂] (L = OC(CF₃)₂CH₂NMe₂, OC(CF₃)₂CH₂C(CH₃)=NMe) were both monomeric, 5-coordinate species, but they crystallised in different geometries. Whereas [GaCl(OC(CF₃)₂CH₂C(CH₃)=NMe)₂] is an almost ideal trigonal bipyramid in the solid state, compound [GaCl(OC(CF₃)₂CH₂NMe₂)₂] is exactly half-way between ideal trigonal bipyramidal and ideal square-based pyramidal geometry. This is probably due to a combination of steric factors (bulky CF₃ groups) and the different backbone size of the two ligands: the C2 backbone in compound [GaCl(OC(CF₃)₂CH₂NMe₂)₂] may not be long enough to allow formation of ideal trigonal bipyramidal geometry whilst minimising the steric interactions between neighbouring CF₃ groups.

Another method of single-source precursor synthesis is to react trialkylgallium reagents with donor-functionalised alcohols (Scheme 3.5). In 2004 (and in subsequent years) this was utilised by Chi *et al.* and Carmalt *et al.* to form single-source precursors. Both mono(alkoxide) (Section 2.1.1) and bis(alkoxide) (Section 2.1.3) compounds of gallium can be isolated although to date, no tris(alkoxide) complexes have yet been reported *via* this route (Scheme 3.5).^{11, 54, 70, 108}



Scheme 3.5. Synthesis of non-fluorinated gallium alkoxides from trialkylgallium reagents

The alkyl gallium fluorinated mono(alkoxides) are monomeric, which is unusual for mono(alkoxide) gallium species which usually form oxygen-bridged dimers. It was thought the reason for this was the CF_3 groups as their steric bulk, coupled with the electron-withdrawing effect, reduced the ability of the alkoxide oxygen to form a bridge hence a monomer was isolated.

As is usual for mono(alkoxide) gallium complexes, the non-halide compounds were all isolated as oxygen-bridged dimers in the solid state, which was confirmed crystallographically (seen in Chapter 2, Figure 2.1). However, gas-phase electron diffraction (GED) of compound $[\text{GaMe}_2(\text{OCH}_2\text{CH}_2\text{NMe}_2)]_2$ revealed that in the gas phase, it existed solely as a monomer (Figure 3.2).⁷⁴ The Ga–N bond length was significantly shorter in the monomer than in the dimer (2.332 Å and 2.471 Å respectively), consistent with a much more strongly bound ligand as would be expected from a less electron-rich complex. This somewhat surprising finding opened up the possibility that relatively involatile gallium alkoxide dimers in the solid state may still prove to be viable CVD precursors.

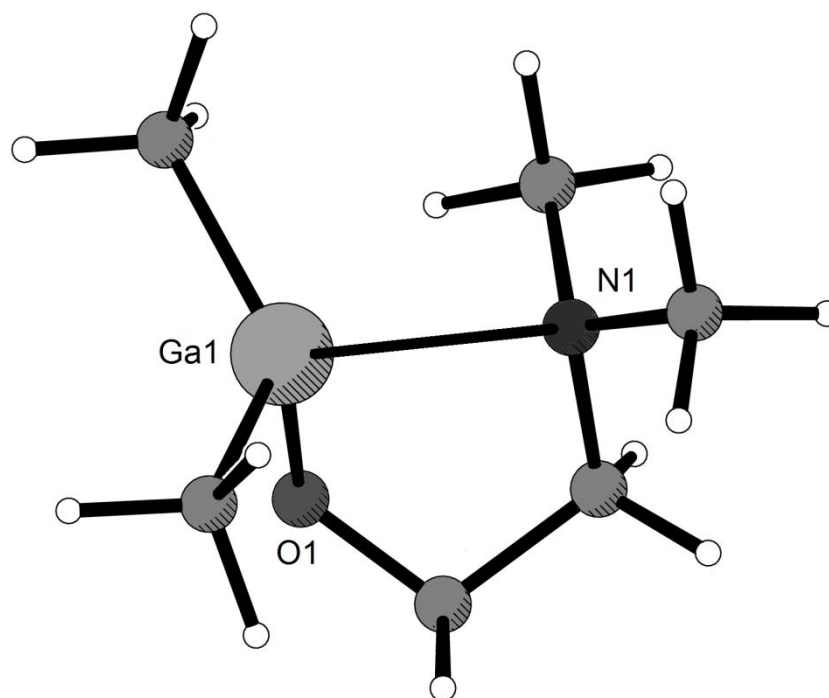
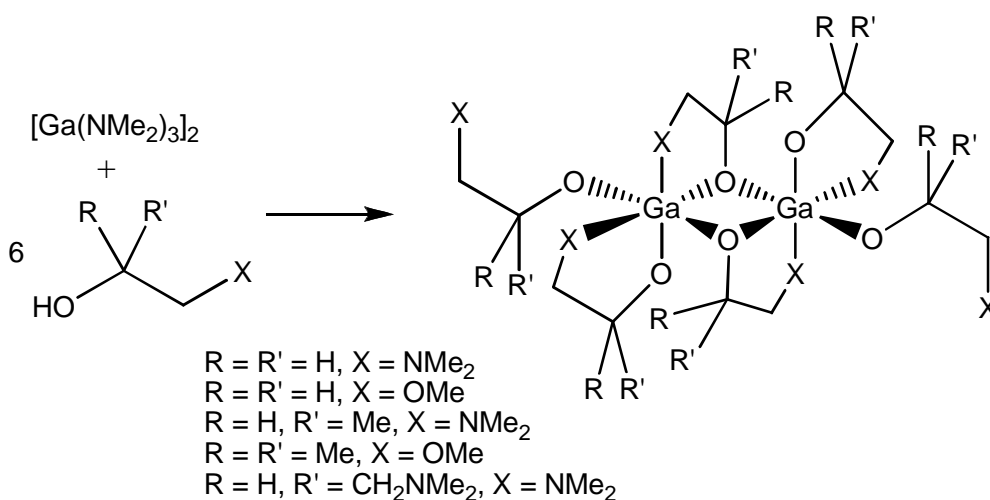


Figure 3.2. Diagram showing the gas-phase structure of compound **24** as determined by GED

LPCVD of compounds $[\text{GaCl}(\text{OC}(\text{CF}_3)_2\text{CH}_2\text{NMe}_2)_2]$ and $[\text{GaMe}_2(\text{OC}(\text{CF}_3)\text{CH}_2\text{NH}^t\text{Bu})]$ was carried out at 500-600 °C substrate temperature and pressure of 3 Torr (a tiny flow of O_2 was used as a carrier gas). Amorphous films were deposited on both quartz and silicon; annealing at 900 °C for 4 hours induced crystallisation. XRD analysis of the annealed films indicated gallium oxide had been formed. XPS data showed a small amount of carbon contamination in the gallium oxide film, but other plausible contaminants such as N, F and Cl were not observed. The Ga:O ratio as measured by XPS indicated a slightly oxygen-deficient film had been formed, but RBS data showed Ga_2O_3 had been formed.

Dimeric gallium mono(alkoxides) $[\text{GaEt}_2(\text{OC}(\text{CXX}')\text{CH}_2\text{L})_2]$ ($\text{X} = \text{X}' = \text{H}$, $\text{L} = \text{NMe}_2$; $\text{X} = \text{CH}_2\text{NMe}_2$, $\text{X}' = \text{H}$, $\text{L} = \text{NMe}_2$; $\text{X} = \text{Me}$, $\text{X}' = \text{H}$, $\text{L} = \text{NMe}_2$; $\text{X} = \text{X}' = \text{Me}$, $\text{L} = \text{OMe}$) were utilised as LPCVD precursors for Ga_2O_3 .¹¹ The LPCVD was carried out on quartz and glass substrates, heated to 600 °C. In each case the films grown were amorphous and no annealing was carried out. The films also contained a significant (*ca.* 10%) amount of carbon contamination, which was found by XPS. This also showed the Ga:O ratio was only 1:1.2, indicating an oxygen-deficient film had been formed.

Since LPCVD resulted in oxygen-deficient films, alkyl gallium mono(alkoxides), $[\text{GaEt}_2(\text{OC}(\text{CXX}')\text{CH}_2\text{L})]_2$, outlined above were also used as aerosol-assisted CVD (AACVD) precursors.^{54,70} All films were deposited on glass at a substrate temperature of 450 °C using toluene as solvent. For each run the precursor was generated *in situ* by reacting the free alcohol with GaR_3 ($\text{R} = \text{Et}, \text{Me}$), rather than using a well-characterized compound. Each film grown was amorphous with only slight carbon contamination (<0.1 at.%), located mainly at the surface, and no nitrogen contamination was observed. EDX of the films indicated the presence of oxygen, gallium and carbon but was an unreliable method of determining the Ga:O ratio due to breakthrough to the underlying glass substrate. WDX was more successful and a ratio very close to the expected 1:1.5 was observed in each case, albeit for exceptionally thin films this dropped to 1:1.3. The success of the *in situ* method indicates that synthesis, isolation and purification of the precursor is not always necessary in order to get successful Ga_2O_3 deposition, a factor which may prove to be an advantage for large-scale synthesis of Ga_2O_3 films.



Scheme 3.6. Synthesis of homoleptic gallium alkoxides with donor-functionalised alkoxides

Although the reaction of trialkylgallium compounds with alcohols yields both mono- and bis-substituted alkoxide complexes, replacement of all three alkyl groups with alkoxide groups was not possible. In order to isolate homoleptic gallium alkoxides with donor-functionalised arms, the amine metathesis route was utilised as outlined in Section 2.1.5. Reacting dimeric $[\text{Ga}(\text{NMe}_2)_3]_2$ with six equivalents of donor-

functionalised alcohol led to the formation of homoleptic gallium tris(alkoxide) complexes (Scheme 3.6).¹⁰

Somewhat surprisingly, the structures outlined in Scheme 3.6 were assigned as an oxygen-bridged dimer on the basis of mass spectrometry and IR spectroscopy (characteristic Ga_2O_2 ring stretches were observed at 557 and 538 cm^{-1}). ^1H NMR spectra were broad, with none of the expected coupling observed. This supported the idea of highly fluxional complexes containing dangling ‘arms’ associating and dissociating from the gallium centre on the NMR timescale: a formulation inconsistent with a monomeric complex where all 3 ‘arms’ were strongly bound to gallium. Unfortunately, due to the oily nature of the products, structural characterisation was not possible hence the exact coordination at the gallium centres remain unknown.

The gallium tris(alkoxides) in Scheme 3.6 were used as AACVD precursors,¹⁰ although they were not isolated prior to use in deposition reactions. In a continuation of the *in situ* methodology previously developed, $[\text{Ga}(\text{NMe}_2)_3]_2$ and the donor-functionalised alcohol (six equivalents) were placed in an AACVD flask, allowed to react for 1 hour and then passed into the CVD chamber. For each compound, deposition was carried out on glass with a substrate temperature of 550 °C. WDX analysis of the as-deposited films showed they were all oxygen-deficient, with a Ga:O ratio of 1:1.15. Subsequent annealing in air at 600 °C improved the Ga:O ratio to the expected 1:1.5 (as measured by WDX) but annealing at this temperature did not induce crystallisation of the films, despite appearing to have a snowflake-like morphology (Figure 3.3 - SEM of Ga_2O_3 deposited from $[\text{Ga}(\text{OCH}_2\text{CH}_2\text{OMe})_3]_2$). XPS data also indicated that Ga_2O_3 had been formed and that carbon contamination was limited to the surface of the film. No nitrogen contamination was observed.

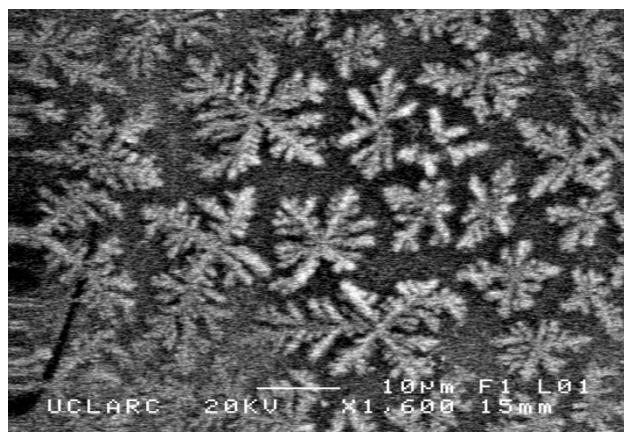
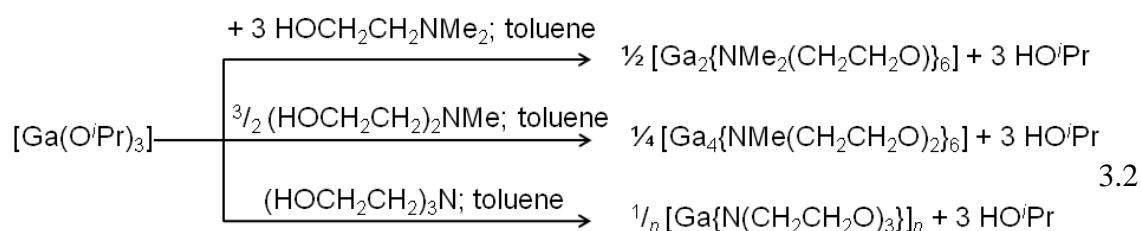


Figure 3.3. SEM image of Ga_2O_3 grown by AACVD of $[\text{Ga}(\text{OCH}_2\text{CH}_2\text{OMe})_3]_2$.¹⁰

Homoleptic gallium alkoxides were also prepared using the alcohol/alkoxide exchange method (Section 2.5.1).³⁰ Starting from $[\text{Ga}(\text{O}^i\text{Pr})_3]$ and the free alcohol, $[\text{Ga}\{\text{NMe}_2(\text{CH}_2\text{CH}_2\text{O})\}]_2$ with one “arm”, as well as compounds $[\text{Ga}\{\text{NMe}_{3-x}(\text{CH}_2\text{CH}_2\text{O})_x\}]_n$ ($X = 2, n = 4$; $X = 3, n = \text{unknown}$) with two and three “arms” respectively, were prepared in good yields (Equation 3.2).



Prior to their use in a spin-coating process to form gallium oxide, the compounds outlined in Equation 3.2 were hydrolysed in boiling water to determine the likely decomposition pathway.³⁰ $\text{GaO}(\text{OH})$ was identified as the hydrolysis product, forming in its crystalline orthorhombic phase. Upon heating, it first become amorphous then started converting to Ga_2O_3 at 250 °C. At 500 °C, rhombohedral gallium oxide was observed by XRD: this then converted to the more usual monoclinic phase at 700 °C.

This data was used to facilitate the spin-coating process. $[\text{Ga}\{\text{NMe}_2(\text{CH}_2\text{CH}_2\text{O})\}]_2$ was hydrolysed and then dropped onto a glass or silicon substrate spinning at 1200-2000 rpm. After drying at 120 °C, the process was repeated a number of times until a sufficiently thick film had been formed. This was then annealed at 500 °C (glass

substrate), affording an amorphous film which was consistent with Ga₂O₃, as identified by EDX. Although the film was adherent on glass substrates, it was poorly adherent on silicon which precluded annealing at temperatures which would enable crystalline Ga₂O₃ to form.

A variety of gallium alkoxide precursors have been used to deposit thin films of gallium oxide, commonly on glass and silica substrates *via* different techniques including sol-gel, spin coating and LP and AACVD. Precursors have been in the form of isolated solids and oils as well as *in situ* solutions, normally depositing amorphous films which require subsequent annealing to produce crystalline Ga₂O₃ films. The precursors described in Section 3.1 have mostly been dimeric or higher coordination cluster numbers, with the exception of those with bulky fluorinated ligands. Although it has been found that dimeric mono(alkoxides) are monomeric in the gas phase, few studies have been conducted using monomeric gallium bis(alkoxide) precursors.

3.2. Results and Discussion

Tailoring the properties of CVD precursors can help to exploit the full potential of CVD. It has been reported previously that the replacement of simple alkoxide groups¹³⁹ by donor-functionalised alkoxides, can result in precursors with improved physical properties and enhanced CVD performance, as discussed in the Chapter 1. Single-source precursors provide a simple way to deposit stoichiometric metal oxide thin films *via* CVD. In this work, gallium chloro bis(alkoxides) of the formula [GaCl(OR)₂] (R = OCH₂CH₂NMe₂, OCH₂CH₂NEt₂, OCH₂CH₂CH₂NMe₂), synthesised *via* the chloro gallium bis(amide) intermediate are used as precursors to gallium oxide thin films. Heteroleptic gallium alkoxides synthesised in Chapter 2 are also used as precursors. Herein, the deposition of these precursors and characterisation of the resultant films are reported.

3.3. Gallium oxide thin films from gallium bis(alkoxides)

3.3.1. Thermal decomposition analysis

In this work, thermogravimetric analysis (TGA) has been used to study the decomposition of some of the precursors discussed in Chapter 2. TGA can help to understand how a compound decomposes as it continuously records changes in the mass of a material whilst being heated. The atmosphere of the sample can be controlled, whether it be from changing the flow gas or sealing the sample in a pan. The total mass loss figure can be used to predict the decomposition pathway of the compound, and provide information about whether a precursor will be able to cleanly decompose to the required binary product. Take for example a gallium alkoxide compound, if the mass loss is consistent with the organic leaving groups surrounding the metal centre, it can be assumed this precursor will decompose to give pure Ga₂O₃. In addition to this, TGA has the ability to record decomposition steps, and where these are identified the prediction of a decomposition pathway results.

Another technique that is useful in determining whether a given complex will be a suitable CVD precursor is differential scanning calorimetry (DSC). In this method two pans, one loaded with sample and the other empty (acting as an inert reference) are simultaneously heated whilst the differences in heat flow into the two is recorded. DSC can give information concerning chemical or physical changes that are accompanied by a gain or loss of heat, as previously discussed a good CVD precursor will be capable of vaporization and must be able to travel across to the substrate without decomposing. Therefore a good precursor will exhibit a melting point at a temperature much lower than the onset of decomposition, allowing it to be thermally vaporized at a stable temperature. Also a necessary requirement of these compounds is that they will decompose to the required product (namely the thin film) at temperatures below 600°C, so that a glass substrate can be used in depositions.

It is important however to mention that this technique does not replicate a CVD experiment and therefore compounds which do not appear to be suitable precursors from these analytical results could still produce thin films.

3.3.1.1. TGA analysis of [GaCl(OCH₂CH₂NMe₂)₂] (2)

The thermogravimetric analysis of [GaCl(OCH₂CH₂NMe₂)₂] (**2**) shows an overall mass loss of 64% (Figure 3.4). The decomposition of **2** does not occur in clean, discrete stages but is continuous from the onset at *ca.* 120 °C throughout the temperature range studied and occurs in three stages. The first mass loss of 32% occurs at 180 °C, the second of 12% at 280 °C and finally the third mass loss of 18% at 380 °C. The overall mass loss of 64% is close to the 66% required for complete decomposition to Ga₂O₃ suggesting that this compound would make a good precursor and could deposit films at low temperatures (less than 400 °C). The DSC of **2** shows a sharp endotherm at 121 °C, which corresponds to the melting point. The broad exotherms observed at 220 and 258 °C could be an effect of the decomposition process. The decomposition of **2** begins at a similar temperature to the melting point suggesting that the molecule could be transported to the substrate without prior decomposition. Hence, these results indicate that **2** would make a suitable CVD precursor. However, it should be noted that as the TGA does not occur in one clean stage, some contamination could be observed in the film deposited.

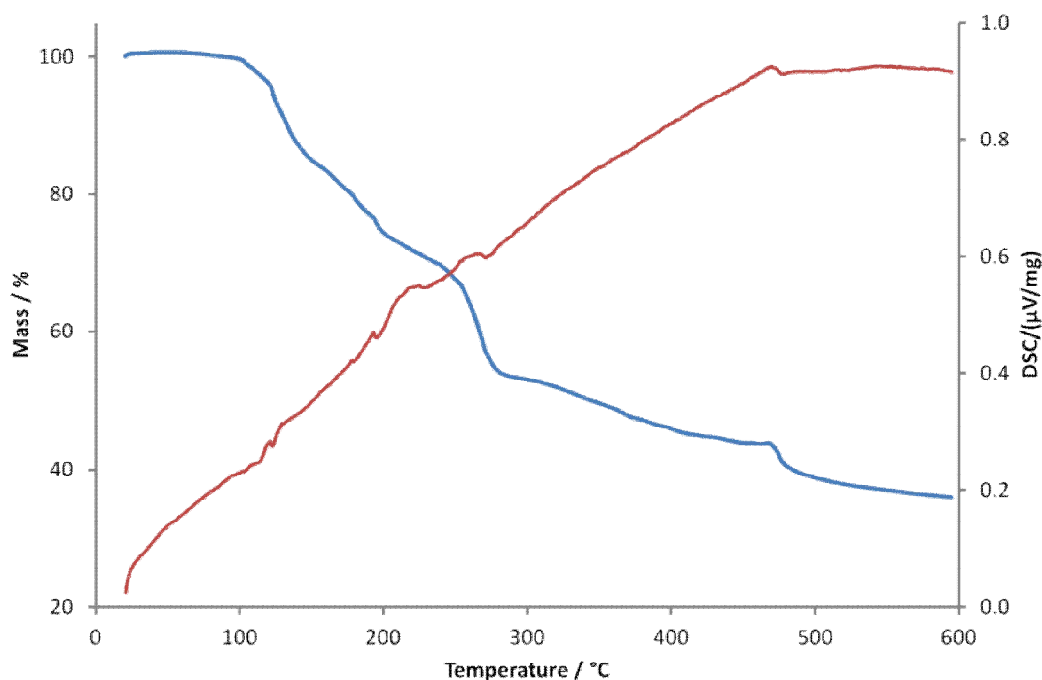


Figure 3.4. TGA and DSC of $[\text{GaCl}(\text{OCH}_2\text{CH}_2\text{NMe}_2)_2]$ (**2**)

3.3.1.2. TGA analysis of $[\text{GaCl}(\text{OCH}_2\text{CH}_2\text{NEt}_2)_2]$ (**3**)

The thermogravimetric analysis of $[\text{GaCl}(\text{OCH}_2\text{CH}_2\text{NEt}_2)_2]$ (**3**) shows an overall mass loss of 65% (Figure 3.5). As with the decomposition of **2**, the decomposition of **3** does not occur in clean, discrete stages but is continuous from the onset at *ca.* 100 °C throughout the temperature range studied and occurs in three stages. The first mass loss of 20% occurs at 155 °C, the second of 33% at 230 °C and finally the third mass loss of 11% at 360 °C. The overall mass loss of 65% is close to the 70% required for complete decomposition to Ga_2O_3 suggesting that this compound would make a good precursor and could deposit films at low temperatures (less than 400 °C). The DSC of **3** shows a sharp endotherm at 81 °C, which corresponds to the melting point. Another exotherm is observed at 228 °C and could be an effect of the decomposition process. The decomposition of **3** begins at a higher temperature than the melting point suggesting that the molecule could be transported to the substrate without prior decomposition. Therefore, these results indicate that **3** would make a suitable CVD precursor. However, it should be noted that as the TGA does not occur in one clean stage, some contamination could be observed in the film deposited.

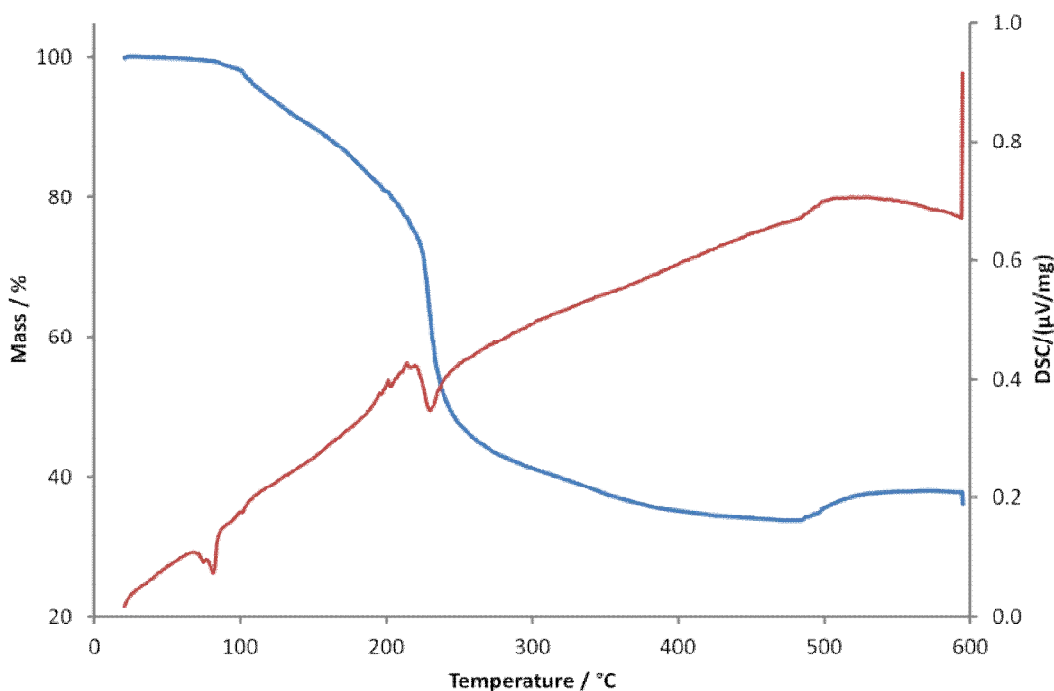


Figure 3.5. TGA and DSC of $[\text{GaCl}(\text{OCH}_2\text{CH}_2\text{NEt}_2)_2]$ (**3**)

3.3.1.3. TGA analysis of $[\text{GaCl}(\text{OCH}_2\text{CH}_2\text{CH}_2\text{NMe}_2)_2]$ (**5**)

The thermogravimetric analysis of $[\text{GaCl}(\text{OCH}_2\text{CH}_2\text{CH}_2\text{NMe}_2)_2]$ (**5**) shows an overall mass loss of 56% (Figure 3.6). As with the decomposition of **2** and **3**, the decomposition of **5** does not occur in clean, discrete stages but is continuous from the onset at *ca.* 95 °C throughout the temperature range studied and occurs in three stages. The first mass loss of 8% occurs at 159 °C, the second of 33% at 260 °C and finally the third mass loss of 14% at 370 °C. The overall mass loss of 56% is not close to the 68% required for complete decomposition to Ga_2O_3 suggesting that this compound may leave behind contaminants in the final film, however could deposit films at low temperatures (less than 400 °C). The DSC of **5** shows a sharp endotherm at 48 °C, which corresponds to the melting point. Another exotherm is observed at 100 °C and an endotherm at 272 °C, which could be an effect of the decomposition process. The decomposition of **5** begins at a higher temperature than the melting point suggesting that the molecule could be transported to the substrate without prior decomposition. These results indicate that **5** would make a suitable CVD precursor however, due to the lack of complete decomposition and that the TGA did not occur in one clean stage, some contamination could be observed in the final Ga_2O_3 film deposited.

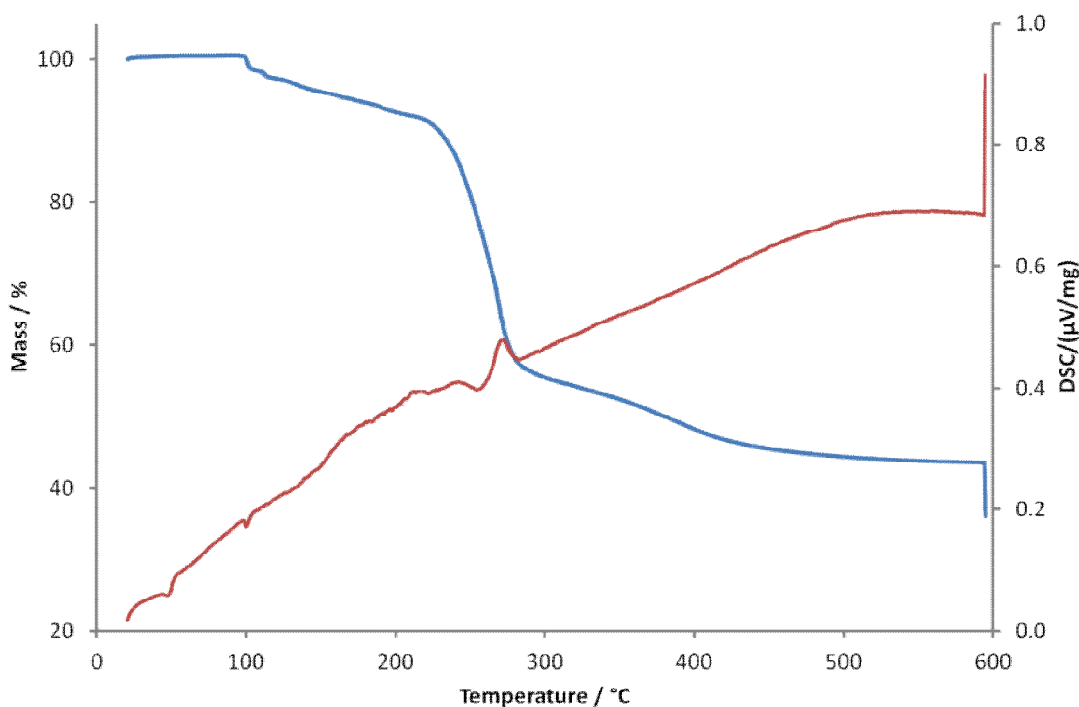
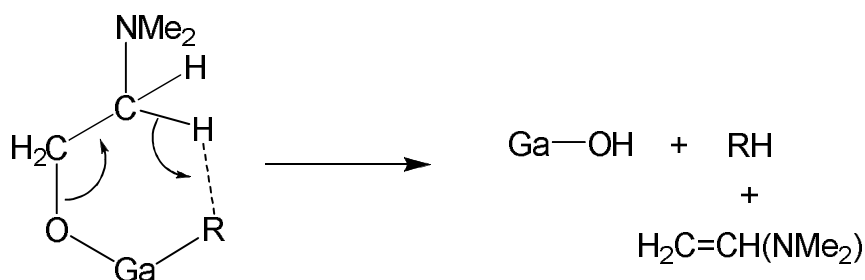


Figure 3.6. TGA and DSC of $[\text{GaCl}(\text{OCH}_2\text{CH}_2\text{CH}_2\text{NMe}_2)_2]$ (**5**)

Additionally the thermal decomposition of a selection of compounds has been studied using TGA and DSC. These techniques have shown the group 13 alkoxides have potential for use as precursors in the production of thin films *via* CVD. All of the compounds analysed, decompose to the desired binary material (M_2O_3), below 400 °C, so are *viable* as low temperature alternatives to many precursors reported.

3.3.2. Decomposition pathway

As shown below in Scheme 3.7, a likely mechanism for the decomposition of typical group 13 alkoxides to the relevant binary product could involve γ -hydride elimination. In this instance the loss of an alkene, $\text{H}_2\text{C}=\text{CH}(\text{NMe}_2)$, *via* γ -hydride elimination from a gallium alkoxide is depicted. If the alkoxide ligand is lost *via* γ -elimination the alkene $\text{H}_2\text{C}=\text{CH}(\text{NMe}_2)$ would be eliminated. The γ -hydrogen could react with the Ga–R group (R = Cl or alkoxide) resulting in the elimination of RH (HCl or ROH).



Scheme 3.7. Likely mechanism for the decomposition of a typical group 13 alkoxide

3.3.3. CVD of Chloro Gallium Bis(alkoxide) Precursors

The AACVD setup as described in Section 1.2.1.7 was utilized. Compounds $[\text{GaCl}(\text{OCH}_2\text{CH}_2\text{NMe}_2)_2]$ (**2**), $[\text{GaCl}(\text{OCH}_2\text{CH}_2\text{NEt}_2)_2]$ (**3**) and $[\text{GaCl}(\text{OCH}_2\text{CH}_2\text{CH}_2\text{NMe}_2)_2]$ (**5**) were used as precursors to deposit onto glass and quartz substrates at 450 °C using toluene as the solvent. A N_2 carrier gas was used at 1 Lmin^{-1} to deliver the aerosol from the bubbler to the reactor. The deposition conditions and thin film characteristics are outlined in Table 3.1.

Gallium oxide thin films deposited between 450 - 550 °C were all adherent and transparent thin films. They were not removed with a tissue nor Scotch tape. The films were not readily scratched with a brass stylus but were with a steel stylus. Glancing angle X-ray powder diffraction patterns for the gallium oxide thin films deposited by precursors **2**, **3** and **5** indicated that they were amorphous, as expected for the deposition of gallium oxide at these temperatures (< 700 °C).^{9, 10, 12} This is an effect of the low deposition temperatures used. Films deposited at 450 °C gave the best surface coverage and this temperature was used to deposit films onto quartz substrates.

To obtain crystalline Ga_2O_3 thin films, films deposited on quartz substrates were annealed at 1000 °C for 12 hours in air. Glancing angle X-ray powder diffraction confirms that the annealed films were crystalline. Figure 3.7 shows the powder XRD of the annealed film grown from $[\text{GaCl}(\text{OCH}_2\text{CH}_2\text{NMe}_2)_2]$ (**2**), which is consistent with the reference standard for monoclinic $\beta\text{-Ga}_2\text{O}_3$. The film gave lattice constants $a = 12.0(2)$, $b = 2.99(1)$ and $c = 5.7(1) \text{ \AA}$ and $\beta = 103.5^\circ$ in agreement with reported data for bulk Ga_2O_3 .¹⁴⁰ Gallium oxide thin films grown from precursors

[GaCl(OCH₂CH₂NEt₂)₂] (**3**) and [GaCl(OCH₂CH₂CH₂NMe₂)₂] (**5**) after annealing were also found to have the same monoclinic β -Ga₂O₃ structure.

Table 3.1 Deposition conditions and Ga₂O₃ thin film properties.

Precursor	T [°C]	Substrate	Trans- mittance [%]	Band Gap [eV]
[GaCl(OCH ₂ CH ₂ NMe ₂) ₂] (2)	450- 550	SiCO coated float glass & quartz	75	3.8
[GaCl(OCH ₂ CH ₂ NEt ₂) ₂] (3)			75	3.8
[GaCl(OCH ₂ CH ₂ CH ₂ NMe ₂) ₂] (5)			74	3.7

The composition of the annealed films were determined by energy dispersive X-ray analysis (EDXA) measurements, the results of which are displayed in Table 3.1. Films were of sufficient thickness that breakthrough to the underlying substrate was not observed. EDXA confirmed the presence of gallium and oxygen in a 1:1.5 ratio confirming the Ga₂O₃ stoichiometry. The presence of residual chlorine or carbon was not observed.

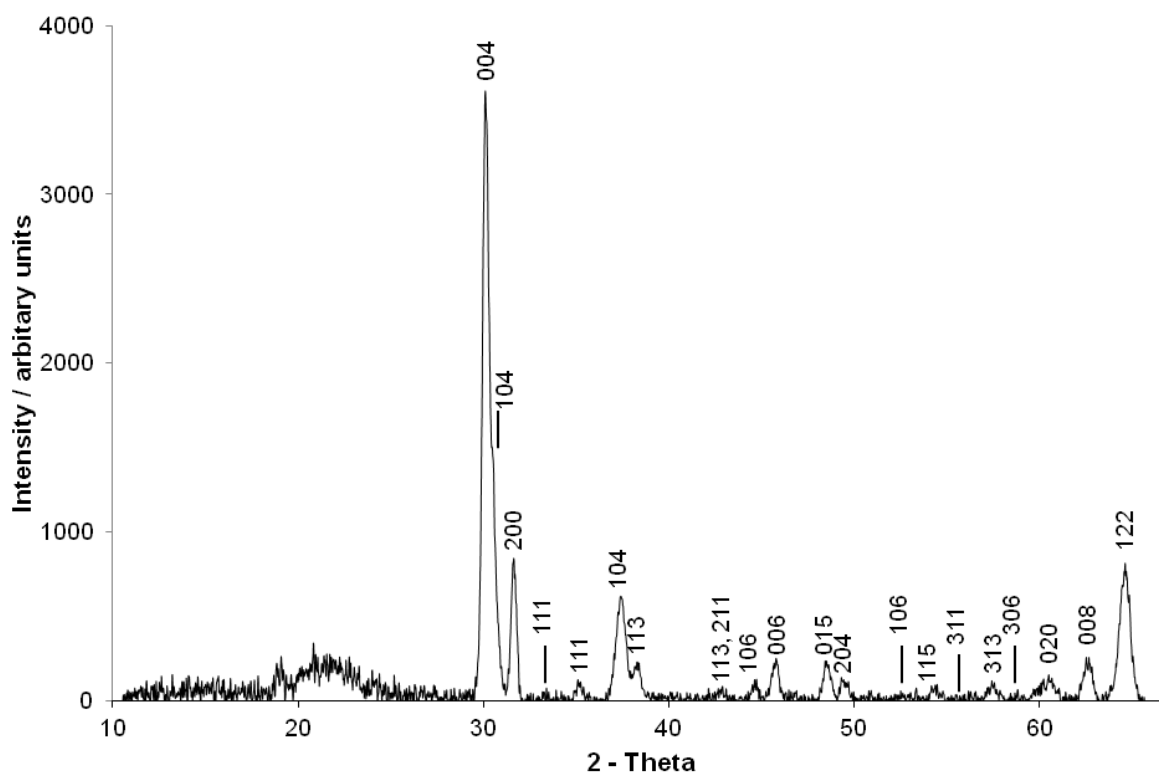


Figure 3.7. X-ray powder diffraction pattern of monoclinic β - Ga_2O_3 as obtained from depositing $[\text{GaCl}(\text{OCH}_2\text{CH}_2\text{NMe}_2)_2]$ (**2**) into quartz substrates and annealing for 12 hours at 1000°C .

SEM analysis was conducted on both the as-deposited and annealed thin films. SEM images of Ga_2O_3 thin films deposited from precursors **2**, **3**, and **5** are shown in Figure 3.8. As-deposited Ga_2O_3 samples were seen to have a very smooth morphology. Features were barely visible with crystallite sizes ranging from 10-30 nm. After annealing, the crystallite size increased to 100 nm, which is expected as annealing causes the film to sinter.

Transmittance and band gap calculations of the annealed thin films are displayed in Table 3.1. Optical measurements were conducted over a range from 250-2000 nm on quartz samples. Measurements for glass samples are not reported as the transmittance for glass overlaps with that of Ga_2O_3 . Transmittance measurements revealed the annealed Ga_2O_3 thin films transmitted 74-75% of visible light (380-780 nm) compared to 76% of plain quartz. By plotting $\alpha h\nu^{1/2}$ against $h\nu$ in eV (Tauc methodology) and extrapolating the flat part of the curve to the x -axis, the value of the indirect band gap can be calculated.¹⁴¹ Band gaps for annealed films were between 3.7-3.8 eV. This is

vastly reduced compared to literature values of 4.9 eV.¹⁴² This reduction in the band gap is unexpected as reductions of this magnitude are usually only seen when doping crystal lattices. However, EDXA revealed no additional elemental incorporation. Films were too thin to calculate film thickness *via* the Swanepoel method.¹⁴³

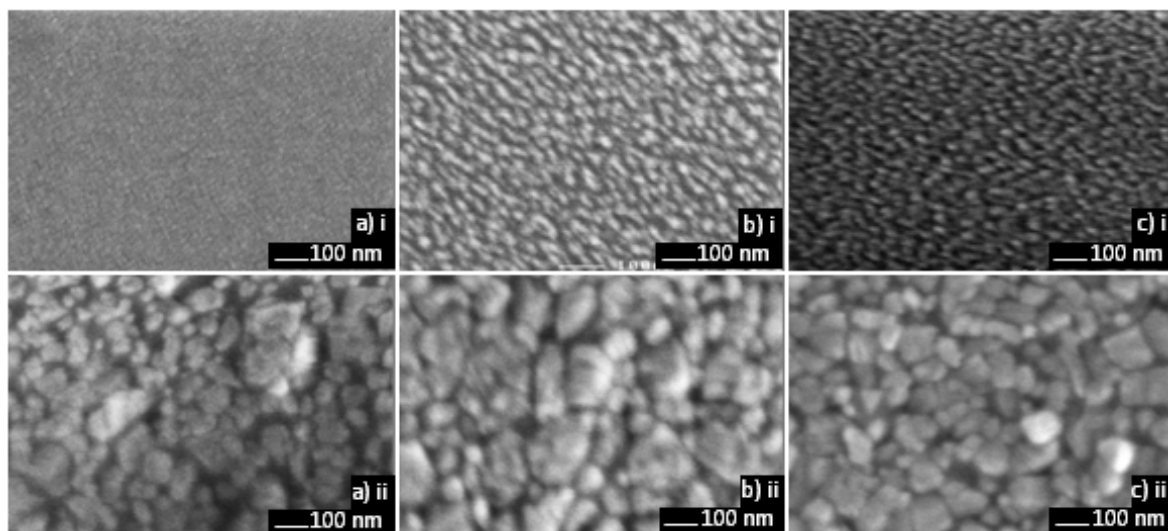


Figure 3.8. SEM images of gallium oxide thin films a) $[\text{GaCl}(\text{OCH}_2\text{CH}_2\text{NMe}_2)_2]$ (2), b) $[\text{GaCl}(\text{OCH}_2\text{CH}_2\text{NEt}_2)_2]$ (3) and c) $[\text{GaCl}(\text{OCH}_2\text{CH}_2\text{CH}_2\text{NMe}_2)_2]$ (5) deposited by AACVD in toluene at 450 °C. Images x) i show the as-deposited amorphous films on SiCO coated float glass. Images x) ii show the annealed films on quartz.

AACVD does not produce uniform thin films. Areas of films can be different in composition across an entire substrate. For example films of TiO_2 are purposely grown with a mixture of rutile and anatase phases for water-splitting purposes.¹⁴⁴ It is likely that the points of analysis used in EDXA and for optical measurements were not the same and the point used for optical measurements may have contained additional elemental incorporation, lowering the band gap that was not observed in EDXA. Several points across the films would need to be analysed to build a more complete picture.

3.3.4. Summary

Chloro gallium bis(alkoxides), $[\text{GaCl}(\text{OR})_2]$ ($\text{R} = \text{CH}_2\text{CH}_2\text{NMe}_2$ (2), $\text{CH}_2\text{CH}_2\text{NEt}_2$ (3), $\text{CH}_2\text{CH}_2\text{CH}_2\text{NMe}_2$ (5)), synthesised from gallium chloride *via* the chloro gallium

bis(amide) intermediate in Chapter 2 were used as single-source precursors to gallium oxide thin films. The precursors were dissolved in hexane and deposited onto glass and quartz at a temperatures of 450-550 °C *via* AACVD As-deposited gallium oxide films were transparent amorphous thin films. Little difference in the resultant films were seen between precursors **2**, **3**, and **5** used. Subsequent annealing at 1000 °C in air crystallised the films which were monoclinic β -Ga₂O₃. EDXA confirmed the Ga₂O₃ film composition and SEM showed very smooth morphology before annealing and a crystallite size increase after annealing. Optical measurements show films have similar transparency to glass and the band gap was calculated to be 3.8-3.7 eV, suggesting some additional doping had occurred. Coverage of the substrate at 450 °C was substantial and thus compounds **2**, **3** and **5** could be viable precursors for use to deposit on gas sensing substrates.

3.4. Gallium oxide thin films from heteroleptic gallium alkoxides

Although EDXA revealed no chlorine contamination of gallium oxide thin films deposited by precursors **2**, **3** and **5**, the substantially reduced band gap measurements suggests some sort of additional elemental incorporation into the Ga₂O₃ lattice, most likely chlorine incorporation. Heteroleptic gallium alkoxides with the formula [Ga(OR)₂(OR')] (R = CH₂CH₂NMe₂, CH₂CH₂NEt₂, CH₂CH₂CH₂NMe₂; R' = Me, Et, ⁱPr, ^tBu) were synthesised in Chapter 2 and were investigated using TGA.

3.4.1. TGA of heteroleptic gallium alkoxides

TGA analysis was performed on compounds **8-13a** The thermogravimetric analysis of [Ga(OCH₂CH₂NMe₂)₂(OMe)] (**8**) is typical of all the TGAs of compounds **8-13a**. The TGA of **8** shows an overall mass loss of 68% (Figure 3.9). The mass loss occurs in one clean step and the remaining 31% is very close to the expected 33% for Ga₂O₃ to remain. The DSC of **8** shows a sharp endotherm at 91 °C, which corresponds to the melting point. An endotherm is observed at 244 °C and another exotherm at 267 °C, which could be an effect of the decomposition process. The decomposition of **8** begins at a

higher temperature than the melting point suggesting that the molecule could be transported to the substrate without prior decomposition. These results indicate that **8** would make a suitable CVD precursor especially as the decomposition occurs in a single step allowing for clean deposition.

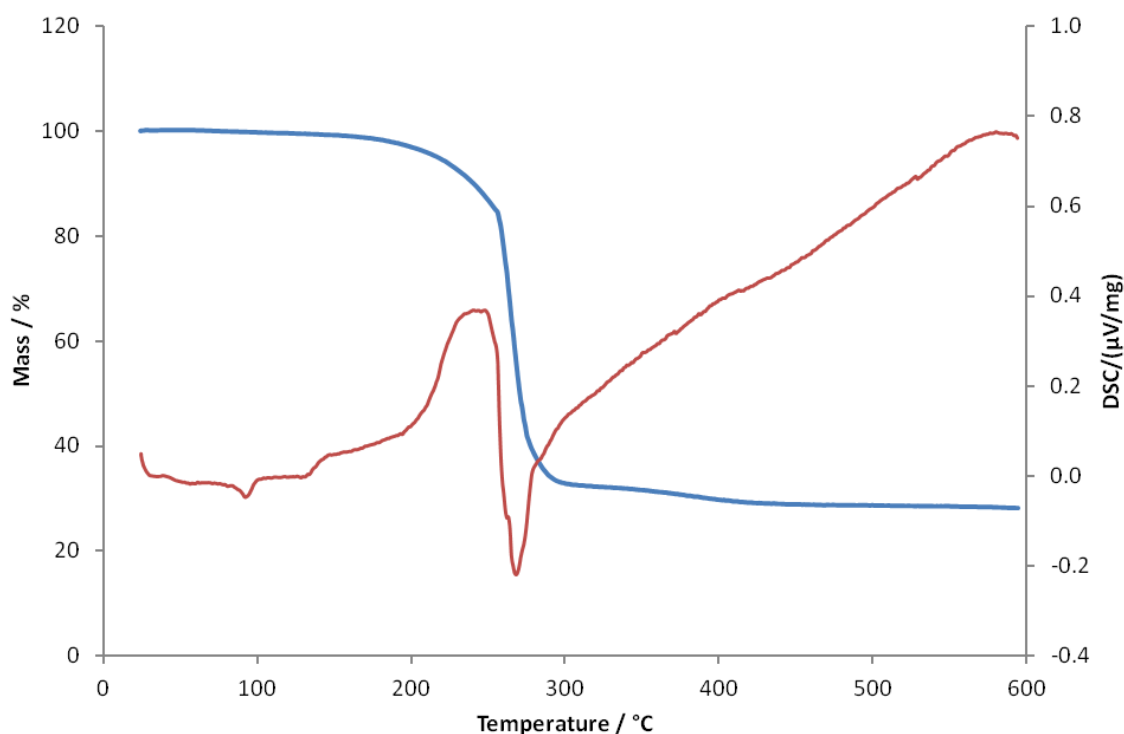


Figure 3.9. Typical TGA of heteroleptic gallium alkoxide. The TGA of $[\text{Ga}(\text{OCH}_2\text{CH}_2\text{NMe}_2)_2(\text{OMe})]$ (**8**) is shown here.

3.4.2. Ga_2O_3 thin films from heteroleptic gallium alkoxides

Compounds $[\text{Ga}(\text{OCH}_2\text{CH}_2\text{NMe}_2)_2(\text{OMe})]$ (**8**) and $[\text{GaCl}(\text{OCH}_2\text{CH}_2\text{NMe}_2)(\text{O}^t\text{Bu})]$ (**11a**) synthesised and characterised in Chapter 2 were used as single-source precursors to gallium oxide thin films. Table 3.2 shows the precursor deposition conditions and properties of the final thin films. Compounds **8** and **11a** were dissolved in DCM or toluene and deposited on glass and quartz substrates at 450 °C. A N_2 carrier gas with a flow rate of 1 Lmin^{-1} was used to transport the aerosol from the bubbler to the reactor.

The resultant thin films deposited from compounds **8** and **11a** were very thin and patchy transparent films. Parts of the film were readily removed with a tissue, however the majority of the films were not removed with a tissue nor Scotch tape, however were

readily scratched with a brass or steel stylus. The as-deposited thin films were found to be amorphous by glancing angle X-ray powder diffraction, as seen with earlier as-deposited gallium oxide thin films and is expected with deposition at 450 °C.¹⁰ Subsequent annealing of the films at 1000 °C for 15 hours afforded crystalline monoclinic β -Ga₂O₃ with diffraction patterns appearing like that of Figure 3.7.

Table 3.2. Precursor conditions from heteroleptic gallium alkoxides and resulting thin film properties.

Precursor	Solvent	Substrate	EDAX	Transmittance [%]
[Ga(OCH ₂ CH ₂ NEt ₂) ₂ (OMe)] (8)	Hexane	Glass and Quartz	Ga _x O _x	30
[GaCl(OCH ₂ CH ₂ NEt ₂)(O ^t Bu)] (11a)	Hexane		Ga _x O _x	unknown
[GaCl(OCH ₂ CH ₂ NEt ₂)(O ^t Bu)] (13a)	Toluene		Ga _x O _x	unknown

The composition of the film was determined by EDXA measurements. EDXA confirmed the presence of gallium and oxygen, however breakthrough to the underlying glass substrate was observed, so gallium to oxygen ratios could not be deduced. The presence of chlorine and carbon were not observed.

SEM images of the gallium oxide thin films deposited by compounds **8** and **11a** are shown in Figure 3.10. Images show films before and after annealing. An SEM image of as-deposited gallium oxide from compound **8** was not obtained as the morphology was very smooth and hard to image. Compound **11a** was-deposited using both DCM and toluene and both as-deposited and annealed images are shown. As-deposited films were seen to be smoother in morphology with crystallite sizes of 10-50 nm. After annealing, the crystallite size increased to 100-150 nm, which is expected as films sinter at elevated temperatures. Images b) i and c) ii in Figure 3.10 show large globular particulates on top of the underlying films. This is likely to be a small amount of precursor material that has settled on top of the film which could be readily removed using a tissue. The film deposited from compound **8** appears to have a more cubic type

morphology compared to that of **11a**. Using different solvents with compound **11a** appears to have made little difference to the film morphology.

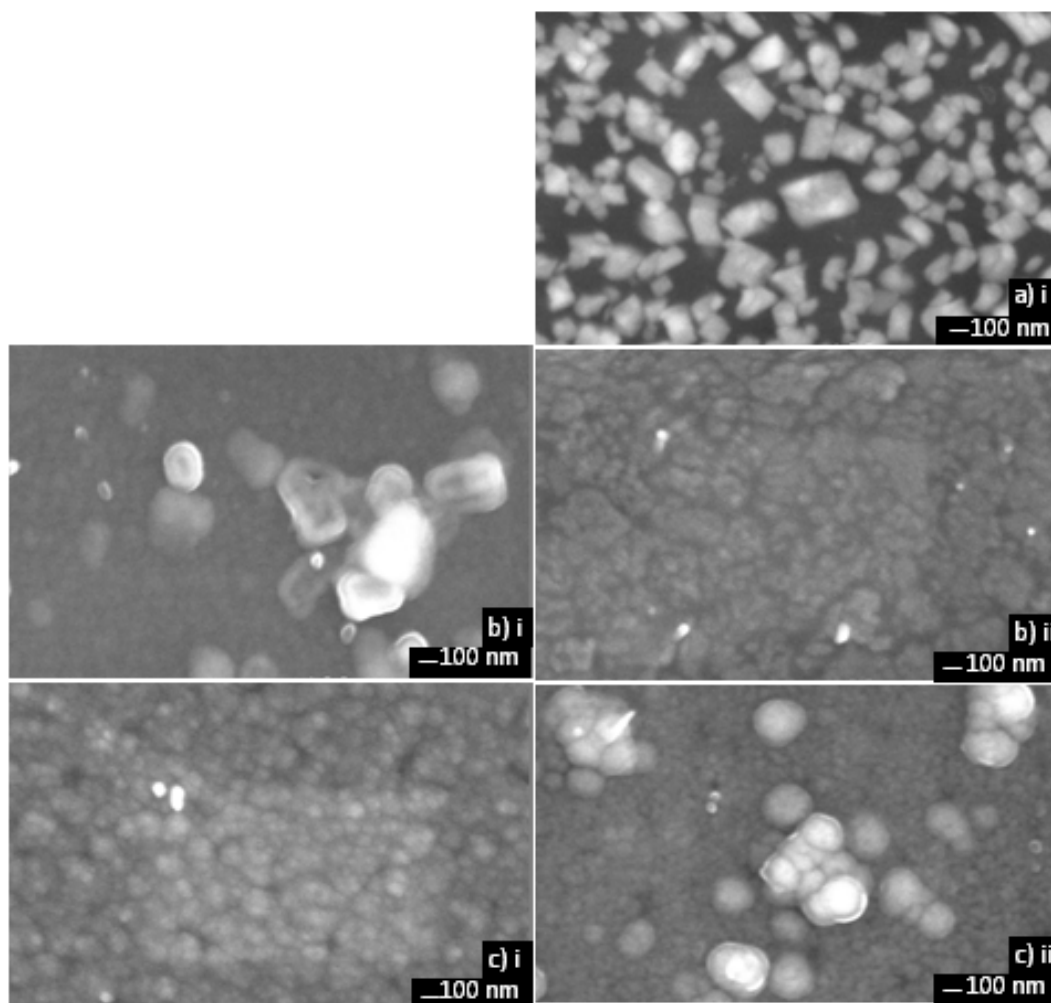


Figure 3.10. SEM images of Ga_2O_3 thin films deposited from a) $[\text{Ga}(\text{OCH}_2\text{CH}_2\text{NMe}_2)_2(\text{OMe})]$ (**8**) from DCM, b) $[\text{GaCl}(\text{OCH}_2\text{CH}_2\text{NMe}_2)(\text{O}^t\text{Bu})]$ (**11a**) from DCM and c) $[\text{GaCl}(\text{OCH}_2\text{CH}_2\text{NMe}_2)(\text{O}^t\text{Bu})]$ (**11a**) from toluene. Images x i show as-deposited films on SiCO coated float glass, images x ii show films after annealing at $1000\text{ }^\circ\text{C}$ on quartz.

Due to the very thin and patchy nature of the films transmittance was only obtained for films deposited from **8**, however the data was not sufficient for Tauc plots and so the band gap was not obtained.

3.4.3. Summary

Heteroleptic gallium alkoxides, $[\text{Ga}(\text{OR})_2(\text{OR}')] (R = \text{CH}_2\text{CH}_2\text{NMe}_2; R' = \text{Me} (\mathbf{8}), \text{'Bu} (\mathbf{11a}))$, synthesised from compound **2** *via* the amido gallium bis(alkoxide) intermediate in Chapter 2 were used as single-source precursors to gallium oxide thin films. Dissolved in DCM or toluene and deposited onto glass and quartz at a temperature of 450 °C *via* AACVD, as-deposited gallium oxide films were transparent, patchy, amorphous thin films. Subsequent annealing at 1000 °C in air crystallised the films which were monoclinic $\beta\text{-Ga}_2\text{O}_3$. EDXA confirmed the presence of gallium and elevated quantities of oxygen, however break through to the underlying glass was observed and the precise film composition could not be measured. SEM showed very smooth morphology before annealing, films deposited from **8** was too featureless to obtain enough contrast for SEM imaging. Subsequent annealing showed an increase in crystallite size. Little difference was seen in morphology between the choice of solvent used.

3.5. Conclusion

Chapter 3 explored the single-source precursors used to deposit gallium oxide thin films. Their use as precursors allows for simpler, cheaper and cleaner deposition to these metal oxide thin films. AACVD allows for a variety of precursors to be employed as they rely solely on their solubility and not volatility. Compounds synthesised in Chapter 2, $[\text{GaCl}(\text{OR})_2] (R = \text{CH}_2\text{CH}_2\text{NMe}_2 (\mathbf{2}), \text{CH}_2\text{CH}_2\text{NEt}_2 (\mathbf{3}), \text{CH}_2\text{CH}_2\text{CH}_2\text{NMe}_2 (\mathbf{5}))$ and $[\text{Ga}(\text{OR})_2(\text{OR}')] (R = \text{CH}_2\text{CH}_2\text{NMe}_2; R' = \text{Me} (\mathbf{8}), \text{'Bu} (\mathbf{11a}))$, were investigated by TGA and used as single-source precursors to resultant gallium oxide thin films.

TGA showed that compounds, of the type $[\text{GaCl}(\text{OR})_2]$, decomposed in a multistep process that may leave behind material other than the desired Ga_2O_3 . Compounds **2**, **3** and **5** were dissolved in hexane and deposited onto glass and quartz at a temperatures of 450-550 °C *via* AACVD. As-deposited gallium oxide films had good coverage at 450 °C and were transparent, amorphous thin films. Little difference in resultant films was seen between precursors **2**, **3**, and **5** used. Subsequent annealing at 1000 °C in air

crystallised the films which were monoclinic β -Ga₂O₃. EDXA confirmed the Ga₂O₃ film composition and SEM showed very smooth morphology before annealing and a crystallite size increase after annealing. Optical measurements show films have similar transparency to glass and the band gap was calculated to be 3.8-3.7 eV, suggesting some additional doping had occurred.

Compounds **8** and **11a** were dissolved in DCM or toluene and deposited onto glass and quartz at a temperature of 450 °C *via* AACVD, as-deposited gallium oxide films were transparent, patchy, amorphous thin films. Subsequent annealing at 1000 °C in air crystallised the films which were monoclinic β -Ga₂O₃. EDXA confirmed the presence of gallium and elevated quantities of oxygen, however break through to the underlying glass was observed and the precise film composition could not be measured. SEM showed very smooth morphology before annealing, films deposited from **8** were too smooth for imaging. Subsequent annealing showed an increase in crystallite size. Little difference was seen in morphology between the choice of solvent used.

For viability as gas sensors, films deposited by compounds **2**, **3**, and **5** show the best coverage and would suitably cover gas sensing substrates, which is necessary for high-quality data collection to observe the sensors response to reducing or oxidising gases. However, the reduction in band gap suggests there is likely chlorine incorporation which may act as an electrical poison during gas sensing. Heteroleptic gallium alkoxide **8** would be the preferred choice of precursor as there are no Ga-Cl bonds involved in the complex. Films produced from **8**, however, were thin and patchy despite being crystalline after annealing. It is likely that coverage on a gas sensing substrate would not be sufficient for testing.

The likely varying film composition across gallium oxide films deposited from **2**, **3** and **5** and also the thin patchy nature of the films deposited from **8** and **11a** make accurate analysis difficult for the resultant gallium oxide thin films. Further testing and analysis is required for complete characterisation of this series of thin films.

Chapter 4 explores single-source precursor routes to indium oxide thin films. Additionally the effect of nitrogen doping on metal oxide materials is explored for the purposes for lowering the material's band gap, making it suitable for visible light

photocatalysis. *In situ* routes to deposit indium oxide thin films are utilised. Indium tris(amides) are reacted with stoichiometric quantities of alcohol before being used as an AACVD precursor in the aim to dope small quantities of nitrogen into the In_2O_3 lattice. Films were characterised and their properties tested. The effect of varying temperature, solvent used and substrate are also explored. Films were additionally tested for their contact angle to water droplets before and after UV irradiation as well as their viability to evolve hydrogen from water under solar conditions.

3.6. Experimental

3.6.1. General Procedures – AACVD

The AACVD setup as previously described in Chapter 1.2.1.7 was used for the deposition of the gallium oxide precursors. Nitrogen (99.99%) was obtained from BOC and used as supplied. Depositions were obtained on SiCO coated float-glass and quartz substrates. Prior to use, the glass substrates were cleaned using propan-2-ol and acetone and then dried in air. Glass substrates of *ca.* 90 mm x 45 mm x 4 mm and quartz substrates of *ca.* 10 mm x 10 mm x 2 mm were used.

The precursor was dissolved in 30 ml of solvent under Schlenk conditions before being vaporized at room temperature by use of a PIFCO ultrasonic humidifier. This produced an aerosol of the precursor in the solvent used. Precursors included: $[\text{GaCl}(\text{OCH}_2\text{CH}_2\text{NMe}_2)_2]$ (**2**) (0.42 g, 1.50 mmol); $[\text{GaCl}(\text{OCH}_2\text{CH}_2\text{NEt}_2)_2]$ (**3**) (0.50 g, 1.50 mmol); $[\text{GaCl}(\text{OCH}_2\text{CH}_2\text{CH}_2\text{NMe}_2)_2]$ (**5**) (0.46 g, 1.50 mmol); $[\text{Ga}(\text{OCH}_2\text{CH}_2\text{NMe}_2)_2(\text{OMe})]$ (**8**) (0.50 g, 1.50 mmol); $[\text{GaCl}(\text{OCH}_2\text{CH}_2\text{NMe}_2)(\text{O}^t\text{Bu})]$ (**11a**) (0.54 g, 1.5 mmol).

Two way taps were used to divert the nitrogen carrier gas through the bubbler. The aerosol was carried into the reactor in a stream of nitrogen gas through a brass baffle to obtain a laminar flow. Depositions were carried out by heating the horizontal bed reactor to the required temperature before diverting the nitrogen line through the aerosol and hence to the reactor. Depositions were carried out in dichloromethane and toluene at a flow rate of 1.0 Lmin^{-1} over a range of substrate temperatures (450 – 550 °C). The

total time for the deposition process was in the region of 30 min – 1.5 h. At the end of the deposition the nitrogen flow through the aerosol was diverted, and only nitrogen passed over the substrate. The glass substrate was allowed to cool with the graphite block to less than 100 °C before it was removed. Coated glass substrates were handled and stored in air. Quartz sheets were further annealed overnight at 1000 °C. Large pieces of glass (*ca.* 4 cm x 2 cm) were used for X-ray powder diffraction and reflectance/transmittance analysis. The coated glass substrate was cut into *ca.* 1 cm x 1 cm squares for subsequent analysis by SEM, EDX and WDX analysis. Quartz sheets were used as-deposited for all analysis.

3.6.2. Analysis Techniques

Thermal gravimetric analysis was conducted on a Netzsch system between 20 – 600 °C. Samples (*ca.* 10 -50 mg) were run under air sensitive conditions in a sealed aluminium pans. X-ray powder diffraction patterns were measured on a Bruker AXS D8 diffractometer using $\text{CuK}\alpha_1$ radiation in glancing angle mode (5° incident angle). The films on the glass substrates were indexed using Unit Cell and compared to database standards. SEM was carried out on a JEOL 6301 filament scanning electron microscope and films were sputtered with gold for 30 seconds prior to analysis. UV/Vis/Near IR transmittance and reflectance spectra were obtained on a Perkin Elmer Lambda 950 spectrometer using as air background and recorded between 250 and 2000 nm.

Chapter 4

Chemical Vapour Deposition of Indium Oxide Thin Films

4. CVD of Indium Oxide Thin Films

Chapter 3 described the deposition of gallium oxide thin films from precursors synthesised in Chapter 2. These films produced amorphous transparent Ga₂O₃ films on glass and quartz substrates and after annealing at 1000 °C crystalline β -phase Ga₂O₃ films were formed. This chapter describes the synthesis and characterisation of single-source indium alkoxide precursors to indium oxide, as well as the reactor conditions used to deposit thin films of indium oxide. The effects of nitrogen doping in metal oxides for the reduction of their bands gaps are explored for their use as water spitting photocatalysts. Followed by the review are the results and discussion of *in situ* precursor routes and their use for the deposition of indium oxide thin films using AACVD. The films were characterised and functional tests are described.

4.1. Precursors to indium oxide

Thin films of indium oxide, In₂O₃, are usually found in the cubic bixeyte structure. Unlike Ga₂O₃, at room temperature In₂O₃ is an electrical conductor and finds use as a TCO material, although it is usually doped with tin to enhance its electrical conductivity.¹⁴⁵ However, this section is solely concerned with the synthesis and characterisation of single-source precursors to undoped indium oxide, in addition to the conditions used to deposit thin films of indium oxide.

4.1.1. Monodentate alkoxides

Compared to simple gallium alkoxides, the structure and reactivity of simple indium alkoxides is less well researched. “[In(O^{*i*}Pr)₃]” was first reported in 1976 as a tetramer, supposedly analogous to [Ga(O^{*i*}Pr)₃]₄.¹⁴⁶ However, subsequent studies revealed it actually existed as an oxo-centred cluster of the type [In₅(μ_5 -O)(μ_3 -O^{*i*}Pr)₄(μ_2 -O^{*i*}Pr)₄(O^{*i*}Pr)₅] (Figure 4.1), but the origin of the central oxide anion was unknown.¹⁴⁷ Similarly to the gallium compound [Ga(O^{*i*}Pr)₃]₄, “[In(O^{*i*}Pr)₃]” was used as a starting point to synthesise a range of simple indium alkoxides by alkoxide/alcohol exchange.

Although later work carried out by Bradley *et al.* indicated that the alkoxides synthesised from “[In(O^{*i*}Pr)₃]₄” may also be complex oxy-alkoxides, rather than a simple oligomer of [In(OR)₃].

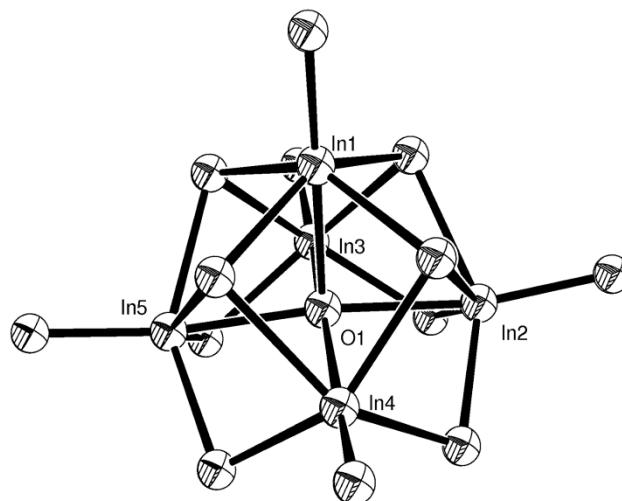
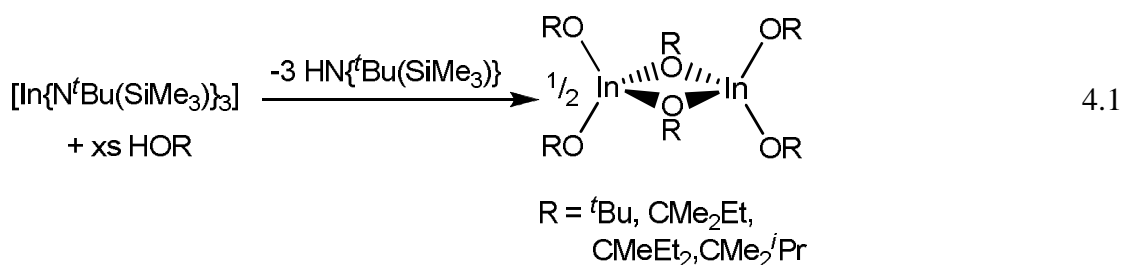


Figure 4.1. ORTEP diagram of the indium cluster [In₅(μ₅-O)(μ₃-O^{*i*}Pr)₄(μ₂-O^{*i*}Pr)₄(O^{*i*}Pr)₅]. Hydrogen and carbon atoms omitted for clarity; the oxo anion (O1) is at the centre of the cluster.¹⁴⁷

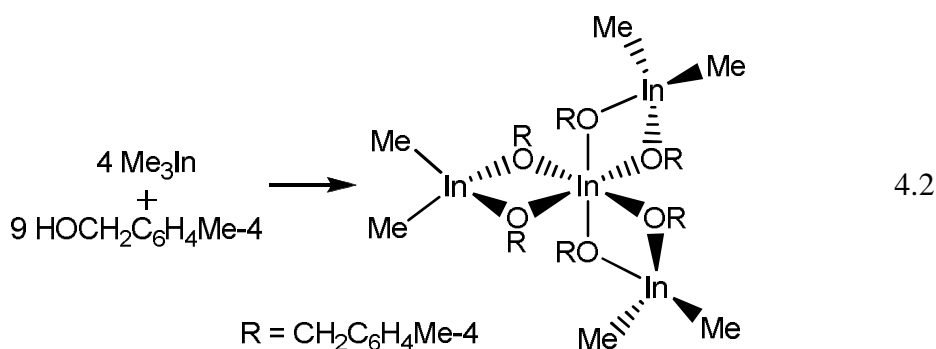
Nonetheless, Cantalini *et al.* used “[In(O^{*i*}Pr)₃]” as a single-source precursor to thin films of In₂O₃ using the sol-gel technique.¹⁴⁸ The indium precursor was dissolved in ethanol, dropped onto a sapphire substrate and spun at 1000-3000 rpm for 20-60 seconds. After baking at 120 °C for 30 minutes, the films were annealed at 500 °C to induce crystallisation. XRD analysis of the annealed film revealed that cubic In₂O₃ had been formed, but XPS data indicated that the film was oxygen-deficient.

The use of amide/alcohol exchange as a technique for synthesising homoleptic indium alkoxides was restricted owing to the fact that simple homoleptic indium amide compounds, e.g. [In(NMe₂)₃]₂, were not readily available. However, Hoffman *et al.* used the bulky indium amides [In{N^{*t*}Bu(SiMe₃)₃}₃] and [In(tmp)₃] (tmp = 2,2,6,6-tetramethylpyrrolidide) as starting materials for the synthesis of a range of homoleptic indium alkoxides by amide/alkoxide exchange.¹⁴⁹ This led to the formation of dimeric homoleptic indium alkoxide precursors from [In{N^{*t*}Bu(SiMe₃)₃}₃], rather than [In(tmp)₃] on economic grounds (Equation 4.1).¹⁰⁴



$[\text{In}(\text{OCMe}_2\text{Et})_3]_2$ was chosen as a precursor owing to its low melting point (40-41 °C). Deposition of In_2O_3 on glass and silicon substrates was accomplished using an LPCVD process whereby the precursor was heated to 50 °C and the substrate was heated to temperatures between 300 and 500 °C. As is typical for the deposition of thin films of In_2O_3 , the films deposited at all temperatures were crystalline as measured by XRD, with cubic In_2O_3 being observed in all cases. RBS spectra indicated that stoichiometric In_2O_3 had been formed and XPS data showed that no carbon contamination was present.

Another indium alkoxide was synthesised by Carmalt *et al.* who reacted InMe_3 with 4-methylbenzylalcohol in a 4:9 ratio (Equation 4.2).¹⁵⁰ Analogously to the gallium case, $[\{\text{Ga}(\text{OR})_3\}\{\text{GaMe}(\text{OR})_2\}_3]$ ($\text{R} = \text{CH}_2\text{C}_6\text{H}_4\text{Me-4}$), a tetrameric molecule was isolated with the ‘core’ of the molecule containing an M:O ratio of 4:6, ideal for In_2O_3 . However, the biggest difference to the gallium analogue was found on the outer metal atoms; whereas only one methyl group was retained in the gallium compound, both methyl groups were retained for the indium precursor.

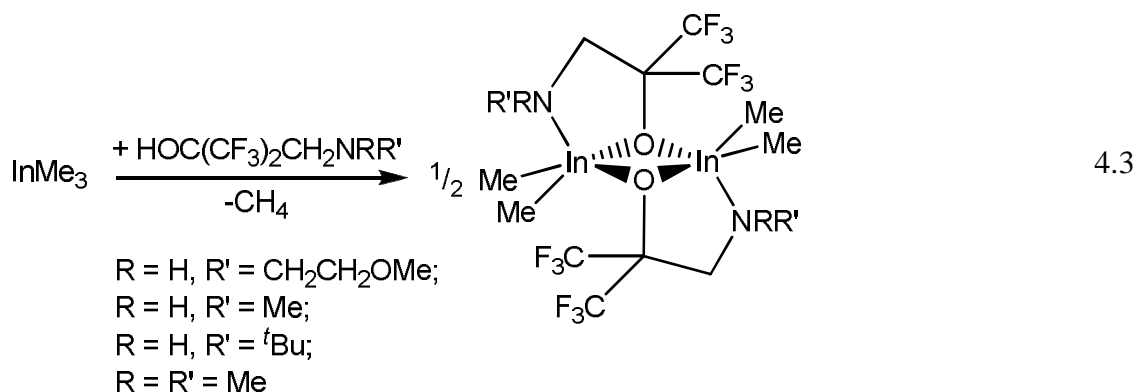


TGA of compound $[\{\text{In}(\text{OR})_3\}\{\text{InMe}_2(\text{OR})_3\}]$ ($\text{R} = \text{CH}_2\text{C}_6\text{H}_4\text{Me-4}$), indicated that decomposition to In_2O_3 was a facile process, but this was not borne out by CVD experiments. A black film was deposited on a glass substrate at 600 °C which was assigned to metallic indium on the basis of XRD analysis. Further investigations

revealed that decomposition of compound $[\{\text{In}(\text{OR})_3\}\{\text{InMe}_2(\text{OR})\}_3]$ occurred before the melting point, which precluded transport of the precursor into the CVD reaction chamber. No further CVD experiments were conducted.

4.1.2. Donor-functionalised alkoxides

Much like the situation for simple alkoxide compounds, there has been less research carried out into donor-functionalised alkoxide compounds of indium than gallium. Indeed, the paucity of suitable indium amide starting materials has resulted in InMe_3 being selected as the starting material of choice for the synthesis of donor-functionalised alkoxide CVD precursors. Chi *et al.* reacted a series of fluorinated donor-functionalised alcohols with InMe_3 , affording a range of dimeric 5-coordinate indium complexes (Equation 4.3).

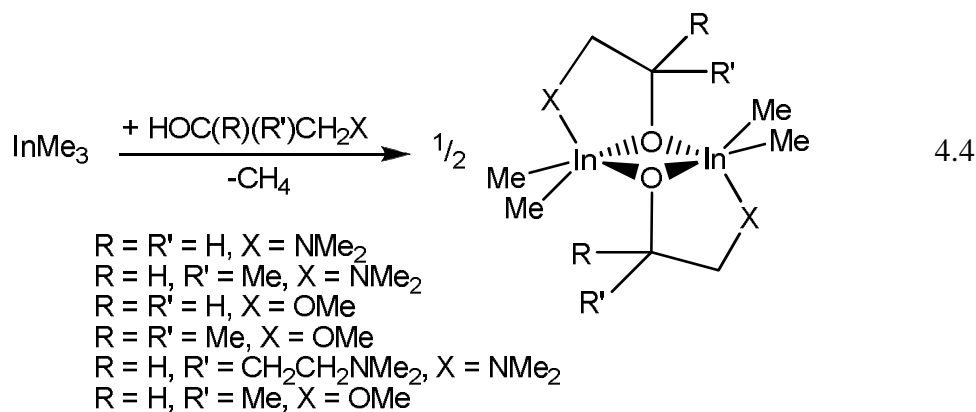


Even though $[\text{InMe}_2(\text{OC}(\text{CF}_3)_2\text{CH}_2\text{NH}(\text{CH}_2\text{CH}_2\text{OMe}))]_2$ had two further ‘arms’ which were capable of coordination to the indium centre, single crystal X-ray analysis revealed that the ‘arms’ were dangling and did not coordinate. It also revealed that a 4-membered In_2O_2 ring was present at the heart of the molecule, analogous to mono(donor-functionalised alkoxide) complexes of gallium with their Ga_2O_2 rings. $[\text{InMe}_2(\text{OC}(\text{CF}_3)_2\text{CH}_2\text{NHMe})]_2$ was selected for LPCVD experiments: deposition occurred on quartz and silicon substrates at temperatures between 400-500 °C. The substrate was heated to 145 °C and the system pressure was maintained at 0.3 torr. All films were crystalline as-deposited, with cubic In_2O_3 being the phase formed, although the degree of crystallinity increased with deposition temperature. XPS data indicated that a small amount of carbon was present as an impurity, but no fluorine could be detected. The In:O ratio, as measured by XPS, showed the films to be very oxygen-

deficient but the more accurate RBS experiments indicated that stoichiometric In_2O_3 had been formed.

The use of non-fluorinated indium alkoxides as CVD precursors to indium oxide was initially developed by Carmalt *et al.* in 2007.¹⁵⁰ InMe_3 and a large excess of alcohol were reacted in toluene for 60 minutes, then the reaction mixture was passed straight into the CVD chamber using AACVD. Deposition occurred on glass at a temperature of 550 °C, affording brown films of cubic In_2O_3 as measured by XRD. WDX data indicated that most of the films were formed of stoichiometric In_2O_3 , with the remainder being sufficiently thin that X-ray breakthrough to the underlying substrate was observed, adversely affecting the WDX analysis. XPS data did not indicate any carbon or nitrogen contamination of the films.

The formation of $[\text{InMe}_2(\text{OR})]_2$ was assumed to take place *in situ* prior to the solution being passed into the CVD reactor. To confirm this, compounds outlined in Equation 4.4 were synthesised and fully characterised (the first 4 compounds in Equation 4.4 were used for CVD) by various spectroscopic techniques.



Single crystal X-ray diffraction of the isolated compounds confirmed that in each case, a dimeric indium mono(alkoxide) had been formed (Figure 4.2). $[\text{InMe}_2(\text{OCH}(\text{Me})\text{CH}_2\text{OMe})]_2$ was subsequently isolated and also fully characterized, but was not used for CVD purposes.⁷⁰ Interestingly, $[\text{InMe}_2(\text{OCH}(\text{CH}_2\text{NMe}_2)_2)]_2$, where each ligand contained two ‘arms’ exhibited an unusual coordination mode whereby both ‘arms’ coordinated to the indium centres. This is in contrast to compound $[\text{InMe}_2(\text{OC}(\text{CF}_3)_2\text{CH}_2\text{NH}(\text{CH}_2\text{CH}_2\text{OMe}))]_2$ which had a dangling ‘arm’, although this oddity can probably be put down to the geometry of the ligand: for

$[\text{InMe}_2(\text{OC}(\text{CF}_3)_2\text{CH}_2\text{NH}(\text{CH}_2\text{CH}_2\text{OMe}))]_2$ the alkoxide occurs at the end of the ligand whereas for $[\text{InMe}_2(\text{OCH}(\text{CH}_2\text{CH}_2\text{NMe}_2)\text{CH}_2\text{NMe}_2)]_2$, the alkoxide occurs in the middle of the ligand. This enables the bridging alkoxide to coordinate to both indium centres in $[\text{InMe}_2(\text{OCH}(\text{CH}_2\text{CH}_2\text{NMe}_2)\text{CH}_2\text{NMe}_2)]_2$ because it has a Lewis base on either side, but for compound $[\text{InMe}_2(\text{OC}(\text{CF}_3)_2\text{CH}_2\text{NH}(\text{CH}_2\text{CH}_2\text{OMe}))]_2$ only one side of the bridging alkoxide has a Lewis base therefore it cannot reach round and coordinate the second Lewis base to an indium centre.

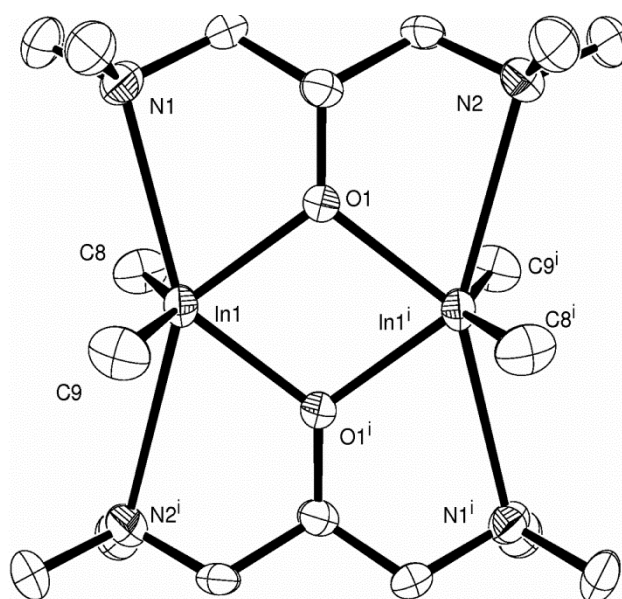
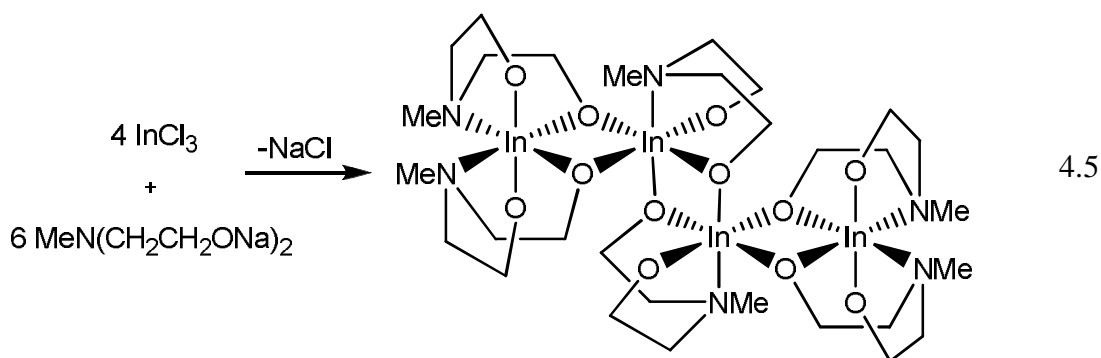


Figure 4.2. An ORTEP diagram of the indium alkoxide $[\text{InMe}_2(\text{OCH}(\text{CH}_2\text{CH}_2\text{NMe}_2)\text{CH}_2\text{NMe}_2)]_2$ showing an unusual coordination mode whereby both “arms” bind to different metal centres. H atoms omitted for clarity.¹⁹

These results are consistent with the case for donor-functionalised gallium alkoxides, where the room temperature reaction of GaMe_3 with an excess of alcohol only leads to the formation of mono(alkoxide) gallium compounds. Heating a mixture of GaMe_3 and excess donor-functionalised alkoxide to $110\text{ }^\circ\text{C}$ results in the formation of a 1:1 mixture of mono- and bis(alkoxide) gallium compounds, and the same is true for indium.¹⁵¹ However, under the reaction conditions inside the CVD flask, the *in situ* formation of indium mono(alkoxides) is the most likely outcome. To date, no bis(donor-functionalised alkoxide) indium compounds have been isolated and fully characterized.

The reaction of InCl_3 with 1.5 equivalents of freshly prepared $\text{MeN}(\text{CH}_2\text{CH}_2\text{ONa})_2$ led to the formation of an indium tris(alkoxide) complex (Equation 4.5).¹⁵² The indium tris(alkoxide) outlined in Equation 4.5 exists as a dimer with two $[\text{InL}_2]$ anions surrounding two central $[\text{InL}]$ cations. One of the ‘arms’ of the ligand on the $[\text{InL}]$ cation bridges to the other $[\text{InL}]$ cation, forming the expected In_2O_2 ring at the centre of the molecule. The two $[\text{InL}_2]$ anions bridge twice to one $[\text{InL}]$ cation, one ‘arm’ from each ligand forming the bridge. This results in the overall formation of an In_4 -containing molecule which can best be described overall as existing in a zig-zag geometry. This is in contrast to the gallium analogue (Section 2.2) where the molecule formed a star-shape with one central Ga^{3+} cation and three $[\text{GaL}_2]$ anions.



The deposition of films of In_2O_3 from the above indium tris(alkoxide) by hydrolysis preceded spin-coating onto a glass or silicon substrate which was dried at $120\text{ }^\circ\text{C}$, before repeating the spin-coating several times to increase the thickness of the film. $[\text{In}(\text{OH})_3]$ was identified as the hydrolysis product. Annealing at $500\text{-}700\text{ }^\circ\text{C}$ completed the process. The indium oxide film obtained was analysed by XRD, which confirmed the cubic phase of In_2O_3 had been formed. EDX analysis confirmed that stoichiometric In_2O_3 had been formed.

Nitrogen doping of indium oxide has been reported by Reyes-Gil *et al.*⁴⁵ By incorporating 4-6.4% of nitrogen into the indium oxide lattice, the band gap is reduced from 3.5 eV to 2.0 eV. This narrowing in band gap is similar to that of $\text{TiO}_2\text{:N}$ which is the most studied photocatalyst. TiO_2 was first reported to split water to produce H_2 and O_2 after UV photoexcitation, by Fujishima and Honda.¹⁵³ Since then, wide band gap semiconductor *n*-type metal oxides have been extensively analyzed for water splitting due to their good stability, nontoxicity, low cost, and catalytic activity. However, the

overall efficiency of metal oxide semiconductors is still too low for commercial use due in part to their poor match to the solar spectrum.

Results using anion doping appear to be promising for reducing the large band gap of metal oxides.¹⁵⁴⁻¹⁵⁷ In particular, nitrogen doping has attracted much attention for the development of visible-light photocatalysts. The most widely investigated N-doped materials to date is $\text{TiO}_{2-x}\text{N}_x$,¹⁵⁷⁻¹⁶⁰ in which the optical absorption becomes red-shifted into the visible range (> 380 nm), while the material retains the stability of the host metal oxide. $\text{TiO}_2\text{:N}$ has displayed efficient photocatalytic oxidation of organic compounds using wavelength up to 550 nm.¹⁵⁷ While there is agreement that N-doping of metal oxides leads to visible-light photoactivity, there are different explanations regarding how N-doping achieves this activity. In particular, two different mechanisms have been proposed which involved either interstitial or substitutional N-doping. The interstitial N-doping is likely to be a NO_x ^{161, 162} or NH_x ¹⁶³ species, which was attributed to the visible-light response.¹⁶¹⁻¹⁶³ The photocurrent densities electrodes of $\text{In}_2\text{O}_3\text{:N}$ reported by Reyes-Gil *et al.* are at least double those of undoped In_2O_3 and approximately 50 times better than $\text{TiO}_2\text{:N}$ electrodes in the visible region.

4.2. Results and Discussion

4.2.1. CVD of indium oxide thin films

A range of indium silyl amide precursors and alcohols were explored in conjunction with a variety of deposition techniques. All conditions used are outlined in Table 4.1. Indium precursors included $[\text{In}\{\text{N}(\text{SiMe}_3)_2\}_3]$, $[\text{In}\{\text{NPh}(\text{SiMe}_3)\}_3]$ and $[\text{In}\{\text{N}^t\text{Bu}(\text{SiMe}_3)\}_3]$ and alcohols HOMe , HO^tBu and $\text{HOCH}_2\text{CH}_2\text{NMe}_2$, which were allowed to mix for 30 min prior to deposition. Indium precursors were synthesised following literature preparations by Hoffman *et al.*¹⁶⁴ Films were deposited onto glass or metal (stainless steel or titanium) coupon substrates using either toluene or hexane as the solvent used for solutions to aerosols. Depositions occurred over temperatures between 350 -550 °C using an N_2 carrier gas at 1 Lmin^{-1} .

To incorporate nitrogen into indium oxide thin films to lower the materials band gap to a suitable energy that corresponds to the visible region, a related *in situ* amide/alcohol exchange route was employed,¹⁰⁴ outlined previously in Section 4.1.1. A precise 1:3 ratio of indium precursor to alcohol was employed in order to dope small quantities of nitrogen into the final In_2O_3 thin film.

Indium oxide thin films deposited using $[\text{In}\{\text{N}(\text{SiMe}_3)_2\}_3]$ or $[\text{In}\{\text{NPh}(\text{SiMe}_3)\}_3]$ with a combination of other conditions resulted in very thin, opaque films that were easily removed with tissue paper. Coverage of the substrate was poor, sometimes with little or no deposition on the bottom substrate plate and coverage on the top plate.

The lack of deposition on the bottom plate is associated with the thermophoretic effect where precursor molecules which have undergone gas phase nucleation, upon entering the CVD chamber, the larger particles cannot pass through the diffusion layer and so ‘bounce’ off of the hotter bottom plate and settle onto the cooler top plate.¹⁵ Films were grown at a lower temperature of 350 °C in attempt to overcome this phenomenon however the resultant films had the same morphology as before. An increase in temperature to 550 °C was also explored in attempt to obtain a crystalline film, however the same results were obtained. Also using an excess of alcohol was investigated but the same film types were seen.

Table 4.1. Conditions used for CVD of indium oxide thin films.

Indium Source	Oxygen Source	Substrate	Solvent	T [°C]	Film description	XRD
[In{N(SiMe ₃) ₂ }] ₃	3 HO ^t Me	SiCO coated float glass	Toluene	350	Thin, opaque, powdery	Amorphous
				450		
	3 HO ^t Bu			350		
				450		
				550		
	3 HOCH ₂ CH ₂ NMe ₂			450		
				Hexane		
[In{NPh(SiMe ₃) ₂ }] ₃	3 HOCH ₂ CH ₂ NMe ₂	Toluene	450			
[In{N ^t Bu(SiMe ₃) ₂ }] ₃	3 HOCH ₂ CH ₂ NMe ₂	SiCO coated float glass	Toluene	350	Thin, transparent adherent film	Crystalline
				400		
				450		
				500		
				550		
			Hexane	350		
				400		
				450		
				500		
				550		
		Titanium	Toluene	450		
					Hexane	
			Steel		Toluene	
					Hexane	

Choy reports that intermediate species in the reactor can undergo homogeneous gas phase reactions where the intermediate species undergoes subsequent decomposition and/or chemical reaction, forming powders and volatile by-products.¹⁴ The powder can be collected on the substrate surface and can act as crystallisation centres, and the by-products are transported away from the deposition chamber. The deposited film can have poor adhesion. The films in these reactions are likely to have undergone some degree of homogeneous polymerisation gas phase reaction before settling on the top plate due to thermophoretic effects. No reaction would have occurred between substrate

and reactant and so the films were powdery and non adherent. GED studies have confirmed that monodentate alkoxides do not stabilise metal centres in the gas phase.⁷⁴

Donor-functionalised alcohols have been observed to stabilise the gas phase complex⁷⁴ in AACVD reactions and have resulted in crystalline films.^{19, 104} By using donor-functionalised alcohols the indium compound in the gas phase would be more stable as a monomer and less likely to polymerize. $[\text{In}\{\text{N}(\text{SiMe}_3)_2\}_3]$ (dissolved in either toluene or hexane) and 3 equivalents of $\text{HOCH}_2\text{CH}_2\text{NMe}_2$ were mixed *in situ* before vaporisation and then transferred to the chamber. This however also resulted in top plate deposition. It is likely that, as seen with other group 13 tris(alkoxides), the product can form cluster complexes of multiple metal centres which would not decompose and react further with the substrate.³⁰ All films were found to be amorphous from XRD analysis and SEM analysis (Section 4.2.4, Figure 4.7) and EDAX were employed, however further analysis was not explored.

$[\text{In}\{\text{N}^t\text{Bu}(\text{SiMe}_3)\}_3]$ was next employed with the donor-functionalised alcohol, $\text{HOCH}_2\text{CH}_2\text{NMe}_2$, for AACVD as its unsymmetrical structure could potentially increase the solubility of the compound and result in smaller dimeric compounds as previously observed by Suh *et al.*¹⁰⁴ Depositions were conducted over temperatures of 350-550 °C on glass substrates which resulted in adherent transparent thin films. Overall coverage varied between samples with 450 °C found to give the maximum surface coverage, therefore this temperature was employed with use on metal coupon substrates which were then tested for their hydrogen evolution. Films were not removed using tissues or scotch tape, nor were they removed using a brass or steel stylus.

4.2.2. X-ray powder diffraction studies

The $\text{In}_2\text{O}_3:\text{N}$ thin films deposited by AACVD from $[\text{In}\{\text{N}^t\text{Bu}(\text{SiMe}_3)\}_3]$ *via* the conditions outlined in were crystalline at all deposition temperatures including temperature ranges from 350-550 °C. X-ray diffraction patterns for the films indicated that they were In_2O_3 cubic phase film, as expected for these films.¹⁹ A typical In_2O_3 XRD spectrum is shown in Figure 4.3. Films deposited by other conditions in Table 4.2 were found to be amorphous.

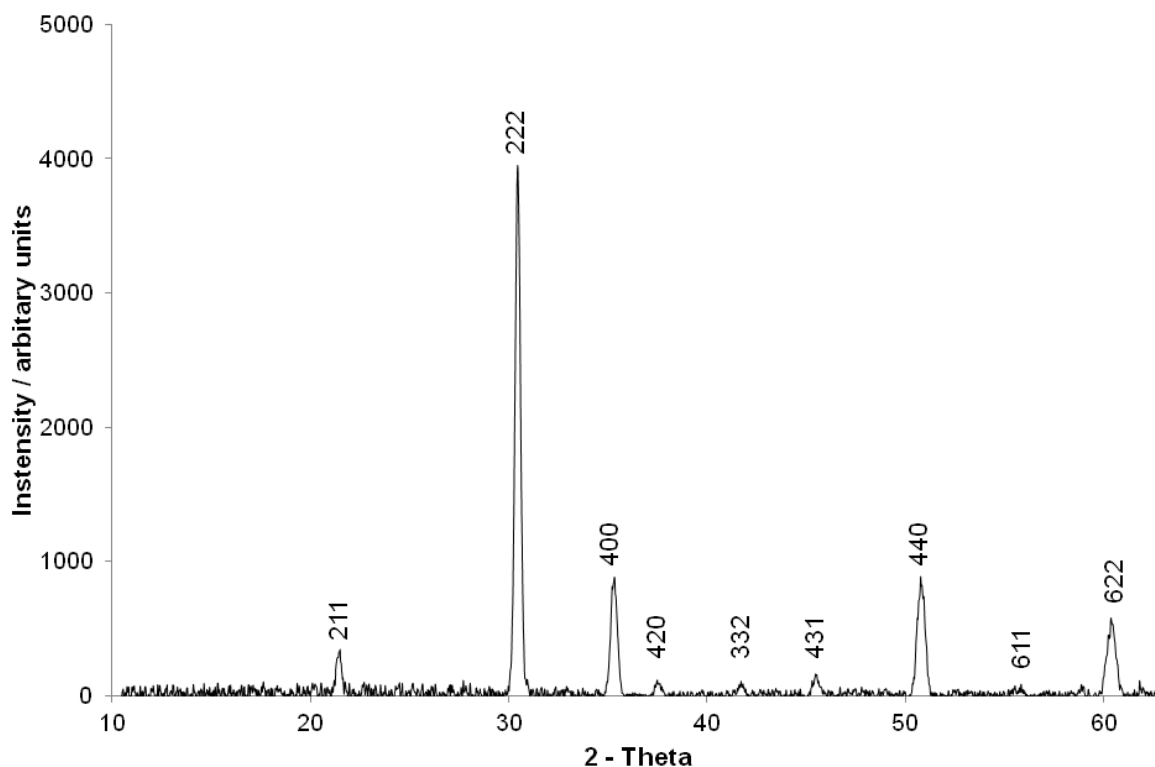


Figure 4.3. XRD pattern of $\text{In}_2\text{O}_3:\text{N}$ thin film deposited by hexane at 450°C on SiCO coated float glass. A typical X-ray powder diffraction spectrum obtained for In_2O_3 thin films.

4.2.3. Film Composition

EDAX analysis revealed that all samples contained indium and elevated quantities of oxygen. The precise ratio of In:O was not obtained due to breakthrough of the underlying glass. Nitrogen incorporation could also not be determined by EDAX as this technique cannot be used to accurately detect lighter elements. XPS was performed on some samples to determine an accurate composition of the nitrogen-doped indium oxide thin films. The results of these are displayed in Table 4.2. All samples were confirmed to have a 1:1.5 ratio of indium to oxygen by XPS, confirming the In_2O_3 formula and have varying amounts of nitrogen incorporation. In_2O_3 films deposited using toluene at 550°C did not show a clear nitrogen peak and the percentage incorporation could not be determined.

Table 4.2. Thin film compositions, optical properties and electronic properties of In_2O_3 thin films formed from the reaction of $[\text{In}\{\text{N}^t\text{Bu}(\text{SiMe}_3)\}_3]$ and 3 $\text{HOCH}_2\text{CH}_2\text{NMe}_2$ and deposited on SiCO coated float glass.

Solvent	T [°C]	XPS elemental composition	XPS nitrogen incorporation [atom %]	Transmittance in visible region %	Band gap [eV]	Sheet resistance [$\Omega \square^{-1}$]
Hexane	400	$\text{In}_2\text{O}_3:\text{N}$	2.94	64	2.9	92
Hexane	450	$\text{In}_2\text{O}_3:\text{N}$	1.52	79	3.1	93
Toluene	450	$\text{In}_2\text{O}_3:\text{N}$	5.52	36	3.1	114
Toluene	550	$\text{In}_2\text{O}_3:\text{N}$	Unknown	33	3.1	192

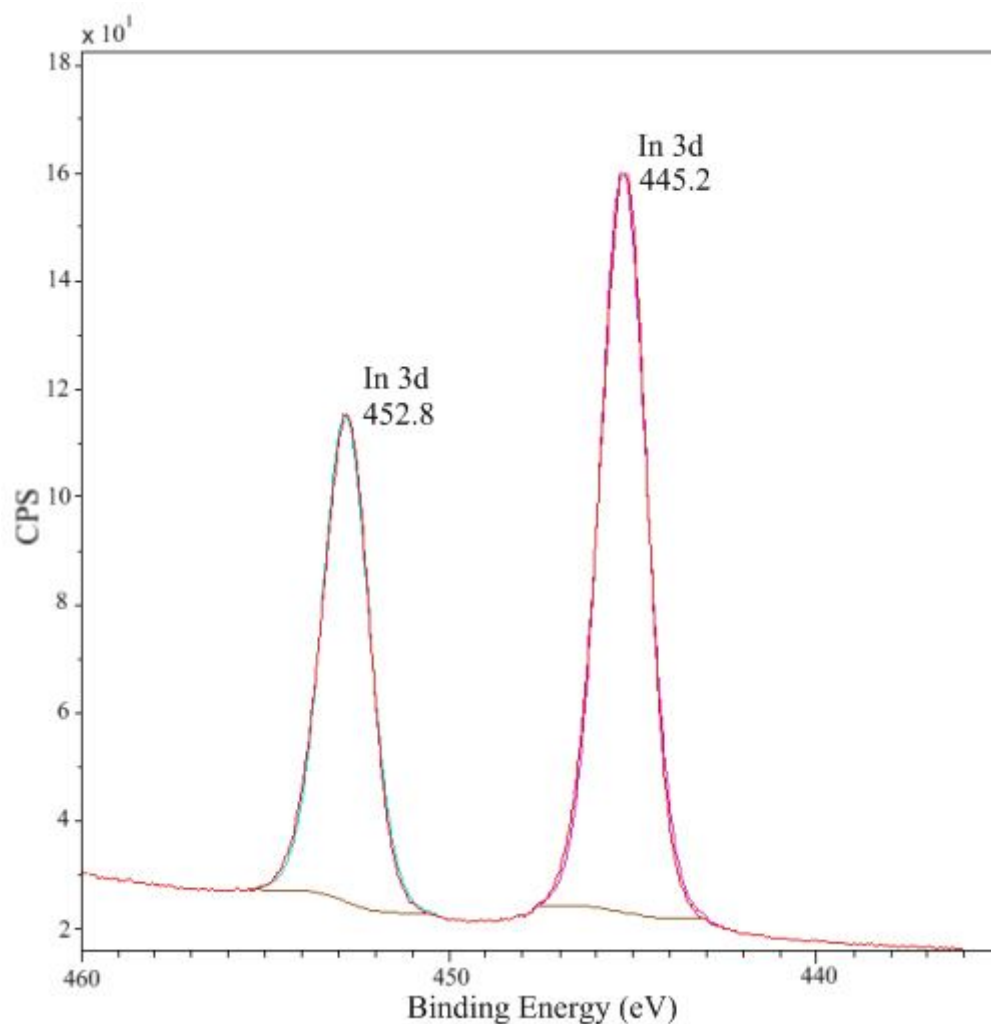


Figure 4.4. Indium XPS 3d peaks from a sample of nitrogen-doped indium oxide formed from the reaction of $[\text{In}\{\text{N}^t\text{Bu}(\text{SiMe}_3)\}_3]$ and 3 $\text{HOCH}_2\text{CH}_2\text{NMe}_2$ with hexane, at 450 °C on SiCO float glass.

The XPS peak profiles for a sample of $\text{In}_2\text{O}_3:\text{N}$ film on glass observed after sputtering were consistent with one environment for indium, oxygen and nitrogen. Binding energies were observed at 445.2 and 452.8 eV, corresponding to the $\text{In } 3d_{5/2}$ $3d_{3/2}$ peaks of In_2O_3 , respectively (Figure 4.4) and in a 1 : 1.5 ratio with each other, which fit with peaks previously reported.¹⁶⁵

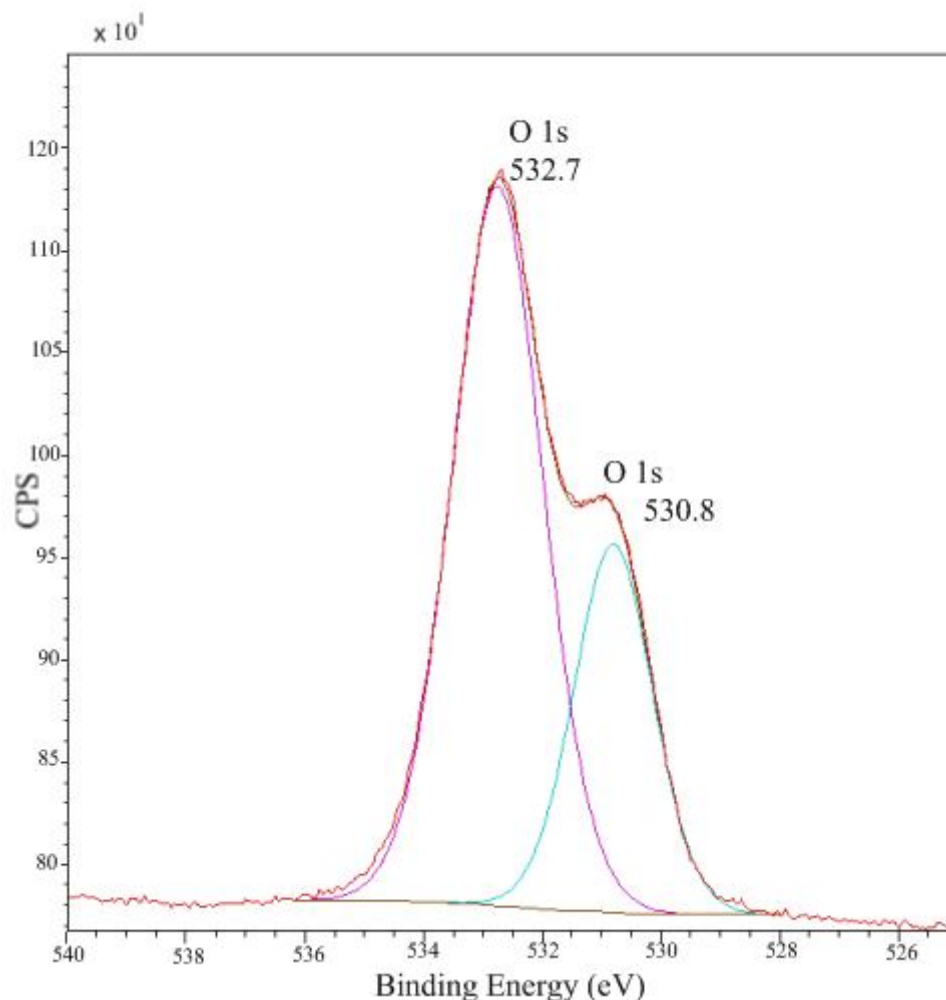


Figure 4.5. Oxygen 1s XPS peaks from a sample of nitrogen-doped indium oxide formed from the reaction of $[\text{In}\{\text{N}^t\text{Bu}(\text{SiMe}_3)\}_3]$ and 3 $\text{HOCH}_2\text{CH}_2\text{NMe}_2$ with hexane, at 450 °C on SiCO float glass.

The O 1s peaks (Figure 4.5) of the same sample can be deconvoluted into two components: two Gauss-Lorentz peaks with the same FWHM of 1.7 eV for both the peaks. This is similar to reported XPS investigations on In_2O_3 samples.¹⁶⁶ The observed O 1s peak at 530.8 eV can be assigned to the lattice oxygen in crystalline In_2O_3 , and O 1s peak at 532.7 eV to adsorbed OH groups on the surface.

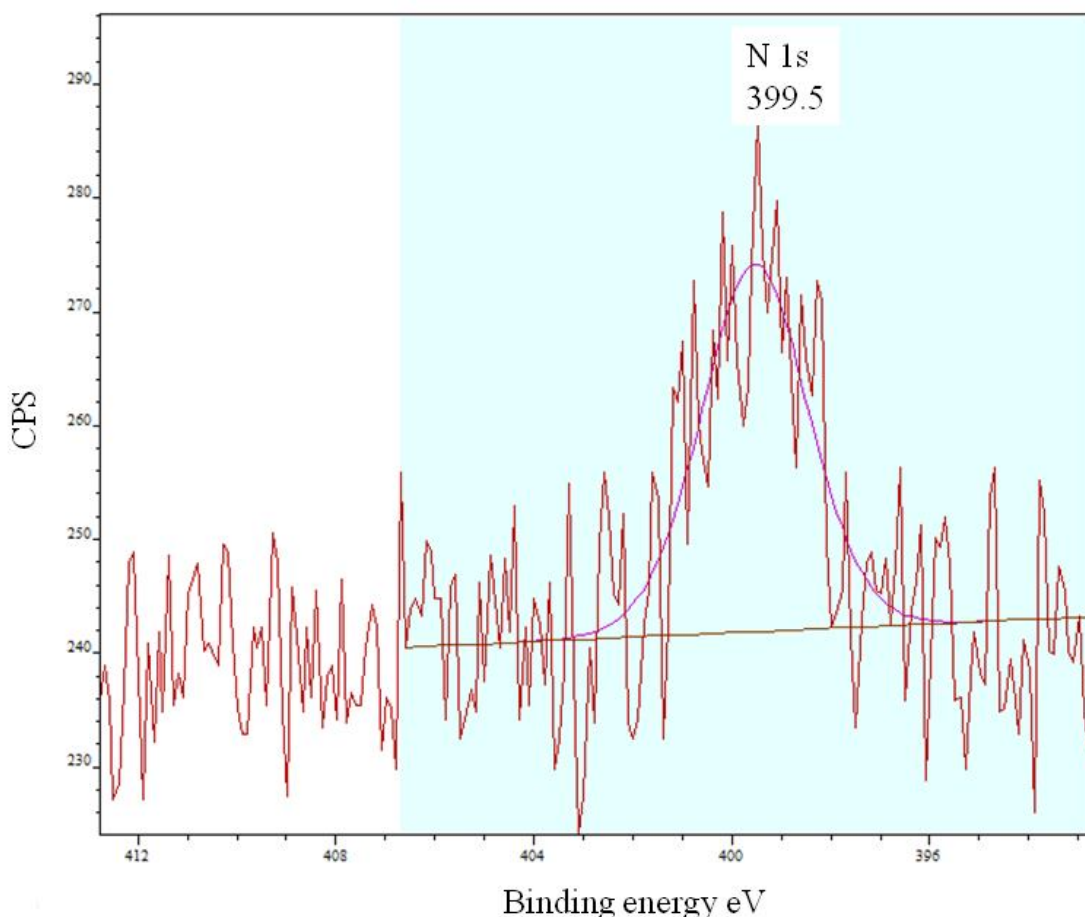


Figure 4.6. Nitrogen 1s XPS peaks from a sample of nitrogen-doped indium oxide formed from the reaction of $[\text{In}\{\text{N}^t\text{Bu}(\text{SiMe}_3)\}_3]$ and 3 $\text{HOCH}_2\text{CH}_2\text{NMe}_2$ with hexane, at 450 °C on SiCO float glass.

The N 1s peak (Figure 4.6) was observed at 399.5 eV which is consistent with nitrogen interstitial incorporation observed previously at 400.0 eV.¹⁶⁷ Substitutional nitrogen doping has been observed at 397.0 eV.¹⁶⁸⁻¹⁷⁰ Nitrogen atoms cause defects within the indium oxide framework. This has been seen in examples of nitrogen-doped titanium dioxide.¹⁶⁷ It has been shown that low concentrations of nitrogen dopant lead to higher photocatalytic activity and interstitial nitrogen is favourable when considering visible light photocatalysis as these promote oxygen vacancies more than the substitutional doping.¹⁶⁷ There was no appreciable difference between the different samples in terms of the nitrogen content. The amount of doping is slightly lower than that seen by Reyes-Gil who report 4 – 6.5 % of nitrogen doping.⁴⁵

4.2.4. Film morphology

SEM analysis was used to look at the film morphology of the indium oxide thin films deposited by AACVD. Figure 4.7 shows a typical SEM image of indium oxide thin films deposited from $[\text{In}\{\text{N}(\text{SiMe}_3)_2\}_3]$ or $[\text{In}\{\text{NPh}(\text{SiMe}_3)\}_3]$ *via* conditions outlined in Table 4.1. The films in Figure 4.7 are globular and have varying topography. This is indicative of gas phase nucleated growth which did not undergo reaction with the substrate. Particulates do not appear crystalline and do not show compact packing on the substrate.

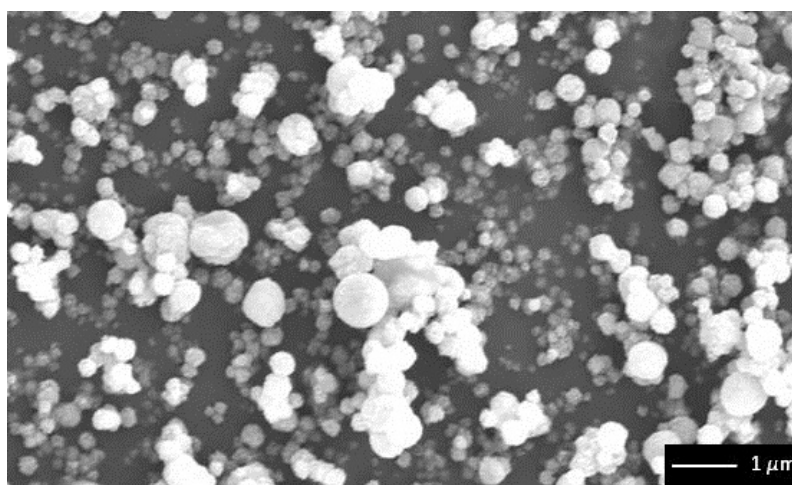


Figure 4.7. In_2O_3 thin film deposited from $[\text{In}\{\text{NPh}(\text{SiMe}_3)\}_3]$ and 3 HOME using toluene at 450 °C, deposited on SiCO coated float glass. A typical SEM of amorphous In_2O_3 deposited using $[\text{In}\{\text{N}(\text{SiMe}_3)_2\}_3]$ or $[\text{In}\{\text{NPh}(\text{SiMe}_3)\}_3]$ *via* conditions outlined in Table 4.1.

Adherent, transparent $\text{In}_2\text{O}_3\text{:N}$ films deposited from $[\text{In}\{\text{N}^t\text{Bu}(\text{SiMe}_3)\}_3]$ and $\text{HOCH}_2\text{CH}_2\text{NMe}_2$ were also investigated using SEM. In the conditions used there are three major variables that can affect morphology: temperature, solvent used and substrate. As expected, with increase in temperature, particulates become larger and more compact as higher temperatures allow for more surface reactions to occur and allow longer time for nucleation and growth. Figure 4.8 shows the SEM images deposited from $[\text{In}\{\text{N}^t\text{Bu}(\text{SiMe}_3)\}_3]$ and $\text{HOCH}_2\text{CH}_2\text{NMe}_2$ using hexane or toluene at different temperatures. Films appear to have discrete crystals that would come from

surface nucleation and growth indicative of the island growth mechanism,²³ however the morphologies observed are not identical. In₂O₃:N films deposited from hexane (Figure 4.8, a) and b)) have a needle-like morphology that become more dense with increasing temperatures. Crystallite needle width increases from 100 nm to 300 nm with increase in temperature. In₂O₃:N films deposited from toluene (Figure 4.8, c) and d)) have a cubic like morphology which does not show an increase in crystallite size with increasing temperature, however cubes do appear to have hollow structures at elevated temperatures. Different morphologies have also been observed with TiO₂^{22, 171} thin films deposited *via* AACVD by varying solvent used. It is possible that solvents complex to the precursor which then allow different initial reaction pathways during deposition onto the substrate that leads to these varying morphologies.

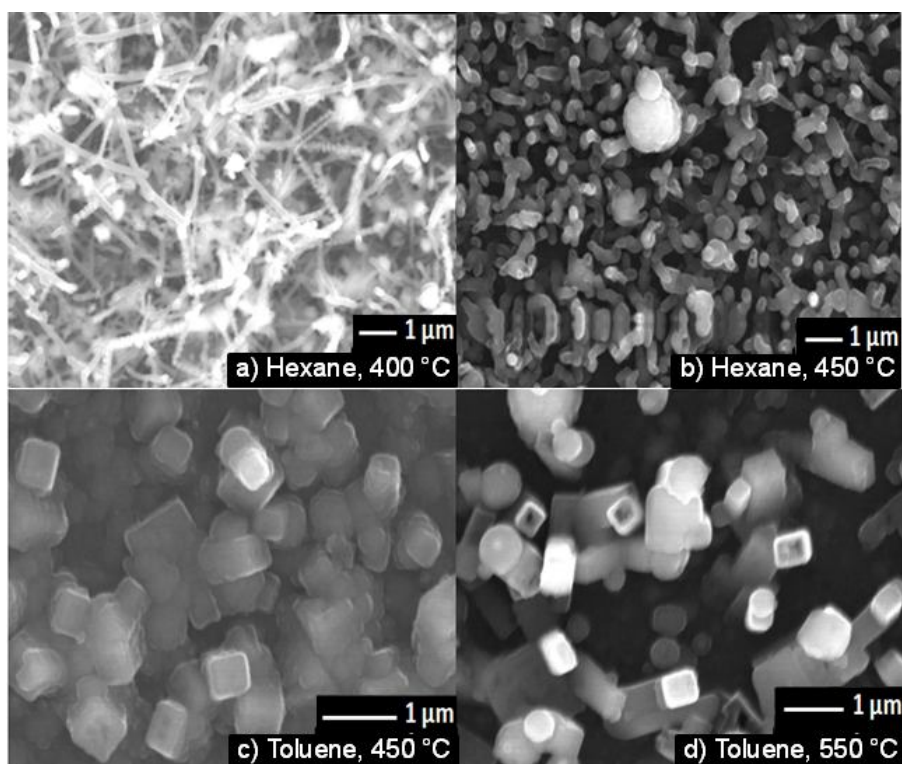


Figure 4.8. SEM images of In₂O₃:N deposited on glass at different temperatures using hexane or toluene.

In₂O₃:N thin films were also deposited on metal coupon (stainless steel and titanium) substrates for use with hydrogen evolution testing under visible light conditions. Figure 4.9 show SEM images that reveal the basic shape of the crystallites were the same under all conditions. Films deposited using hexane were smaller in size, 50 -100 nm compared

to those deposited from toluene, 300 nm which is expected as hexane AACVD depositions occur much quicker than those using toluene. The longer deposition time allows more time for a crystallite to nucleate and grow. Morphologies on metal coupons compared to those on glass (Figure 4.8) were different showing that the substrate has a directing effect during deposition of these $\text{In}_2\text{O}_3:\text{N}$ thin films.

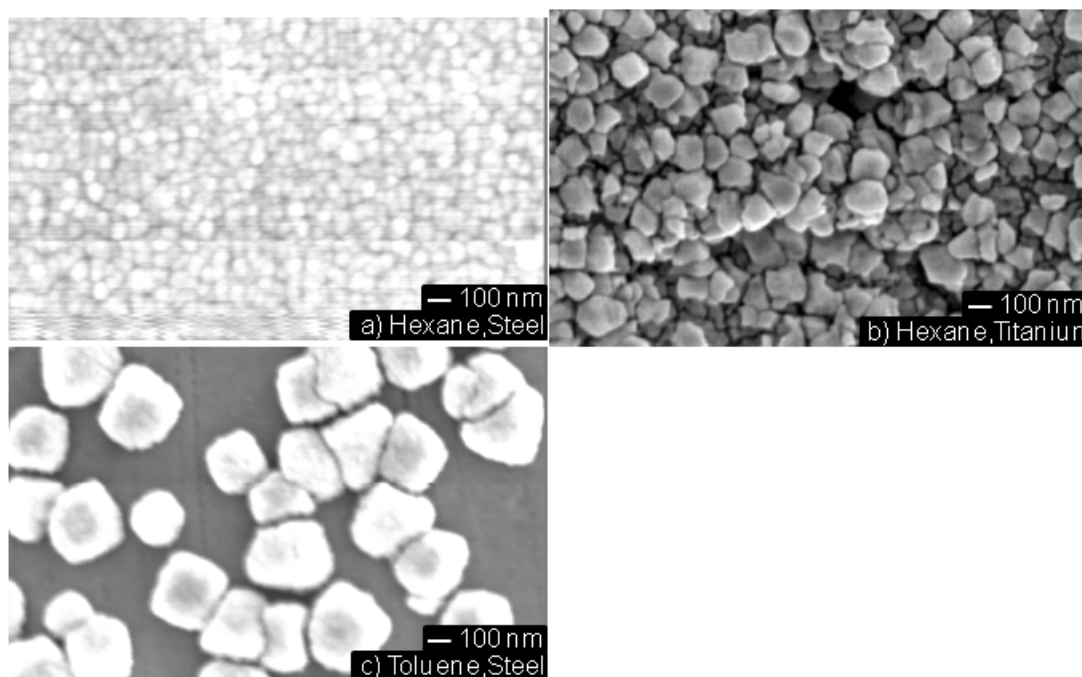


Figure 4.9. SEM images of $\text{In}_2\text{O}_3:\text{N}$ deposited on steel and titanium coupons at 450 °C using hexane or toluene.

4.2.5. Optical measurements

Optical measurements were made between 250 – 2000 nm. Glass samples were measured for their transmittance in the visible region (380-780 nm)¹⁷² and are displayed in Table 4.2. Hexane-deposited samples have transmittance of 64-79%, slightly decreased from plain glass of 80%, whereas toluene-deposited samples have a lower transmittance of 33-39%. By plotting $\alpha h\nu^{1/2}$ against $h\nu$ in eV (Tauc methodology) and extrapolating the flat part of the curve to the x-axis the value of the assumed indirect band gap can be calculated.¹⁴¹ $\text{In}_2\text{O}_3:\text{N}$ thin films were found to have band gaps of 2.9-3.1 eV which is a decrease from literature values of 3.5 eV.¹⁷³ This reduction in band

gap is a result of the interstitial incorporation of nitrogen atoms into the indium oxide lattice. Although the percentage incorporation of nitrogen is similar to that reported by Reyes-Fil et al, the reduction in band gap is nowhere near the 2.0 eV reported.⁴⁵ However a significant reduction in band gap is observed which may overlap with the region needed for visible light water splitting. Film thickness can often be calculated from optical measurements using the Swanepoel method,¹⁴³ however in the case of the samples reported in this chapter, the films were too thin and the data not sufficient for such calculations.

4.2.6. Electrical properties

The sheet resistance and resistivity of $\text{In}_2\text{O}_3\text{:N}$ films, shown in Table 4.2, were calculated from the current and voltage measured by a four point probe.¹⁷⁴ Calculations for sheet resistance are shown in Equation 4.6.

$$R_s = F \frac{V}{I} \quad 4.6$$

R_s = sheet resistance, V = voltage, I = current, F = the correction factor which for the four point probe device used was 4.53.

Films had a sheet resistance of between 92-192 Ωcm^{-1} . These values are quite high for TCO materials with ITO deposited by CVD having literature values of 23 Ωcm^{-1} .¹⁷⁵ Conductivity was not calculated as a film's thickness is required for these calculations, and those reported in this chapter are too thin for thickness to be measured. The films are expected to have poor conductivity due to the very thin nature of the films. Thicker films are required for additional calculations and are likely to increase conductivity.

4.2.7. Water contact angle measurements

Contact angle measurements to water droplets were taken before and after UV irradiation at 254 nm for 15 hours. Films suitable for photocatalysis are expected to have increased contact angles and become superhydrophilic after irradiation as they

decompose surface materials.¹⁷⁶ The contact angles of a range of $\text{In}_2\text{O}_3:\text{N}$ films deposited on glass and metal coupons are displayed in Table 4.3.

Films deposited using hexane were shown to have contact angles to water droplets of 75-110° whereas films deposited using toluene had contact angles of 40 -100°. Hexane-deposited films were expected to have higher contact angles, from the SEM images of the films can be seen that they are rougher in appearance to those deposited by toluene and thus more hydrophobic.¹⁷⁷ Contact angles decreased after irradiation by varying amounts. Most samples showed an insignificant decrease in contact angle with the exception of In_2O_3 on titanium deposited using hexane which became notably hydrophilic with a contact angle to a water droplet of 12° (Figure 4.10). This is due to the surface becoming hydroxylated and wetting becomes easier.¹⁷¹

Table 4.3. Water contact angles of In_2O_3 samples before and after irradiation 254 nm for 15 hours

Sample			Water contact angle [°]	
Substrate	Solvent	T [°C]	before irradiation	after irradiation
Glass	Hexane	400	103.0	100.4
		450	84.5	86.9
	Toluene	450	41.6	21.8
		550	58.2	36.1
Steel	Hexane	450	75.0	42.2
	Toluene		96.8	92.6
Titanium	Hexane		109.8	12.2
	Toluene		98.9	68.1

Figure 4.10 shows water contact angle images of a typical measurement from a $\text{In}_2\text{O}_3:\text{N}$ sample both before and after irradiation and also $\text{In}_2\text{O}_3:\text{N}$ on titanium deposited from hexane showing it's hydrophobic nature before irradiation and hydrophilic nature after irradiation.

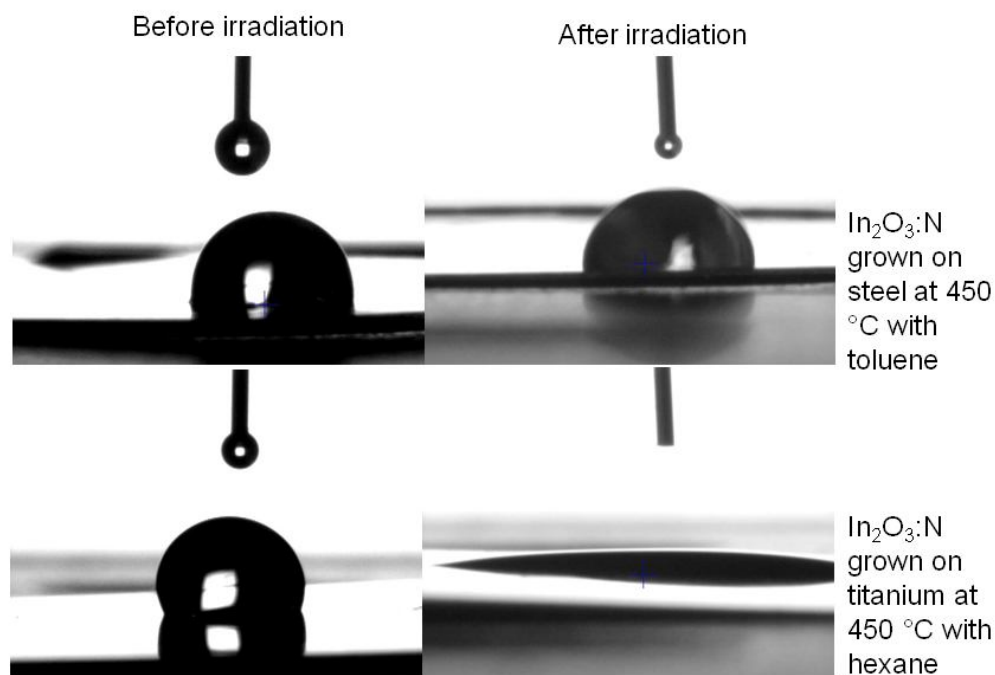


Figure 4.10. Water contact angle measurements before and after irradiation at 254 nm for 15hrs. Top images show typical before and after measurements, bottom images show $\text{In}_2\text{O}_3:\text{N}$ grown on a titanium coupon at 450°C with hexane.

4.2.8. Hydrogen evolution

As $\text{In}_2\text{O}_3:\text{N}$ samples deposited *via* the conditions in Table 4.2 showed a reduction in band gap to ~ 3.1 eV and nitrogen incorporation similar to that previously seen by Reyes-Gil *et al*, the samples were tested for their water splitting properties despite not showing any superhydrophobic properties during water contact angle measurements. $\text{In}_2\text{O}_3:\text{N}$ films deposited on steel or titanium coupons were coated with platinum (as used as a co-catalyst) on the reverse side of the coupon *via* sputtering before use for hydrogen evolution testing. Samples were irradiated under solar conditions and measured for hydrogen evolution. The results of three samples of $\text{In}_2\text{O}_3:\text{N}$ deposited on steel and titanium from hexane or toluene are displayed in Table 4.4. Titanium, toluene-deposited $\text{In}_2\text{O}_3:\text{N}$ results were not recorded as the film was too thin.

Table 4.4. Hydrogen evolution for In₂O₃:N deposited on metal coupon substrates under solar simulated conditions.

Sample			Hydrogen Evolution [$\mu\text{mol hr}^{-1} \text{m}^{-2}$]
Substrate	Solvent	T [°C]	
Steel	Hexane	450	10.8
	Toluene		2.3
Titanium	Hexane		5.8

The samples evolved hydrogen at rates of 2-11 $\mu\text{mol hr}^{-1}\text{m}^{-2}$. This rate of hydrogen evolution is low compared to samples of TiO₂ deposited by APCVD onto steel substrates which evolved hydrogen at a rate of 1,340 $\mu\text{mol hr}^{-1}\text{m}^{-2}$.¹⁷⁸ Films were found to be cubic phase In₂O₃ after hydrogen testing evolution and therefore the hydrogen produced was not a result of any chemical side reactions. Despite some hydrogen evolution, the films would not be suitable visible-light photocatalysts. Additionally after 4 hours of irradiation, the films partially delaminated from the metal coupon surface.

4.3. Conclusion

Chapter 4 described the single-source precursors used to deposit In_2O_3 thin films. By nitrogen doping the indium oxide lattice, the band gap has been found to be reduced to an energy suitable for visible light water splitting. An *in situ* indium amido/alcohol exchange reaction was employed as the precursor to these films using a precise 1:3 ratio of indium precursor to alcohol to allow small incorporation of nitrogen into the indium oxide lattice. Precursors used included $[\text{In}\{\text{N}(\text{SiMe}_3)_2\}_3]$, $[\text{In}\{\text{NPh}(\text{SiMe}_3)\}_3]$ and $[\text{In}\{\text{N}^t\text{Bu}(\text{SiMe}_3)\}_3]$ and alcohols HOME, HO^tBu and HOCH₂CH₂NMe₂.

When $[\text{In}\{\text{N}(\text{SiMe}_3)_2\}_3]$ and $[\text{In}\{\text{NPh}(\text{SiMe}_3)\}_3]$ were used as precursors with alcohols, thin, powdery, amorphous films were obtained that were readily removed with a tissue. SEM revealed these films had a globular morphology that were indicative of gas phase nucleation that had deposited, but not reacted onto the substrate. This combination of *in situ* precursors were not suitable as precursors to adherent nitrogen-doped indium oxide thin films.

When $[\text{In}\{\text{N}^t\text{Bu}(\text{SiMe}_3)\}_3]$ was used with HOCH₂CH₂NMe₂, thin, transparent and adherent films were deposited. These films were crystalline cubic In_2O_3 at all temperatures. XPS analysis showed films had a metal to oxygen ratio of 1:1.5 confirming the formations of $\text{In}_2\text{O}_3\text{:N}$. XPS also showed films had 1.5-5.5 atomic% interstitial nitrogen incorporation, slightly lower than previous describe by Reyes-Gil *et al.* who report 4.0-6.4% incorporation.

SEM analysis showed temperature, solvent used and substrate have an effect on morphology. For glass substrates, with increase in temperature, crystallite size also increases. Films also appear denser as the elevated temperatures allow more nucleation and growth of the thin films during deposition. Solvents used to dissolve precursors were hexane and toluene which both led to different morphologies. Hexane resulted in needle-like crystallites that increase in size with increased temperature. Toluene resulted in cubic-like crystallites that remained the same size with increasing temperature however hollow cubic structures were visible at higher temperature films. With metal substrates the morphology was similar across all samples including those deposited on

stainless steel or titanium, however the morphology does differ to that deposited on glass. The change in film topography suggests that solvent and substrate have morphological directing effects.

Optical measurements reveal that the hexane-deposited samples transmitted 64-79% of visible light, whereas toluene-deposited samples transmitted only 33-36% of visible light. Band gaps of the $\text{In}_2\text{O}_3:\text{N}$ films were calculated to be between 2.9-3.1 eV, which is a reduction compared to the literature values for undoped In_2O_3 of 3.5 eV. Sheet resistance calculations revealed the films had a sheet resistance of between 92-192 Ωsq^{-1} which are poor compared to that of ITO thin films deposited by CVD which are 5-10 times more conductive.

Contact angles of water droplets were measured for films. Films deposited using hexane were shown to have contact angles to water droplets of 75-110° whereas films deposited using toluene had contact angles of 40-100°. Hexane-deposited films were expected to have higher contact angles, from SEM images the films can be seen to be rougher in appearance to those deposited by toluene and thus more hydrophobic. Contact angles decreased after irradiation by varying amounts. Most samples showed an insignificant decrease in contact angle with the exception of In_2O_3 on titanium deposited using hexane which became notably hydrophilic with a contact angle to a water droplet of 12°. This is due to the surface becoming hydroxylated and wetting becomes easier. This behaviour made the films suitable for photocatalytic testing.

Films deposited on stainless steel or titanium substrates were sputter coated on the reverse side of the coupon with platinum to act as a co-catalyst. Films exposed to solar radiation evolved H_2 at rates of 2-11 $\mu\text{mol hr}^{-1}\text{m}^{-2}$. This rate of hydrogen evolution was low compared to samples of TiO_2 deposited by APCVD onto steel substrates reported by Hyett *et al.* which evolved hydrogen at a rate of 1,340 $\mu\text{mol hr}^{-1}\text{m}^{-2}$. Films were found to be cubic phase In_2O_3 after hydrogen evolution testing and therefore the hydrogen produced was not a result of any chemical side reactions. Despite some hydrogen evolution, the films would not be suitable visible-light photocatalysts. Furthermore, after 4 hours of irradiation, films partially delaminated from the metal coupon surface. The $\text{In}_2\text{O}_3:\text{N}$ deposited *via* AACVD cannot be directly compared to

those produced by Reyes-Gil *et al.* as they did not report hydrogen evolution measurements.

This chapter has described the successful deposition to In_2O_3 of an *in situ* reaction between $[\text{In}\{\text{N}^t\text{Bu}(\text{SiMe}_3)\}]_3$ and $\text{HOCH}_2\text{CH}_2\text{NMe}_2$ via AACVD. This *in situ* precursor combination proves to be a successful way to deposit transparent conducting indium oxide thin films. Although the films are not suitable as visible light water splitting catalysts, this study does show interstitial nitrogen doping into In_2O_3 via the CVD method with definitive reduction of the band gap. Additionally changing the solvent used during deposition also has an effect on morphology.

Chapter 5 investigates the gas sensing properties of indium oxide. The sensors were prepared by two different routes: the first set of In_2O_3 sensors investigated in this work were prepared by continuous hydrothermal flow synthesis (CHFS; produced by Sofia Elouali, UCL) and the second set included both In_2O_3 and $\text{In}_2\text{O}_3:\text{M}$ ($\text{M} = \text{Ti}$ or Ta) sensors were prepared by aerosol-assisted chemical vapour deposition (AACVD; produced by Joe Manzi, UCL). Test gases included reducing gases ethanol, butane, ammonia, and carbon monoxide and the oxidising gas nitrogen dioxide at environmentally relevant concentrations.

4.4. Experimental

4.4.1. General Procedures – AACVD

The AACVD setup as previously described in Chapter 1.2.1.7 was used for the deposition of the indium oxide *in situ* precursors. Nitrogen (99.99%) was obtained from BOC and used as supplied. Depositions were obtained on SiCO coated float-glass and pure titanium (99.6%, Goodfellow) or stainless steel (316, Corus) coupons. Prior to use, substrates were cleaned using propan-2-ol and acetone and then dried in air. Glass substrates of *ca.* 90 mm x 45 mm x 4 mm and metal coupons of steel or titanium of *ca.* 30 mm x 30 mm x 1 mm were used.

The precursor was dissolved in 30 ml of solvent under Schlenk conditions before addition of 3 equivalents of alcohol. The solution was allowed to stir for 30 min before being vaporized at room temperature by use of a PIFCO ultrasonic humidifier. This produced an aerosol of the precursor in the solvent used. Precursors were synthesized following literature procedures previously reported and are outlined in Table 4.1 of this chapter.¹⁶⁴ [In{N(SiMe₃)₂}₃] (0.50 g, 0.84 mmol) with MeOH (0.10 cm³, 2.52 mmol), *t*-BuOH (0.24 cm³, 2.25 mmol), HOCH₂CH₂NMe₂ (0.25 cm³, 2.52 mmol); [In{NPh(SiMe₃)₃] (0.51 g, 0.84 mmol) with (0.25 cm³, 2.52 mmol); [In{N^{*t*}Bu(SiMe₃)₃] (0.46 g, 0.84 mmol) with HOCH₂CH₂NMe₂ (0.25 cm³, 2.52 mmol).

Two way taps were used to divert the nitrogen carrier gas through the bubbler. The aerosol was carried into the reactor in a stream of nitrogen gas through a brass baffle to obtain a laminar flow. Depositions were carried out by heating the horizontal bed reactor to the required temperature before diverting the nitrogen line through the aerosol and hence to the reactor. Depositions were carried out in hexane and toluene at a flow rate of 1.0 Lmin⁻¹ over a range of substrate temperatures (350 – 550 °C). The total time for the deposition process was in the region of 30 min – 1.5 h. At the end of the deposition the nitrogen flow through the aerosol was diverted, and only nitrogen passed over the substrate. The glass substrate was allowed to cool with the graphite block to less than 100 °C before it was removed. Coated glass substrates were handled and stored in air. Large pieces of glass (*ca.* 4 cm x 2 cm) were used for X-ray powder diffraction and reflectance/transmittance analysis and water contact angle measurements. The coated glass substrate was cut into *ca.* 1 cm x 1 cm squares for subsequent analysis by SEM, EDX and WDX analysis. Metal coupons were used as-deposited for all analysis. The metal coupons were also sputter coated with a platinum co-catalyst on the reverse side to the thin film using a current of 40 mA, an argon pressure of 0.1 mbar, and a deposition time of 4 min, before use in hydrogen evolution testing.

4.4.2. Analysis Techniques

X-ray powder diffraction patterns were measured on a Bruker AXS D8 diffractometer using CuK α_1 radiation in glancing angle mode (5° incident angle). The films on the glass substrates were indexed using Unit Cell and compared to database standards. SEM

was carried out on a JEOL 6301 filament scanning electron microscope, and WDX was obtained on a Philips XL30SEM instrument. UV/Vis/Near IR transmittance and reflectance spectra were obtained on a Perkin Elmer Lambda 950 spectrometer using as air background and recorded between 200 and 2000 nm. High resolution X-ray photoelectron spectroscopy (XPS) was performed on a Kratos AXIS ULTRA with a mono-chromated Al $K\alpha$ X-ray source (1486.6eV) typically operated at 10mA emission current and 12kV anode potential at the University of Nottingham. The data were analysed using CasaXPSTM software and calibrated to the C (1s) signal at 284.7 eV, attributed to adventitious carbon.

Water contact angle measurements were determined on a FTA 1000 contact angle measurement system. Samples were measured both prior to and post-irradiation by UV light (284nm), with a drop of deionised water $\sim 6.5 \mu\text{L}$ discharged from a Gauge 30 needle and photographed side on. Measurements were taken as an average of three readings. Water photoreductions were carried out with a silica glass reactor consisting of a central walled glass chamber surrounded by an outer glass water jacket (water was circulated through the jacket by an external chiller maintained at 19 °C). The vessel was filled with 40 cm³ of a solution comprising of 1:1 EtOH:H₂O containing 0.1 M HCl, kept under continuous stirring. The metal coupons were suspended from a rubber septum which was also used to seal the reactor to the outside atmosphere. 0.25 cm³ of gas was removed from the headspace at regular intervals and analysed for hydrogen *via* gas chromatography by a Varian CP-3800 GC equipped with a 5A molecular sieve column. Coupons were exposed to simulated solar light irradiation (UVA irradiance of 17.5mWcm⁻²) using a Xe 75W light source (Photon Technology International, West Sussex, UK).

Chapter 5

Gas Sensing

5. Gas Sensing

Chapter 4 explored the deposition of indium oxide thin films onto glass and metal substrates and investigated their properties. In this chapter the gas sensing applications of indium oxide films are explored. The sensors are manufactured *via* two different methods and their response to both reducing and oxidising gases are tested.

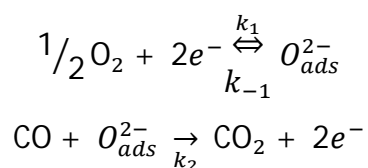
Metal oxide gas sensors are a type of chemical sensor, which may be defined as a simple to use, robust device that is capable of reliable quantitative or qualitative recognition of atomic, molecular or ionic species. Gas sensing can be achieved in a variety of manners, for example by electrochemical devices,¹⁷⁹ solid state semi-conducting metal oxide devices,¹⁸⁰ metal phthalocyanine devices,¹⁸¹ electrolytic fuel cells¹⁸² and infrared spectroscopy.¹⁸³

5.1. Metal Oxide Semiconductor Gas Sensors

The current widely held view of metal oxide semiconductor gas sensors¹⁸⁴ states that the conductivity of semi-conducting oxides in air is determined by the trapping of electrons in surface states associated with surface adsorbed oxygen. If interstitials or oxygen vacancies are immobile in the lattice, then the behaviour is described in terms of electron distribution between bulk and surface states. The surface conductivity is sensitive to small amounts of reactive gas as catalytic surface processes result in a change in the surface coverage of the oxygen surface trap states. If oxygen defects are mobile within the lattice then the conductivity is determined by the equilibrium between bulk lattice defects and oxygen in the gas phase, and sensitivity to trace reactive gases is lost. A further case for gas sensing can arise where there is a time dependence on the equilibration of lattice and surface states.¹⁸⁰ Conductivity time dependence can also be observed as a result of lattice defect migration, which alters the potential and thus the charge carrier distribution near the surface.¹⁸⁰ Due to a microstructural effect, part of the conductivity is gas sensitive due to modification in surface reactions whilst the

conductivity contributed by the bulk far enough away from the surface is not gas sensitive.¹⁸⁵ If the films are especially thin (100s of nm) then dense films such as those produced by CVD methodology may produce high quality gas sensors as they allow for a high number of surface sites for gas adsorption. The most widely used semiconductor in solid-state gas sensors is tin oxide, which gives a large response to a number of reducing gases.¹⁸⁶ Elements, including platinum,¹⁸⁷ gold¹⁸⁸ and antimony,¹⁸⁹ are often doped into the tin oxide, or a thin layer is applied to the surface in order to improve selectivity and response.^{186, 190} Other types of metal oxide gas sensors that have been reported include tungsten oxide,¹⁹¹ chromium titanate,¹⁹² indium oxide,³⁴ gallium oxide¹⁰ and zinc oxide.¹⁹³

Typically solid-state gas sensors are made of semiconductor materials. The band structure of these materials creates electronic lattice defects; these defects may be mobile and migrate to the surface of the material creating an increased number of trap states and thus catalytic sites. Reactions at these sites result in a change of the fractional surface coverage of this acceptor state and thus a change in conductivity. For example, in a *p*-type semiconductor where holes are majority charge carriers and electrons the minority, the resistance will increase in the presence of a reducing gas (CO, alcohols, alkanes, etc.). Scheme 5.1 shows a simple, formal model for sensor response at reactions sites which are sensitive to the partial pressure of carbon monoxide.



Scheme 5.1. A formal model for sensor response at reactions sites, sensitive to the partial pressure of carbon monoxide. *k* – rate constant of surface reaction.

The classification *n* and *p* is used to describe gas sensitive semiconductor materials because it is believed that this reflects the charge type of the majority carrier in the two cases and is outlined in Table 5.1. In an *n*-type semiconducting oxide, oxygen adsorption decreases the charge carrier density at the surface; this is balanced by the charge carried on the ionized donors. A *p*-type semiconducting oxide in contrast has an increased charge carrier density at the surface due to adsorption; this increase in charge

is balanced by holes in the valence band. When determining the sign of gas response (resistance increase or decrease) the classification is as follows: gases can be classified as oxidising or reducing, and oxides classified as *p* or *n* type according to the sign of response: *n*-type oxides show a resistance decrease in the presence of reducing gases (*n*-type response), and resistance increase to oxidising gases (*p*-type response); *p*-type oxides show opposite behaviour.¹⁸⁰ Indium oxide is an *n*-type sensor, response to reducing gases is defined as R_0/R and response to oxidising gases is defined as R/R_0 . Where R_0 is the point immediately prior to exposure to gas and R is the resistance when exposed to a gas.

Table 5.1. Sign of resistance change (increase) to change in gas atmosphere.¹⁸⁰

Classification	Decrease P_{O_2}	Oxidising gases	Reducing gases
<i>n</i>	-	+	-
<i>p</i>	+	-	+

5.1.1. Indium Oxide Gas Sensors

Indium oxide films have been investigated as solid-state gas sensors and are used in industrial and technological applications such as toxic/dangerous gas detection.¹⁹⁴ Gallium oxide has been prepared by physical vapour deposition methods such as magnetron sputtering and electron beam evaporation.^{195, 196} It has been reported to have a response to reducing gases at lower temperatures (~ 500 °C)¹⁹⁷ and a response to oxidizing gases at elevated temperatures (> 900 °C).¹⁹⁸ Indium oxide however, is the focus of this work due to time restraints.

Gas sensors prepared by AACVD from the reaction of gallium amide compounds $[Ga(NMe_2)_3]_2$ and donor-functionalised alcohols have been explored by Basharat *et al.* and were found to have an *n*-type response to ethanol.¹⁰ Group 13 metal oxides sensors, prepared in a variety of ways have been shown to be responsive to a range of gases.^{199, 200} Many studies have been conducted that aim to improve the performance of In_2O_3 gas sensors. One way of significantly improving sensor performance is by producing crystallites with reduced dimensions, which has been previously reported.²⁰¹ Indium

oxide has been prepared by drop coating,²⁰² screen printing,²⁰³ and sol-gel,²⁰⁴ often as nanomaterials²⁰⁵ and CVD.¹⁹ Indium oxide can also be doped with other metals²⁰⁶ to improve sensitivity²⁰⁷ and selectivity towards both reducing^{37,208} and oxidising³⁸ gases.

In this chapter two types of indium oxide gas sensors have been synthesised and tested for their gas sensing properties. The first investigation synthesised In₂O₃ nanoparticles *via* the continuous hydrothermal flow synthesis (CHFS) method and uses the drop coating method to deposit films onto gas sensing substrates. The second investigation used the *in situ* reaction of InMe₃ and a donor-functionalised alcohol to form In₂O₃ thin films using the AACVD method, as this route has previously been reported to be successful in forming thin films suitable for gas sensing.¹⁹

5.2. Gas sensing of nano-indium oxides prepared *via* continuous hydrothermal flow synthesis

5.2.1. Background

Smaller indium oxide particle sizes have been found to result in improved gas responses during sensing.^{192,201,209-212} For example, a study carried out by Korotecenkov reported as high as a 10³ increase in response to ozone at 300 °C, with concomitant drop in response time, when the average In₂O₃ primary particle size was reduced from 80 nm to 15 nm.²¹¹

While many direct and rapid formations of colloids have been reported in the literature *via* organometallic synthetic methods, these are air-sensitive and require the use of solvents and other chemical modifiers over a period of 3-7 hours.²¹³⁻²¹⁵ In contrast to batch processes, continuous hydrothermal flow synthesis (CHFS) reactions offer a rapid and controllable method of producing semiconductor nanoparticles including TiO₂,^{216,217} rare earth oxide solid solutions,²¹⁸ potential SOFC cathodes,²¹⁹ Ni/YSZ anodes,²²⁰ and bioceramics.^{221,222} In CHFS, a superheated water stream (near or above the critical

temperature, $T_c = 374$ °C, and pressure $P_c = 22$ MPa) is brought into contact with a flow containing metal salt(s) resulting in the rapid precipitation and crystallisation of nanoparticulate products which are then cooled in-line within seconds of the initial nucleation. This very short duration under such extreme hydrothermal conditions limits particle growth, while the relatively high temperature of reaction can produce materials that are either only obtained under batch processes after many hours or are difficult to access directly such as In_2O_3 or other kinetic products.

In this work, a rapid and continuous hydrothermal flow synthesis method was used to prepare In_2O_3 nano-powders directly in water only without the use of further chemical modifiers. These powders were prepared by Sofia Elouali, UCL. The resulting suspension was used to prepare drop-coated gas sensor devices. Sensors were drop-coated two or three times to explore the difference in thickness and were tested for sensitivity to a variety of gases in environmentally relevant concentrations.²²³

5.2.2. Sensor characterisation

The In_2O_3 nanoparticles were deposited using drop coating onto gas sensor substrates and their gas sensing properties explored. The gas sensor substrates consisted of gold electrodes on an alumina tile and the whole assembly was subsequently annealed at 600 °C for 10 minutes. In_2O_3 sensors were of two thicknesses, with mean values of 62.9 μm for two layer coverage and 80.9 μm for three layer coverage of the substrate. The XRD and Raman patterns were collected pre- and post-testing and the comparison showed the indium oxide retained its cubic crystalline phase.³⁴

The resistance was measured between the two electrodes of an interdigitized gold electrode structure on an alumina tile (Figure 5.11). The sensors were tested for their response to a variety of reducing gases (ethanol (0-20 ppm), ammonia (0-10 ppm), butane (0-10 ppm), carbon monoxide (0-200 ppm)) or the oxidising gas nitrogen dioxide (0-16 ppb). Gas response was measured as the ratio between R_0 (the point immediately prior to exposure to ethanol) and R (the resistance when exposed to a gas). In_2O_3 gas sensing substrates showed an n -type response to the first reducing gas, ethanol,

at different concentrations over time at an operating temperature of 300 °C (Figure 5.1). *n*-type responses are classified as such.

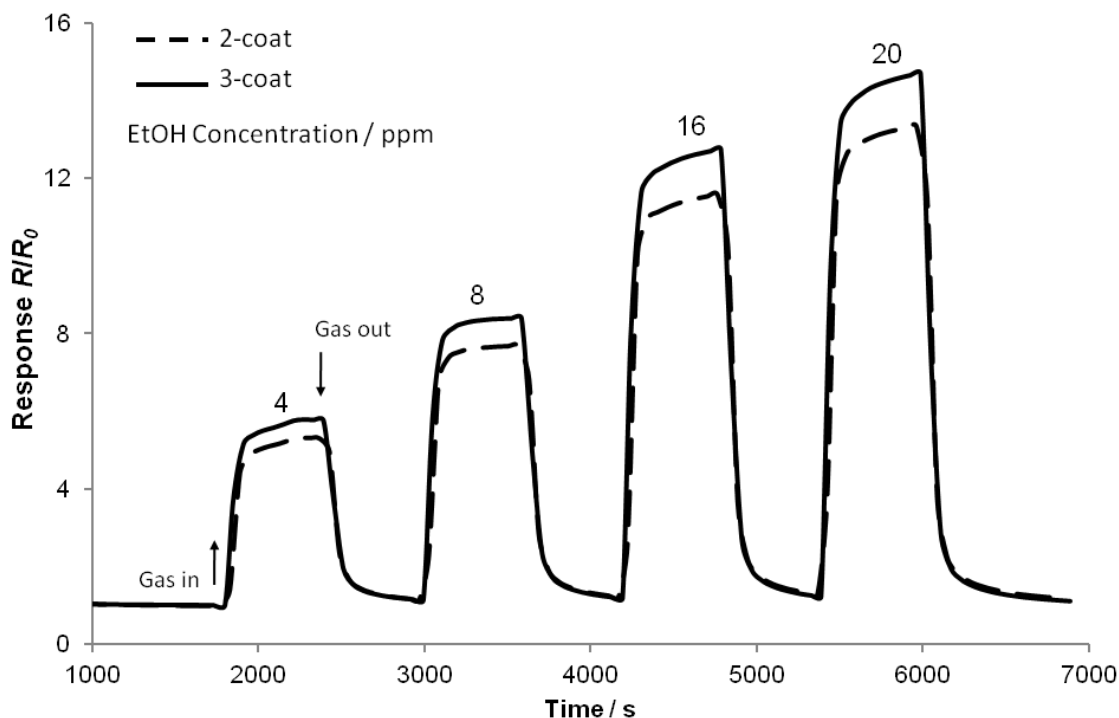


Figure 5.1. Gas response (R/R_0) of In_2O_3 sensors, prepared by CHFS, upon exposure to differing concentrations of ethanol in flowing air over time at an operating temperature of 300 °C. Arrows indicate when gas flow of ethanol was turned on and off.

The gas response was rapid and a near plateau was reached within minutes of exposure to ethanol, as shown in Figure 5.1. The almost square response shape observed indicates that the sensors rapidly respond to ethanol, quickly achieving a steady state.¹⁹² When the ethanol flow was stopped, the response drops to near baseline level and then tails off at a similar rate to the baseline. This response behaviour indicates that there is a lack of surface sites suitable for reaction. The resistive gas response for each concentration is shown in Table 5.2. The highest response of two- and three-coat sensors were 13.4 and 14.7 respectively, to 20 ppm concentration of ethanol at the optimum operating temperature of 300 °C.

Table 5.2. Maximum gas response (R/R_0) of two- and three-coat In_2O_3 gas sensors at optimum operating temperatures on exposure to different concentrations of reducing gases ethanol, ammonia, butane and carbon monoxide

Ethanol Concentration / ppm	Maximum Response R/R_0 300 °C		Ammonia Concentration / ppm	Maximum Response R/R_0 400 °C	
	2-coat	3-coat		2-coat	3-coat
4	5.32	5.78	2	1.06	1.05
18	7.69	8.39	4	1.18	1.28
16	11.59	12.74	8	1.31	1.63
20	13.36	14.69	16	1.46	1.81

Butane Concentration / ppm	Maximum Response R/R_0 450 °C		CO Concentration / ppm	Maximum Response R/R_0 450 °C	
	2-coat	3-coat		2-coat	3-coat
1.25	1.21	1.19	25	1.22	1.20
2.5	2.45	3.84	50	1.47	1.73
5	3.04	3.48	100	2.07	2.38
10	3.23	3.62	200	2.22	2.56

The response of the thicker three-coat sensor is greater than that of the thinner two-coat sensor. The difference in the two sensors can be explained by the thicker three-coat sensor having a larger quantity of material and most likely a larger total surface area. Therefore, a larger number of surface sites are available for adsorption and reaction to occur.

The In_2O_3 gas sensors were also tested against the reducing gas ammonia, as indium oxide has previously been reported to show good sensitivity to NH_3 .²⁰¹ Figure 5.2 shows the variation in the sensor response as a function of the temperature upon exposure to increasing ammonia concentrations.

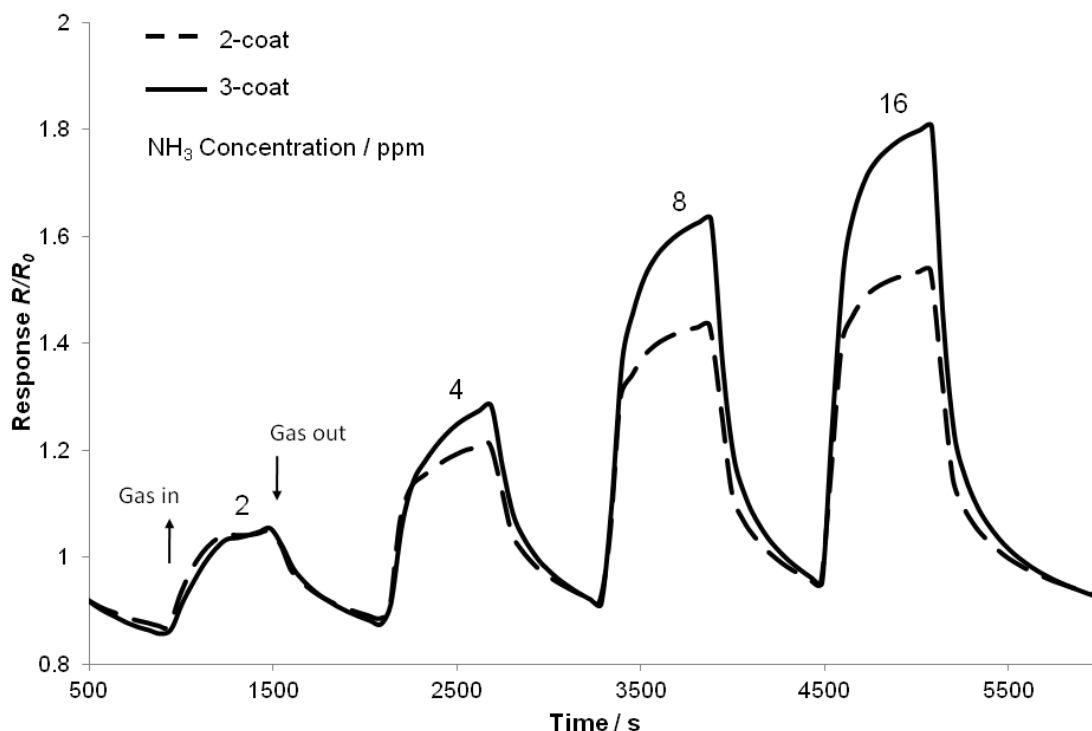


Figure 5.2. Gas response (R/R_0) of In_2O_3 sensors, prepared by CHFS, upon exposures to differing concentrations of ammonia in flowing air over time at an operating temperature of 400 °C. Arrows indicate when gas flow of ammonia was turned on and off.

The gas response was rapid and a shark-fin-like profile was reached within minutes of exposure to ammonia, as shown in Figure 5.2. The shark-fin response shape observed indicates that both sensors do not saturate during the duration of the experiment. When the ammonia flow was stopped, the response drops to near baseline level but takes longer to reach the baseline again compared to the response with ethanol. This response behaviour indicates a large number of surface sites suitable for reaction with ammonia and as such that the resistance of the sensor has a significant proportion deriving from surface reactions. The resistive gas response for each concentration at the optimum operating temperatures of 400 °C is summarised in Table 5.2. The highest response of two- and three-coat sensors were 1.62 and 1.81 respectively to 10 ppm concentration of ammonia.

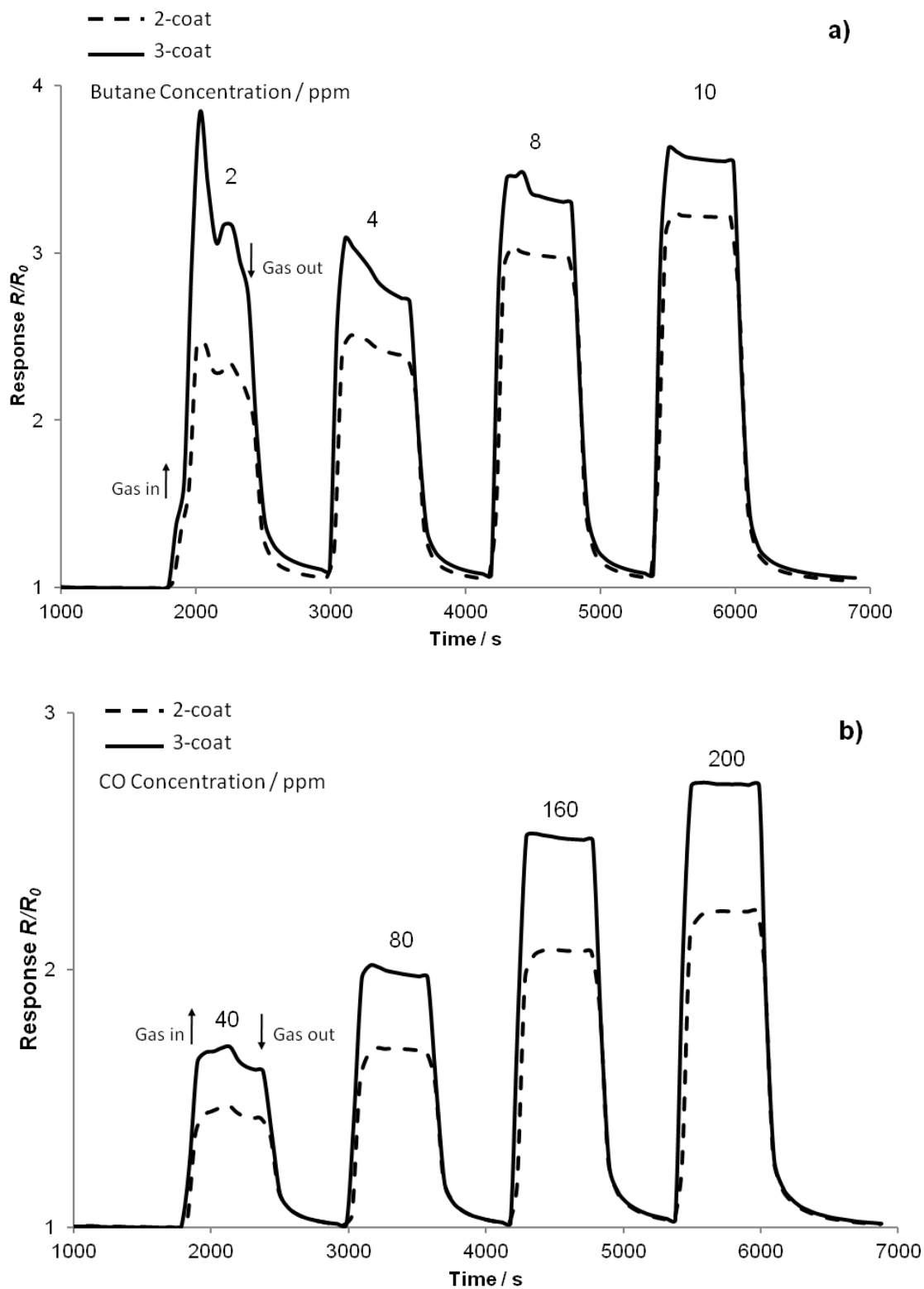


Figure 5.3. Gas response (R/R_0) of In_2O_3 sensors, prepared by CHFS, upon exposures to differing concentrations of a) butane and b) carbon monoxide in flowing air over time at an operating temperature of 450 °C. Arrows indicate when gas flow of ammonia was turned on and off.

The optimum operating temperature for ammonia detection in this work was found to be 400 °C. Above this temperature the sensor response decreased until at 600 °C it was barely detectable. Once again the three-coat sensor gave larger responses than the two-coat sensor and this is again attributed to a larger number of surface sites available for reaction. The observed responses compare favourably to those observed by Makhija *et al.*³⁷ who observed similar magnitude responses but at much higher concentrations of ammonia - between 100 & 500 ppm.

In order to test cross sensitivity the In₂O₃ gas sensors were also tested against a variety of other gases (NO₂ (0-16 ppb); CO (0-200 ppm); butane (0-10 ppm)). The optimum temperature of these sensors to butane and carbon monoxide gases was found to be 450 °C. Figure 5.3 shows the response of two sensors as a function of increasing gas concentration at an operating temperature of 450 °C. For response to both butane and carbon monoxide, the gas response is once again rapid. Figure 5.3 b) shows the almost square response shape observed on exposure to carbon monoxide indicates that the sensors rapidly respond to carbon monoxide, quickly achieving a steady state response. However Figure 5.3 a) shows the sensors response to butane is unlike that of the other reducing gases and could be due to a reaction product that gives a *p*-type response.²²⁴ Other possibilities exist including localised band bending,²²⁵ complex surface catalytic reactions,²²⁶ surface scattering,²²⁷ the action of hydroxyl groups,²²⁸ or surface defects.²²⁹ It is most likely that some type of complex catalytic reaction is occurring on the sensor layer surface in this instance, an alternative explanation would require that this type of response was observed with all reducing gases and this is not the case. When the gas flow for both gases was stopped, the response drops to baseline. This response behaviour indicates a lack of surface sites suitable for reaction and that the resistance of the sensor is dominated by the bulk contribution. The maximum gas response for both gases at each concentration are shown in Table 5.2. At 10 ppm of butane and 200 ppm of carbon monoxide, the two-coat and three-coat sensors have maximum responses of 3.23 and 3.62: butane, and 2.22 and 2.56: carbon monoxide respectively.

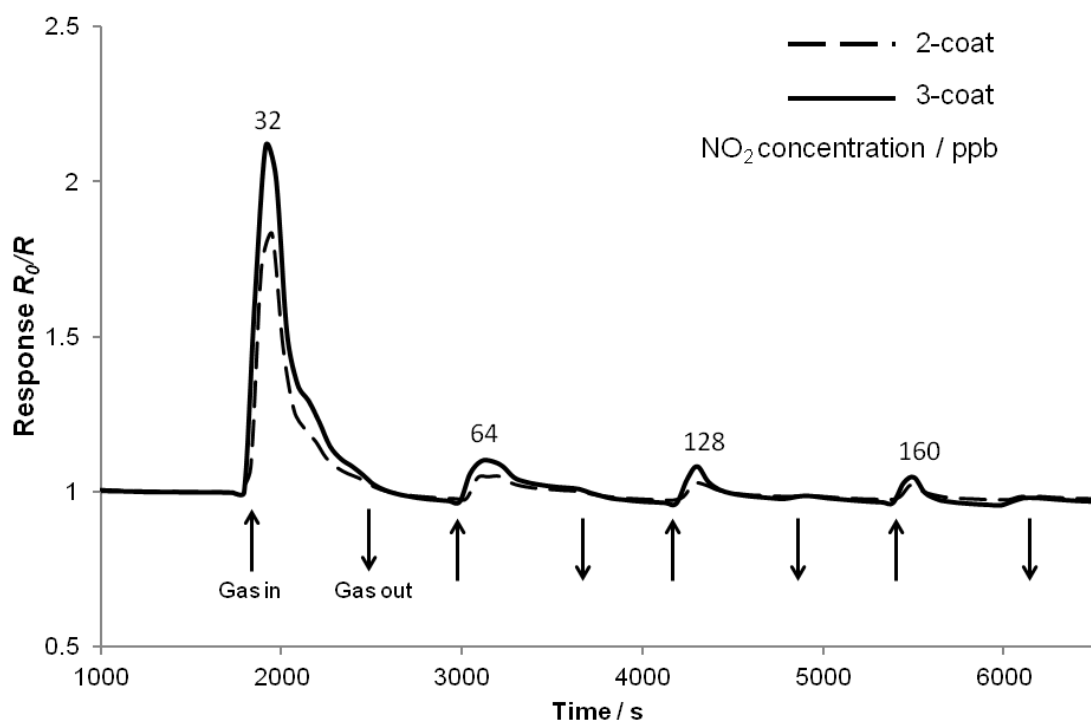


Figure 5.4. Gas response (R_0/R) of In_2O_3 sensors, prepared by CHFS, upon exposures to differing concentrations of NO_2 in flowing air over time at an operating temperature of 450°C . Arrows indicate when gas flow of NO_2 was turned on and off

Figure 5.4 shows the variation in the sensor response as a function of increasing NO_2 concentration. The gas response initially increases then diminishes rapidly and is highest for the lowest concentration of NO_2 gas. This is attributed to the catalytic reduction of NO_2 to NO_x (to which the In_2O_3 sensor is insensitive) as has been observed previously.^{230, 231} When relatively high concentrations of NO_2 is present this reaction is rapid and the NO_x by-product appears to only slowly desorb from the sensor surface blocking further adsorption of NO_2 .

Figure 5.5 shows the maximum response to the different gases. The maximum response of all the gases are quite similar with the exception of ethanol, which has a response of more than four times that of the other gases. Consequently there is selectivity towards ethanol over the other gases.

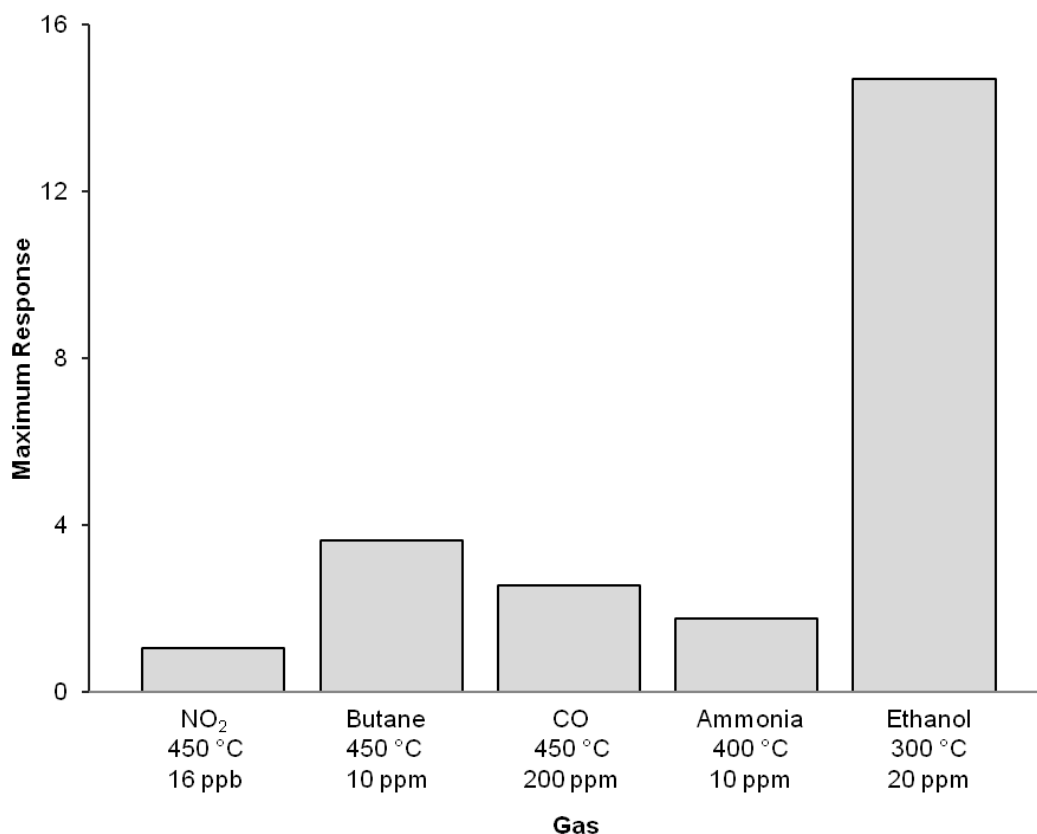


Figure 5.5. Maximum gas response of three-coat In₂O₃ sensors, prepared by CHFS, to different gases in flowing air at their optimum operating temperatures

The most widely accepted theory of metal oxide semiconductor gas sensing states that when a metal oxide semiconductor gas sensor is exposed to air, oxygen species are adsorbed on the surface of the sensor and go on to be ionized by electrons from the materials conduction band to form species such as O²⁻.²³² As such, in air, the measured resistance of In₂O₃ and other *n*-type semiconductors will increase due to the lower concentration of free electrons in the materials conduction band.²³³ On exposure to a reducing gas, such as ethanol, surface reaction between the oxygen species and analyte gas can occur, leading to the release of electrons trapped in the ionized oxygen species back into the materials conduction band, thereby lowering the measured resistance.

The ability of the sensor material to adsorb and ionize oxygen species is fundamental to the sensor performance. The good performance observed here is likely to be the result of the crystallite size being small; having a mean size of 13.7 nm, observed using TEM.³⁴ This causes two important effects: firstly, the surfaces of the crystallites become significantly more reactive and likely to adsorb oxygen and form ionized

oxygen species.²³⁴⁻²³⁶ Additionally, the surface to volume ratio of the materials is also significantly increased. This means that the amount of oxygen that can be adsorbed and ionized is maximised.

The sensors prepared in this work were selective towards ethanol (Figure 5.5) and gave response magnitudes to 20 ppm in great excess of previously reported In_2O_3 sensors based on other processing methodologies.^{201, 207, 237} The sensors described here show a response of 14.69 to a 20 ppm pulse of ethanol comparing favourably with a response of 6.5 to 50 ppm ethanol by In_2O_3 nanorods prepared solvothermally,²³⁷ 1.60 to 400 ppm by polymer encapsulated In_2O_3 nanoparticles,²⁰¹ or 2.0 to 100 ppm by In_2O_3 nanowires.²⁰⁷ These results are comparable to those recently reported for porous nanowires films that gave a response of 15 to 20 ppm ethanol.²⁰⁷

As has been reported previously and demonstrated here, a reduction of the sensor material crystallite size can dramatically increase sensor sensitivity and performance. The continuous hydrothermal synthesis technique has the advantages of being readily scalable and capable of producing highly crystalline nano-powders and is ideally suited for producing materials for metal oxide semiconductor gas sensors.

5.2.3. Summary

Cubic-phase nano-indium oxide has been prepared directly for the first time using a continuous hydrothermal flow synthesis reactor at an elevated temperature of 307 °C at the mixing point where nanoparticles are nucleated and formed. The In_2O_3 nanopowders were utilized in sensor devices and their gas sensing properties examined. It was found that the devices exhibited selectivity towards ethanol and were significantly more responsive to this gas than previously reported In_2O_3 sensor devices. The almost square response shape observed for ethanol indicates that the sensors rapidly respond to ethanol. When the ethanol flow was stopped, the response drops to near baseline level suggesting a lack of surface sites suitable for reaction. Further work will be required to better understand how crystallite size, surface area and nanostructure of the indium oxide, affects reactivity and selectivity for gas sensing.

5.3. Gas sensing of tantalum- and titanium- doped indium oxide thin films *via* AACVD

5.3.1. Background

A range of precursors can be used to deposit In_2O_3 films.^{238, 239} The production of thin films by chemical vapour deposition (CVD) affords inexpensive, adhesive, reproducible films with low impurity levels. However, In_2O_3 films are difficult to prepare by thermal CVD methods due to the lack of precursor materials with high vapour pressure and low decomposition temperatures. Thus, there have been few reports of dual-source thermal CVD routes to In_2O_3 , although polycrystalline indium oxide thin films have been deposited *via* plasma metal organic CVD²⁴⁰ or atmospheric pressure CVD of InMe_3 and O_2 .²⁴¹ Polycrystalline indium oxide thin films have been grown by the aerosol-assisted CVD method *via* the *in situ* formation of indium alkoxide precursors from InMe_3 and donor-functionalised alcohols at 550 °C.¹⁹

Doping indium oxide with titanium and tantalum using an aerosol-assisted CVD method has not been previously reported. In this work, the synthesis of In_2O_3 and titanium- and tantalum-doped In_2O_3 thin films, synthesised based on work previously reported, was carried out by Joe Manzi.¹⁹ The films were deposited by the AACVD *in situ* reaction of InMe_3 and a donor-functionalised alcohol with the transition metal alkoxide precursor produced from the *in situ* reaction of the metal amide and donor-functionalised alcohol (where M = Ti or Ta) analogous to the route to gallium oxides reported by Basharat *et al.* from the *in situ* reaction of gallium amide and donor-functionalised alcohols.¹⁰ Films were found to have substitutional doping from either Ti or Ta in the region on 6.5 and 2.3 atomic% doping, respectively by XPS. Films deposited on gas sensing substrates are also tested for their sensitivity to increasing concentrations of a variety of reducing gases and also to the oxidising gas NO_2 .

5.3.2. Sensor characterisation

Films of In_2O_3 , $\text{In}_2\text{O}_3:\text{Ti}$ and $\text{In}_2\text{O}_3:\text{Ta}$ were deposited *via* AACVD onto gas sensor substrates and their gas sensing properties explored. The films were then annealed at 600 °C for 48 hours to remove surface carbon from the films and stabilise the baseline.

Gas response was measured as the ratio between R_0 (the point immediately prior to exposure to ethanol) and R (the resistance when exposed to ethanol). The resistance was measured between the two electrodes of an interdigitized gold electrode structure on an alumina tile. In_2O_3 gas sensing substrates showed an *n*-type response to ethanol at different concentrations over time at an operating temperature of 500 °C (Figure 5.6).

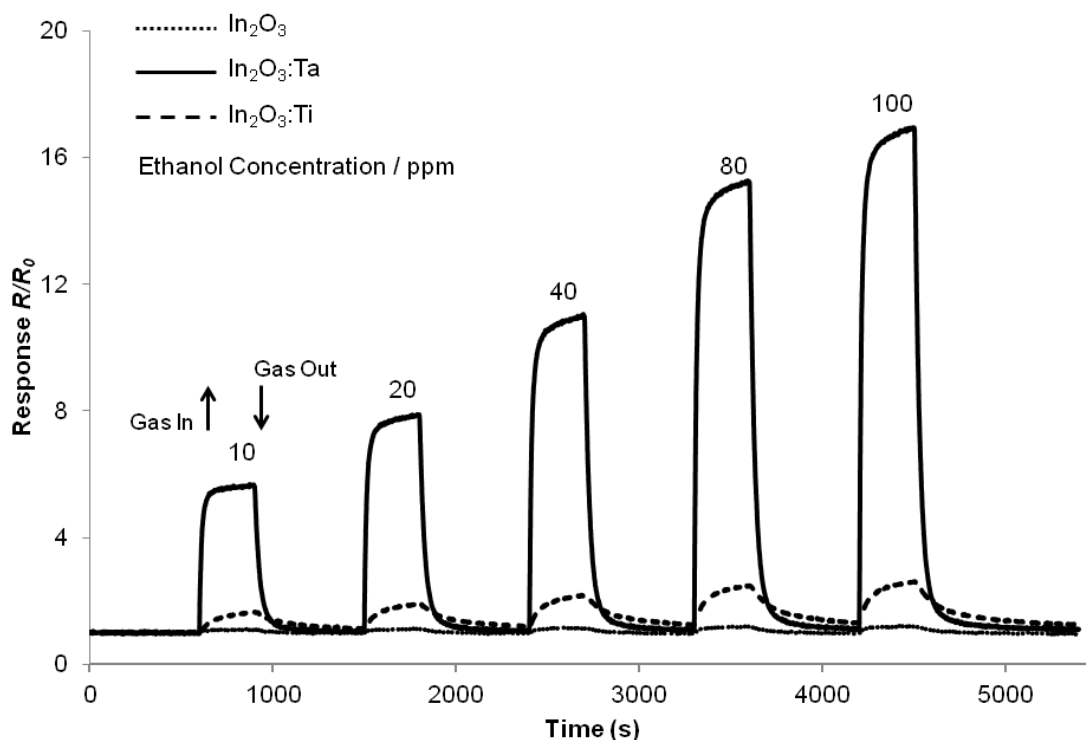


Figure 5.6. Gas response (R/R_0) of In_2O_3 sensors, prepared by AACVD, upon exposures to differing concentrations of ethanol in flowing air over time at an operating temperature of 500 °C. Arrows indicate when gas flow of ethanol was turned on and off.

The gas response was rapid and a near plateau was reached within a minute of exposure to ethanol for all sensors, as shown in Figure 5.6. The shark-fin shape seen in Figure 5.6 indicates that the sensors do not saturate during the duration of the experiment. When

the ethanol flow was stopped, the response drops to the baseline. This response behaviour indicates a lack of surface sites suitable for reaction. The maximum resistive gas response for each concentration is shown in Table 5.3. At 100 ppm of ethanol the undoped indium oxide sensor has the least sensitivity with maximum response of 1.31. $\text{In}_2\text{O}_3:\text{Ti}$ is slightly more sensitive to ethanol than the undoped sensor with a maximum response of 2.49, however the $\text{In}_2\text{O}_3:\text{Ta}$ shows large sensitivity to ethanol and has a high response value of 16.95.

Table 5.3. Maximum response R/R_0 of the sensors to increasing concentrations of ethanol at an operating temperature of 500 °C; ammonia at 450 °C; carbon monoxide at 450 °C and of R_0/R to increasing concentrations of NO_2 at an operating temperature of 400 °C.

Ethanol Concentration / ppm	Maximum Response R/R_0 500 °C			Ammonia Concentration / ppm	Maximum Response R/R_0 450 °C	
	In_2O_3	$\text{In}_2\text{O}_3:\text{Ti}$	$\text{In}_2\text{O}_3:\text{Ta}$		In_2O_3	$\text{In}_2\text{O}_3:\text{Ta}$
10	1.15	1.66	5.69	5	1.02	1.25
20	1.18	1.92	7.90	10	1.03	1.38
40	1.23	2.20	11.06	20	1.04	1.53
80	1.29	2.49	15.28	40	1.06	1.72
100	1.31	2.62	16.95	50	1.07	1.79

NO_2 Concentration / ppb	Maximum Response R_0/R 400 °C			CO Concentration / ppm	Maximum Response R/R_0 450 °C	
	In_2O_3	$\text{In}_2\text{O}_3:\text{Ti}$	$\text{In}_2\text{O}_3:\text{Ta}$		In_2O_3	$\text{In}_2\text{O}_3:\text{Ta}$
5	1.14	1.38	1.16	100	1.04	1.20
10	1.18	1.51	1.25	200	1.07	1.28
20	1.23	1.64	1.45	400	1.09	1.39
40	1.29	1.76	1.82	800	1.11	1.53
80	1.30	1.80	3.01	1000	1.12	1.58

The $\text{In}_2\text{O}_3:\text{Ta}$ had a much larger response than the In_2O_3 and $\text{In}_2\text{O}_3:\text{Ti}$ sensors. The addition of titanium or tantalum into the In_2O_3 film can introduce extra levels into the band structure that lower the activation energy for the formation energy of O_2^- and like on the surface.²⁴² The larger response from the $\text{In}_2\text{O}_3:\text{Ta}$ film can be attributed to the smaller particle size and increased number of grain boundaries.^{192, 243}

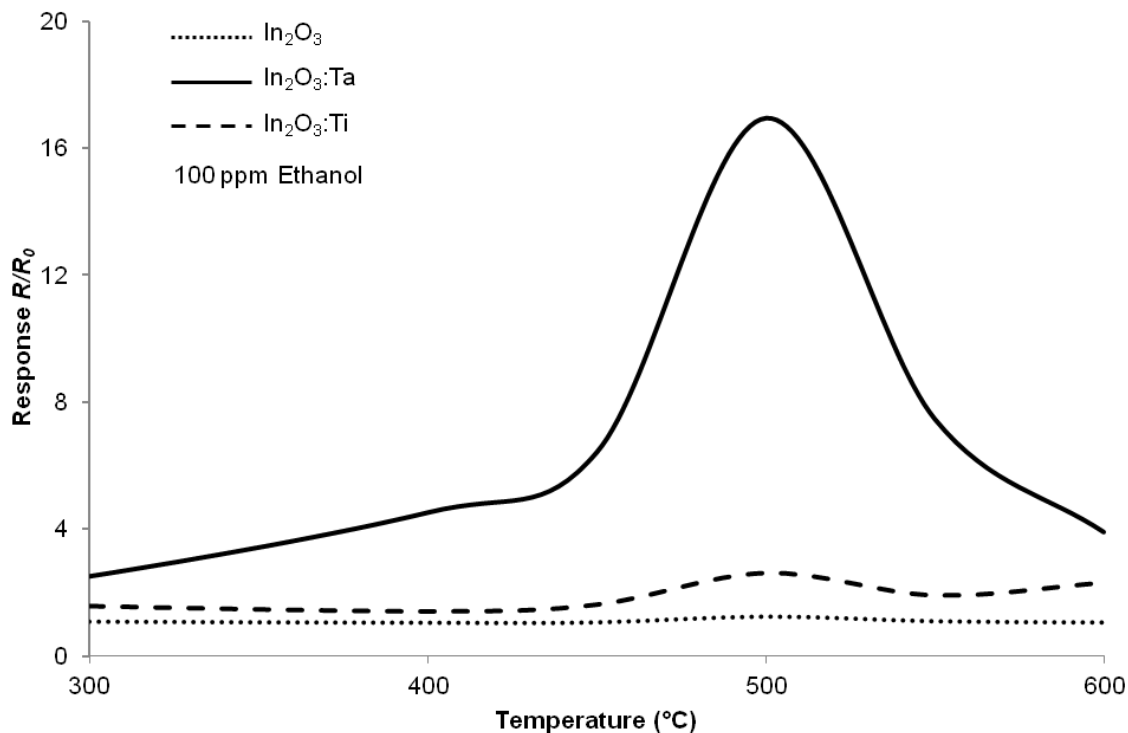


Figure 5.7. Gas response (R/R_0) of In_2O_3 sensors, prepared by AACVD, as a function of temperature. Sensors are exposed to 100 ppm of ethanol in dry air.

The response to ethanol was also tested at different temperatures: 300, 400, 450, 500, 550 and 600 °C. Figure 5.7 shows the response of the three sensors to 100 ppm of ethanol in dry air as a function of temperature. Room temperature was also tested but no response was observed and has been omitted from Figure 5.8. Maximum response of all three sensors can be seen at 500 °C.

Additionally, the sensors were tested against ammonia and carbon monoxide to investigate the behaviour of the sensors towards other reducing gases. The optimum temperature of these sensors to ammonia and carbon monoxide gases was found to be 450 °C. Figure 5.8 shows the response of two sensors as a function of increasing gas concentration at 450 °C. The undoped In_2O_3 and $\text{In}_2\text{O}_3:\text{Ta}$ sensors have been chosen here as the $\text{In}_2\text{O}_3:\text{Ti}$ showed similar results to the undoped In_2O_3 sensor and so $\text{In}_2\text{O}_3:\text{Ti}$ sensor results have been omitted. The relatively high level of noise in the $\text{In}_2\text{O}_3:\text{Ta}$ data was due to a high baseline resistance and a small electrical signal, as such a precise value for maximum response is more difficult to determine. For response to both ammonia and carbon monoxide, the gas response is once again rapid and a shark-fin

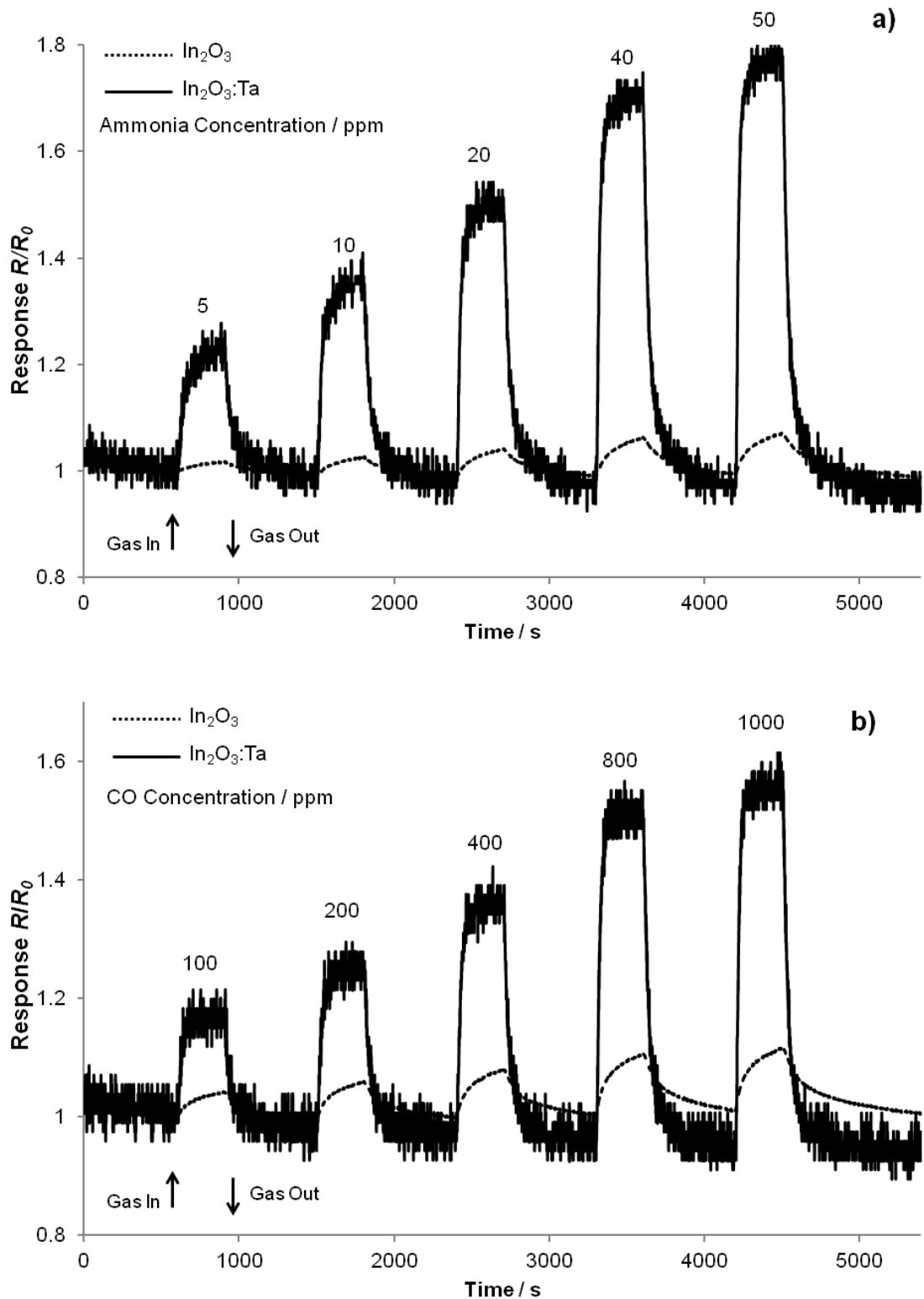


Figure 5.8. Gas response (R/R_0) of In_2O_3 sensors, prepared by AACVD, upon exposures to differing concentrations of a) ammonia and b) carbon monoxide in flowing air over time at an operating temperature of 450 °C. Arrows indicate when gas flow was turned on and off.

shape was reached within a minute of exposure to ammonia in dry air and an almost square response shape is reached for carbon monoxide in dry air. This shows the sensors do not fully saturate during exposure to ammonia, however so fully saturate on exposure to carbon monoxide for the given duration of the experiment. When the gas flow was stopped, the response drops to baseline. This saturating response behaviour indicates a lack of surface sites suitable for reaction and that the resistance of the sensor is dominated by the bulk contribution. The maximum gas response for both gases at each concentration are shown in Table 5.3. At 50 ppm of ammonia and at 1000 ppm of carbon monoxide the undoped indium oxide sensor has the least sensitivity and the $\text{In}_2\text{O}_3:\text{Ta}$ sensor has largest sensitivity to both gases with maximum responses of 1.79 and 1.07: ammonia and 1.58 and 1.12: carbon monoxide for the undoped In_2O_3 and $\text{In}_2\text{O}_3:\text{Ta}$ sensors respectively at 450 °C.

The sensors were also tested against NO_2 to investigate the behaviour of the sensors to an oxidising gas. Figure 5.9 shows the response of the three sensors as a function of increasing NO_2 concentration at 400 °C. Once again, the relatively high level of noise in the $\text{In}_2\text{O}_3:\text{Ta}$ data was due to a high base line resistance and a small electrical signal, therefore determining a value for maximum response is more difficult. The gas response is once again rapid and a shark-fin shape was reached within a minute of exposure to NO_2 in dry air. Once again this shows the sensors do not fully saturate during the duration of the experiment. When the NO_2 flow was stopped, the response drops to baseline. This response behaviour indicates a lack of surface sites suitable for reaction and that the resistance of the sensor is dominated by the bulk contribution. The resistive gas response for each concentration is shown in Table 5.3. At 80 ppb of NO_2 the undoped indium oxide sensor has the least sensitivity, followed by $\text{In}_2\text{O}_3:\text{Ti}$ and once again the $\text{In}_2\text{O}_3:\text{Ta}$ sensor has largest sensitivity to NO_2 with maximum responses of 1.30, 1.80 and 3.01 respectively at an operating temperature of 400 °C.

As $\text{In}_2\text{O}_3:\text{Ta}$ showed the greatest sensitivity to ethanol and NO_2 , it was also tested against other gases in environmentally relevant concentrations²⁴⁴ including butane, ammonia and carbon monoxide to test for cross-sensitivity along with undoped In_2O_3 for comparison. Figure 5.10 shows the maximum response to the different gases.

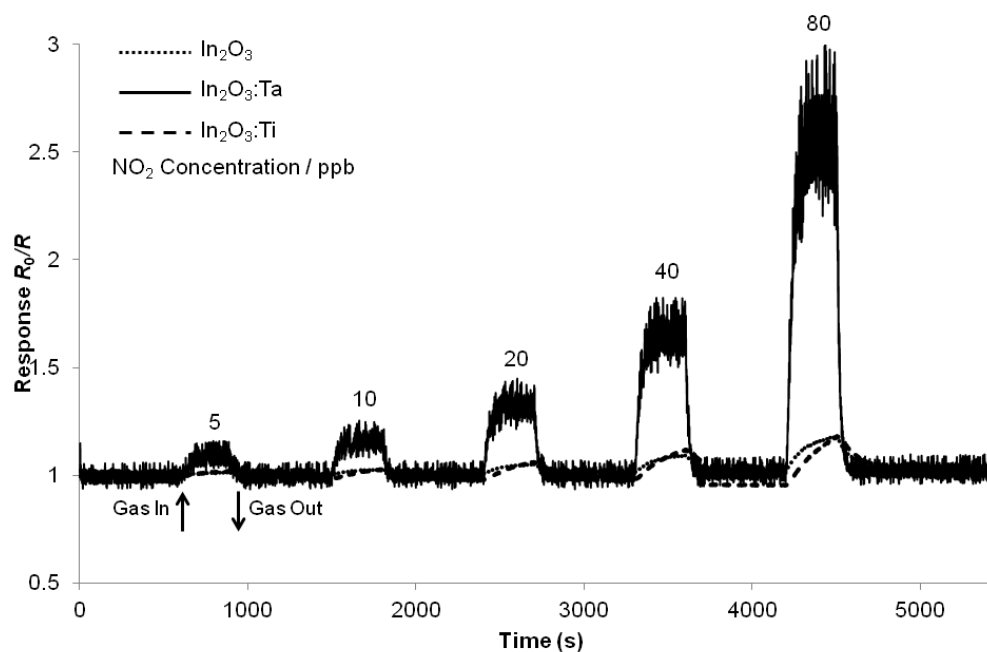


Figure 5.9. Gas response (R_0/R) of In_2O_3 sensors, prepared by AACVD, upon exposures to differing concentrations of NO_2 in flowing air over time at an operating temperature of 400°C . Arrows indicate when gas flow of NO_2 was turned on and off.

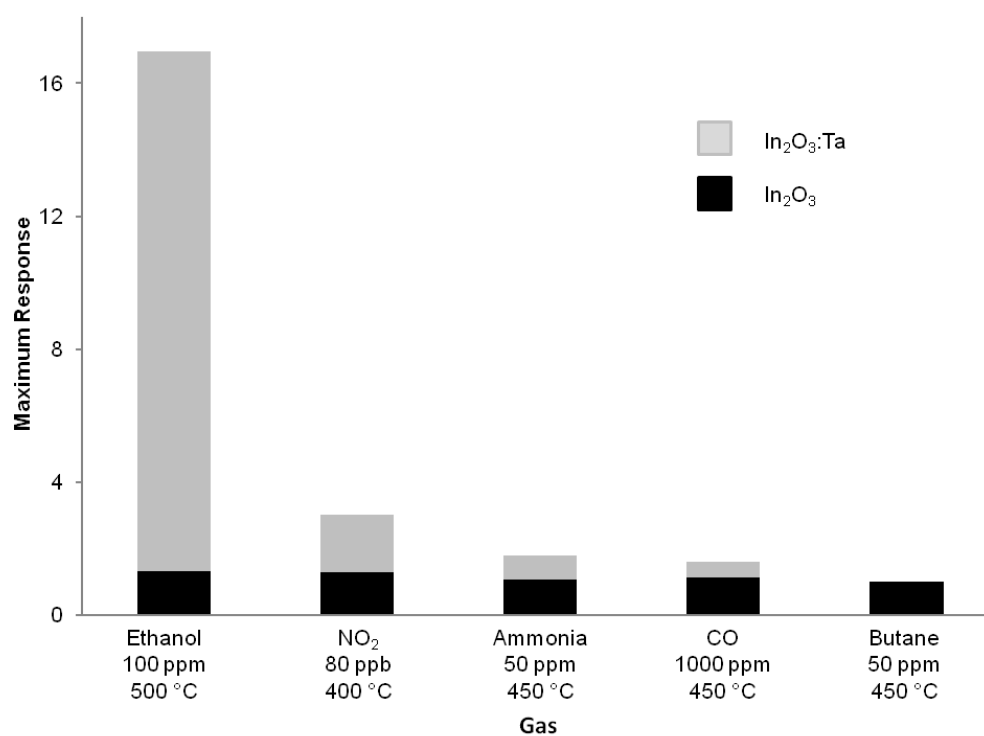


Figure 5.10. Maximum gas response of In_2O_3 and In_2O_3 :Ta sensors, prepared by AACVD, to different gases in flowing air at optimum operating temperatures. In_2O_3 :Ti results are omitted as their performance was very similar to that of In_2O_3 .

Both sensors have some sensitivity towards ethanol, NO₂, ammonia and carbon monoxide, however no response is observed in the presence of butane. The undoped In₂O₃ sensor shows little response above the value of 1 to all gases, whereas the In₂O₃:Ta can be seen to have a similar response to NO₂, ammonia and carbon monoxide, but a greater sensitivity to ethanol. Consequently there is selectivity towards ethanol over the other gases.

The ability of the sensor material to adsorb and ionize oxygen species is key to the sensor performance. The good performance observed here by the In₂O₃:Ta sensor is likely to be the result of two factors. Firstly a reduced crystallite size, 80 nm diameter, was observed relative to the undoped In₂O₃ sensor. This causes two important effects: firstly, the surface of the crystallites becomes more reactive and likely to adsorb oxygen and form ionized oxygen species.^{232, 234, 245} The surface area to volume ratio of the film is also significantly increased. This means that the amount of oxygen adsorbable and ionisable is increased relative to the undoped sensor. Secondly, films prepared by CVD tend to be somewhat denser than other sensors prepared from powders by screen printing,³ consequently, the physical connectivity between grains is increased and the energy barriers caused by grain boundaries reduced. As a result the contribution to the conductivity from the surface of the material is increased and dominates the response behaviour.²³⁴

The In₂O₃:Ta sensors prepared in this work were selective towards ethanol (Figure 5.10) and gave response magnitudes to 100 ppm in excess of previously reported In₂O₃ sensors based on other processing methodologies.²³⁵⁻²³⁷ These sensors show a response of 16.95 to a 100 ppm pulse of ethanol comparing favourably with a response of 1.60 to 400 ppm ethanol by polymer encapsulated In₂O₃ nanoparticles,²³⁶ 6.5 to 50 ppm ethanol by In₂O₃ nanorods prepared solvothermally,²³⁵ or 2.0 to 100 ppm by In₂O₃ nanowires.²³⁷

Chemical vapour deposition techniques represent facile ways to prepare metal oxide gas sensors. Control over key materials properties such as doping and microstructure can be easily achieved. These techniques have the key advantage of already being used in the microelectronics industry, as such, simple integration into MEMS and silicon based devices is possible with operating temperature reduction.

5.3.3. Summary

Films of In_2O_3 were grown from InMe_3 and ROH ($\text{R} = \text{CH}_2\text{CH}_2\text{NMe}_2, \text{CH}_2\text{CH}_2\text{OMe}, \text{CH}_2\text{CH}_2\text{NEt}_2, \text{CH}_2\text{CH}_2\text{CH}_2\text{NMe}_2$) and also films of $\text{In}_2\text{O}_3:\text{M}$ ($\text{M} = \text{Ti}, \text{Ta}$) were grown from the reactions of InMe_3 and $\text{HOCH}_2\text{CH}_2\text{NMe}_2$ with $\text{M}(\text{NMe}_2)_x$ and $\text{HOCH}_2\text{CH}_2\text{NMe}_2$ under AACVD conditions. This represents the first titanium and tantalum-doped indium oxide films reported by AACVD. Films were deposited onto glass substrates at 450 °C and shown by X-ray diffraction to be polycrystalline cubic In_2O_3 with substitutional doping from either Ti or Ta in the region on 6.5 and 2.3 atomic% doping, respectively. Gas sensing responses were tested to reducing (ethanol, carbon monoxide, butane and ammonia) and oxidising gas (nitrogen dioxide). The films showed no sensitivity to butane and small responses to the others. Tantalum-doped In_2O_3 films showed the greatest response of all the films with the greatest selectivity towards ethanol.

5.4. Conclusions

Chapter 5 discussed the gas sensing response of indium oxide sensors to a number of reducing and oxidising gases. The sensors were prepared by two different routes: the first set of In_2O_3 sensors investigated in this work were prepared by continuous hydrothermal flow synthesis (CHFS; produced by Sofia Elouali, UCL) and the second set included both In_2O_3 and $\text{In}_2\text{O}_3:\text{M}$ ($\text{M} = \text{Ti}$ or Ta) sensors were prepared by aerosol-assisted chemical vapour deposition (AACVD; produced by Joe Manzi, UCL). Test gases included reducing gases ethanol, butane, ammonia, and carbon monoxide and the oxidising gas nitrogen dioxide at environmentally relevant concentrations.

Cubic-phase nano-indium oxide has been prepared directly for the first time using a continuous hydrothermal flow synthesis reactor at an elevated temperature of 307 °C at the mixing point where nanoparticles are nucleated and formed. The In_2O_3 nanopowders were utilized in sensor devices and their gas sensing properties examined. It was found that the devices exhibited selectivity towards ethanol over other gases (14.7 to a 20 ppm pulse of ethanol) and were significantly more responsive to this gas than previously

reported In_2O_3 sensor devices. The almost square response shape observed for ethanol indicates that the sensors rapidly responded to ethanol. When the ethanol flow was stopped, the response drops to near baseline level suggesting a lack of surface sites suitable for reaction, i.e. that the resistance of the sensor is dominated by the bulk contribution. This seems somewhat surprising given that sensing material is made up of nanoparticles for which significant grain boundaries are present.

Films of In_2O_3 $\text{In}_2\text{O}_3:\text{M}$ ($\text{M} = \text{Ti}, \text{Ta}$) were grown from the reactions of InMe_3 and $\text{HOCH}_2\text{CH}_2\text{NMe}_2$ with $\text{M}(\text{NMe}_2)_x$ and $\text{HOCH}_2\text{CH}_2\text{NMe}_2$ under AACVD conditions. This represents the first titanium and tantalum-doped indium oxide films reported by AACVD. Films were deposited onto glass substrates at $450\text{ }^\circ\text{C}$ and shown by X-ray diffraction to be polycrystalline cubic In_2O_3 with substitutional doping from either Ti or Ta in the region on 15 and 5 wt.% doping, respectively. The films showed no sensitivity to butane and small responses to the others. Tantalum-doped In_2O_3 films showed the greatest response of all the films with the greatest selectivity towards ethanol of 7.9 at 20 ppm.

In_2O_3 nanopowders and $\text{In}_2\text{O}_3:\text{Ta}$ thin films show selectivity towards the reducing gas ethanol over other gases. In_2O_3 nanopowders produced from CHFS had the greatest response at 14.7 to 20 ppm of ethanol compared to the $\text{In}_2\text{O}_3:\text{Ta}$ sensors prepared by AACVD with a response of 7.9 also to 20 ppm ethanol. This is due to the larger surface area of the nanopowders providing more surface sites for gases to adsorb to compared to the thin films. However both sensors show greater response to ethanol than other previously reported nanomaterial indium oxide sensors.

5.5. Experimental

The sensors used for both nano-indium oxide and doped indium oxide films consisted of a gold track printed on the top of an alumina tile and a platinum heater track printed on the reverse side of the tile (Figure 5.11). Gold electrodes were formed by laser trimming to produce an interdigitized section with gap and finger widths of $50\text{ }\mu\text{m}$. Contacts to the devices were formed by spot welding $50\text{ }\mu\text{m}$ -diameter platinum wire to pads of the

track material in the corner of the sensor chip. The sensor heater was kept at constant resistance and hence constant temperature by incorporating it into a Wheatstone bridge.

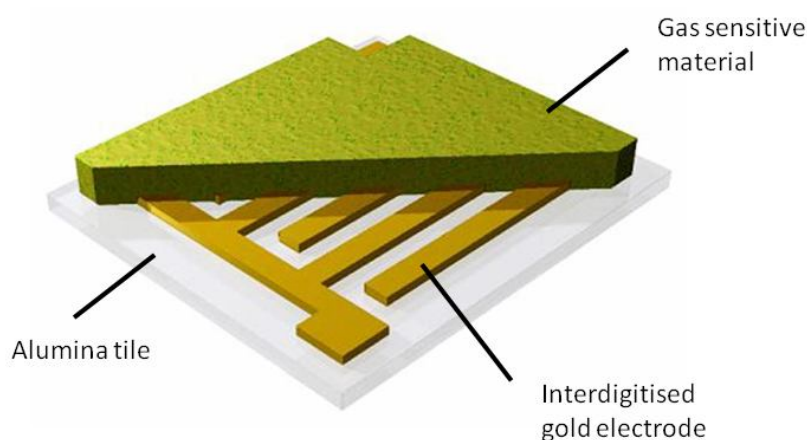


Figure 5.11. Schematic of a gas sensor chip. The chip consists of an alumina tile with interdigitized gold electrodes on the surface.

Electrical experiments were formed on a locally constructed test rig (Figure 5.12).^{192, 246} Various concentrations of test gases were diluted from cylinders of synthetic air (79% nitrogen, 21% oxygen) containing target analytes: ethanol (0-20 ppm, NP; 0-100 ppm, CVD ppm), ammonia (0-10 ppm, NP; 0-50 ppm, CVD), butane (0-10 ppm, NP; 0-50 ppm CVD), carbon monoxide (0-200 ppm, NP; 0-1000 ppm CVD) or nitrogen dioxide (0-16 ppb, NP; 0-80 ppb, CVD). The devices were investigated over a variety of temperatures between 300 and 600 °C. (NP – Indium oxide nanopowder sensors, CVD – indium oxide and metal doped indium oxide sensor deposited by CVD). Lower concentrations of gas were used for nanopowder indium oxide sensors due to their high sensitivity.

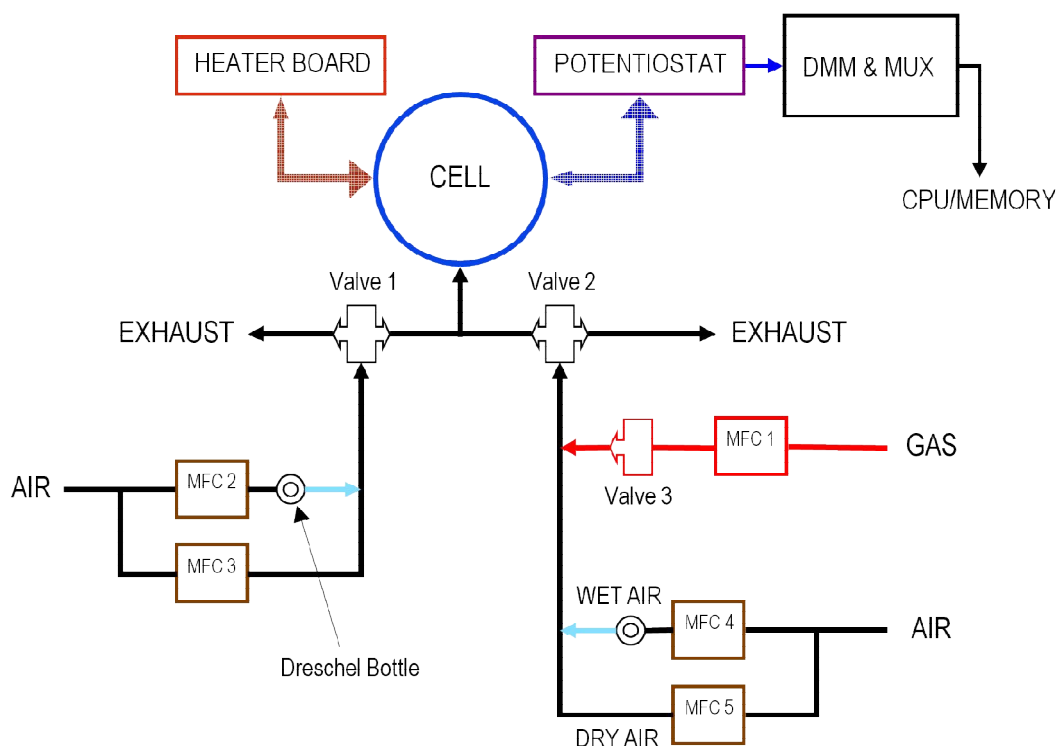


Figure 5.12. Schematic of gas sensing test rig used to investigate the response of both indium oxide nanopowder and CVD films. Sensors are loaded into the cell. MFC – Mass Flow Controller, DMM – Digital MultiMeter, MUX – Multiplexing, CPU – Computer Processing Unit.

5.5.1. Preparation of nano-indium oxides *via* continuous hydrothermal flow synthesis

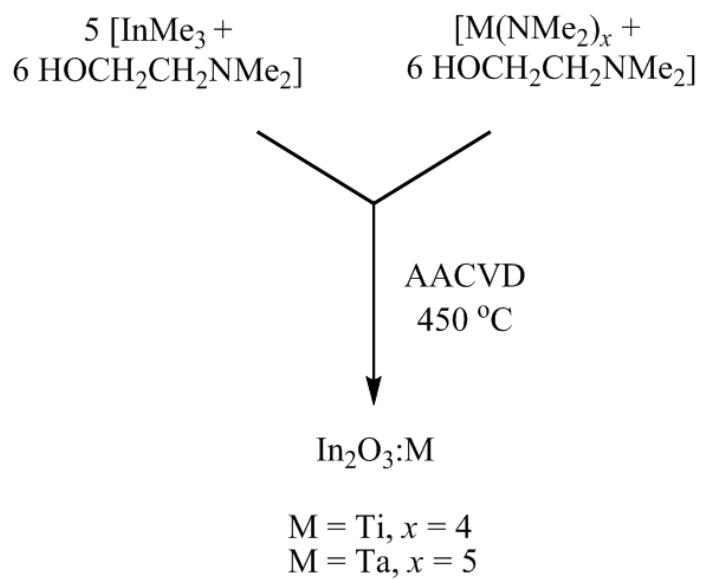
The experimental section and sensor preparation of the nano-indium oxide drop-coated sensors was carried out by Sofia Elouali, UCL in collaboration as part of this work. The experimental procedure was as follows: The $\text{In}(\text{NO}_3)_3 \cdot \text{H}_2\text{O}$ solution was pumped into the CHFS system^{217, 219, 221, 222, 233, 246} at 10 mL min^{-1} and diluted in-line with a further 10 mL min^{-1} flow of DI water at a T-piece pre-mixer. The diluted room temperature feed then met a 20 mL min^{-1} flow of DI water (preheated to $400 \text{ }^\circ\text{C}$) within a stainless steel co-current mixer resulting in the rapid crystallisation and precipitation of nano-sized In_2O_3 particles. The product flow was cooled in-line *via* a water jacket cooler and continuously collected at the exit of the back pressure regulator before being concentrated *via* centrifugation and re-suspended in a volume of 40 mL. The resulting

concentrated lemon-yellow suspension was cleaned of waste solutes *via* dialysis using visking tubing, water changes were carried out at regular intervals until the conductivity of the immersion water was no longer above 30 μS .

Nano-indium oxide films were deposited onto commercially produced 3 x 3 mm sensor substrates (City Technology, Portsmouth, UK). 12 μL drops of the In_2O_3 nanoparticle suspension were deposited onto the substrate, with air-drying between separate depositions. The sensors were fired at 600 $^\circ\text{C}$ for 2 hours in air using a muffle furnace.

5.5.2. Gas sensing of tantalum and titanium-doped indium oxide thin films *via* AACVD

The synthesis of the films was carried out by Joe Manzi, UCL in collaboration as part of this work. The experimental procedure was as follows: thin films of In_2O_3 and transition metal doped In_2O_3 were deposited onto commercially produced 3 x 3 mm sensor substrates. Doped and undoped indium oxide films were deposited *via* AACVD from the *in situ* reaction of InMe_3 and $\text{HOCH}_2\text{CH}_2\text{NMe}_2$ with the *in situ* transition metal reaction of $\text{M}(\text{NMe}_2)_x$ ($\text{M} = \text{Ti}$, $x = 4$; $\text{M} = \text{Ta}$, $x = 5$) and $\text{HOCH}_2\text{CH}_2\text{NMe}_2$ as outlined in Scheme 5.2. The sensors were set on top of a glass substrate and covered by a steel mask to prevent deposition onto the gold electrodes and heated to 450 $^\circ\text{C}$ using nitrogen at 1.2 L min^{-1} as the carrier gas. The sensors were heated to 600 $^\circ\text{C}$ for 48 hours to remove carbon contamination.



Scheme 5.2. AACVD reaction of InMe_3 and $\text{HOCH}_2\text{CH}_2\text{NMe}_2$ with $\text{M}(\text{NMe}_2)_x$ and $\text{HOCH}_2\text{CH}_2\text{NMe}_2$ to deposit In_2O_3 and $\text{In}_2\text{O}_3:\text{M}$ onto gas sensing substrates

Chapter 6

Conclusions and Future Work

6. Conclusions and Future Work

6.1. Conclusions

This work was concerned with the synthesis and characterisation of precursors to group 13 metal oxide thin films, their subsequent deposition *via* AACVD, and functional testing for the applications of these resultant thin films.

Chapter 2 described the synthesis and characterisation of novel gallium bis(alkoxides) of the type $[\text{GaCl}(\text{OR})_2]$ ($\text{R} = \text{CH}_2\text{CH}_2\text{NMe}_2$ (**2**); $\text{CH}_2\text{CH}_2\text{NEt}_2$ (**3**); $\text{CH}_2\text{CH}_2\text{CH}_2\text{NMe}_2$ (**5**)). The two-step reaction of gallium trichloride and two equivalents of lithium dimethylamide, followed by amide/alcohol exchange resulted in the cleanest and highest yielding route to compounds **2**, **3** and **5**. $[\text{GaCl}_2(\text{OCH}_2\text{CH}_2\text{NEt}_2)]_2$ (**4**) was also formed as a by-product during the synthesis of compound **3**. The two-step amido/alkoxide exchange route was also used to synthesise heteroleptic gallium alkoxides of the formula $[\text{Ga}(\text{OR})_2(\text{OR}')]_n$ ($\text{R} = \text{CH}_2\text{CH}_2\text{NMe}_2$ and $\text{R}' = \text{Me}$, $n = 2$ (**8**), Et , $n = 1$ (**9**), $i\text{Pr}$, $n = 1$ (**10**); $\text{R} = \text{CH}_2\text{CH}_2\text{NEt}_2$ and $\text{R}' = i\text{Pr}$, $n = 1$ (**12**) from starting materials **2** and **3**. Additionally compounds of the type $[\text{Ga}(\text{OR})\text{Cl}(\text{O}^t\text{Bu})]$ ($\text{R} = \text{CH}_2\text{CH}_2\text{NMe}_2$ (**11a**); $\text{CH}_2\text{CH}_2\text{NEt}_2$ (**13a**) were formed on the addition of *tert*-butanol. These compounds were difficult to isolate in high purity however spectroscopic data suggested the formation of the named products.

Chloro gallium bis(alkoxides) **2**, **3**, and **5** were found to be diastereotopic and their ^1H NMR spectra were compared. Compound **5** was investigated by variable temperature ^1H NMR and the free energy of activation at the coalescence temperature of 259 K was estimated to be $12.6 \text{ kcal mol}^{-1}$. The interconversion of compound **5** was also explored using DFT calculations. Inversion of the six membered ($\text{Ga-OCH}_2\text{CH}_2\text{CH}_2\text{NMe}_2$) ring followed by rotation about the Ga-O bond was thought to be the mechanism by which the interconversion occurs, which was made possible due to the dative $\text{N} \rightarrow \text{Ga}$ bond.

The synthesis of group 13 bis(β -diketonate) complexes was also attempted. A variety of routes were explored including salt metathesis, hydride elimination, methane elimination and amine elimination. These procedures all resulted in the formation of

gallium tris(β -diketonate). The salt metathesis approach was also utilised in the attempt to synthesise indium bis(β -diketonates). This also resulted in the indium tris(β -diketonate). These synthetic routes have failed due to the high kinetic and thermodynamic stability of $[M(\text{bdk})_3]$ ($M = \text{Ga}, \text{In}$) and also a facile rearrangement of the intermediate $[\text{GaCl}(\text{bdk})_2]$ to the extremely stable homoleptic gallium β -diketonates.

Novel chloro gallium bis(alkoxides) and heteroleptic gallium alkoxides have been synthesised during this work. Due to their monomeric nature and good metal to oxygen ratio they possess suitable qualities for single-source precursors to M_2O_3 thin films using CVD. Although chloro gallium bis(alkoxides) contain a direct Ga-Cl bond which could potentially lead to film contamination of the final metal oxide films, the CVD of these compounds has been explored. In Chapter 3, the thermal decomposition and successful AACVD of compounds **2**, **3**, **5**, **8** and **11a** were investigated and the subsequent Ga_2O_3 thin films were characterised.

TGA showed that compounds of the type $[\text{GaCl}(\text{OR})_2]$ decomposed in a multistep process that may leave behind material other than the desired Ga_2O_3 . Compounds **2**, **3** and **5** were dissolved in toluene and deposited onto glass and quartz at temperatures of 450-550 °C *via* AACVD. As deposited gallium oxide films had good coverage at 450 °C and were transparent, amorphous thin films. Little difference in resultant films was observed between precursors **2**, **3**, and **5**. Subsequent annealing at 1000 °C in air crystallised the films which were monoclinic β - Ga_2O_3 . EDXA confirmed the Ga_2O_3 film composition and SEM showed very smooth morphology before annealing and a crystallite size increase after annealing. Optical measurements show films have similar transparency to glass and the band gap was calculated to be 3.8-3.7 eV, suggesting some additional doping had occurred.

Compounds **8** and **11a** were dissolved in DCM or toluene and deposited onto glass and quartz at a temperature of 450 °C *via* AACVD, as deposited gallium oxide films were transparent, patchy, amorphous thin films. Subsequent annealing at 1000 °C in air crystallised the films which were monoclinic β - Ga_2O_3 . EDXA confirmed the presence of gallium and elevated quantities of oxygen, however break through to the underlying glass was observed and the precise film composition could not be measured. SEM showed very smooth morphology before annealing, films deposited from **8** were too

smooth for imaging. Subsequent annealing showed an increase in crystallite size. Little difference was seen in morphology between the choice of solvent used.

Chapter 4 described the single-source precursors used to deposit In_2O_3 thin films. An *in situ* indium amido/alcohol exchange reaction was employed as the precursor to these films using stoichiometric quantities of each to allow small incorporation of nitrogen into the indium oxide lattice. Precursors used included $[\text{In}\{\text{N}(\text{SiMe}_3)_2\}_3]$, $[\text{In}\{\text{NPh}(\text{SiMe}_3)_2\}_3]$ and $[\text{In}\{\text{N}^t\text{Bu}(\text{SiMe}_3)_2\}_3]$ and alcohols HOME, HO^tBu and $\text{HOCH}_2\text{CH}_2\text{NMe}_2$.

When $[\text{In}\{\text{N}(\text{SiMe}_3)_2\}_3]$ and $[\text{In}\{\text{NPh}(\text{SiMe}_3)_2\}_3]$ were used as precursors with alcohols, thin, powdery, amorphous films were obtained that were readily removed with a tissue. SEM revealed these films had a globular morphology that were indicative of gas phase nucleation that had deposited, but not reacted onto the substrate cause by thermophoresis. This combination of *in situ* precursors were not suitable as precursors to adherent nitrogen doped indium oxide thin films. When $[\text{In}\{\text{N}^t\text{Bu}(\text{SiMe}_3)_2\}_3]$ was used with $\text{HOCH}_2\text{CH}_2\text{NMe}_2$, thin, transparent and adherent films were deposited. These films were crystalline cubic In_2O_3 at all temperatures. XPS analysis showed films had a metal to oxygen ratio of 1:1.5 confirming the formations of $\text{In}_2\text{O}_3:\text{N}$. XPS also showed films had 1.5-5.5 atomic % interstitial nitrogen incorporation.

SEM analysis showed temperature, solvent used and substrate have an effect on morphology. For glass substrates, with increase in temperature, crystallite size also increases. Films also appear denser as the elevated temperatures allow more nucleation and growth of the thin films during deposition. Solvents used to dissolve precursors were hexane and toluene which both lead to different morphologies. Hexane resulted in needle-like crystallites that increase in size with increased temperature. Toluene resulted in cubic-like crystallites that remained the same size with increasing temperature however hollow cubic structures were visible at higher temperature films. With metal substrates the morphology is similar across all samples including those deposited on stainless steel or titanium, however the morphology does differ to that deposited on glass. Change in film topography suggests that solvent and substrate have morphological directing effects.

Optical measurements revealed that the hexane deposited samples transmitted 64-79% of visible light, where as toluene deposited samples transmitted only 33-36% of visible light. Band gaps of the $\text{In}_2\text{O}_3\text{:N}$ films were calculated to be between 2.9-3.1 eV, which is a reduction compared to the literature values for undoped In_2O_3 of 3.5 eV. Sheet resistance calculations revealed the films had a sheet resistance of between 92-192 Ωcm^{-1} which are poor compared to that of ITO thin films deposited by CVD which are 5-10 times more conductive.

Contact angles of water droplets were measured for films. Films deposited using hexane were shown to have contact angles to water droplets of 75-110° where as films deposited using toluene had contact angles of 40-100°. Contact angles decreased after irradiation by varying amounts. Most samples showed an insignificant decrease in contact angle with the exception of In_2O_3 on titanium deposited using hexane which became notably hydrophilic with a contact angle to a water droplet of 12°. This is due to the surface becoming hydroxylated and wetting becomes easier. This behaviour made the films suitable for a potential photocatalyst. Films deposited on stainless steel or titanium substrates exposed to solar radiation evolved H_2 at rates of 2-11 $\mu\text{mol hr}^{-1}\text{m}^{-2}$ and were unchanged after testing. This rate of hydrogen evolution was low compared to literature values of TiO_2 samples.

Chapter 4 described the successful deposition to In_2O_3 of an *in situ* reaction between $[\text{In}\{\text{N}^t\text{Bu}(\text{SiMe}_3)\}]_3$ and $\text{HOCH}_2\text{CH}_2\text{NMe}_2$ via AACVD. This *in situ* precursor combination proved to be a successful way to deposit transparent conducting indium oxide thin films. Although the films are not suitable as visible light water splitting catalysts, this study does show interstitial nitrogen doping into In_2O_3 via the CVD method with definitive reduction of the band gap.

Chapter 5 discussed the gas sensing response of indium oxide sensors to a number of reducing and oxidising gases. The sensors were prepared by two different routes: the first set of In_2O_3 sensors investigated in this work were prepared by continuous hydrothermal flow synthesis (CHFS) and the second set included both In_2O_3 and $\text{In}_2\text{O}_3\text{:M}$ ($\text{M} = \text{Ti}$ or Ta) sensors were prepared by AACVD. Test gases included reducing gases ethanol, butane, ammonia, and carbon monoxide and the oxidising gas nitrogen dioxide at environmentally relevant concentrations.

In_2O_3 nanopowders and $\text{In}_2\text{O}_3:\text{Ta}$ thin films show selectivity towards the reducing gas ethanol over other gases. In_2O_3 nanopowders produced from CHFS had the greatest response at 14.7 to 20 ppm of ethanol compared to the $\text{In}_2\text{O}_3:\text{Ta}$ sensors prepared by AACVD with a response of 7.9 also to 20 ppm ethanol. This is due to the larger surface area of the nanopowders providing more surface sites for gases to adsorb to compared to the thin films. However both sensors show greater response to ethanol than other previously reported nanomaterial indium oxide sensors.

This work described the process of design and synthesis of a precursor to film deposition and subsequent applications of these materials. Focused on group 13 metal oxides, single-source precursors in the form of novel gallium alkoxides as well as *in situ* reactions between indium amides and donor-functionalised alcohols have been used to deposit thin films of Ga_2O_3 and $\text{In}_2\text{O}_3:\text{N}$ via AACVD. Isolated gallium alkoxide compounds were suitable single-source precursors however substitution for indium analogues was not possible and so the *in situ* route was utilised. Both routes prove to be successful in producing these group 13 semiconducting materials and subsequent photocatalysis and gas sensing applications were explored. Thus complete development from design and synthesis of precursors through to applications has been explored throughout this work.

6.2. Future work

Group 13 alkoxides prove to be suitable precursors for the deposition of metal oxide thin films. As outlined in Chapter 2, there are many more gallium alkoxide compounds reported in the literature than there are indium analogues. Chloro indium bis(alkoxides) as well as heteroleptic indium alkoxides followed by deposition of these precursors would complement the work completed on gallium alkoxides. Indium alkoxides are often less stable than their gallium equivalents and so the two-step route employed for gallium alkoxide synthesis may need to be amended for the route to be successful. Isolation of amido indium bis(alkoxides) could also be utilised as alternative precursors to $\text{In}_2\text{O}_3:\text{N}$. Additionally, this work focused on the use of donor-functionalised alkoxide

ligands, changing to another donor-functionalised ligand set (e.g. β -ketoiminato ligands) may give rise to different properties in the resultant metal oxide thin films.

AACVD conditions of all routes explored as part of this work could be optimised to grown thicker films which would then be useful for complete characterisation. Additionally, little is known about the mechanisms that occur between the precursor and the substrate. Using computational methodology, further thermogravimetric analysis and spectroscopic analysis of exhaust by-products may reveal more information about the decomposition pathways that take place within a CVD reactor.

As part of this work, doped indium oxide thin films were explored for their gas sensing properties. Further investigation into doping with different elements and varying their percentage incorporation could lead to interesting film, photocatalytic and gas sensing properties. Furthermore, the doping of metal oxide nanoparticles into group 13 metal oxide thin films is a relatively unexplored area. Gallium doped indium oxide has been shown to improve the conductivity of the films,²³⁹ incorporating nanoparticles could lead to attractive changes in the resultant metal oxide thin film properties.

7. References

1. M. L. Hitchman and K. F. Jensen (editors), *Chemical Vapour Deposition Principles and Applications*, Academic Press, London, 1993.
2. C. G. Granqvist and A. Hultåker, *Thin Solid Films*, 2002, **411**, 1.
3. R. Binions, C. J. Carmalt and I. P. Parkin, *Meas. Sci. Technol.*, 2007, **18**, 190.
4. P. Erhart, A. Klein, R. Egdell and K. Albe, *Phys. Rev. B*, 2007, **75**, 1.
5. M. Nieminen, L. Niinisto and E. Rauhala, *J. Mater. Chem.*, 1996, **6**, 27.
6. M. Ogita, S. Yuasa, K. Kobayashi, Y. Yamada, Y. Nakanishi and Y. Hatanaka, *Appl. Surf. Sci.*, 2003, **212**, 397.
7. M. Ogita, N. Saika, Y. Nakanishi and Y. Hatanaka, *Appl. Surf. Sci.*, 1999, **142**, 188.
8. Y. Li, A. Trinchi, W. Wlodarski, K. Galatsis and K. Kalantar-zadeh, *Sensor. Actuat. B Chem.*, 2003, **93**, 431.
9. R. Binions, C. J. Carmalt, I. P. Parkin, K. F. E. Pratt and G. A. Shaw, *Chem. Mater.*, 2004, **16**, 2489.
10. S. Basharat, C. J. Carmalt, R. Binions, R. Palgrave and I. P. Parkin, *Dalton Trans.*, 2008, 591.
11. S. Basharat, C. J. Carmalt, S. J. King, E. S. Peters and D. A. Tocher, *Dalton Trans.*, 2004, 3475.
12. G. A. Battiston, R. Gerbasi, M. Porchia, R. Bertinello and F. Caccavale, *Thin Solid Films*, 1996, **279**, 115.
13. B. Ballarin, G. A. Battiston, F. Benetollo, R. Gerbasi, M. Porchia, D. Favretto and P. Traldi, *Inorg. Chim. Acta*, 1994, **217**, 71.
14. K. L. Choy, *Prog. Mater. Sci.*, 2003, **48**, 57.
15. A. C. Jones and M. L. Hitchman, *Chemical Vapour Deposition: Precursors, Processes and Applications*, Royal Society of Chemistry, Cambridge, 2009.
16. W. S. Rees Jr., *CVD of nonmetals*, VCH, Weinham, 1996.
17. L. I. Maissel and M. H. Francombe, *An introduction to thin films*, Gordon and Breach, London, 1973.
18. K. Seshan, *Handbook of Thin Film Deposition*, 2nd edn., Noyes Publications, Norwich, 2002.

19. S. Basharat, C. J. Carmalt, S. A. Barnett, D. A. Tocher and H. O. Davies, *Inorg. Chem.*, 2007, **46**, 9473.
20. C. E. Knapp, D. Pugh, P. F. McMillan, I. P. Parkin and C. J. Carmalt, *Inorg. Chem.*, 2011, **50**, 9491.
21. J. Kane, H. P. Schweizer and W. Kern, *Thin Solid Films*, 1975, **29**, 155.
22. C. Edusi, G. Hyett, G. Sankar and I. P. Parkin, *Chem. Vapor. Depos.*, 2011, **17**, 30.
23. K. Oura, V. Lifshits, A. Saranin, A. Zotov and M. Katayama, *Surface Science: An Introduction*, Springer, Berlin, 2003.
24. L. Kong, J. Ma, C. Luan, Z. Zhu and Q. Yu, *Surface Science*, 2010, **605**, 977.
25. A. Niskanen, K. Arstila, M. Ritala and M. Leskela, *J. Electrochem. Soc.*, 2005, **152**, F90.
26. S. E. Potts, W. Keuning, E. Langereis, G. Dingemans, M. C. M. van de Sanden and W. M. M. Kessels, *J. Electrochem. Soc.*, 2010, **157**, P66.
27. H. Lee, K. Kim, J.-J. Woo, D.-J. Jun, Y. Park and Y. S. Kim, *ECS Trans.*, 2009, **25**, 587.
28. P. Michorczyk and J. Ogonowski, *Applied Catalysis A: General*, 2003, **251**, 425-433.
29. T. Miyata, T. Nakatani and T. Minami, *Thin Solid Films*, 2000, **373**, 145-149.
30. S. Mishra, S. Daniele, S. Petit, E. Jeanneau and M. Rolland, *Dalton Trans.*, 2009, 2569.
31. Z. R. Dai, Z. W. Pan and Z. L. Wang, *J. Phys. Chem. B*, 2002, **106**, 902.
32. J. N. Avaritsiotis and R. P. Howson, *Thin Solid Films*, 1981, **80**, 63-66.
33. S. Sharma and M. K. Sunkara, *J. Am. Chem. Soc.*, 2002, **124**, 12288-12293.
34. S. Elouali, L. G. Bloor, R. Binions, I. P. Parkin, C. J. Carmalt and J. A. Darr, *Langmuir*, 2012, **21**, 1879.
35. Y. Xu and X. Zhou, *Sensor. Actuat. B Chem.*, 2000, **65**, 2-4.
36. M. Fleischer, L. Hoillbauer and H. Meixner, *Sensor. Actuat. B Chem.*, 1994, **18-19**, 119.
37. K. K. Makihija, A. Ray, R. M. Patel, U. B. Rivedi and H. N. Kapse, *Bull. Mater. Sci.*, 2005, **28**, 9-17.
38. T. Takeda, K. Suzuki and M. Nakane, *Sensor. Actuat. B Chem.*, 1993, **13**, 404.
39. L. Mîinea, S. Suh, S. G. Bott, J. Liu, W. Chuc and D. M. Hoffman, *J. Mater. Chem.*, 1999, **9**, 929.

40. M. Valet and D. M. Hoffman, *Chem. Mater.*, 2001, **13**, 2135-2143.
41. D. H. Kuo, C. W. Hsu and C. H. Liang, *J. Electrochem. Soc.*, 2008, **155**, K156.
42. C.-Y. Kuo, S.-Y. Lu and T.-Y. Wei, *J. Crystal Growth*, 2005, **285**, 400-407.
43. J. Park, G. A. Horley, P. O'Brien, A. C. Jones and M. Motevalli, *J. Mater. Chem.*, 2001, **11**, 2346.
44. T. Ohta, *Solar-Hydrogen Energy Systems*, Pergamon Press, Oxford, 1979.
45. K. R. Reyes-Gil, E. A. Reyes-Garcia and D. Raftery, *J. Phys. Chem. C*, 2007, **111**, 14579.
46. J. Sato, N. Saito, H. Nishiyama and Y. Inoue, *J. Phys. Chem. B*, 2001, **105**, 6061-6063.
47. A. C. Jones, *J. Mater. Chem.*, 2002, **12**, 2576.
48. K. G. Caulton and L. G. Hubert-Pfalzgraf, *Chem. Rev.*, 1990, **90**, 969-995.
49. A. C. Jones, T. J. Leedham, P. J. Wright, M. J. Crosbie, D. J. Williams, H. O. Davies, K. A. Fleeting, P. O'Brien and M. E. Pemble, *Mat. Sci. Semicon. Proc.*, 1999, **2**, 165.
50. A. C. Jones, S. A. Rushworth and J. Auld, *J. Cryst. Growth*, 1995, **146**, 503.
51. L. Miñea, S. Suh, S. G. Bott, J. Liu, W. Chuc and D. M. Hoffman, *J. Mater. Chem.*, 1999, **9**, 929.
52. D. J. Otway and W. S. Rees, *Coord. Chem. Rev.*, 2000, **210**, 279.
53. A. P. Purdy, A. D. Berry, R. T. Holm, M. Fatemi and D. K. Gaskill, *Inorg. Chem.*, 1989, **28**, 2799.
54. S. Basharat, C. J. Carmalt, R. Palgrave, S. A. Barnett, D. A. Tocher and H. O. Davies, *J. Organomet. Chem.*, 2008, **693**, 1787.
55. P. P. Power, *Chem. Rev.*, 1999, **99**, 3463.
56. C. J. Carmalt, *Coord. Chem. Rev.*, 2001, **223**, 217.
57. C. J. Carmalt and S. J. King, *Coord. Chem. Rev.*, 2006, **250**, 682.
58. G. E. Coates and R. G. Hayter, *J. Chem. Soc.*, 1953, 2519.
59. Y. Aleksandrov, N. Chikinova, G. Makin, V. Alferov and I. Stepanova, *Zh. Obsh. Khim.*, 1984, **54**, 963.
60. Y. Aleksandrov, N. Chikinova, G. Makin, V. Bregadze and L. Golubinskaya, *Metallorgan. Khim.*, 1989, **2**, 524.
61. N. Chikinova, V. Alferov, V. Alyasov, Y. Aleksandrov, N. Vyshinskii and V. Tsvetkov, *Zh. Obsh. Khim.*, 1989, **59**, 1795.
62. G. Mann, H. Olapinski and R. Ott, *Z. Anorg. Allg. Chem.*, 1974, **410**, 195.

63. S. Chitsaz, E. Iravani and B. Neumüller, *Z. Anorg. Allg. Chem.*, 2002, **628**, 2279.
64. H.-U. Schwering, E. Jungk and J. Weidlein, *J. Organomet. Chem.*, 1975, **91**, C4.
65. M. Power, W. Cleaver, A. Apblett and A. Barron, *Polyhedron*, 1992, **11**, 477.
66. W. Cleaver, A. Barron, A. McGufey and S. Bott, *Polyhedron*, 1994, **13**, 2831.
67. A. Keys, T. Barbarich, S. Bott and A. Barron, *Dalton Trans.*, 2000, 577.
68. N. N. Chamazi, M. M. Heravi and B. Neumüller, *Z. Anorg. Allg. Chem.*, 2007, **633**, 1239.
69. Y. Shen, Y. Pan, X. Jin, X. Xu, X. Sun and X. Huang, *Polyhedron*, 1999, **18**, 2423.
70. C. E. Knapp, L. Pemberton, C. J. Carmalt, D. Pugh, P. F. McMillan, S. A. Barnett and D. A. Tocher, *Main Group Chem.*, 2010, **9**, 31.
71. H. Schumann, S. Wernik, B. C. Wassermann and F. Girgsdies, *J. Organomet. Chem.*, 2001, **621**, 317.
72. S. Basharat, C. E. Knapp, C. J. Carmalt, S. A. Barnett and D. A. Tocher, *New J. Chem.*, 2008, **32**, 1513.
73. A. Willner, A. Hepp and N. W. Mitzel, *Dalton Trans.*, 2008, 6832.
74. C. E. Knapp, C. J. Carmalt, P. McMillan, D. A. Wann, H. E. Robertson and D. W. H. Rankin, *Dalton Trans.*, 2008, 6880.
75. C. E. Knapp, D. A. Wann, A. Bil, J. T. Schirlin, H. E. Robertson, P. F. McMillan, D. W. H. Rankin and C. J. Carmalt, *Inorg. Chem.*, 2012, **51**, 3324.
76. B. Louie, S. Rettig, A. Storr and J. Trotter, *Can. J. Chem.*, 1985, **63**, 3019.
77. D. Cooper, S. J. Rettig, A. Storr and J. Trotter, *Can. J. Chem.*, 1986, **64**, 566.
78. E. Onyiriuka and A. Storr, *Can. J. Chem.*, 1987, **1987**, 1367.
79. A. Mar, S. Rettig, A. Storr and J. Trotter, *Can. J. Chem.*, 1988, **66**, 101.
80. G. E. Coates and R. Whitcombe, *J. Chem. Soc.*, 1956, 3351.
81. H. Schmidbaur, *Angew. Chem. Int. Edit. Engl.*, 1965, **4**, 152.
82. B. Armer and H. Schmidbaur, *Chem. Ber.*, 1967, **100**, 1521.
83. D. Bradley, D. Frigo, M. Hursthouse and B. Hussain, *Organometallics*, 1988, **7**, 1112.
84. T. Trentler, S. Goel, K. Hickman, A. Viano, M. Chiang, A. Beatty, P. Gibbons and W. Buhro, *J. Am. Chem. Soc.*, 1997, **119**, 2171.
85. H. Schumann, J. Kaufmann, B. C. Wassermann, F. Girgsdies, N. Jaber and J. Blum, *Z. Anorg. Allg. Chem.*, 2002, **628**, 971.

-
86. T.-Y. Chou, Y. Chi, S.-F. Huang, C.-S. Liu, A. J. Carty, L. Scoles and K. A. Udachin, *Inorg. Chem.*, 2003, **42**, 6041.
87. E. Hecht, T. Gelbrich, K.-H. Thiele and J. Sieler, *Main Group Chem.*, 2000, **3**, 109.
88. Y. Shen, J. Han, H. Gu, Y. Zhu and Y. Pan, *J. Organomet. Chem.*, 2004, **689**, 3461.
89. B. Neumüller, *Chem. Soc. Rev.*, 2003, **32**, 50.
90. S. R. Bindal, P. N. Kapoor and R. C. Mehrotra, *Inorg. Chem.*, 1968, **7**, 385.
91. M. Veith, S. Faber, H. Wolfanger and V. Huch, *Chem. Ber.*, 1996, **129**, 381.
92. N. N. Chamazi, M. M. Heravi and B. Neumüller, *Z. Anorg. Allg. Chem.*, 2007, **633**, 709.
93. M. Veith, S. Hill and V. Huch, *Eur. J. Inorg. Chem.*, 1999, 1343.
94. H. Schumann, R. Mohtachemi and M. Schwichtenberg, *Z. Naturforsch.*, 1988, **43b**, 1510.
95. R. C. Mehrotra and R. K. Mehrotra, *Curr. Sci.*, 1964, **33**, 241.
96. H. Funk and A. Paul, *Z. Anorg. Allg. Chem.*, 1964, **330**, 70.
97. A. Tanner and R. Reinmann, *Z. Naturforsch.*, 1965, **20b**, 524.
98. H. Booch, A. Paul and H. Funk, *Z. Anorg. Allg. Chem.*, 1965, **337**, 145.
99. S. R. Bindal, V. K. Mathur and R. C. Mehrotra, *J. Chem. Soc.*, 1969, 863.
100. S. Daniele, D. Tcheboukov and L. G. H. Pfalzgraf, *J. Mater. Chem.*, 2002, **12**, 2519.
101. D. Pugh, L. G. Bloor, I. P. Parkin and C. J. Carmalt, *Chem. Eur. J.*, 2012, **18**, 6079.
102. S. Chatterjee, S. R. Bindal and R. C. Mehrotra, *J. Indian Chem. Soc.*, 1976, **53**, 867.
103. S. Daniele, D. Tcheboukov, L. G. Hubert-Pfalzgraf and S. Lecocq, *Inorg. Chem. Commun.*, 2002, **5**, 347.
104. S. Suh and D. M. Hoffman, *J. Am. Chem. Soc.*, 2000, **122**, 9396.
105. A. H. Wolfgang and W. H. O. R. Norbert, *Angew. Chem. Int. Edit.*, 1995, **34**, 2187.
106. N. Hollingsworth, M. Kanna, G. Kociok-Kohn, K. C. Molloy and S. Wongnawa, *Dalton Trans.*, 2008, 631.
107. C. E. Knapp, Synthesis, chemical vapour deposition and structural studies of group 13 alkoxides. Doctoral thesis, UCL (University College London), 2010.

-
108. Y. Chi, T.-Y. Chou, Y.-J. Wang, S.-F. Huang, A. J. Carty, L. Scoles, K. A. Udachin, S.-M. Peng and G.-H. Lee, *Organometallics*, 2004, **23**, 95.
109. D. A. Atwood, A. H. Cowley, R. A. Jones, M. A. Mardones, J. L. Atwood and S. G. Bott, *J. Coord. Chem.*, 1992, **26**, 285
110. K. H. Thiele, E. Hecht, T. Gelbrich and U. Dumichen, *J. Organomet. Chem.*, 1997, **540**, 89-94.
111. S. J. Rettig, A. Storr and J. Trotter, *Can. J. Chem.*, 1975, **53**, 58.
112. H. Schumann, M. Frick, B. Heymer and F. Girgsdies, *J. Organomet. Chem.*, 1996, **512**, 117.
113. R. Harris, *Nuclear Magnetic Resonance Spectroscopy - A Physicochemical View*, Longman Scientific & Technical, 1986.
114. C. E. Housecroft and A. G. Sharpe, *Inorganic Chemistry (3rd ed.)*, Prentice Hall, 2008.
115. H. Schumann, J. Kaufmann, B. C. Wassermann, F. Girgsdies, N. Jaber and J. Blum, *Zeitschrift für anorganische und allgemeine Chemie*, 2002, **628**, 971.
116. A. Ortiz, J. C. Alonso, E. Andrade and C. Urbiola, *J. Electrochem. Soc.*, 2001, **148**, F26.
117. S. Bhattacharya, S. Singh and V. D. Gupta, *J. Chem. Crystallogr.*, 2002, **32**, 299.
118. M. Neiminen, L. Niinisto and E. Rauhala, *J. Mater. Chem.*, 1996, **6**.
119. Q. Peng, D. Hojo, K. J. Park and G. N. Parsons, *Thin Solid Films*, 2008, **516**, 4997.
120. P. Wu, Y.-M. Gao, R. Kershaw, K. Dwight and A. Wold, *Mater. Res. Bull.*, 1990, **25**, 357.
121. S. Venkat, N. Pammi, B. S. Sahu, N.-J. Seong and S.-G. Yoon, *J. Vac. Sci. Technol. B*, 2008, **26**, 909.
122. R. A. Sailer, A. Wagner, C. Schmit, N. Klaverkamp and D. L. Schluz, *Surf. Coat. Tech.*, 2008, **203**, 835.
123. S. Reich, H. Suhr and B. Waimer, *Thin Solid Films*, 1990, **189**, 293.
124. D. Pugh, L. G. Bloor, S. Sathasivam, I. P. Parkin and C. J. Carmalt, *Eur. J. Inorg. Chem.*, 2011, 1953.
125. O. T. Beachley, J. R. Gardinier and M. R. Churchill, *Organometallics*, 2003, **22**, 1145.
126. C. Xu, T. H. Baum, I. Guzei and A. L. Rheingold, *Inorg. Chem.*, 2000, **39**, 2008.

127. S. Bhattacharya, N. Seth, D. K. Srivastava, V. D. Gupta, H. Noth and M. Thomann-Albach, *Dalton Trans.*, 1996, 2815.
128. A. B. Pangborn, M. A. Giardello, R. H. Grubbs, R. K. Rosen and F. J. Timmers, *Organometallics*, 1996, **15**, 1518-1520.
129. J. L. Atwood, S. G. Bott, F. M. Elms, C. Jones, C. L. Raston and Inorg. Chem. 1991, 3792., *Inorg. Chem.*, 1991, **30**, 3792.
130. T. B. Karpishin, T. D. P. Stack and K. N. Raymond, *J. Am. Chem. Soc.*, 1993, **115**, 182.
131. R. Nomura, S. Inazawa and H. Matsuda, *Polyhedron*, 1987, **6**, 507.
132. J. Ni, L. Wang, Y. Yang, H. Yan, S. Jin and T. J. Marks, *Inorg. Chem.*, 2005, **44**, 6071.
133. L. G. Bloor, D. Pugh and C. J. Carmalt, *Coord. Chem. Rev.*, 2011, **255**, 1293.
134. D. H. Kim, S. H. Yoo, T.-M. Chung, K.-S. An, H.-S. Yoo and Y. Kim, *Bull. Korean Chem. Soc.*, 2002, **23**, 225.
135. Y. Kokubun, K. Miura, F. Endo and S. Nakagomi, *Appl. Phys. Lett.*, 2007, **90**, 031912.
136. Y. Li, A. Trinchi, W. Wlodarski, K. Galatsis and K. Kalantar-Zadeh, *Sens. Actuators B*, 2003, **93**, 431.
137. M. Valet and D. M. Hoffman, *Chem. Mater.*, 2001, **13**, 2135.
138. S. Basharat, W. Betchley, C. J. Carmalt, S. Barnett, D. A. Tocher and H. O. Davies, *Organometallics*, 2007, **26**, 403.
139. C. J. Carmalt and S. J. King, *Coord. Chem. Rev.*, 2006, **250**, 682-709.
140. J. Ahman, G. Svensson and J. Albertsson, *Acta Cryst.*, 1996, **52**, 1336.
141. J. Tauc Ed, *Proceedings of the International School of Physics, Enrico Fermi, Course XXXIV, The Optical Properties of Solids*, 1966.
142. L. Nagarajan, R. A. De Souza, D. Samuelis, I. Valov, A. Borger, J. Janek, K.-D. Becker, P. C. Schmidt and M. Martin, *Nat. Mater.*, 2008, **7**, 391.
143. R. Swanepoel, *J. Phys. E*, 1983, **16**, 1214.
144. H. Xie, L. Zhu, L. Wang, S. Chen, D. Yang, L. Yang, G. Gao and H. Yuan, *Particuology*, 2011, **9**, 75.
145. H. L. Hartnagel, A. L. Dawar, A. K. Jain and C. Jagadish, *Semiconducting Transparent Thin Films*, IOP Publishing, Bristol, 1995.
146. S. Chatterjee, S. R. Bindal and R. C. Mehrotra, *J. Indian Chem. Soc.*, 1976, **53**, 867.

-
147. D. C. Bradley, H. Chudzynska, D. M. Frigo, M. B. Hursthouse and M. A. Mazid, *Chem. Commun.*, 1988, 1258.
148. C. Cantalini, W. Wlodarski, H. T. Sun, M. Z. Atashbar, M. Passacantando and S. Santucci, *Sens. Actuators B*, 2000, **65**, 101.
149. L. A. Miinea, S. Suh and D. M. Hoffman, *Inorg. Chem.*, 1999, **38**, 4447.
150. S. Basharat, C. J. Carmalt, S. A. Barnett, D. A. Tocher and H. O. Davies, *Inorg. Chem.*, 2007, **46**, 9473.
151. S. Basharat, C. J. Carmalt, S. J. King, E. S. Peters and D. A. Tocher, *Dalton Trans.*, 2004, 3475.
152. S. Mishra, S. Daniele, S. Petit, E. Jeanneau and M. Rolland, *Dalton Trans.*, 2009, 2569.
153. A. Fujishima and K. Honda, *Nature*, 1972, **238**, 37.
154. S. U. M. Khan, M. Al-Shahry and W. B. Ingler Jr., *Science*, 2002, **297**, 2243.
155. K. Noworyta and J. Augustynski, *J. Electrochem. Solid-State Lett.*, 2004, **7**, E31.
156. J. H. Park, S. Kim and A. J. Bard, *Nano Lett.*, 2006, **6**, 24.
157. R. Asahi, T. Morikawa, T. Ohwaki, K. Aoki and Y. Taga, *Science*, 2001, **293**, 269.
158. S. Yin, H. Yamaki, M. Komatsu, Q. Zhang, J. Wang, Q. Tang, F. Saito and T. Sato, *J. Mater. Chem.*, 2003, **13**, 2996.
159. X. Chen and C. Burda, *J. Phys. Chem. B*, 2004, **108**, 15446.
160. Y. Aita, M. Komatsu, S. Yin and T. Sato, *J. Solid. State. Chem.*, 2004, **117**, 3235.
161. Y. Sakatani, J. Nunoshige, H. Ando, K. Okusako, H. Koike, T. Takata, J. N. Kondo, M. Hara and K. Domen, *Chem. Lett.*, 2003, **32**, 1156.
162. S. Sato, *Chem. Phys. Lett.*, 1986, **123**, 126.
163. O. Diwald, T. L. Thompson, T. Zubkov, E. G. Goralski, S. D. Walck and J. T. J. Yates, *J. Phys. Chem. B*, 2004, **108**, 6004.
164. J. Kim, S. G. Bott and D. M. Hoffman, *Inorg. Chem.*, 1998, **37**, 3835.
165. D. T. Clark, T. Fok, G. G. Roberts and R. W. Sykes, *Thin Solid Films*, 1980, **70**, 261.
166. S. Suh and D. M. Hoffman, *J. Am. Chem. Soc.*, 2000, **122**, 9396-9404.
167. C. W. Dunnill, Z. Ansari, A. Kafizas, S. Perni, D. J. Morgan, M. Wilson and I. P. Parkin, *J. Mater. Chem.*, 2011, **21**, 11854.
168. C. W. Dunnill and I. P. Parkin, *Chem. Vapor. Depos.*, 2009, **15**, 171.

-
169. C. W. Dunnill, Z. A. Aiken, J. Pratten, M. Wilson, D. J. Morgan and I. P. Parkin, *J. Photochem. Photobiol. A*, 2009, **207**, 244.
170. C. W. Dunnill and I. P. Parkin, *Dalton Trans.*, 2011, **40**, 1635.
171. C. Edusi, G. Sankar and I. P. Parkin, *Chem. Vapor. Depos.*, 2012, DOI: 10.1002/cvde.201106961.
172. D. Lapedes, *Dictionary of Scientific & Technical Terms: Second Edition*, McGraw Hill, New York, 1978.
173. D. Liu, W. W. Lei, B. Zou, S. D. Yu, J. Hao, K. Wang, B. B. Liu, Q. L. Cui and G. T. Zou, *J. Appl. Phys.*, 2008, **104**, 083506.
174. D. K. Schroder, *Semiconductor Material and Device Characterization, 2nd Edition*, John Wiley & Sons, New York, 1998.
175. A. Golan, J. Bregman, Y. Shapira and M. Eizenberg, *Appl. Phys. Lett.*, 1990, **57**, 2205.
176. Y. C. Lee, Y. P. Hong, H. Y. Lee, H. Kim, Y. J. Jung, K. H. Ko, H. S. Jung and K. S. Hong, *J. Colloid Interfac. Sci.*, 2003, **267**, 127.
177. C. R. Crick and I. P. Parkin, *J. Mater. Chem.*, 2009, **19**, 1074.
178. G. Hyett, J. A. Darr, A. Mills and I. P. Parkin, *Chem. Vapor. Depos.*, 2010, **16**, 301.
179. V. C. Gonçalves and D. T. Balogh, *Sensors and Actuators B: Chemical*, 2011, **162**, 307.
180. D. E. Williams, *Sensors and Actuators B: Chemical*, 1999, **57**, 1.
181. X. Wang, S. Ji, H. Wang and D. Yan, *Organic Electronics*, 2011, **12**, 2230.
182. K. Nishida, M. Ishii, S. Tsushima and S. Hirai, *J. Power Sources*, 2011, **199**, 155.
183. N. B. Ekua, M. P. Germano, O. C. William, Q. L. Peter and F. G. Claire, *Appl. Phys. A*, 2012, **100**, 011104.
184. D. Niemeyer, D. Williams, P. Smith, K. Pratt, B. Slater, C. Catlow and A. Stoneham, *J. Mater. Chem.*, 2002, **12**, 667.
185. D. Williams and K. Pratt, *Sensor. Actuat. B Chem.*, 2000, **70**, 214.
186. P. T. Moseley, J. O. W. Norris and D. E. Williams, in *Techniques and Mechanisms in Gas Sensing*, Adam Hilger, Bristol, Editon edn., 1991.
187. L. Erades, D. Grandjean, C. Nayral, K. Soulantica, B. Chaudret, P. Menini, F. Parret and A. Maisonnat, *New. J. Chem.*, 2006, **30**, 1026-1035.
188. V. N. Mishra and R. P. Agarwal, *Microelectronics Journal*, 1998, **29**, 861.

-
189. B. Suparna, B. Ali and P. S. Devi, *Nanotechnology*, 2011, **22**, 275506.
190. X. Li, J. H. Cho, P. Kurup and Z. Gu, *Sensors and Actuators B: Chemical*, 2011, **162**, 251.
191. C. Zhang, A. Boudiba, M.-G. Olivier, R. Snyders and M. Debliquy, *Thin Solid Films*, 2012, **520**, 3679.
192. S. C. Naisbitt, K. F. E. Pratt, D. E. Williams and I. P. Parkin, *Sensor. Actuat. B Chem.*, 2006, **114**, 969.
193. G. Jimenez-Cadena, E. Comini, M. Ferroni, A. Vomiero and G. Sberveglieri, *Materials Chemistry and Physics*, 2010, **124**, 694.
194. C. M. Ghimbeu, M. Lumbreras, M. Siadat and J. Schoonman, *Materials Chemistry and Physics*, 2009, **114**, 933.
195. N. C. Oldham, C. M. Garland and T. C. McGill, *J. Vac. Sci. Technol. A*, 2002, **20**, 809.
196. A. Ortiz, J. C. Alonso, E. Andrade and C. Urbiola, *J. Electrochem. Soc.*, 2001, **148**, F26.
197. T. Schwebel, M. Fleischer, H. Meixner and C. D. Kohl, *Sensor. Actuat. B Chem.*, 1998, **49**, 46.
198. M. Fleischer and H. Meixner, *Sensor. Actuat. B Chem.*, 1995, **26-27**, 81.
199. W. Y. Chung, *J. Mater. Sci.-Mater. El.*, 2001, **12**.
200. J. Frank, A. Fleischer, A. Zimmer and H. Meixner, *Sensors Journal, IEEE*, 2001, **1**, 318.
201. N. Yamazoe, *Sensor. Actuat. B Chem.*, 1991, 7.
202. Y.-M. Sung, D.-H. Kim, D.-K. Lee and D.-H. Lee, *Frontier Appl. Plasma Technol.*, 2011, **4**, 46.
203. D. N. Chavan, V. B. Gaikwad, G. E. Patil, D. D. Kajale and G. H. Jain, *Sensor. Trans. J.*, 2011, **129**, 122.
204. C. Ishibashi, T. Hyodo, Y. Shimizu and M. Egashira, *Sensor. Letts.*, 2011, **9**, 369.
205. Y. Xie, S. Z and J. Liu, *Adv. Mater. Res.*, 2011, **239-242**, 322.
206. N. Singh, R. K. Gupta and P. S. Lee, *ACS Appl. Mater. Inter.*, 2011, **3**, 2246.
207. J. Liu, Z. Guo, K. Zhu, W. Wang, C. Zhang and X. Chen, *J. Mater. Chem.*, 2011, **21**, 11412.
208. C. Shekhar, K. I. Gnanasekar, E. Prabhu, V. Jayaraman and T. Gnanasekaran, *Sensor. Actuat. B Chem.*, 2011, **8155**, 19.

-
209. Q. Tang, W. Zhou, W. Zhang, S. Ou, K. Jian, W. Yu and Y. Qian, *Cryst. Grow. Des.*, 2005, **5**, 147.
210. G. Korotcenkov, A. Cerneavski, V. Brinzari, A. Vasiliev, M. Ivanov, A. Cornet, J. Morante, A. Cabot and J. Arbiol, *Sensor. Actuat. B Chem.*, 2004, **99**, 297.
211. J. Xu, X. H. Wang and J. N. Shen, *Sensor. Actuat. B Chem.*, 2006, **115**, 642.
212. B. X. Li, Y. Xie, M. Jing, G. X. Rong, Y. C. Tang and G. Z. Zhang, *Langmuir*, 2006, **22**, 9380.
213. K. Yao, D. Caruntu, Z. Zeng, J. Chen, C. J. O'Connor and W. Zhou, *J. Phys. Chem. C*, 2009, **113**, 14812.
214. Z. Zhang, J. B. M. Goodall, D. J. Morgan, S. Brown, R. J. H. Clark, J. C. Knowles, N. J. Mordan, J. R. Evans, A. F. Carley, M. Bowker and J. A. Darr, *J. Euro. Ceram. Soc.*, 2009, **29**, 2343.
215. Z. Zhang, S. Brown, J. B. M. Goodall, X. Weng, K. Thompson, K. Gong, S. Kellici, R. J. H. Clark, J. R. G. Evans and J. A. Darr, *J. Alloys Compd.*, 2009, **476**, 451.
216. X. L. Weng, B. Perston, X. Z. Wang, I. Abrahams, T. Lin, S. F. Yang, J. R. G. Evans, N. J. Mordan, A. F. Carley, M. Bowker, J. C. Knowles, I. Rehman and J. A. Darr, *App. Catal. B*, 2009, 405.
217. X. L. Weng, P. Boldrin, I. Abrahams, S. J. Skinner and J. A. Darr, *Chem. Mater.*, 2007, **19**, 4382.
218. X. L. Weng, D. Brett, V. Yufit, P. Shearing, N. Brandon, M. Reece, H. X. Yan, C. Tighe and J. A. Darr, *Solid State Ionics*, 2010, **181**, 827.
219. A. A. Chaudhry, S. Haque, S. Kellici, P. Boldrin, I. Rehman, A. K. Fazal and J. A. Darr, *Chem. Commun.*, 2006, 2286.
220. A. A. Chaudhry, J. B. M. Goodall, M. Vickers, J. K. Cockcroft, I. Rehman, J. C. Knowles and J. A. Darr, *J. Mater. Chem.*, 2008, **18**, 5900.
221. P. Boldrin, A. K. Hebb, A. A. Chaudhry, L. Otley, B. Thiebaut, P. Bishop and J. A. Darr, *Ind. Eng. Chem. Res.*, 2007, **46**, 4830.
222. G. S. Henshaw, D. H. Dawson and D. E. Williams, *J. Mater. Chem.*, 1995, **5**, 1791.
223. G. F. Fine, L. M. Cavanagh, A. Afonja and R. Binions, *Sensors*, 2010, **10**, 5468.
224. P. Varsani, A. Afonja, D. E. Williams, I. P. Parkin and R. Binions, *Sensors and Actuators B: Chemical*, 2011, **160**, 475.
225. V. Dusastre and D. E. Williams, *J. Mater. Chem.*, 1999, **9**, 965.

-
226. I. Jimenez, M. A. Centeno, R. Scotti, F. Morazzoni, A. Cornet and J. R. Morante, *J. Electrochem. Soc.*, 2003, **150**, H72.
227. Y. S. Kim, S. C. Ha, K. Kim, H. Yang, S. Y. Choi, Y. T. Kim, J. T. Park, C. J. Lee, J. Choi, J. Paek and K. Lee, *Appl. Phys. Lett.*, 2005, **86**, 213105.
228. G. Korotcenkov, V. Brinzari, V. Golovanov, A. Cerneavschi, V. Matolin and A. Tadd, *App. Surf. Sci.*, 2004, **227**, 122.
229. N. Savage, B. Chwieroth, A. Ginwalla, B. R. Patton, S. A. Akbar and P. K. Dutta, *Sensor. Actuat. B*, 2001, **79**, 17.
230. R. Binions, H. Davies, A. Afonja, S. Dungey, D. Lewis, D. E. Williams and I. P. Parkin, *J. Electrochem. Soc.*, 2009, **156**, J46.
231. M. Ali, C. Y. Wang, C.-C. Röhlig, V. Cimalla, T. Stauden and O. Ambacher, *Sensor. Actuat. B Chem.*, 2008, **129**, 467.
232. A. Gurlo, N. Barsan, M. Ivanovska, U. Weimar and W. Göpel, *Sensor. Actuat. B Chem.*, 1998, **47**, 92.
233. C. Wang, Y. Dai, J. Pezoldt, B. Lu, T. Kups, V. Cimalla and O. Ambacher, *Cryst. Grow. Des.*, 2008, **8**, 1257.
234. M. E. Franke, T. J. Koplín and U. Simon, *Small*, 2006, **2**, 36.
235. J. Xu, Y. Chen and J. Shen, *Mater. Lett.*, 2008, **62**, 1363.
236. K. K. Makhija, A. Ray, R. M. Patel, U. B. Rivedi and N. H. Kapse, *Bull. Mater. Sci.*, 2005, **28**, 9.
237. C. Xiangfeng, W. Caihong, J. Dongli and Z. Chengmu, *Chem. Phys. Lett.*, 2004, **399**, 461.
238. L. G. Bloor, D. Pugh and C. J. Carmalt, *Coord. Chem. Rev.*, 2011, **255**, 1293-1318.
239. C. E. Knapp, A. Kafizas, I. P. Parkin and C. J. Carmalt, *J. Mater. Chem.*, 2011, **21**, 12644.
240. T. Maruyama and T. Kitamura, *Jpn. J. Appl. Phys.*, 1989, **28**, L1096.
241. T. Maruyama and K. Fukui, *Jpn. J. Appl. Phys.*, 1990, **29**, L1705.
242. S. Matsushima, Y. Teraoka, N. Miura and N. Yamazoe, *Jpn. J. Appl. Phys.*, 1988, **27**, 1798.
243. N. Yamazoe, *Sensor. Actuat. B*, 1991, **7**, 19.
244. G. F. Fine, L. M. Cavanagh, A. Afonja and R. Binions, *Sensors*, 2010, **10**, 5468-5502.

245. C. Xu, J. Taamaki, N. Mirua and N. Yamazoe, *Sensor. Actuat. B Chem.*, 1991, **3**, 147.
246. G. P. Schwartz, W. A. Sunder and J. E. Griffiths, *J. Electrochem. Soc.*, 1982, **129**, 1361.

8. Publications

1. Leanne G. Bloor, Joe Manzi, Russell Binions, Ivan P. Parkin, David Pugh, Ayo Afonja, Christopher S. Blackman, Sanjayan Sathasivam and Claire J. Carmalt, *Tantalum and Titanium doped In_2O_3 Thin Films by Aerosol-Assisted Chemical Vapour Deposition and their Gas Sensing Properties*, submitted to *Chemistry of Materials* and awaiting final revisions, May **2012**.
2. David Pugh, Leanne G. Bloor, Ivan P. Parkin and Claire J. Carmalt, *Gallium Hydride Complexes Stabilised by Multidentate Alkoxide Ligands: Precursors to Thin Films of Ga_2O_3 at Low Temperatures*, *Chemistry - A European Journal*, **2012**, 18, 6079.
3. Sofia Elouali, Leanne G. Bloor, Russell Binions, Ivan P. Parkin, Claire J. Carmalt and Jawwad A. Darr, *Gas Sensing with Nano-Indium Oxides (In_2O_3) Prepared via Continuous Hydrothermal Flow Synthesis*, *Langmuir*, **2012**, 28, 1879.
4. Leanne G. Bloor, Claire J. Carmalt and David Pugh, *Single-source precursors to gallium and indium oxide thin films*, *Coordination Chemistry Reviews*, **2011**, 225, 1293.
5. David Pugh, Leanne G. Bloor, Sanjayan Sathasivam, Ivan P. Parkin and Claire J. Carmalt, *Gallium and Indium β -Diketonate Complexes: AACVD of $[In(thd)_3]$ and the Attempted Synthesis of Gallium and Indium Bis(β -diketonates)*, *European Journal of Inorganic Chemistry*, **2011**, 2011, 1953.
6. David Pugh, Leanne G. Bloor, Savio Moniz and Claire J. Carmalt, *Main Group Single-Source Precursors*, book chapter for *Comprehensive Inorganic Chemistry*, submitted in **2011**, In press, expected publication Jan **2013**.

9. Appendix - Crystallographic Data

Table 9.1. Crystal data and structure refinement for [GaCl(OCH₂CH₂NEt₂)₂] (3).

Empirical formula	C ₁₂ H ₂₈ ClGaN ₂ O ₂
Formula weight	337.53
Temperature	150(2) K
Wavelength	0.71073 Å
Crystal system	Monoclinic
Space group	P21/c
Unit cell dimensions	a = 15.924(2) Å α = 90°. b = 7.0297(9) Å β = 114.538(2)°. c = 15.4616(19) Å γ = 90°.
Volume	1574.5(3) Å ³
Z	4
Density (calculated)	1.424 Mg/m ³
Absorption coefficient	1.915 mm ⁻¹
F(000)	712
Crystal size	0.40 x 0.40 x 0.05 mm ³
Theta range for data collection	1.41 to 28.24°.
Index ranges	-20 ≤ h ≤ 21, -9 ≤ k ≤ 9, -20 ≤ l ≤ 19
Reflections collected	2618
Independent reflections	3677 [R(int) = 0.0354]
Completeness to theta	= 28.24° 94.3 %
Absorption correction	Semi-empirical from equivalents
Max. and min. transmission	0.9103 and 0.5147
Refinement method	Full-matrix least-squares on F ²
Data / restraints / parameters	3677 / 0 / 167
Goodness-of-fit on F ²	1.060
Final R indices	[I > 2σ(I)] R1 = 0.0305, wR2 = 0.0778
R indices (all data)	R1 = 0.0345, wR2 = 0.0818
Largest diff. peak and hole	0.759 and -0.817 e.Å ⁻³

Table 9.2. Crystal data and structure refinement for [GaCl₂(OCH₂CH₂NEt₂)₂] (4).

Empirical formula	C ₁₂ H ₂₈ Cl ₄ Ga ₂ N ₂ O ₂
Formula weight	513.60
Temperature	120(2) K
Wavelength	0.71073 Å
Crystal system	Monoclinic
Space group	P21/c
Unit cell dimensions	a = 7.2890(3) Å α = 90°. b = 13.0836(4) Å β = 96.584(2)°. c = 10.5300(4) Å γ = 90°.
Volume	997.58(6) Å ³
Z	2
Density (calculated)	1.710 Mg/m ³
Absorption coefficient	3.242 mm ⁻¹
F(000)	520
Crystal size	0.22 x 0.13 x 0.04 mm ³
Theta range for data collection	3.22 to 27.51°.
Index ranges	-9 ≤ h ≤ 9, -16 ≤ k ≤ 16, -13 ≤ l ≤ 13
Reflections collected	10833
Independent reflections	2285 [R(int) = 0.0423]
Completeness to theta	= 28.24° 99.5 %
Absorption correction	Semi-empirical from equivalents
Max. and min. transmission	0.8813 and 0.5357
Refinement method	Full-matrix least-squares on F ²
Data / restraints / parameters	2285 / 0 / 102
Goodness-of-fit on F ²	1.085
Final R indices	[I > 2σ(I)] R1 = 0.0278, wR2 = 0.0578
R indices (all data)	R1 = 0.0348, wR2 = 0.0603
Largest diff. peak and hole	0.362 and -0.470 e.Å ⁻³

Table 9.3. Crystal data and structure refinement for [GaCl(OCH₂CH₂CH₂NMe₂)₂] (**5**).

Empirical formula	C ₁₀ H ₂₄ Cl Ga N ₂ O ₂
Formula weight	309.48
Temperature	150(2) K
Wavelength	0.71073 Å
Crystal system	Monoclinic
Space group	P21/c
Unit cell dimensions	a = 0.0997(17) Å α = 90°. b = 9.9824(17) Å β = 113.718(9)°. c = 15.543(2) Å γ = 90°.
Volume	1434.7(4) Å ³
Z	4
Density (calculated)	1.433 Mg/m ³
Absorption coefficient	2.094 mm ⁻¹
F(000)	648
Crystal size	0.20 x 0.20 x 0.10 mm ³
Theta range for data collection	2.49 to 28.27°.
Index ranges	-12 ≤ h ≤ 13, -13 ≤ k ≤ 12, -20 ≤ l ≤ 20
Reflections collected	11541
Independent reflections	3362 [R(int) = 0.0317]
Completeness to theta	= 28.24° 94.3 %
Absorption correction	Semi-empirical from equivalents
Max. and min. transmission	0.8179 and 0.6794
Refinement method	Full-matrix least-squares on F ²
Data / restraints / parameters	3362 / 0 / 149
Goodness-of-fit on F ²	1.044
Final R indices	[I > 2σ(I)] R1 = 0.0325, wR2 = 0.0853
R indices (all data)	R1 = 0.0406, wR2 = 0.0901
Largest diff. peak and hole	0.911 and -0.725 e.Å ⁻³